Experiments towards a Quantum Information Network with Squeezed Light and Entanglement

Warwick Paul Bowen

B. Sc. (Hons.), University of Otago, 1998.

A thesis submitted for the degree of
Doctor of Philosophy

The Australian National University

October, 2003

To Eluca

My one true love.

Declaration

This thesis is an account of research undertaken between April 1999 and October 2003 at The Department of Physics, Faculty of Science, The Australian National University, Canberra, Australia.

Except where acknowledged in the customary manner, the material presented in this thesis is, to the best of my knowledge, original and has not been submitted in whole or part for a degree in any university.

Warwick P. Bowen
10th October, 2003

Acknowledgements

This thesis was made possible by the support I received from many friends, family, and colleagues. I am extremely grateful to each of them. Firstly, thank you Ping Koy Lam and Hans Bachor, you have been the most fantastic supervisors. Hans, your ability to judge the evolution of our field is remarkable, and something that can only be truly appreciated with hindsight; and Ping Koy, your insight and breadth of knowledge never ceases to amaze, and the friendship that has developed over the last few years is one that I will treasure. Special thanks also to Tim Ralph, my Ph.D. advisor. Tim, there are so many things I could say, but perhaps the essence is your natural ability to get to the heart of the matter. You make complicated stuff simple, so that even I can understand it.

During my time at the A.N.U. I've been lucky enough to be involved with many talented people. Of everyone, Roman Schnabel deserves particular attention for slaving in the lab with me for what seemed like forever before we finally saw some squeezing, and had a beer. I appreciate also Dan Shaddock, Ben Buchler, and Nicolas Treps, I learnt so much from each of you. Specific thanks to Roman for lab-work in Chapters 3-5, and 7; to Nicolas in Chapters 3, 5, 7, and 8; to Ben in Chapter 5; and to Andrew Lance, Thomas Symul, and Tomáš Tyc in Chapter 6. I deeply appreciate sharing a lab and a laugh with Ulrik Andersen, Shane Bennetts, Marcus Bode, Simon Chelkowski, Aśka Dolińska, Nicolai Grosse, Magnus Hsu, Mat Lawrence, and Kirk McKenzie. The gravitational wave group at A.N.U. provided me with a fantastic laboratory and exquisite experience with optics, interferometers, and control systems. Jong Chow, Glenn Devine, Mal Gray, David McClelland, Ben Sheard, and Bram Slagmolen, thank you. I highly value the interaction I have had with the atom optics guys (and guyettes) John Close, Cameron Fletcher, Simon Haine, Joe Hope, Jessica Lye, Adele Morrison, Nick Robins, and Craig Savage. I particularly appreciate your approachability and patience with my naive quantum optical perspective. I also deeply appreciate Aiden Byrne, Neil Manson, and John Sandeman for their irrepressible good humour and support throughout my Ph.D. Special thanks go to Magnus, Kirk, John, Andrew, Ping Koy, and Hans for proof-reading this thesis; and to Aśka for allowing me to use some of her fantastic cartoons.

The work in Chapter 9 was performed in Jeff Kimble's laboratories at the California Institute of Technology. I am immensely grateful to Jeff for making my visit possible, and for providing such a wonderful environment to do science. His inspiring and thorough approach to research is something I will always admire and aspire to. I was privileged to work closely with Alex Kuzmich, from whom I learnt much about science, integrity, and tennis. Theresa Lynn and JM Geremia, my fellow tennis students, you made my stay in Pasadena all the more enjoyable. I appreciate also the company and advice of Kevin Birnbaum, Andrea Boca, Dave Boozer, James Chou, Andrew Doherty, Lu-Ming Duan, Win Goh, Jason Mckeever, Tracy Northup, and Sheri Stoll. I was extremely lucky in my Pasadena housemates Franchi and Mils. You guys were truly the perfect housemates, I miss you heaps.

Over the last four years I've had the opportunity to collaborate with Barry Sanders, and Claude Fabre. I greatly appreciate both the opportunity to develop this collaboration, and the experience I gained through the interaction.

The electronic circuits used for control systems throughout this thesis were for the most part

designed by Mal Gray, and built by Russell Koehne. Without access to their skills this thesis would have been a pale shade of what it is today. I must also extend the warmest thanks to the A.N.U. Physics department general staff. Zeta Hall, Sharon Lopez, Susan Maloney, Andrew Papworth, and Jenny Willcoxson, thanks for smoothing out the many bumps in the road before they even entered my horizon. Without the support of Brett Brown, Paul MacNamara, Paul Tant, and Chris Woodland in the Physics workshop, the majority of this thesis would not have been possible. They did a truly fantastic job, especially when I went to them needing work done yesterday.

In the last four years in Canberra I have developed many treasured friendships. I would particularly like to mention Clem, Sylvia, Mat, Liz, Minh, Kathryn, Ben, Nic, and Wendy, all of whom have made my life here both memorable and enjoyable. My family in New Zealand have always supported me in whatever I endeavour. Sometimes the Tasman sea seems much wider than it really is.

Most importantly I thank my wife, Eluca. Luca, over the last four years you have been a constant source of inspiration, support, and love. The good times, you made so much better, and the tough times, with you, weren't so tough. 나는 당신을 무척 사랑해요.

Abstract

Quantum information science is a new and promising field of research that combines the techniques developed in quantum mechanics with those of information science. One primary experimental goal of the field is to implement a quantum information network consisting of nodes of atoms at which quantum computational algorithms can be performed connected by optical links. This thesis presents the development of techniques applicable to such a network in the continuous variable regime of quantum mechanics.

We develop a pair of optical parametric amplifiers, each producing a stable strongly squeezed output field at 1064 nm. These optical parametric amplifiers form the work-horse utilised for the majority of the experiments performed in this thesis. The output fields are either amplitude or phase squeezed depending on our control system, with 4.4 dB of squeezing below the quantum noise limit consistently observed. A quadrature entangled state is generated by interfering the squeezed fields on a 50/50 beam splitter. The signature of this form of entanglement is strong correlations between the amplitude and phase quadratures of a pair of fields. We demonstrate that the correlations exhibited in our case are non-classical using a criterion for wave function inseparability, and through observation of the EPR paradox. Since the efficacy of quantum information protocols depends strongly on the properties of the entanglement used, we perform a complete characterisation of our entanglement, introducing a convenient physically relevant characterisation technique. The entanglement is utilised in a quantum teleportation protocol, demonstrating that the quantum statistics of a field can be transferred to another field via detection and classical communication. We investigate in some detail methods that can be used to characterise continuous variable quantum teleportation, and propose a new method that has a direct correspondence to entanglement swapping. We introduce a scheme to perform quantum secret sharing using our entangled state and quantum electro-optical feed-forward. In quantum secret sharing an encoded secret state is distributed securely to a group of players. In ideal circumstances, even if some of the players are malicious, or some distribution channels faulty, the secret can be reconstructed perfectly.

We consider techniques to implement the transfer of quantum states from optical to atomic media. In the continuous variable regime such a transfer has been achieved for polarisation states. We investigate continuous variable polarisation states, demonstrating the transformation of our quadrature squeezed states into a variety of polarisation squeezed states; with one such state exhibiting squeezing of three of the four Stokes operators. Utilising our quadrature entanglement, we then generate continuous variable polarisation entanglement between two Stokes operators of a pair of fields. Interacting this entanglement with a pair of atomic ensembles could provide a macroscopic, spatially separated, source of atomic entanglement. Finally, we investigate the interaction between optical Raman pulses and a cold Cesium atomic ensemble. We manipulate such an ensemble with a sequence of optical pulses, producing non-classically correlated photon pairs. The non-classicality of the correlation is verified through a violation of the Cauchy-Schwarz inequality. The technology developed during this investigation has been shown to enable a feasible quantum information network, quantum memory, and 'on demand' single photon sources.

Contents

Declaration **v**

Acknowledgements **vii**

Abstract **ix**

Glossary of terms **xxi**

1 Introduction **1**

I Quantum optical techniques and quadrature squeezing **5**

Overview 7

2 Theoretical concepts and experimental techniques **9**

- 2.1 The uncertainty principle 9
- 2.2 Squeezing a single electromagnetic oscillation 11
  - 2.2.1 The Wigner function and the ball and stick picture 13
- 2.3 The quantum optics of optical sidebands 14
- 2.4 Amplitude and phase modulation 16
- 2.5 The humble beam splitter 20
  - 2.5.1 Modelling optical attenuation using beam splitters 20
  - 2.5.2 Relative phase error signals for beam splitter inputs 22
- 2.6 Measuring the efficiency of optical processes 24
  - 2.6.1 Inefficiencies due to scattering and absorption in optics 24
  - 2.6.2 Inefficiencies in the photodetection process 24
  - 2.6.3 Inefficiencies in optical mode-matching 25
- 2.7 Detecting quantum states of light 26
  - 2.7.1 Balanced self homodyne detection 27
  - 2.7.2 Balanced homodyne detection 27
  - 2.7.3 Analysis using a spectrum analyser 29
- 2.8 Optical resonators 29
  - 2.8.1 Modelling of optical resonators 30
  - 2.8.2 Error signals to control the length of optical resonators 32
- 2.9 Feedback control of resonance and interference 37
  - 2.9.1 Limitations to the control bandwidth 38
  - 2.9.2 Using preloading to improve the control bandwidth 41
  - 2.9.3 Experimental characterisation of control bandwidth 41
- 2.10 The second order optical nonlinearity 43
  - 2.10.1 Second order nonlinear optical processes 43
  - 2.10.2 Conservation laws and the phase matching condition 44
  - 2.10.3 Equations of motion 46

2.11 Summary . . . 49

3 Generation of quadrature squeezing 51
3.1 The laser . . . 52
3.2 Spectral and spatial mode cleaning resonator . . . 53
3.3 Second harmonic generation . . . 54
3.4 Optical parametric amplification . . . 57
  3.4.1 Classical behaviour . . . 58
  3.4.2 Squeezing of the output coupled field . . . 59
  3.4.3 Generation of squeezed fields . . . 61
  3.4.4 Characterisation of the squeezed fields . . . 63
3.5 Regimes of optical parametric amplification . . . 64
  3.5.1 Classical behaviour of a front seeded optical parametric amplifier . . . 64
  3.5.2 Noise properties of the output fields . . . 66
3.6 Optical parametric amplifiers as unitary squeezers . . . 68
3.7 Recovery of low frequency squeezing . . . 69
  3.7.1 Introduction . . . 69
  3.7.2 Theoretical Background . . . 69
  3.7.3 Experiment . . . 71
3.8 Summary . . . 73

II Quantum communication protocols 75
Overview . . . 77

4 Generation and characterisation of quadrature entanglement 79
4.1 Introduction . . . 79
4.2 Production of continuous variable entanglement . . . 81
4.3 Characterisation of continuous variable entanglement . . . 82
  4.3.1 Gaussian entanglement and the correlation matrix . . . 83
  4.3.2 The inseparability criterion . . . 84
  4.3.3 The EPR paradox criterion . . . 87
  4.3.4 The photon number diagram . . . 88
4.4 Experiment . . . 95
  4.4.1 Generation and measurement of entanglement . . . 96
  4.4.2 Characterisation of the correlation matrix . . . 98
  4.4.3 Characterisation of the inseparability and EPR paradox criteria . . . 99
  4.4.4 Representation of results on the photon number diagram . . . 101
4.5 A simple scheme to reduce $\bar{n}_{\mathrm{excess}}$ with minimum effect on $\bar{n}_{\mathrm{min}}$ . . . 103
4.6 Conclusion . . . 107

5 Quantum teleportation 109
5.1 Introduction . . . 110
5.2 Continuous variable teleportation protocol . . . 111
5.3 Characterisation of teleportation . . . 113
  5.3.1 Fidelity . . . 114
  5.3.2 The conditional variance product and signal transfer . . . 115
  5.3.3 A gain normalised conditional variance product . . . 118

5.3.4 A comparison of fidelity, the T-V diagram, and the gain normalised conditional variance product . . . 120
5.3.5 Entanglement swapping . . . 121
5.4 Experiment . . . 124
5.4.1 Teleportation apparatus . . . 124
5.4.2 Teleportation results . . . 127
5.4.3 Experimental loopholes . . . 131
5.5 Conclusion . . . 133

6 Quantum secret sharing 135
6.1 Introduction . . . 135
6.2 The dealer protocol . . . 137
6.3 The {1,2} reconstruction protocol . . . 138
6.4 The {2,3} reconstruction protocol . . . 138
6.5 Characterisation of the reconstructed state . . . 141
6.6 The cups and balls magic trick without a trick . . . 145
6.7 Conclusion . . . 146

III Interaction of optical fields with atomic ensembles 147
Overview . . . 149

7 Polarisation squeezing 151
7.1 Introduction . . . 151
7.2 Theoretical background . . . 152
7.3 Experiment . . . 155
7.3.1 Measuring the Stokes operators . . . 156
7.3.2 Quantum polarisation states from a single squeezed beam . . . 156
7.3.3 Quantum polarisation states from two quadrature squeezed beams . . . 158
7.4 Poincaré sphere visualisation of polarisation states . . . 160
7.5 Channel capacity achievable using polarisation squeezed beams . . . 162
7.6 Conclusion . . . 165

8 Continuous variable polarisation entanglement 167
8.1 Introduction . . . 167
8.2 Theory . . . 168
8.2.1 Characterising entanglement . . . 168
8.2.2 Generalisation of entanglement criteria to Stokes operators . . . 171
8.3 Experiment . . . 172
8.3.1 Transformation to polarisation entanglement . . . 172
8.3.2 Individual characteristics of the two polarisation entangled beams . . . 173
8.3.3 Measurement of the degree of inseparability . . . 174
8.3.4 Measurement of the degree of EPR paradox . . . 175
8.3.5 An explanation of the transformation between quadrature and polarisation entanglement . . . 177
8.4 Polarisation entanglement of all three Stokes operators . . . 179
8.5 A look at the correlation function . . . 181
8.6 Summary and conclusion . . . 182

9 Non-classical photon pairs from an atomic ensemble **183**
9.1 Introduction 183
9.2 Proposal for quantum communication with atomic ensembles 185
9.3 Verification of the non-classical nature of the fields 187
9.3.1 A Cauchy-Schwarz inequality based on coincidence rates 187
9.3.2 Expected violations of the Cauchy-Schwarz inequality 189
9.4 Experimental realisation 191
9.4.1 Experimental configuration 191
9.4.2 Observed singles rates and their implications 195
9.4.3 Conditional photon statistics of the output field 197
9.4.4 Observed violations of the Cauchy-Schwarz inequality 199
9.5 Conclusion 200

10 Conclusions **201**
10.1 Summary 201
10.1.1 Quantum information protocols 201
10.1.2 Interaction of optical fields with atomic ensembles 202
10.1.3 Progress towards quantum enhancement of measurement devices 202
10.2 Outlook 202
10.2.1 Potential technological improvements 202
10.2.2 Future direction for the entanglement resource 203
10.2.3 The status of quantum information networks 203
10.2.4 Potential enhancement of measurement devices 204

A A more detailed analysis of quantum optical sidebands **205**
A.1 The time domain annihilation operator 205
A.1.1 Annihilation operators in a rotating frame 205
A.2 Detection of an optical field 206
A.3 System time delays and the sideband operator 208

B Electronic circuits **211**
B.1 Detector circuits 211
B.2 High voltage amplifier circuit 213
B.3 Servo circuits 214
B.4 Temperature controller circuits 216

C Sundry equipment and mechanical components **219**

Bibliography **221**

List of Figures

1.1 Thesis structure 2

2.1 Photon number distribution for coherent and squeezed states 13
2.2 Wigner function and ball and stick picture of coherent and squeezed states 13
2.3 Phase and amplitude modulation via the electro-optic effect 17
2.4 Phase and amplitude modulation in the frequency domain 18
2.5 The beam splitter 20
2.6 Equivalence of an inefficient linear process to an efficient linear process, with environmental coupling though a beam splitter. 21
2.7 Sideband picture of modulation locking of the interference at a beam splitter. . . 24
2.8 Typical spectrum recorded by a spectrum analyser. 30
2.9 A model of a passive optical resonator. 31
2.10 Phase and intensity response of a passive resonator 34
2.11 Phase and intensity response of a passive resonator around the resonance frequency 35
2.12 Interference of TEM_{00} and TEM_{01} modes for tilt locking. 36
2.13 Transverse intensity profile of a misaligned beam reflected from a resonator, on and off the resonance frequency. 36
2.14 Typical Pound-Drever-Hall and Tilt locking error signals. 37
2.15 A schematic of a typical control system. 37
2.16 An ideal PZT modelled in terms of masses connected by springs. 39
2.17 Frequency response of a PZT showing the effects of preloading and imperfect counterweighting. 40
2.18 PZT and counterweight interaction modelled by masses connected with springs. . 40
2.19 PZT preloading modelled in terms of masses connected by springs. 41
2.20 Experimentally determined amplitude and phase response of a PZT 42
2.21 Second order non-linear optical processes. 44
2.22 The effect of phase mismatch on the efficiency of ideal single-pass second harmonic generation using MgO:LiNbO_3. 46

3.1 Measurements of the FSR, RRO, and linewidth of a typical Innolight Mephisto Nd:YAG laser. 52
3.2 Mode cleaner schematic. 53
3.3 Frequency spectra of the field transmitted through the mode cleaner in high and low finesse modes. 54
3.4 Second harmonic generator configuration. 55
3.5 Conversion efficiency of second harmonic generator as a function of power and input coupler reflectivity. 57
3.6 Regenerative gain of an optical parametric amplifier. 59
3.7 Squeezing from an optical parametric amplifier as a function of pump power. . . 60
3.8 Amplitude and phase quadrature spectra for the field exiting an optical parametric amplifier operating at half threshold in the deamplification regime. 61

3.9 Detailed schematic of system used to generate a pair of squeezed fields. 62
3.10 Squeezing trace observed for the output of one OPA in a homodyne detector with swept local oscillator phase. 63
3.11 Squeezing spectra observed from the two OPAs. 64
3.12 Regenerative gain for each optical parametric amplification regime. 66
3.13 Predicted squeezing for each optical parametric amplifier regime as a function of pump power. 67
3.14 Squeezed vacuum production via classical noise cancellation 70
3.15 Low frequency squeezing results. 72
3.16 An alternative scheme to cancel the classical noise. 72

4.1 Axes of the photon number diagram representation of entanglement. 90
4.2 Schematic of a quantum teleportation experiment. 93
4.3 Schematic of a dense coding experiment. 94
4.4 The apparatus used to generate and characterise quadrature entangled beams. . . 96
4.5 Frequency spectra of the amplitude and phase quadrature variances of our individual quadrature entangled beams. 97
4.6 Frequency spectra of the amplitude and phase quadrature sum and difference variances between beams x and y. 97
4.7 Frequency spectra of the same-quadrature correlation matrix elements between entangled beams x and y. 98
4.8 Frequency spectrum of the degree of inseparability $\mathcal{I}$ between the amplitude and phase quadratures of our quadrature entangled state. 100
4.9 Conditional variance of the amplitude and phase quadratures of beam x given a measurement of that quadrature on beam y. 100
4.10 Frequency spectrum of the degree of EPR paradox between the amplitude and phase quadratures of our entangled state. 101
4.11 Comparison of the EPR and inseparability criteria for quadrature entanglement with varied detection efficiency. 102
4.12 Frequency spectra of the axes of the photon number plot. 103
4.13 Representation of the quadrature entangled state on the photon number diagram. . 104
4.14 Two dimensional slice of the photon number diagram for $\bar{n}_{\text{bias}} = 0$. 105
4.15 Paths mapped out onto the photon number diagram when loss is introduced to the entanglement. 106
4.16 Schematic of a simple experiment to reduce $\bar{n}_{\text{excess}}$. 107
4.17 Optimum paths for the feedforward technique to reduce $\bar{n}_{\text{excess}}$ represented on the photon number diagram. 108

5.1 Time line for a quantum teleportation experiment. 112
5.2 A continuous variable quantum teleportation protocol. 112
5.3 Approaches to characterisation of quantum teleportation. 113
5.4 Relationship between the fidelity of teleportation and errors in the teleportation gain. 115
5.5 A teleportation cloning limit in terms of signal transfer and reconstruction noise. 117
5.6 The gain normalised condition variance product measure of teleportation as a function of teleportation gain. 120
5.7 Fidelity of teleportation as a function of the teleportation gain. 121
5.8 Fidelity represented on the T-V diagram. 122
5.9 Entanglement swapping analysis. 125

5.10 Teleportation apparatus. 126
5.11 Frequency response of the teleportation apparatus. 126
5.12 A typical teleportation result. 128
5.13 An experimental analysis of the fidelity of teleportation.. 129
5.14 A comparison of the fidelity of teleportation when assuming unity teleportation gain, to that after verification of the gain. 130
5.15 T-V graph representation of the teleportation results. 131
5.16 Experimental results for the gain normalised conditional variance product measure of teleportation. 132
5.17 Experimental results for the teleportation loophole where one quadrature has zero coherent amplitude. 132
5.18 Experimental demonstration of the teleportation loophole when Victor incurs loss that is unaccounted for. 133

6.1 A (2,3) quantum secret sharing protocol. 136
6.2 Production of the shares in a quantum secret sharing scheme. 137
6.3 Reconstruction of a quantum secret using feedforward. 139
6.4 Calculated signal transfer and reconstruction noise for a quantum secret sharing scheme. 144
6.5 Wall painting from the tomb of Beni Hassan, Egypt 2500 BC. 145

7.1 Quantum and classical Poincaré spheres. 153
7.2 Stokes operator measurement apparatus. 154
7.3 Polarisation analysis on a single quadrature squeezed beam. 157
7.4 Measured Stokes operator variances of a single quadrature squeezed beam. . . . 157
7.5 Apparatus to produce a polarisation squeezed beam from a bright coherent beam and a quadrature squeezed beam. 157
7.6 Measured Stokes operator variances for a polarisation squeezed beam produced from a bright coherent beam and a quadrature squeezed beam. 158
7.7 Apparatus used to produce a polarisation squeezed beam by combining two quadrature squeezed beams. 158
7.8 Measured Stokes operator variances of a polarisation squeezed beams produced by combining two phase squeezed beams. 158
7.9 Measured Stokes operator variances of a polarisation squeezed beams produced by combining two amplitude squeezed beams. 159
7.10 Rotation of the quantum Stokes vector represented on the Poincaré sphere. 160
7.11 Poincaré sphere representation of various polarisation states. 161
7.12 Calculated channel capacities for information transfer using various continuous variable polarisation states. 164

8.1 Production of a pair of arbitrary polarisation modes. 171
8.2 Experimental production and characterisation of continuous variable polarisation entanglement. 173
8.3 Experimental measurement of the Stokes operator variances of the entangled beams. 173
8.4 Experimental measurement of the Stokes operator sum or difference variances between the entangled beams. 174
8.5 Experimental measurement of the Stokes operator inseparability criteria. 175
8.6 Experimental measurement of the Stokes operator conditional variances between the entangled beams. 176

8.7 Experimental measurement of the degree of EPR paradox between $\hat{S}_2$ and $\hat{S}_3$ for a polarisation entangled state. 176
8.8 Poincaré sphere representation of the conditional knowledge of one entangled beam obtained through measurements on the other. 177
8.9 Calculated Poincaré sphere representation of the conditional knowledge of one polarisation entangled beam obtained through measurements on the other, where the entanglement is produced from four quadrature squeezed beams. 180

9.1 Sequence of events used to generate non-classically correlated photon pairs from an ensemble of Cesium atoms. 185
9.2 Apparatus to generate single photons from an atomic ensemble. 192
9.3 Timing sequence for coincidence detection from an atomic ensemble. 193
9.4 Temporal profiles of the *write* and *read* pulses, and fields 1 and 2. 195
9.5 Time-resolved coincidences between the *write* and *read* photons. 198

B.1 Typical low noise, high quantum efficiency RF detector circuit. 211
B.2 Tilt detector circuit. 212
B.3 High voltage amplifier circuit. 213
B.4 Typical Piezo servo circuit. 214
B.5 Laser controlling servo circuit. 215
B.6 Front end interface of home built milli-Kelvin temperature controller. 216
B.7 Servo circuit of home built milli-Kelvin temperature controller. 217
B.8 Power supply of home built milli-Kelvin temperature controller. 218

List of Tables

2.1 Summary of the efficiencies of linear optical elements used in the experiments presented in this thesis. 25

3.1 Summary of the parameters characterising the SHG and OPAs developed for the work presented in this thesis. 56
3.2 An analysis of the four regimes of optical parametric amplification. 68

6.1 Summary of the performance of the quantum secret sharing protocol. 146

C.1 Sundry equipment used for the experiments of this thesis. 220

Glossary of terms

Term	Definition
$\tilde{O}$	An arbitrary operator in the time domain and rotating frame
$\hat{O}$	An arbitrary operator describing the electromagnetic oscillator at frequency ω
$\bar{O}$	The expectation value of operator $\hat{O}$; $\bar{O} = \langle \hat{O} \rangle$
$\delta\hat{O}$	The expectation fluctuations of operator $\hat{O}$; $\delta\hat{O} = \hat{O} - \bar{O}$
$\Delta\hat{O}$, $(\Delta^2\hat{O})$	The standard deviation (variance) of operator $\hat{O}$
$\Delta^2_{x\pm y}\hat{O}$	The sum and difference variance of operator $\hat{O}$ between sub-systems x and y, $\Delta^2_{x\pm y}\hat{O} = \min\{\langle(\hat{O}_x \pm \hat{O}_y)^2\rangle\}$
$\Delta^2_{x\|y}\hat{O}$	The conditional variance of operator $\hat{O}$ in sub-system x after measurement of the operator in sub-system y, $\Delta^2_{x\|y}\hat{O} = \Delta^2\hat{O}_x - \|\langle\delta\hat{O}_x\delta\hat{O}_y\rangle\|^2/\Delta^2\hat{O}_y$
η	The efficiency of a process
ϵ	Beam splitter transmission
γ	Total resonator decay rate
$\gamma_{\rm ic}$, $\gamma_{\rm oc}$, $\gamma_{\rm l}$	Resonator input/output coupler and intra-cavity loss decay rates
Ω	Laser carrier frequency
ω	Laser sideband frequency
$\hat{a}$, $(\hat{a}^\dagger)$	The field annihilation (creation) operator
$\hat{a}_\omega$	$\hat{a}$ for an individual electromagnetic oscillator originally at frequency ω
α	The coherent amplitude of $\hat{a}$, $\alpha = \langle\hat{a}\rangle$
α^+	The real part of coherent amplitude of $\hat{a}$; $\alpha^+ = \Re\{\langle\hat{a}\rangle\}$
α^-	The imaginary part of coherent amplitude of $\hat{a}$; $\alpha^- = \Im\{\langle\hat{a}\rangle\}$
$\hat{X}^+$	The amplitude quadrature of $\hat{a}$
$\hat{X}^-$	The phase quadrature of $\hat{a}$
$\hat{S}_{0,1,2,3}$	The four Stokes operators
$\tilde{\mathcal{S}}$	Collective atomic mode annihilation operator
$\hat{n}$	The photon number operator
$\bar{n}_{\rm min}$	The mean number of photons required to maintain a given entangled state
$\bar{n}_{\rm bias}$	The mean number of photons in an entangled state due to bias between the quadratures
$\bar{n}_{\rm excess}$	The mean number of photons in and entangled state due to impurity
C	Channel capacity
V_q	Noise (product) added to output of teleportation protocol
T_q	Signal transfer from input to output of teleportation protocol
EPR	Einstein-Podolsky-Rosen; or quadrature entanglement
$\mathcal{I}$	The degree of inseparability between two sub-systems
$\mathcal{E}$	The degree of observation of the EPR paradox between two sub-systems
$\mathcal{F}$	The Fidelity or state overlap between two states
$\mathcal{M}$	The gain normalised conditional variance measure of teleportation
ρ	Density matrix describing a quantum state

P	Optical power, $P = \hbar\omega\alpha^*\alpha$
i, I	Electrical current
g_D	Overall gain of the photodetection process
$\mathbb{F}$	Fourier transform
$\mathbb{F}^{-1}$	Inverse Fourier transform
$\chi^{(i)}$	i^{th} order nonlinear susceptibility
Λ	$\chi^{(i)}$ nonlinear interaction strength
g_c	Collective atomic nonlinear interaction strength
C_{ij}	Coincidence rate between fields i and j
N_{ij}	Number of coincidences between fields i and j
g_{ij}	Normalised correlation function between fields i and j
Δ	Frequency detuning (when not preceding an operator - see above)
DC	Direct current - or low frequency
RF	Radio frequency
SHG	Second harmonic generator
OPO	Optical parametric oscillator
OPA	Optical parametric amplifier
G_R	Optical parametric amplifier regenerative gain
BS	Non-polarising beam splitter
PBS	Polarising beam splitter
H	Horizontally polarised
V	Vertically polarised
SNR	Signal to noise ratio
PID	Proportional-Intergal-Differential servo
HV	High voltage amplifier
TC	Temperature controller
PDH	Pound-Drever-Hall locking
FSR	Free spectral range
RRO	Laser resonant relaxation oscillation

Chapter 1

Introduction

The field of *quantum optics* investigates how the quantum mechanical properties of optical fields can be manipulated, characterised, and utilised. Until recently, experiments in the field were motivated primarily by a desire to test properties of the microscopic world. As laser physics has advanced, however, many new quantum optical techniques have been developed that offer the potential to improve the technology utilised in many fields, including interferometry[1], spectroscopy[2], microscopy[3], and lithography[4]. These techniques could not only provide better methods to interrogate the microscopic world, but also real improvements to data storage and manipulation techniques[5], and enhancements of biological and medical applications such as atomic force microscopy[6]. Over the last two decades the field has been further invigorated by the realisation that computers utilising quantum mechanical techniques, or *quantum computers*, can far out-perform conventional computers for some problems[7, 8]. The new field of *quantum information science*, which investigates how quantum mechanics can be used to improve information processing and communication, then came into being. One of the primary experimental goals of quantum information science is to develop a *quantum information network* analagous to the internet. Although the specific details of an optimal quantum information network have yet to be resolved, it is generally accepted that such a network would consist of atomic nodes where information is processed, connected by optical links through which quantum optical fields can be distributed[9]. There are still many developments required before quantum information networks become feasible. In particular, techniques to effectively perform the quantum information protocols required at the atomic nodes[10], to store quantum states for long periods of time[11, 12], and to transfer quantum states between atomic and optical media must be developed[12, 13]. This thesis experimentally examines some of these unresolved issues, with the majority of the work focussing on optical technology within the *continuous variable regime* of quantum mechanics. In the continuous variable regime measurements can yield any result from a continuum of possible results, this contrasts the *discrete variable regime* where only a limited number of specific results are possible.

The thesis is divided into three Parts as shown in Fig. 1.1. The first Part introduces the theoretical and experimental techniques used throughout the thesis, and describes the techniques used to generate optical *squeezed states*. These squeezed states have proved to be the most readily accessible optical fields with demonstrably quantum mechanical behaviour in the continuous variable regime. Furthermore, they can be directly applied to improve the resolution of optical measurements[14], and have been shown to be useful in many quantum information protocols[15]. The squeezed states generated for the work presented in this thesis were produced in a pair of below threshold optical parametric amplifiers, developed during the course of my Ph.D.. Both optical parametric amplifiers could be stably locked with amplitude or phase squeezed output fields.

In the second Part of this thesis, we analyse several quantum information protocols that can be facilitated using squeezed states. In the work presented in Chapter 4 we used our pair of squeezed

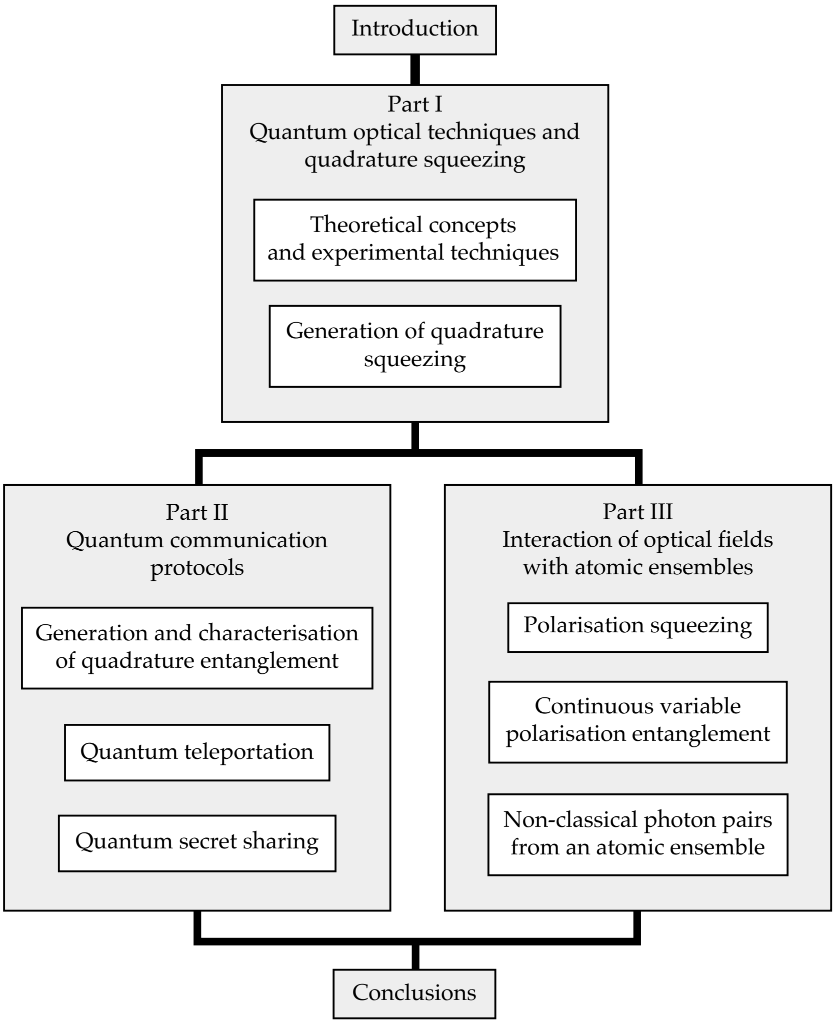

Figure 1.1: Thesis structure

states to produce *quadrature entanglement* between two optical fields. These entangled fields exhibited non-classical correlations between their amplitude and phase quadratures. Entanglement of this form was first described by Einstein as ‘spooky interactions at a distance’[16], and is the core ingredient of most continuous variable quantum information protocols[15]. The efficacy of a given quantum information protocol depends strongly on the specific properties of the entangled state utilised. We thoroughly characterise our entangled state, and propose a new, experimentally convenient and intuitive characterisation method, the *photon number diagram*, which partitions the mean number of photons in the entangled state into meaningful categories. In Chapter 5 the entangled state is directly applied in a quantum teleportation protocol, which can perform useful functions in quantum computation[17]. The protocol itself demonstrates that the quantum statistics of an optical field can be transferred onto another field using measurement and conventional communication. We analyse our experiment using several techniques, and demonstrate that it could be used to perform entanglement swapping, which is an important quantum communication technique[18]. Chapter 6 proposes a scheme to perform secret sharing of quantum states of light utilising the entanglement of Chapter 4. Such a scheme has the potential to facilitate error correction in a quantum computer or communication system, and allows the secure transmission of information even in the presence of malicious parties and faulty communication channels[19].

In the final Part of this thesis we consider the interaction between optical fields and atomic ensembles. Chapters 7 and 8 investigate quantum polarisation states in the continuous variable regime. These states are of particular relevance to the implementation of quantum information networks since quantum state transfer has been demonstrated from them to the collective spin state of atomic ensembles[20]. In Chapter 7 we experimentally transform the amplitude and phase squeezed fields generated in our optical parametric amplifiers onto a polarisation basis, demonstrating a variety of polarisation squeezed fields. The polarisation of a field can be described using the four Stokes operators. One of our polarisation squeezed fields exhibited simultaneous squeezing of three of the four Stokes operators. We then transform our quadrature entanglement onto a polarisation basis, resulting in the first observation of continuous variable polarisation entanglement between a pair of fields. The entanglement is exhibited through non-classical correlations of two Stoke operators between the fields. We propose an extension utilising two pairs of quadrature entangled fields, that should exhibit non-classical correlations between three of the Stokes operators. Finally, in Chapter 9 we experimentally investigate the interaction of optical fields with an atomic ensemble. Such systems have been shown to enable quantum information networks with entanglement purification and quantum memory capabilities[21]. We demonstrate that after manipulating the atomic ensemble using appropriate optical pulses, non-classically correlated photon pairs are emitted. The non-classicality of the correlation was confirmed through violation of the Cauchy-Schwarz inequality. The time interval separating the photons could be tuned, and their spatial modes were well defined. This represents an enabling step towards an atomic ensemble quantum information network[21], and has potential as an 'on demand' single photon source with applications in multi-photon quantum information protocols[22].

Throughout this thesis, motivation for the work presented is given primarily from the context of quantum information science. There was a deeper underlying motivation, however, to investigate the behaviour of quantum mechanical systems and to develop techniques to control systems at a quantum mechanical level. Some of the research performed during my Ph.D. was focussed towards these sort of investigations. Included in that work were experimental demonstrations of two-dimensional displacement measurements to better than the quantum noise limit [23, 24, 25]; of squeezing using periodically-poled Lithium-Niobate [26]; of the recovery of squeezing obscured by low frequency classical noise [27]; and of a non-modulation based method to control second harmonic generation [28]. For the sake of continuity these results have, for the most part, been omitted from this thesis.

The thesis is formulated predominantly in the *Heisenberg picture* of quantum mechanics, where the operators describing our optical fields evolve with time. We switch to the *Schrödinger picture* in places so that the photon statistics of the fields can be conveniently examined. Operators in the Heisenberg picture can be represented complimentarily in the frequency and time domains. Our usual approach to modelling experimental systems is to propagate the operators in the time domain, and to switch to the frequency domain for analysis after measurement.

The majority of this thesis has been published, submitted to, or accepted for publication in international peer-reviewed journals. Some selected articles resulting from the work performed during my Ph.D. are:

1. **Quadrature entanglement:** W. P. Bowen, R. Schnabel, P. K. Lam, and T. C. Ralph. *An experimental investigation of criteria for continuous variable entanglement.* Physical Review Letters **90**, 043601 (2003).

2. **Polarisation entanglement:** W. P. Bowen, N. Treps, R. Schnabel, and P. K. Lam. *Experimental demonstration of continuous variable polarization entanglement.* Physical Review Letters **89**, 253601 (2002).

3. **Polarisation squeezing:** W. P. Bowen, R. Schnabel, H.-A. Bachor, and P. K. Lam. *Polarization Squeezing of Continuous Variable Stokes Parameters.* Physical Review Letters **88**, 093601 (2002).

4. **Displacement measurements to better than the quantum noise limit:** N. Treps, N. B. Grosse, W. P. Bowen, C. Fabre, H.-A. Bachor and P. K. Lam. *A Quantum Laser Pointer.* Science **301**, 940 (2003).

5. **Quantum optical manipulation of atomic ensembles:** A. Kuzmich, W. P. Bowen, A. D. Boozer, A. Boca, C. W. Chou, L.-M. Duan and H. J. Kimble *Generation of Nonclassical Photon Pairs for Scalable Quantum Communication with Atomic Ensembles.* Nature **423**, 731 (2003).

6. **Quantum teleportation:** W. P. Bowen, N. Treps, B. C. Buchler, R. Schnabel, T. C. Ralph, H.-A.Bachor, T. Symul, and P. K. Lam. *Experimental investigation of continuous variable quantum teleportation.* Physical Review A **67**, 032302 (2003).

7. **Advancement of squeezing technology:** W. P. Bowen, R. Schnabel, N. Treps, H.-A. Bachor, and P. K. Lam. *Recovery of continuous wave squeezing squeezing at low frequencies.* Journal of Optics B: Quantum and Semi-Classical Optics **4**, 421 (2002).

8. **Quantum secret sharing:** A. Lance, T. Symul, W. P. Bowen, T. Tyc, B. C. Sanders, and P. K. Lam. *Continuous Variable (2,3) Threshold Quantum Secret Sharing Schemes.* New Journal of Physics **5**, 4 (2003).

Refs. [24, 25, 26, 28, 29, 30, 31, 32, 33, 34, 35, 36, 37, 38] were also published during the course of my Ph.D..

Part I

Quantum optical techniques and quadrature squeezing

Overview

The first two Chapters of this thesis are concerned with the description of quantum states in the continuous variable regime, and the generation of optical squeezed states. The development of quantum optical methods to describe squeezed states is explicitly linked to the understanding of coherent states. The concept of the *coherent state*, a minimum uncertainty state with noise independent of the quadrature of measurement, was introduced by Schrödinger in 1926[39]. This concept pre-empted the field of quantum optics, which lay more-or-less dormant until the discovery of the laser in 1960 [40]. The laser provided optical fields of exquisite coherence enabling experiments that were previously thought unfeasible. It was soon-after found that the traditional description of optical fields in terms of the harmonic oscillator and number states was not well suited to the output of a conventional laser. More that thirty years after their introduction, Glauber[41] re-examined the coherent states and found them to provide a natural description of the output field of a laser. Shortly thereafter, in a number of works Glauber's formalism was extended to describe minimum uncertainty states with noise dependent on the quadrature of measurement, these states were later termed the *squeezed states* [42, 43, 44, 45, 46]. At that time there was much excitement about squeezed states since the quantum noise on optical fields had been found to limit the sensitivity of many measurement devices [14]. Squeezed states were expected to overcome this limitation. Experiments then began with the objective to observe squeezed states. In 1985 Slusher *et al.* [47, 48] did just that, observing optical field squeezing via a four-wave mixing process facilitated by the $\chi^{(3)}$ nonlinear susceptibility of a beam of sodium atoms. Squeezing has now been observed in a diverse range of systems utilising both the $\chi^{(2)}$ and $\chi^{(3)}$ nonlinearities, for a good summary see [49]. These include, but are not restricted to: fibre squeezing via the Kerr effect [50], squeezing via subthreshold optical parametric oscillation [51, 52] and optical parametric amplification[53], second harmonic squeezing[54], microwave squeezing from a Josephson-parametric amplifier[55], optical soliton squeezing [56], mode-locked optical parametric oscillation [57], semiconductor squeezing [58], waveguide squeezing [59, 60], and most recently squeezing using polarisation self-rotation in atomic ensembles[61].

To date, the most stable and strongly squeezed optical fields have been achieved in via optical parametric processes [2, 51, 52, 53, 62, 63, 64]. The following two Chapters of this thesis introduce some theoretical models required to understand this particular set of squeezing processes; the experimental tools used to generate optical squeezing via optical parametric amplification, and to characterise, and manipulate the resulting state; a theoretical analysis of squeezing via optical parametric amplification; and finally an analysis of the squeezed fields generated and used throughout the work presented in thesis[27].

Chapter 2

Theoretical concepts and experimental techniques

This Chapter introduces the quantum optical techniques utilised throughout my thesis. In the first three Sections we introduce the uncertainty principle, the field states relevant to our experiments, and methods to characterise those states. We then discuss photodetection of an optical field, and introduce the specific *sideband* states examined by this process. Each of these sideband states is a coherent sum of the states of a pair electromagnetic oscillations with frequencies on either side of the optical carrier frequency. We introduce optical modulation as a technique to manipulate the sideband states. We then turn to the more technical issues of controlling optical interference, characterising the efficiency of various optical processes, and accurate measurement of quantum states. We introduce methods to model optical resonators, and techniques to accurately control their length; before finally discussing the second order optical nonlinearities through which optical frequency conversion, optical parametric amplification, and squeezing are made possible.

2.1 The uncertainty principle

In a Newtonian universe, given complete knowledge of the universe at one instant, its future behavior also becomes completely known. This concept posed a dilemma for philosophers and people who believed in free will. This dilemma was made irrelevant when in 1927 Heisenberg introduced the Heisenberg uncertainty principle [65], which, at some level, replaced this absolute determinism with unpredictable randomness. The Heisenberg uncertainty principle states that it is impossible to simultaneously obtain precise knowledge of two non-commuting observables. That is, given the commutation relation between two arbitrary observables $\hat{A}$ and $\hat{B}$

$$[\hat{A}, \hat{B}] = \hat{A}\hat{B} - \hat{B}\hat{A} = C, \tag{2.1}$$

where C is a complex constant; the product of the uncertainties of simultaneous measurements on the observables is bounded by

$$\Delta\hat{A}\Delta\hat{B} \geq \frac{1}{2}|C|, \tag{2.2}$$

where $\Delta\hat{A}$ and $\Delta\hat{B}$ are the standard deviation of measurements of $\hat{A}$ and $\hat{B}$ performed on an ensemble of identically prepared systems. For an arbitrary operator $\hat{O}$ this standard deviation is given by

$$\Delta\hat{O} = \sqrt{\langle\hat{O}^2\rangle - \langle\hat{O}\rangle^2}. \tag{2.3}$$

If $|C| > 0$ the observables $\hat{A}$ and $\hat{B}$ are non-commuting, the precision of our knowledge of observable $\hat{A}$ then dictates the maximum precision we can obtain for observable $\hat{B}$, and visa versa. Of course given that it is impossible to determine the observable $\hat{B}$ (or $\hat{A}$) to better than this precision, it is natural to ask whether it really exists to better than that precision? The *hidden variable* model of quantum mechanics states that at all times observables $\hat{A}$ and $\hat{B}$ both have well defined values, and that it is simply impossible for us to determine their values simultaneously. On the other hand, the standard model of quantum mechanics states that, before we measure the operators, they are in a super-position of all possible measurement outcomes. In 1964 Bell proposed a method to distinguish between these two models [66], and experimental tests were performed by Kasday *et al.* [67] in 1970. The result was that the standard form of quantum mechanics was correct, and the hidden variable model was false. This means that, not only does the Heisenberg uncertainty principle set bounds on how well we can simultaneously know two noncommuting observables, but also on how precisely they exist. It is this ability of quantum mechanics to allow superpositions of several possible outcomes to exist simultaneously, that facilitates entanglement - one of the main topics studied in this thesis - which Einstein termed as "*spooky interactions at a distance*".

The most common example of the Heisenberg uncertainty principle is that between the position and momentum of a free particle. This uncertainty principle can be interrogated via the Heisenberg microscope [68], which measures the position of a particle by interacting it with a photon of light. During the process the photon necessarily imparts some momentum to the particle. The more accurately the position is determined, the more disruptive the measurement is to the momentum. So although the microscope allows - in theory - a perfect measurement of the position of the particle, in the process it would completely disrupt the particle's momentum. The same uncertainty principle exists when the particle is trapped in a harmonic potential. The particle then oscillates in the potential in a simple harmonic manner. This situation is highly analogous to the oscillation of the electromagnetic field at some frequency ω, which is the system interrogated throughout this thesis. In the Heisenberg picture of quantum mechanics an electromagnetic oscillation at frequency ω is representable by the field annihilation operator $\hat{a}(\omega)$, which together with its conjugate, the field creation operator $\hat{a}^\dagger(\omega)$, satisfy the boson commutation relation

$$[\hat{a}(\omega), \hat{a}^\dagger(\omega)] = 1. \tag{2.4}$$

The annihilation and creation operators are non-Hermitian, and therefore not measurable. On the other hand, their real and imaginary parts are Hermitian. The real part of $\hat{a}(\omega)$ is the amplitude quadrature of the field $\hat{X}^+(\omega)$ - which is analogous to the position of a particle in a harmonic potential - and the imaginary part is the phase quadrature of the field $\hat{X}^-(\omega)$ - which is itself analogous to the momentum of a particle in a harmonic potential

$$\begin{aligned} \hat{X}^+(\omega) &= \hat{a}^\dagger(\omega) + \hat{a}(\omega) & (2.5) \\ \hat{X}^-(\omega) &= i(\hat{a}^\dagger(\omega) - \hat{a}(\omega)). & (2.6) \end{aligned}$$

An arbitrary quadrature operator $\hat{X}^\theta(\omega)$ can also be defined

$$\hat{X}^\theta(\omega) = \hat{a}(\omega)e^{-i\theta} + \hat{a}^\dagger(\omega)e^{i\theta} = \hat{X}^+(\omega)\cos\theta + \hat{X}^-(\omega)\sin\theta. \tag{2.7}$$

We see that this arbitrary quadrature operator is a linear combination of the amplitude and phase quadratures.

Perhaps unsurprisingly given their analogous nature to the position and momentum of a particle in a harmonic potential, the amplitude and phase quadrature operators do not commute. Their commutation relation is dictated by the boson commutation relation of Eq. (2.4), and is given by

$$[\hat{X}^{+}(\omega), \hat{X}^{-}(\omega)] = 2i. \tag{2.8}$$

Eq. (2.2) then yields an uncertainty relation between the quadratures

$$\Delta\hat{X}^{+}(\omega)\Delta\hat{X}^{-}(\omega) \geq 1. \tag{2.9}$$

We see then, that precise simultaneous determination of the amplitude and phase quadratures of a light field is not possible. The fluctuations in the measurements of each quadrature are referred to as the *quantum noise* of the electromagnetic field. Electromagnetic fields that satisfy Eq. (2.9) in the equality are termed *minimum uncertainty*. Manipulation of the balance of this uncertainty relation - that is, enhancing the measurement precision of one quadrature at the cost of the other - is one of the core technologies used in this thesis, and is termed *squeezing*.

2.2 Squeezing a single electromagnetic oscillation

The ground state of an electromagnetic oscillation is the vacuum state, or in other words the state with zero photons in it, and can be represented in the Schrödinger picture as $|0\rangle$. Of course, we have already seen that for any electromagnetic oscillation the amplitude and phase quadratures must satisfy an Heisenberg uncertainty relation. So even though the vacuum state has no photons, its electromagnetic field still fluctuates. In fact $\Delta\hat{X}^{+} = \Delta\hat{X}^{-} = 1$, so that the fluctuations of the amplitude and phase quadratures of a vacuum state are equal. Thus processes such as optical loss that couple vacuum states, or *vacuum noise*, to a system will have the unavoidable consequence of also introducing fluctuations to the system amplitude and phase quadratures. The fluctuations of a vacuum state pose a limit to most optical measurement devices that is sometimes termed the *quantum noise limit*, or from an engineering perspective the *shot noise limit*.

One result of the coupling of vacuum noise to optical systems is that the output of an ideal laser has the same fluctuations as a vacuum state, that is $\Delta\hat{X}^{+} = \Delta\hat{X}^{-} = 1$. Such a state is termed a *coherent state*. In the Schrödinger picture of quantum mechanics coherent states are the eigenstates of the annihilation operator

$$\hat{a}(\omega)|\alpha(\omega)\rangle = \alpha(\omega)|\alpha(\omega)\rangle, \tag{2.10}$$

and can be produced by applying the displacement operator $D[\alpha(\omega)] = e^{-\frac{1}{2}|\alpha(\omega)|^2} e^{\alpha(\omega)\hat{a}^{\dagger}(\omega)} e^{-\alpha^{*}(\omega)\hat{a}(\omega)}$ to a vacuum state

$$D[\alpha(\omega)]|0\rangle = |\alpha(\omega)\rangle. \tag{2.11}$$

The coherent state contains a non-deterministic number of photons. This may be seen through an expansion in terms of Fock, or number, states

$$|\alpha(\omega)\rangle = \sum |n\rangle\langle n|\alpha(\omega)\rangle = e^{-\frac{1}{2}|\alpha(\omega)|^2} \sum \frac{\alpha(\omega)^n}{\sqrt{n!}}|n\rangle \tag{2.12}$$

where $|n\rangle$ are the Fock states, or in other words the electromagnetic oscillation states that contain exactly n photons, and $\alpha(\omega)$ is the coherent amplitude of the field at frequency ω, $\alpha(\omega) = \langle\hat{a}(\omega)\rangle$.

From Eq. (2.12) the coherent state photon number distribution can be seen to be

$$P(n) = |\langle n|\alpha(\omega)\rangle|^2 = \frac{|\alpha(\omega)|^{2n} e^{-|\alpha(\omega)|^2}}{n!}. \tag{2.13}$$

We see that the photon number distribution of a coherent state is Poissonian. Since any truly random system exhibits Poissonian statistics the photon number distribution of a coherent state is therefore entirely random. The average number of photons in a coherent state is $\bar{n} = |\alpha|^2$, and the standard deviation of the photon number is $\Delta n = |\alpha|$.

We are interested in states that have different noise properties to the vacuum state. One of the simplest classes of these states is the *squeezed states*. That is, states for which either $\Delta\hat{X}^+ < 1$ or $\Delta\hat{X}^- < 1$. Of course, the Heisenberg uncertainty principle of Eq. (2.9) must still be satisfied, so that the noise in the non-squeezed quadrature must be greater than unity. In fact, due to the optical loss and other imperfections present in any real experiment, the product $\Delta\hat{X}^+\Delta\hat{X}^-$ is always greater than unity.

Mathematically, the squeezed state can be derived from the vacuum state via the *unitary squeeze operator* $S[r(\omega), \phi(\omega)]$ [69]

$$S[r(\omega), \phi(\omega)] = \exp\left(\frac{r(\omega)}{2}\left(e^{-2i\phi(\omega)}\hat{a}(\omega)^2 - e^{2i\phi(\omega)}\hat{a}^\dagger(\omega)^2\right)\right), \tag{2.14}$$

where $\phi(\omega)$ defines the quadrature of the squeezing relative to some local oscillator, and $r(\omega)$ is the so called *squeeze factor* which is real and positive and can be directly related to the standard deviation of the squeezed quadrature

$$\Delta\hat{X}^{\phi(\omega)}(\omega) = e^{-r(\omega)}. \tag{2.15}$$

The pure squeezed state $|\alpha(\omega), \phi(\omega), r(\omega)\rangle$ can then be obtained by applying this squeeze operator to the vacuum state in conjunction with the displacement operator

$$|\alpha(\omega), \phi(\omega), r(\omega)\rangle = D[\alpha(\omega)]S[r(\omega), \phi(\omega)]|0\rangle \tag{2.16}$$

The photon number distribution of a squeezed state is given by [46]

$$P(n) = |\langle n|\alpha(\omega), \phi(\omega), r(\omega)\rangle|^2, \tag{2.17}$$

with

$$\langle n|\alpha, \phi, r\rangle = \sqrt{\frac{e^{in\phi}\tanh^n r}{2^n n! \cosh r}} \exp\left(-\frac{1}{2}\left(|\alpha|^2 + \alpha^{*2} e^{i\phi}\tanh r\right)\right) H_n\left[\frac{\alpha + \alpha^* e^{i\phi}\tanh r}{\sqrt{2e^{i\phi}\tanh r}}\right], \tag{2.18}$$

where $H_n[x]$ are the Hermite polynomials. This photon distribution can be broader or narrower than the Poissonian distribution evident for coherent states, depending on the coherent amplitude $\alpha(\omega)$ and the quadrature of the squeezing $\phi(\omega)$. Fig. 2.1 shows photon distributions for some typical states. In this case we have chosen the coherent amplitude $\alpha(\omega)$ to be real and positive. We see that the photon number distribution of an amplitude squeezed state ($\phi(\omega) = 0$) is narrower, while that of a phase squeezed state ($\phi(\omega) = \pi/2$) is broader than the equivalent distribution for a coherent state. Fig. 2.1 d) shows the photon number distribution for a vacuum squeezed state, which is strikingly different from the other three photon distributions shown. Only even photon numbers have non-zero probabilities. This 'pairing' of photons can be used to explain much of the unusual behaviour of the squeezed state. Amplitude and phase squeezed states also exhibit photon pairing, although it is disguised by the presence of photons due to the coherent amplitude $\alpha(\omega)$ of the state.

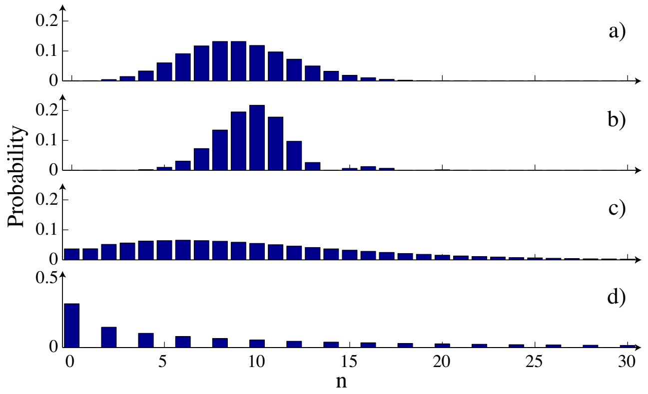

Figure 2.1: Photon number distribution for: a) a coherent state with $\alpha(\omega) = 3$, b) a pure amplitude squeezed state with $\alpha(\omega) = 3$ and $\Delta^2 X^+(\omega) = 0.2$, c) a pure phase squeezed state with $\alpha(\omega) = 3$ and $\Delta^2 X^-(\omega) = 0.2$, and d) a pure vacuum squeezed state with $\alpha(\omega) = 0$ and $\Delta^2 X^+(\omega) = 0.02$.

2.2.1 The Wigner function and the ball and stick picture

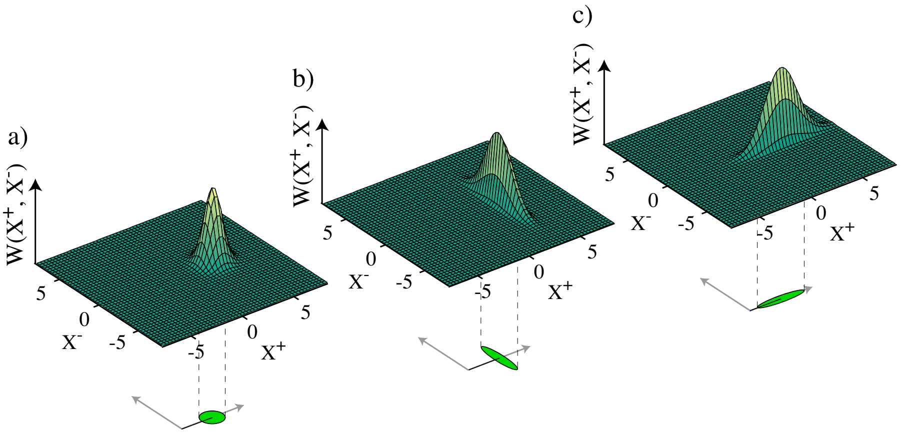

Figure 2.2: Wigner function and ball and stick picture for: a) a coherent state with $\alpha(\omega) = 1.5$, b) a pure amplitude squeezed state with $\alpha(\omega) = 1.5$ and $\Delta^2 X^+(\omega) = 0.2$, and c) a pure phase squeezed state with $\alpha(\omega) = 1.5$ and $\Delta^2 X^-(\omega) = 0.2$.

Any quantum state can be fully characterised by its density matrix $\hat{\rho}$. Typically the density matrix is expressed in terms of Fock states. For the coherent, squeezed, and entangled states considered throughout this thesis, this expression results in a density matrix of infinite dimension. Furthermore, the density matrix does not provide a particularly intuitive representation of the state. In classical optics we can represent an electromagnetic oscillation perfectly by its coherent amplitude $\alpha(\omega)$, this coherent amplitude may be perfectly stable, or, if the field is partially incoherent, it may fluctuate in some manner. This fluctuation could then be represented as a joint-probability distribution for the real and imaginary parts of the coherent amplitude (the amplitude and phase quadratures). Of course such a distribution is forbidden by quantum mechanics, since it implicitly assumes that at any given time the oscillation exists with well defined amplitude and phase quadratures. We know that this is not true as a result of the Heisenberg uncertainty principle present between the quadratures. It is possible, however, to define quasi-probability distributions for the electromagnetic oscillation. Perhaps the most intuitive such distribution is the Wigner function [70]. The Wigner function is a one-to-one map of the density matrix and can be written in the Schrödinger picture as [71]

$$W(X^+(\omega), X^-(\omega)) = \frac{1}{\pi}\int_{-\infty}^{\infty} \exp(ixX^-(\omega)) \left\langle X^+(\omega) - \frac{x}{4}\right| \hat{\rho} \left| X^+(\omega) + \frac{x}{4}\right\rangle dx, \qquad (2.19)$$

where since the Wigner function is a quasi-probability distribution with $\hat{X}^{\pm}$ treated as classical quantities, the respective decorations () have been removed. One somewhat surprising feature of the Wigner function is that it can have negative values. In a conventional probability distribution this would be highly unphysical. Negative values are allowed in this quasi-probability distribution since simultaneous exact measurements of the amplitude and phase quadratures are not possible. Ensemble measurements on a quadrature of the state measure the projection of the Wigner function onto that quadrature, and always yield a positive definite probability distribution.

With the exception of Chapter 9, all of the states investigated in this thesis have Gaussian statistics. The Wigner function is then a very natural representation of the state. In this one exceptional case the Wigner function is equivalent to a classical probability distribution, and is a two-dimensional Gaussian. The Wigner function $W_{\rm G}$ of a displaced Gaussian state with semimajor and semiminor axe variances of $\Delta^2\hat{X}^{\pm}(\omega)$ and coherent amplitude $\alpha(\omega) = \alpha^+(\omega) + i\alpha^-(\omega)$ is [71]

$$W_{\rm G}(X^+(\omega), X^-(\omega)) = \frac{2}{\pi\Delta\hat{X}^+(\omega)\Delta\hat{X}^-(\omega)} \exp\left(-\frac{(X^+(\omega)-2\alpha^+(\omega))^2}{2\Delta^2\hat{X}^+(\omega)} - \frac{(X^-(\omega)-2\alpha^-(\omega))^2}{2\Delta^2\hat{X}^-(\omega)}\right). \qquad (2.20)$$

Wigner functions corresponding to a coherent state, and displaced amplitude and phase squeezed states are shown in Fig. 2.2. The Wigner function of any Gaussian state can be completely defined by its standard deviation contour, and a stick representing the coherent amplitude of the state[1]. This is the so called '*ball and stick picture*' used to represent Gaussian quantum states in many textbooks, and is shown in Fig. 2.2 for each of the Wigner functions plotted. The standard deviation contour of a Gaussian Wigner function is an ellipse, and is fully characterised by the width of the ellipse along its semimajor and semiminor axes, which for a squeezed state correspond to the standard deviations of the anti-squeezed and squeezed quadratures, respectively. Therefore, the Wigner function of a Gaussian state may be fully characterised by its coherent amplitude $\alpha(\omega)$, and the width of its semimajor and semiminor axes, which throughout this thesis are given by $\Delta\hat{X}^+(\omega)$ and $\Delta\hat{X}^-(\omega)$ (not necessarily respectively). We can, therefore, achieve a complete characterisation of the states relevant to the experiments presented in this thesis through measurements of $\alpha(\omega)$, $\Delta\hat{X}^+(\omega)$, and $\Delta\hat{X}^-(\omega)$.

2.3 The quantum optics of optical sidebands

Previously in this thesis we have discussed the quantum mechanical description of an electromagnetic oscillation in terms of field annihilation and creation operators[2]. We have introduced some simple linear operations that can be performed on these operators, and their representation in terms

---

[1] Note that the stick is actually twice the length of $\alpha(\omega)$, this is a result of the definitions of $\hat{X}^+(\omega)$ and $\hat{X}^-(\omega)$ $(\langle\hat{X}^{\pm}(\omega)\rangle = 2\alpha^{\pm}(\omega))$

[2] A more detailed analysis of this Section can be found in Appendix A

of the measurable Hermitian amplitude $\hat{X}^+(\omega)$ and phase $\hat{X}^-(\omega)$ quadrature operators. In reality, however, we cannot directly measure the quadrature operators at a particular frequency ω. Instead, choosing a frame rotating at our laser carrier frequency Ω and moving back into the Heisenberg picture, we interrogate the time varying field annihilation operator $\tilde{a}(t)$,

$$\tilde{a}(t) = \int_{-\Omega}^{\infty} \hat{a}_{\Omega+\omega}(\omega) e^{i\omega t} d\omega, \tag{2.21}$$

where ω now denotes the frequency separation from the laser carrier, and the sub-script $\Omega + \omega$ labels the electromagnetic oscillation at that optical frequency, which in the rotating frame appears at frequency ω. Throughout this thesis we distinguish the rotating time domain annihilation operator via the decoration $\tilde{}$, as opposed to the frequency domain decoration $\hat{}$. Each measurement performed on an electromagnetic field is a combined measurement on all of the infinite electromagnetic oscillations defining each frequency component of the field. It is easy to show from Eq. (2.21) that for $\omega < \Omega$ the frequency domain annihilation operator can be extracted from its time domain counterpart via the Fourier transform

$$\hat{a}_{\Omega+\omega}(\omega) = \mathbb{F}\left(\delta\tilde{a}(t)\right) \tag{2.22}$$

where throughout this thesis $\mathbb{F}(\hat{O})$ denotes the Fourier transform of the operator $\hat{O}$ from time to frequency domain.

The time domain annihilation operator $\tilde{a}(t)$ has properties similar to its frequency domain counterpart. It satisfies the boson commutation relation

$$[\tilde{a}(t), \tilde{a}^\dagger(t)] = 1, \tag{2.23}$$

and analogous amplitude and phase quadrature operators can be defined

$$\begin{aligned} \tilde{X}^+(t) &= \tilde{a}^\dagger(t) + \tilde{a}(t) && (2.24)\\ \tilde{X}^-(t) &= i\left(\tilde{a}^\dagger(t) - \tilde{a}(t)\right). && (2.25) \end{aligned}$$

Similarly to $\tilde{a}(t)$ (see Eq. (2.22)), when $\omega < \Omega$ the frequency domain amplitude and phase quadrature operators can be extracted from their time domain counterparts via

$$\hat{X}^\pm(\omega) = \mathbb{F}\left(\delta\tilde{X}^\pm(t)\right). \tag{2.26}$$

Photodetection of a field is described by the photoelectric effect, with electrons being liberated from a material when it is subjected to a radiant field[3]. Within the bandwidth of the detectors, the photocurrent produced is directly proportional to the number of photons in the field

$$\begin{aligned} i(t) &= g_D\tilde{n}(t) = g_D\tilde{a}^\dagger(t)\tilde{a}(t) && (2.27)\\ &= g_D\Big(\alpha(t) + \delta\tilde{a}^\dagger(t)\Big)\Big(\alpha(t) + \delta\tilde{a}(t)\Big) && (2.28)\\ &= g_D\alpha(t)^2 + g_D\alpha(t)\left(\delta\tilde{a}^\dagger(t) + \delta\tilde{a}(t)\right) && (2.29)\\ &= g_D\alpha(t)^2 + g_D\alpha(t)\delta\tilde{X}^+(t), && (2.30) \end{aligned}$$

---

[3] A detailed quantum mechanical analysis of this process can be found in [72, 73, 74], for the work presented in this thesis, however, the following analysis is sufficient.

where g_D is the gain of the detection process, and $\alpha(t) = \langle \tilde{a}(t) \rangle$ is the coherent amplitude of the laser which throughout this thesis is assumed to be real without loss of generality. Since the linewidth of a laser field is typically extremely narrow, and the power within the linewidth is much larger than the power in the same frequency band around any other frequency, we have neglected the second order term $\delta\tilde{a}^\dagger(t)\delta\tilde{a}(t)$. This process is termed the *linearisation approximation*. The optical beams used for the majority of the work presented in this thesis were bright with $\alpha(t) \gg |\langle \delta\tilde{a}^\dagger(t)\delta\tilde{a}(t)\rangle|$, so that this approximation is valid throughout. The exception is Chapter 9 where experiments were performed involving single photon Fock states. Detailed discussions of the linearisation approximation may be found in the theses of Ping Koy Lam [75] and Ben Buchler [76]. We see that photodetection directly interrogates the time domain amplitude quadrature operator of the field. However, many frequency dependent noise sources are present in a real situation. Some examples of these are acoustic noise, laser relaxation oscillation noise, and thermal noise. These noise sources make it extremely difficult to observe the quantum mechanical behavior of the light field in the time domain. Taking the Fourier transform of the fluctuating part of the detector photocurrent, we can restrict our analysis to a frequency band in which no significant noise sources are present. This Fourier transform yields the frequency domain amplitude quadrature operator

$$i(\omega) = \mathbb{F}\left(\delta i(t)\right) = g_D \alpha(t) \hat{X}^+_{\Omega+\omega}(\omega). \tag{2.31}$$

Of course, the current $i(t)$ contains contributions from electromagnetic oscillations at both $\Omega - \omega$, and $\Omega + \omega$, each of which generates a current at frequency ω, so that the current we obtain is more accurately written as

$$I(\omega) = i(\omega) + i(-\omega) = g_D \alpha(t) \left(\hat{X}^+_{\Omega+\omega}(\omega) + \hat{X}^+_{\Omega-\omega}(-\omega) \right). \tag{2.32}$$

We see that the detection process performs a joint measurement on electromagnetic oscillations at frequencies $\Omega \pm \omega$. This pair of operators can be thought of as sidebands on either side of the carrier, and henceforth we term this composite system the *sideband picture*. The *sideband annihilation operator* $\hat{a}_{\text{sidebands}}(\omega)$ associated to the detection process is given by

$$\hat{a}_{\text{sidebands}}(\omega) = \frac{1}{\sqrt{2}} \left(\hat{a}_{\Omega-\omega}(-\omega) + \hat{a}_{\Omega+\omega}(\omega) \right), \tag{2.33}$$

where we have introduced the factor of $1/\sqrt{2}$ to retain the boson commutation relation.

In the Schrödinger picture, operating with this operator on a joint vacuum state in the modes at frequencies $\Omega \pm \omega$ ($|\Omega - \omega, \Omega + \omega\rangle = |0,0\rangle$) would put one photon into the sidebands in an equal superposition state

$$\hat{a}_{\text{sidebands}}(\omega)|0,0\rangle = \frac{1}{\sqrt{2}}|1,0\rangle + \frac{1}{\sqrt{2}}|0,1\rangle. \tag{2.34}$$

Sideband quadrature operators can be defined in the same manner as the frequency and time domain quadrature operators were previously.

2.4 Amplitude and phase modulation

Amplitude and phase modulations perform two functions in the work presented in this thesis. They provide error signals that allow control of the various interferometers and resonators utilised in the experiment, and they perform the function of the displacement operator of Eq. (2.11) transforming a vacuum sideband state into an arbitrary coherent state. In this Section we discuss how optical modulations are produced in the laboratory, we provide a description of optical modulation useful for the discussion of interferometric and resonator control later in this thesis, and perform a simple quantum optical analysis.

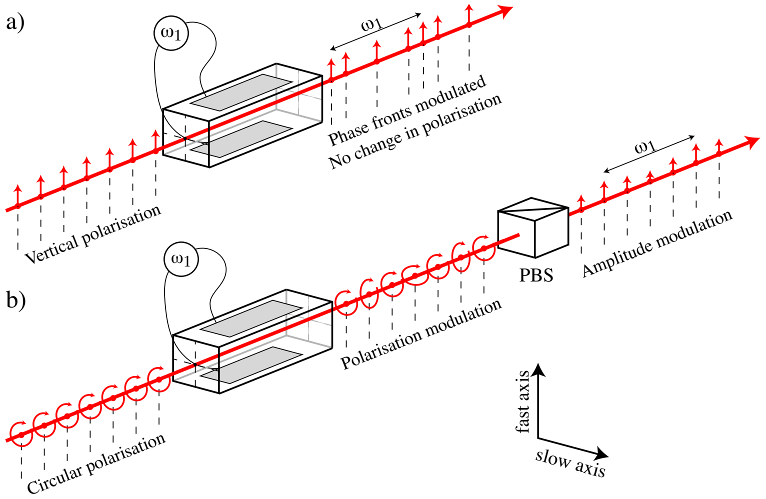

Figure 2.3: a) Phase and b) amplitude modulation using the electro-optic effect, PBS: polarising beam splitter.

Phase and amplitude modulations of a beam can be produced through modulations of the optical path length and attenuation experienced by the beam, respectively. Phase modulation can be achieved relatively easily by varying the position of a mirror in the beam path. The frequency of this type of modulation is limited to rather low frequencies ($f_{\rm mod} \lesssim 200$ KHz), however. At higher frequencies a more effective technique is to electro-optically modulate the refractive index of a crystal such as LiNbO$_3$ in the beam path. Using this technique it is possible to achieve phase modulation at frequencies as high as 10 GHz.

In a frame rotating at its carrier frequency (Ω), a phase modulated optical field $\tilde{a}_{PM}(t)$ can be represented by the expression

$$\tilde{a}_{PM}(t) = \tilde{a}(t) e^{i\xi \cos(\omega_1 t)} \tag{2.35}$$

where here ξ is the depth of modulation[4], ω_1 is the frequency of modulation, and $\tilde{a}(t)$ is the optical field prior to modulation. For the small modulation depths ($\xi \ll 1$) used throughout the work presented in this thesis, the field $\tilde{a}_{PM}(t)$ can be decomposed into a component at the laser carrier frequency Ω and sidebands at frequencies ω_1 and $-\omega_1$ away from the carrier

$$\tilde{a}_{PM}(t) \approx \tilde{a}(t)\left(1 + i\xi\cos(\omega_1 t)\right) = \tilde{a}(t)\left(1 + i\frac{\xi}{2}e^{i\omega_1 t} + i\frac{\xi}{2}e^{-i\omega_1 t}\right). \tag{2.36}$$

---

[4] $\xi = 1$ implies complete modulation, and $\xi = 0$ no modulation at all.

Taking the Fourier transform we find

$$\hat{a}_{PM}(\omega) = \mathbb{F}\left(\tilde{a}_{PM}(t)\right) \tag{2.37}$$

$$= \hat{a}(\omega) + i\frac{\xi}{2}\hat{a}(\omega - \omega_1) + i\frac{\xi}{2}\hat{a}(\omega + \omega_1) \tag{2.38}$$

$$\approx \hat{a}(\omega) + i\frac{\xi}{2}\delta(\omega_1)\alpha(t) + i\frac{\xi}{2}\delta(-\omega_1)\alpha(t) \qquad \text{for } \xi \ll 1, \tag{2.39}$$

where $\delta(\omega)$ is the Dirac delta function centered at ω. We see that the phase modulation has transferred optical power from the carrier into sidebands at frequencies $\pm\omega_1$. It is then possible to intuitively represent a phase modulation on a frequency axis with three phasors one each at Ω and $\pm\omega_1$, as shown in Fig. 2.4. The upper and lower sideband phasors rotate in clockwise and anti-clockwise directions, respectively at frequency ω_1 relative to the carrier.

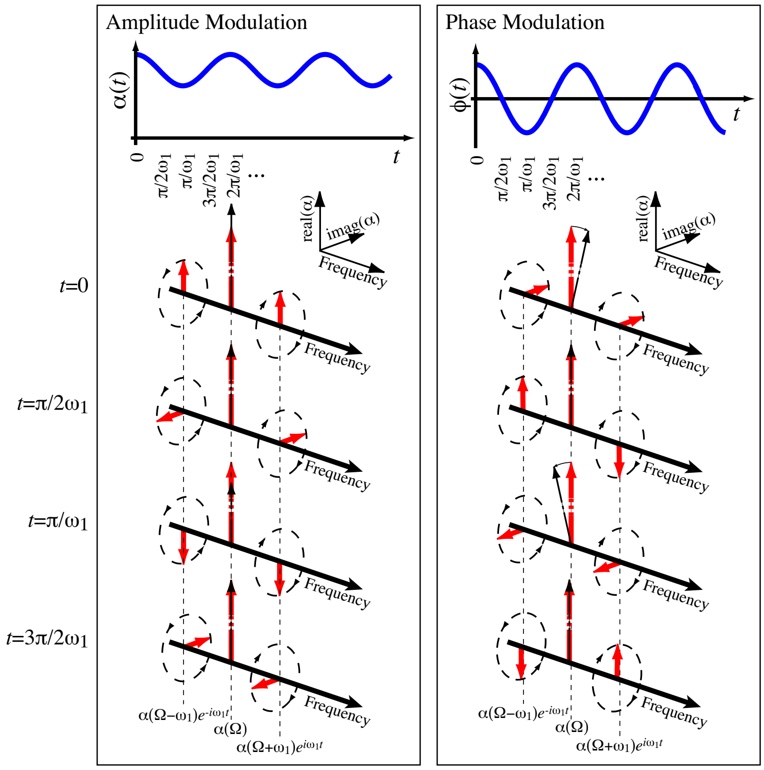

Figure 2.4: Amplitude and phase modulated optical fields represented as phasors at frequencies Ω and $\pm\omega_1$.

Unlike phase modulation which can be directly achieved via the electro-optic effect, amplitude modulation typically requires two stages. As shown in Fig. 2.3 b), the optical field is prepared with circular polarisation and is passed through a birefringent electro-optic crystal. The phase of the vertically polarised component of the field is modulated, whilst the horizontally polarised component is unmodulated. The net effect is to modulate the polarisation of the output field. Selecting only the horizontal component of the output field with a polarising beam splitter results in a purely amplitude modulated field[5]. Clearly this process attenuates the original field by 50 %

---

[5] Note that in reality amplitude modulators typically consist of two or four electro-optic crystal in a configuration to minimise polarisation rotation due to thermal drift in the modulator.

which could critically degrade the results of any quantum optical experiment. It is possible to use alternative configurations to achieve amplitude modulation with higher efficiency, however issues then arise such as parasitic phase modulation and thermal instability in the polarisation of the field exiting the electro-optic crystal. Throughout the work presented in this thesis we prefer to operate in the stable regime, sacrificing 50 % of the field, and arrange our experimental setup so that the experimental outcomes are insensitive to this loss.

In a frame rotating at its carrier frequency (Ω), an amplitude modulated optical field $\tilde{a}_{AM}(t)$ can be expressed as

$$\tilde{a}_{AM}(t) = \tilde{a}(t)\left(1 + \xi\cos(\omega_1 t)\right) = \tilde{a}(t)\left(1 + \frac{\xi}{2}e^{i\omega_1 t} + \frac{\xi}{2}e^{-i\omega_1 t}\right). \tag{2.40}$$

Again, we can take the Fourier transform

$$\begin{aligned} \hat{a}_{AM}(\omega) &= \mathbb{F}\left(\tilde{a}_{AM}(t)\right) && (2.41)\\ &= \hat{a}(\omega) + \frac{\xi}{2}\hat{a}(\omega+\omega_1) + \frac{\xi}{2}\hat{a}(\omega-\omega_1) && (2.42)\\ &\approx \hat{a}(\omega) + \frac{\xi}{2}\delta(\omega_1)\alpha(t) + \frac{\xi}{2}\delta(-\omega_1)\alpha(t) \qquad \text{for } \xi \ll 1. && (2.43) \end{aligned}$$

Notice that, similar to the phase modulation considered above, amplitude modulation of an optical field transfers power from the carrier frequency Ω to sidebands at frequencies $\Omega \pm \omega_1$. We can therefore also represent an amplitude modulation on a frequency axis with phasors at frequencies Ω and $\Omega \pm \omega_1$, as shown in Fig. 2.4. In this case at times $t = 2\pi m/\omega_1$, where m is an integer, both sideband phasors are in phase with the carrier. This contrasts the case for phase modulation where, at those times, both sideband are orientated $\pi/2$ out of phase with the carrier.

From Eq. (2.33) the sideband annihilation operators for the amplitude and phase modulated fields at frequency ω_1 are found to be

$$\hat{a}_{PM,\text{sidebands}}(\omega_1) = \hat{a}_{\text{sidebands}}(\omega_1) + i\frac{\xi}{\sqrt{2}}\alpha(t) \tag{2.44}$$

$$\hat{a}_{AM,\text{sidebands}}(\omega_1) = \hat{a}_{\text{sidebands}}(\omega_1) + \frac{\xi}{\sqrt{2}}\alpha(t). \tag{2.45}$$

We see then that, so long as the modulation depth is small ($\xi \ll 1$), optical modulation performs the role of the displacement operator on the sideband annihilation operator (see Eq. (2.11)). Amplitude modulation at frequency ω_1 of an optical field performs the displacement $D[\xi\alpha(t)/\sqrt{2}]$, displacing the sideband annihilation operator at frequency ω_1 along the axis of the amplitude quadrature; and correspondingly phase modulation performs the displacement $D[i\xi\alpha(t)/\sqrt{2}]$, displacing the state along the axis of the phase quadrature. Combinations of amplitude and phase modulations, when applied to a vacuum sideband state, can generate any arbitrary sideband coherent state. Furthermore, these optical modulations allow us to encode an arbitrary signal on the sideband state without any noise penalty. These properties of optical modulation have resulted in it becoming one of the core technologies in continuous variable quantum information protocols. It is one of the main building blocks utilised in quantum electro-optic feedforward which will be utilised in Chapter 5. Henceforth when in the frequency domain we discuss almost solely operators in the sideband picture, therefore in general we neglect the subscript 'sidebands'.

At this point it should be clear that the frequency and time domains offer two alternative descriptions of optical field states. It is natural to use the time domain to describe experimental apparatus, and to transform to the frequency domain to analyse experimental results. We use this convention throughout this thesis. The reader should be aware that a coherent state in the time domain corresponds to a vacuum state at sideband frequencies $\omega \neq 0$; amplitude/phase squeezed states in the time domain correspond to vacuum squeezed states at sideband frequencies $\omega \neq 0$; a coherent state in the frequency domain corresponds to a modulated coherent state in the time domain; and so on. For more details regarding the quantum optics of optical sidebands I refer you to Appendix A.

2.5 The humble beam splitter

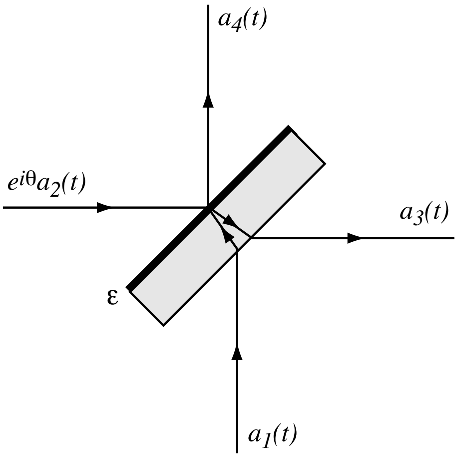

Figure 2.5: A schematic diagram of a beam splitter. $\hat{a}_1(\omega)$ and $\hat{a}_2(\omega)$ are the fields incident, $\hat{a}_3(\omega)$ and $\hat{a}_4(\omega)$ are the fields exiting, and ϵ is the beam splitter transmission.

The beam splitter is one of the most powerful and simple tools in quantum optics. It can be used, among other things, to characterise quantum states, to generate entangled states, and to enhance squeezed states. Fig. 2.5 shows a schematic diagram of a beam splitter, it has two incident fields $\tilde{a}_1(t)$ and $\tilde{a}_2(t)$ with a relative phase of θ between them, the beam splitter transmission is given by ϵ. On transmission the phase of each field remains unchanged, on reflection from a hard surface the phase is flipped by π. We therefore obtain the output fields $\tilde{a}_3(t)$ and $\tilde{a}_4(t)$

$$\tilde{a}_3(t) = \sqrt{1-\epsilon}\,\tilde{a}_1(t) + \sqrt{\epsilon}\,e^{i\theta}\tilde{a}_2(t) \tag{2.46}$$
$$\tilde{a}_4(t) = \sqrt{\epsilon}\,\tilde{a}_1(t) - \sqrt{1-\epsilon}\,e^{i\theta}\tilde{a}_2(t) \tag{2.47}$$

We see that the beam splitter couples the incident fields $\tilde{a}_1(t)$ and $\tilde{a}_2(t)$ together, with a coupling strength dependent on the beam splitter transmission ϵ.

2.5.1 Modelling optical attenuation using beam splitters

Optical attenuation (or loss) is a very significant effect in experimental quantum optics. Indeed it is, perhaps, the limiting factor in most squeezing related experiments. Some examples of processes that introduce losses to an experiment are: imperfections in photodetection, optical coatings, and spatial mode matching. These inefficiencies attenuate the field we are interested in, and introduce vacuum fields. It is therefore desirable to minimise inefficiencies in any quantum optical experiment. It is impossible to remove all losses however, and a model to accurately predict the effect

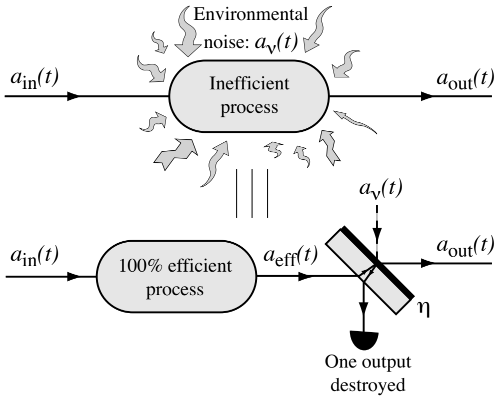

Figure 2.6: Equivalence of an inefficient linear process to an efficient linear process, with environmental coupling though a beam splitter.

of losses is essential. All of the examples given above, and indeed most linear processes[6], can be modelled by a 100 % efficient equivalent process that performs the transformation $\tilde{a}_{\rm in}(t) \rightarrow \tilde{a}_{\rm eff}(t)$ with coupling to the environment via a beam splitter, as shown in Fig. 2.6. We can define this transformed state $\tilde{a}_{\rm eff}(t)$ as the beam splitter input $\tilde{a}_1(t)$ in Fig. 2.5; and the other input $\tilde{a}_2(t)$ as the vacuum state $\tilde{a}_\nu(t)$ coupled to the original state during the process. The beam splitter transmission ϵ governs the efficiency of the process, so that $1-\epsilon$ gives the loss experienced by the state, and $\tilde{a}_4(t)$ then represents the field annihilation operator of the state after loss $\tilde{a}_{\rm out}(t)$. The assumption here is that the other beam splitter output $\tilde{a}_3(t)$ is destroyed, so that any information it contained about the fluctuations of the original state is lost. The annihilation operator of the state after the effect of loss is then given by

$$\tilde{a}_{\rm out}(t) = \sqrt{\epsilon}\,\tilde{a}_{\rm eff}(t) - \sqrt{1-\epsilon}\,\tilde{a}_\nu(t) \tag{2.48}$$

where the concept of ‘phase’ has no meaning for the vacuum state and we have therefore neglected the term $e^{i\theta}$. If $\epsilon = 1$, the process is perfectly efficient, and the original state is recovered at the output, and as $\epsilon \rightarrow 0$ the output state approaches the vacuum state $\tilde{a}_\nu(t)$ with no connection to the original state.

To demonstrate the effect of finite levels of loss let us consider the amplitude quadrature of the output state

$$\tilde{X}^+_{\rm out}(t) = \sqrt{\epsilon}\tilde{X}^+_{\rm eff}(t) - \sqrt{1-\epsilon}\tilde{X}^+_\nu(t). \tag{2.49}$$

Remembering that the variance of any quadrature of a vacuum state is unity ($\Delta^2\tilde{X}^+_\nu(t) = 1$) the variance of the amplitude quadrature of the output state is given by

$$\Delta^2\tilde{X}^+_{\rm out}(t) = \langle\delta\tilde{X}^+_{\rm out}(t)^2\rangle = \epsilon\Delta^2\tilde{X}^+_{\rm eff}(t) + 1 - \epsilon. \tag{2.50}$$

The question of most relevance to this thesis is: what effect does this loss have on a squeezed state? We see that it places a lower bound on the variance of the output state given by $1-\epsilon$. So that, no matter how strongly the original state is squeezed, the output state cannot have $\Delta^2\tilde{X}^+_{\rm out}(t) <$

---

[6] The exception, although not relevant to this thesis, is processes that couple the system to a thermal reservoir, or indeed to any environment other than vacuum.

$1-\epsilon$. Therefore, minimisation of optical loss is crucial for experiments that require a high level of squeezing.

2.5.2 Relative phase error signals for beam splitter inputs

We have just seen how optical losses can degrade a quantum optical experiment. Many other non-ideal effects are also present, perhaps the most significant of these are effects that alter the length of optical paths throughout the experiment. Such effects include mechanical drift of optical mounts; thermal drift in lenses, beam splitters, and crystals; and vibrations that arise due to acoustic noise (people talking for example), and coupling of external mechanical vibrations to the system (people walking for example). Most quantum optical experiments utilise interferometers and resonators that require precisely controlled optical beam paths to function properly. It is therefore necessary to measure and correct for the effects of each of these vibrations. A signal carrying information about drift of the system is termed an *error signal*. The ideal error signal is zero when the system is correctly controlled, and varies linearly with the drift. This Section describes the techniques used throughout this thesis to obtain error signals to control the relative phase of the inputs of a beam splitter. A quantum optical treatment of these techniques is unnecessary here, and we therefore only consider the coherent amplitude of the light fields. For the most part, we follow the treatment given in [77].

Power difference error signal

Perhaps the simplest method used to control the relative phase of the input fields to a beam splitter is to balance the power of the beam splitter output fields. Here we restrict ourselves to the case where the transmissivity of the beam splitter is $\epsilon = 1/2$, although the more general case is quite simply modelled it is not relevant to the work presented in this thesis. Neglecting the fluctuation terms and taking $\epsilon = 1/2$, detection of the beam splitter output fields given in Eqs. (2.46) and (2.47) yields the photocurrents

$$\begin{aligned} i_3(t) &= g_D\alpha_3^*(t)\alpha_3(t) = g_D\left(\frac{1}{2}\alpha_1(t)^2+\frac{1}{2}\alpha_2(t)^2+\alpha_1(t)\alpha_2(t)\cos\theta\right) && (2.51)\\ i_4(t) &= g_D\alpha_4^*(t)\alpha_4(t) = g_D\left(\frac{1}{2}\alpha_1(t)^2+\frac{1}{2}\alpha_2(t)^2-\alpha_1(t)\alpha_2(t)\cos\theta\right), && (2.52)\end{aligned}$$

where $\alpha_1(t)$ and $\alpha_2(t)$ are the coherent amplitudes of the input fields at the laser carrier frequency. Subtracting one photocurrent from the other provides the power difference error signal E_{PD}

$$\begin{aligned} E_{\mathrm{PD}} = i_3(t)-i_4(t) &= 2g_D\alpha_1(t)\alpha_2(t)\cos\theta && (2.53)\\ &\approx 2g_D\alpha_1(t)\alpha_2(t)\left(\frac{\pi}{2}-\theta\right) \qquad \text{for } \theta\approx\frac{\pi}{2} && (2.54)\\ &\approx 2g_D\alpha_1(t)\alpha_2(t)\left(\frac{\pi}{2}+\theta\right) \qquad \text{for } \theta\approx-\frac{\pi}{2}. && (2.55)\end{aligned}$$

We see that this simple technique provides an error signal that is zeroed at $\theta = \pm\pi/2$, and that is linear with θ around those points. Notice also that the zero point of the error signal is independent of the power of the input fields to the beam splitter.

Offset locking error signal

Of course, we may not always have access to both of the fields exiting the beam splitter, and we may wish to control the relative phase to a value other than $\theta = \pm\pi/2$. It is possible to generate an error signal from only one output field (or a fraction of it) by comparing the detected photocurrent to some pre-defined offset voltage V_{offset}. The error signal thus obtained E_{OL} is given by

$$\begin{aligned} E_{\text{OL}} &= i_3(t) - V_{\text{offset}} && (2.56) \\ &= g_D\left(\frac{1}{2}\alpha_1(t)^2 + \frac{1}{2}\alpha_2(t)^2 + \alpha_1(t)\alpha_2(t)\cos\theta\right) - V_{\text{offset}} && (2.57) \end{aligned}$$

This technique has the advantage that the error signal can be zeroed arbitrarily by adjusting V_{offset}, although the slope of the error signal goes to zero around $\theta = 0$, so that controlling the relative phase near $\theta = 0$ is difficult. The error signal zero point for this technique is dependent on the coherent amplitudes $\alpha_1(t)$ and $\alpha_2(t)$. This is a significant drawback since in most experimental situations the laser power is only stable to around $2 - 5$ %.

Sideband modulation error signal

Alternative techniques are available to generate error signals using sideband modulations. Here we consider the case where one of the fields input to the beam splitter is phase modulated at frequency ω. That is $\alpha_{PM,1}(t) = \alpha_1(t)(1 + i\xi\sin(\omega t))$. Rather than consider only the case when $\epsilon = 1/2$ as was done above, due to relevance in Chapter 5 we include an arbitrary beam splitter ratio ϵ. The detected photocurrent from the beam splitter output $\alpha_3(t)$ is then given by

$$\begin{aligned} i_3(t) &= g_D\big((1-\epsilon)\alpha_1(t)^2 + \epsilon\alpha_2(t)^2 + 2\sqrt{\epsilon(1-\epsilon)}\,\alpha_1(t)\alpha_2(t)\cos\theta \\ &\quad + 2\xi\sqrt{\epsilon(1-\epsilon)}\,\alpha_1(t)\alpha_2(t)\sin\theta\sin(\omega t)\big), && (2.58) \end{aligned}$$

where we have assumed the modulation depth is small $\xi \approx 0$, neglecting the second order term in ξ.

Eq. (2.58) contains a term fluctuating with frequency ω. The signal contained in this term can be extracted by multiplying the photocurrent with an electronic local oscillator at frequency ω. The convolution theorem tells us that this multiplication in the time domain is equivalent to a convolution in the frequency domain. This process shifts the frequency components of the photocurrent both up and down by ω. The down shifted component is the component of interest to us, and the process is thus termed *mixing down*. The phase of the electronic local oscillator is critical, and should be in phase with the signal that we wish to extract. In this case, we choose an electronic local oscillator of the form $\sin(\omega t)$. The mixed down photocurrent is then given by

$$\begin{aligned} i_3(t)\times\sin(\omega t) &= g_D\left[(1-\epsilon)\alpha_1(t)^2 + \epsilon\alpha_2(t)^2 + 2\sqrt{\epsilon(1-\epsilon)}\,\alpha_1(t)\alpha_2(t)\cos\theta\right]\sin(\omega t) \\ &\quad + 2g_D\xi\sqrt{\epsilon(1-\epsilon)}\,\alpha_1(t)\alpha_2(t)\sin\theta\sin^2(\omega t) && (2.59) \\ &= g_D\left[(1-\epsilon)\alpha_1(t)^2 + \epsilon\alpha_2(t)^2 + 2\sqrt{\epsilon(1-\epsilon)}\,\alpha_1(t)\alpha_2(t)\cos\theta\right]\sin(\omega t) \\ &\quad + g_D\xi\sqrt{\epsilon(1-\epsilon)}\,\alpha_1(t)\alpha_2(t)\sin\theta\,(1-\cos(2\omega t))\,. && (2.60) \end{aligned}$$

low pass filtering this signal to remove components with frequencies $\geq \omega$, we obtain the sideband error signal E_{SB}

$$\begin{aligned} E_{\text{SB}} &= g_D\xi\sqrt{\epsilon(1-\epsilon)}\,\alpha_1(t)\alpha_2(t)\sin\theta && && (2.61) \\ &\approx g_D\xi\sqrt{\epsilon(1-\epsilon)}\,\alpha_1(t)\alpha_2(t)\theta && \text{for}\,\theta\approx 0 && (2.62) \\ &\approx g_D\xi\sqrt{\epsilon(1-\epsilon)}\,\alpha_1(t)\alpha_2(t)(\pi-\theta) && \text{for}\,\theta\approx\pi. && (2.63) \end{aligned}$$

We see that this sideband error signal is zero when $\theta = \{0, \pi\}$, and is linear for small phase errors around those points. Similar to the power difference error signal, the zero crossing is independent of the coherent amplitudes $\alpha_1(t)$ and $\alpha_2(t)$, and furthermore it is independent of the beam splitter reflectivity ϵ.

The error signal $E_{\rm SB}$ can be understood via the sideband picture as shown in Fig. 2.7. The original phase sidebands are rotated relative to the carrier field. The resulting sidebands can be separated into a component of phase modulation and a component of amplitude modulation. It is the component of amplitude modulation that is detected, and provides an error signal.

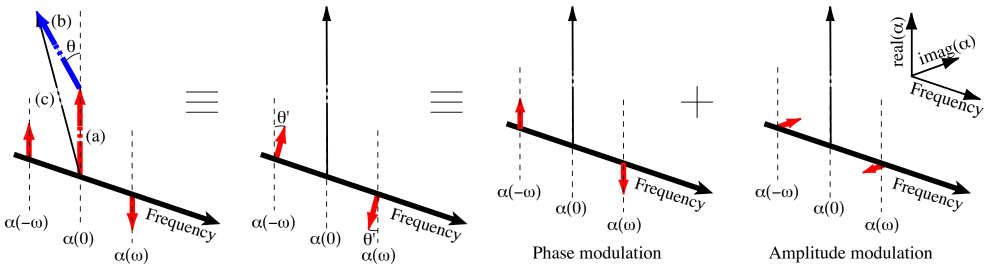

Figure 2.7: The field in the sidebands of a beam splitter output field can be broken into a component of phase modulation and a component of amplitude modulation. (a) $\alpha_1(t)$, (b) $e^{i\theta}\alpha_2(t)$, and (c) $e^{i\theta'}\alpha_3(t)$ where θ' depends on $\alpha_1(t)$, $\alpha_2(t)$, and θ.

Note that linear combinations of the error signals $E_{\rm PD}$ and $E_{\rm SB}$ can produce an error signal zeroed, and linear around, any arbitrary relative phase θ. In the work presented in this thesis, however, this technique was unnecessary since error signals were only required for $\theta = \{-\pi/2, 0, \pi/2, \pi\}$.

2.6 Measuring the efficiency of optical processes

The main inefficiencies in the experiments presented in this thesis result from the photodetection process, non-optimal di-electric coatings on optics, and non-optimum spatial mode-matching.

2.6.1 Inefficiencies due to scattering and absorption in optics

The loss associated with scattering and absorption at the di-electric coatings on optics is easily characterised since the optical beam remains accessible after transmission or reflection through the element. All that is required is a direct comparison of the optical power before and after the optical element. Table 2.1 provides a list of the efficiencies of the optical elements commonly used in the work presented in this thesis.

2.6.2 Inefficiencies in the photodetection process

The loss in photodetection is less easily measured. It may be indirectly characterised by comparing the current i flowing through the photodiode to the power P in the incident optical beam. If the photodetection is 100 % efficient, each photons in the optical beam should generate one electron in the photodetector current. The efficiency of detection is therefore given by

$$\eta_{\rm detectors} = \frac{N_{\rm electrons}}{N_{\rm photons}} = \left(\frac{\hbar\Omega}{P}\right)\frac{i}{\varepsilon} \qquad (2.64)$$

Optical element	Manufacturer	Part number	Efficiency
1064 nm optical isolator	Gsänger	FR 1060/5	95 %
532 nm optical isolator	Gsänger	FR 532/5	95 %
0^{th} order $\lambda/4$ and $\lambda/2$ @ 1064/532 nm	Rimkevicius	N/A	99.5 %
0^{th} order $\lambda/2$ @ 1064 nm	Newport	10RP02-34	99.8 %
0^{th} order$\lambda/4$ @ 1064 nm	Newport	10RP04-34	99.8 %
0^{th} order$\lambda/2$ @ 532 nm	Newport	10RP02-16	99.8 %
0^{th} order$\lambda/4$ @ 532 nm	Newport	10RP04-16	99.8 %
Lenses @ 1064/532 nm	Rimkevicius	N/A	99.5 %
Lenses @ 1064 nm	Newport	KPXxxxAR.18	99.8 %
Lenses @ 532 nm	Newport	KPXxxxAR.14	99.8 %
Polarising beam splitters @ 1064 nm	Newport	05BC16PC.9	99 %
Polarising beam splitters @ 532 nm	Newport	05BC16PC.3	99 %
50/50 beam splitters @ 1064 nm	LASTEK	BS1-1064-50-1037-458	99.8 %
50/50 beam splitters @ 1064 nm	Newport	05BC16NP.9	99.8 %
T:1064/R:532 nm dichroic beam splitters	LASTEK	BSR51-1025	99.8 %
T:532/R:1064 nm dichroic beam splitters	LASTEK	BSR15-1025	99.8 %
1064 nm dielectric mirrors	Rimkevicius	N/A	99.5 %
1064 nm dielectric mirrors	New Focus	5104	99 %
532 nm dielectric mirrors	New Focus	5101	99 %
Phase modulators @ 1064nm	Gsänger	LM0202-PHAS	95 %
Amplitude modulators @ 1064nm	Gsänger	LM0202 P 5W IR	50 %

Table 2.1: Summary of the efficiencies of linear optical elements used in the experiments presented in this thesis.

where $N_{\mathrm{electrons}}$ and N_{photons} are the number of electrons and photons, respectively, $\hbar\Omega$ is the energy of a single photon, and ε is the charge of a single electron. A very nice analysis of the efficiency of a number of different photodiodes using this technique is presented in the thesis of Ping Koy Lam [75]. Epitaxx ETX-500 photodiodes were utilised for detection of the quantum fluctuations of the optical field throughout this thesis, these diodes were characterised to have an efficiency of $93\ \pm\ 2\%$.

2.6.3 Inefficiencies in optical mode-matching

Let us now consider the mode-matching efficiency for the interference of two beams on the beam splitter in Fig. 2.5 with $\epsilon = 0.5$. In Eqs. (2.46) and (2.47) the modes $\tilde{a}_1(t)$ and $\tilde{a}_2(t)$ were assumed to be in identical polarisation and spatial modes. In an experimental situation this is never the case. In general, the modes $\tilde{a}_1(t)$ and $\tilde{a}_2(t)$ will overlap, and therefore interfere, with some efficiency η. Let us define the spatial mode of $\tilde{a}_1(t)$ as a reference. Both modes incident on the beam splitter can then be expanded into a part that resides in that spatial mode, and a part in an orthogonal mode that does not interfere with $\tilde{a}_1(t)$, $(\tilde{a}_{\mathrm{ref}}(t), \tilde{a}_{\mathrm{orth}}(t))$. Considering only the coherent amplitudes here the fields input to the beam splitter then become

$$\begin{aligned}(\alpha_{1,\mathrm{ref}}(t), \alpha_{1,\mathrm{orth}}(t)) &= (\alpha_1(t), 0) &(2.65)\\ (\alpha_{2,\mathrm{ref}}(t), \alpha_{2,\mathrm{orth}}(t)) &= \left(\sqrt{\eta}\,\alpha_2(t), \sqrt{1-\eta}\,\alpha_2(t)\right), &(2.66)\end{aligned}$$

and the coherent amplitude of the output state $\alpha_3(t)$ is given by

$$(\alpha_{3,\mathrm{ref}}(t), \alpha_{3,\mathrm{orth}}(t)) = \frac{1}{\sqrt{2}}\left(\alpha_1(t) + e^{i\theta}\sqrt{\eta}\,\alpha_2(t), e^{i\theta}\sqrt{1-\eta}\,\alpha_2(t)\right). \tag{2.67}$$

Calculating the intensity of the reference and orthogonal modes we find

$$\begin{aligned} \alpha^*_{3,\mathrm{ref}}(t)\alpha_{3,\mathrm{ref}}(t) &= \frac{1}{2}\left(\alpha_1^2(t) + \eta\alpha_2^2(t) + 2\sqrt{\eta}\cos\theta\alpha_1(t)\alpha_2(t)\right) & (2.68)\\ \alpha^*_{3,\mathrm{orth}}(t)\alpha_{3,\mathrm{orth}}(t) &= \frac{1}{2}\left((1-\eta)\alpha_2^2(t)\right). & (2.69) \end{aligned}$$

The photocurrent i_3 obtained when this total field impinges on a photodetector is given by

$$\begin{aligned} i_3 &= g_D\left(\alpha^*_{3,\mathrm{ref}}(t)\alpha_{3,\mathrm{ref}}(t) + \alpha^*_{3,\mathrm{orth}}(t)\alpha_{3,\mathrm{orth}}(t)\right)\\ &= \frac{g_D}{2}\left(\alpha_1^2(t) + \alpha_2^2(t) + 2\sqrt{\eta}\cos\theta\alpha_1(t)\alpha_2(t)\right), \end{aligned} \tag{2.70}$$

where g_D is the gain of the photodetection process. Notice that as the relative phase θ between the input modes $\alpha_1(t)$ and $\alpha_2(t)$ changes we observe an interference fringe. The visibility VIS of this fringe is defined as

$$VIS = \frac{\max_\theta\{i_3\} - \min_\theta\{i_3\}}{\max_\theta\{i_3\} + \min_\theta\{i_3\}} = \frac{2\sqrt{\eta}\,\alpha_1(t)\alpha_2(t)}{\alpha_1^2(t) + \alpha_2^2(t)}, \tag{2.71}$$

We see that given knowledge of $\alpha_1(t)$ and $\alpha_2(t)$ it is possible to infer the efficiency of mode-matching $\eta_{mode-match}$

$$\eta_{mode-match} = \frac{VIS^2\left(\alpha_1^2(t) + \alpha_2^2(t)\right)^2}{4\alpha_1^2(t)\alpha_2^2(t)}. \tag{2.72}$$

Indeed, if the power in each of the input modes is arranged to be equal ($\alpha_1^2(t) = \alpha_2^2(t)$) we obtain a simple relationship between the visibility and mode-matching efficiency of the interference

$$\eta_{mode-match} = VIS^2. \tag{2.73}$$

In general it is possible to arrange the power of the two beam splitter inputs to be equal. Throughout almost the entirety of the work presented in this thesis we balanced the power of the two input beams and characterised the visibility of interference to determine the mode-matching efficiency η. Through careful design of the experimental optical path lengths and lens arrangements, and using beam steering mirrors and polarising optics, we could typically achieve mode-matching efficiencies in the range $\eta = 0.92$ to 0.99. These efficiencies were usually limited not by the focussing, alignment, or polarisation of the optical fields, but rather by variations from a perfect Gaussian transverse modeshape.

2.7 Detecting quantum states of light

In Section 2.3, the process of photodetection was introduced. We showed that the component of the resulting photocurrent at frequency ω was directly related to the amplitude quadrature of the sideband annihilation operator at that frequency. This Section describes how this photocurrent component can be normalised to the quantum noise limit, how the phase quadrature of the sideband annihilation operator can be determined, and how we convert the detected photocurrent into a frequency spectra using a spectrum analyser.

2.7.1 Balanced self homodyne detection

Consider an optical field $\tilde{a}_1$ split on a 50/50 beam splitter ($\epsilon = 1/2$), clearly a vacuum field $\tilde{a}_\nu$ enters the unused port of the beam splitter. Detecting the two output fields $\tilde{a}_3$ and $\tilde{a}_4$ yields the photocurrents

$$\begin{aligned} i_3(t) &= g_D \tilde{a}_3^\dagger(t)\tilde{a}_3(t) = \frac{g_D}{2}\left(\alpha_1(t)^2 + \alpha_1(t)\left(\delta\tilde{X}_1^+(t) + \delta\tilde{X}_\nu^+(t)\right)\right) && (2.74)\\ i_4(t) &= g_D \tilde{a}_4^\dagger(t)\tilde{a}_4(t) = \frac{g_D}{2}\left(\alpha_1^2(t) + \alpha_1(t)\left(\delta\tilde{X}_1^+(t) - \delta\tilde{X}_\nu^+(t)\right)\right), && (2.75)\end{aligned}$$

where g_D is the gain of the photodetection process. The sum and difference of these photocurrents are

$$\begin{aligned} i_{\text{sum}}(t) &= i_3(t) + i_4(t) = g_D\left(\alpha_1^2(t) + \alpha_1(t)\tilde{X}_1^+(t)\right) && (2.76)\\ i_{\text{diff}}(t) &= i_3(t) - i_4(t) = g_D\alpha_1(t)\tilde{X}_\nu^+(t), && (2.77)\end{aligned}$$

Taking the Fourier transform of the fluctuations of these currents yields the sum and difference photocurrent fluctuations as a function of frequency

$$\begin{aligned} i_{\text{sum}}(\omega) &= \mathbb{F}\left(\delta i_{\text{sum}}(t)\right) = g_D\alpha_1(t)\hat{X}_1^+(\omega) && (2.78)\\ i_{\text{diff}}(\omega) &= \mathbb{F}\left(\delta i_{\text{diff}}(t)\right) = g_D\alpha_1(t)\hat{X}_\nu^+(\omega). && (2.79)\end{aligned}$$

Notice that in the frequency domain the sum and difference photocurrents are directly proportional to the sideband amplitude quadrature operator of the input field, and vacuum field entering the unused beam splitter input port, respectively. Remembering that $\Delta^2\hat{X}_\nu^+(\omega) = 1$, the variances of these sum and difference photocurrent components are given by

$$\begin{aligned} \Delta^2 i_{\text{sum}}(\omega) &= \left\langle \left(i_{\text{sum}}(\omega)\right)^2 \right\rangle - \left\langle \left(i_{\text{sum}}(\omega)\right) \right\rangle^2 = g_D^2\alpha_1(t)^2\Delta^2\hat{X}_1^+(\omega) && (2.80)\\ \Delta^2 i_{\text{diff}}(\omega) &= \left\langle \left(i_{\text{sum}}(\omega)\right)^2 \right\rangle - \left\langle \left(i_{\text{sum}}(\omega)\right) \right\rangle^2 = g_D^2\alpha_1(t)^2. && (2.81)\end{aligned}$$

So that the ratio of the variances of the sum and difference photocurrents gives a measurement of the amplitude quadrature variance of the input field $\Delta^2\hat{X}_1^+(\omega)$ calibrated to the vacuum noise level

$$\frac{\Delta^2 i_{\text{sum}}(\omega)}{\Delta^2 i_{\text{diff}}(\omega)} = \Delta^2\hat{X}_1^+(\omega). \tag{2.82}$$

This technique provides an accurate method to characterise the sideband amplitude quadrature of a light field.

2.7.2 Balanced homodyne detection

To characterise the phase quadrature we replace the vacuum field $\tilde{a}_\nu(t)$ input to the beam splitter for self homodyne with a bright local oscillator $\tilde{a}_{\text{LO}}(t)$. Given that $\alpha_{\text{LO}}(t) \gg \alpha_1(t)$, the action of this local oscillator is to arbitrarily rotate the coherent amplitudes of the two beam splitter outputs, which, as we will see in the following analysis, allows the homodyne detector to measure an arbitrary quadrature of the input state.

In this case detecting the output fields $\tilde{a}_3(t)$ and $\tilde{a}_4(t)$ yields the photocurrents

$$\begin{aligned} i_3(t) &= g_D\tilde{a}_3^\dagger(t)\tilde{a}_3(t) = \frac{g_D}{2}\Big(\alpha_1(t)^2 + \alpha_{\mathrm{LO}}(t)^2 + 2\cos\theta\alpha_1(t)\alpha_{\mathrm{LO}}(t) + \\ &\quad \alpha_1(t)\left(\delta\tilde{X}_1^+(t) + \delta\tilde{X}_{\mathrm{LO}}^{-\theta}(t)\right) + \alpha_{\mathrm{LO}}(t)\left(\delta\tilde{X}_{\mathrm{LO}}^+(t) + \delta\tilde{X}_1^\theta(t)\right)\Big) \end{aligned} \tag{2.83}$$

$$\begin{aligned} i_4(t) &= g_D\tilde{a}_4^\dagger(t)\tilde{a}_4(t) = \frac{g_D}{2}\Big(\alpha_1(t)^2 + \alpha_{\mathrm{LO}}(t)^2 - 2\cos\theta\alpha_1(t)\alpha_{\mathrm{LO}}(t) + \\ &\quad \alpha_1(t)\left(\delta\tilde{X}_1^+(t) - \delta\tilde{X}_{\mathrm{LO}}^{-\theta}(t)\right) + \alpha_{\mathrm{LO}}(t)\left(\delta\tilde{X}_{\mathrm{LO}}^+(t) - \delta\tilde{X}_1^\theta(t)\right)\Big), \end{aligned} \tag{2.84}$$

where θ is the relative phase of the input fields, and the arbitrary quadrature operator $\tilde{X}^\theta(t)$ is defined in Eq. (2.7). As before, we take the sum and difference of these photocurrents

$$i_{\mathrm{sum}}(t) = i_3(t) + i_4(t) = g_D\left(\alpha_1(t)^2 + \alpha_{\mathrm{LO}}(t)^2 + \alpha_{\mathrm{LO}}(t)\delta\tilde{X}_{\mathrm{LO}}^+(t)\right) \tag{2.85}$$

$$i_{\mathrm{diff}}(t) = i_3(t) - i_4(t) = g_D\left(2\cos\theta\alpha_1(t)\alpha_{\mathrm{LO}}(t) + \alpha_{\mathrm{LO}}(t)\delta\tilde{X}_1^\theta(t)\right), \tag{2.86}$$

where since $\alpha_{\mathrm{LO}}(t) \gg \alpha_1(t)$ we have neglected the fluctuation terms not containing the local oscillator coherent amplitude $\alpha_{\mathrm{LO}}(t)$. We again take the Fourier transform of the fluctuations of these currents to obtain the sum and difference photocurrent fluctuations in the frequency domain

$$i_{\mathrm{sum}}(\omega) = \mathbb{F}\left(\delta i_{\mathrm{sum}}(t)\right) = g_D\alpha_{\mathrm{LO}}(t)\hat{X}_{\mathrm{LO}}^+(\omega) \tag{2.87}$$

$$i_{\mathrm{diff}}(\omega) = \mathbb{F}\left(\delta i_{\mathrm{diff}}(t)\right) = g_D\alpha_{\mathrm{LO}}(t)\hat{X}_1^\theta(\omega). \tag{2.88}$$

Notice that $i_{\mathrm{diff}}(\omega)$ measures a quadrature of the input state dependent on the relative phase of the input fields θ, and that $i_{\mathrm{sum}}(\omega)$ measures the amplitude quadrature of the local oscillator independent of θ. Calculated in the same manner as above, the variances of the frequency domain sum and difference photocurrents are given by

$$\Delta^2 i_{\mathrm{sum}}(\omega) = g_D^2\alpha_{\mathrm{LO}}(t)^2\Delta^2\hat{X}_{\mathrm{LO}}^+(\omega) \tag{2.89}$$

$$\Delta^2 i_{\mathrm{diff}}(\omega) = g_D^2\alpha_{\mathrm{LO}}(t)^2\Delta^2\hat{X}_1^\theta(\omega). \tag{2.90}$$

Assuming that the sidebands of the local oscillator at frequencies $\Omega \pm \omega$ are in vacuum states so that $\Delta^2\hat{X}_{\mathrm{LO}}^+(\omega) = 1$, the ratio of the sum and difference variances gives

$$\frac{\Delta^2 i_{\mathrm{diff}}(\omega)}{\Delta^2 i_{\mathrm{sum}}(\omega)} = \Delta^2\hat{X}_1^\theta(\omega), \tag{2.91}$$

which is a calibrated measurement of the arbitrary quadrature of the input state defined by $\Delta^2\hat{X}_1^\theta(\omega)$. $\hat{X}_1^{\theta=0}(\omega) = \hat{X}_1^+(\omega)$, and $\hat{X}_1^{\theta=\pi/2}(\omega) = \hat{X}_1^-(\omega)$, so this balanced homodyne technique allows calibrated measurements of both the amplitude and phase quadratures.

Of course, we must be careful to ensure that the local oscillator is in a vacuum state at the frequencies we are interested in. An alternative approach using the same apparatus, and the one adopted through the majority of this thesis, is to always measure $\Delta^2 i_{\mathrm{diff}}(\omega)$ and to block the input state (but not the local oscillator) to provide the normalisation. In this case, since there is no optical power entering the input port of the beam splitter, we can be sure that the input becomes a vacuum state, and hence that $\Delta^2\hat{X}_{1,\mathrm{blocked}}^\theta(\omega) = 1$, for any θ and ω. The ratio of the difference current variances with the input unblocked and blocked is given by

$$\frac{\Delta^2 i_{\mathrm{diff,unblocked}}(\omega)}{\Delta^2 i_{\mathrm{diff,blocked}}(\omega)} = \Delta^2 \hat{X}_1^{\theta}(\omega), \tag{2.92}$$

which also provides a calibrated measurement of $\Delta^2 \hat{X}_1^{\theta}(\omega)$.

2.7.3 Analysis using a spectrum analyser

In a squeezing related experiment it is usual to analyse the output photocurrents in a spectrum analyser. Spectrum analysers are by no means simple devices. The detailed operation of a spectrum analyser, however, will not be examined in this thesis. An elegant analysis can be found in the thesis of Ben Buchler [76]. The outcome of this analysis is that when normalised, as discussed prior in this Section, the spectrum analyser provides the spectral power density $V(\omega)$ defined by

$$V(\omega) = \left\langle \left(\hat{X}_1^{\theta}(\omega) \right)^2 \right\rangle, \tag{2.93}$$

where θ is determined by the arrangement of the detection apparatus. Expanding $\hat{X}_1^{\theta}$ in terms of its coherent amplitude and fluctuations we see that

$$\begin{aligned} V(\omega) &= \left\langle \left(2\alpha_1(\omega) + \delta\hat{X}_1^{\theta}(\omega) \right)^2 \right\rangle & (2.94) \\ &= \left\langle 4\alpha_1(\omega)^2 + 4\alpha_1(\omega)\delta\hat{X}_1^{\theta}(\omega) + \left(\delta\hat{X}_1^{\theta}(\omega) \right)^2 \right\rangle & (2.95) \\ &= 4\alpha_1(\omega)^2 + 4\alpha_1(\omega) \left\langle \delta\hat{X}_1^{\theta}(\omega) \right\rangle + \left\langle \left(\delta\hat{X}_1^{\theta}(\omega) \right)^2 \right\rangle & (2.96) \\ &= 4\alpha_1(\omega)^2 + \Delta^2\hat{X}_1^{\theta}(\omega). & (2.97) \end{aligned}$$

So the spectrum analyser does not measure straight-forwardly the variance spectra of the operator $\hat{X}_1^{\theta}(\omega)$. Instead it measures the sum of the coherent amplitude (scaled by four), and the variance. The systems analysed in the work presented in this thesis had $\alpha_1(\omega) = 0$ unless a coherent amplitude was encoded via optical modulation. An encoded coherent amplitude typically had a bandwidth of ≈ 20 kHz. On the other hand the variance spectra was typically constant over a frequency range of ≈ 200 kHz. Therefore, both the variance and coherent amplitude of the operator $\hat{X}_1^{\theta}$ could be obtained from a frequency spectra with $\Delta\omega/2\pi > 20$ kHz centered around ω. Fig. 2.8 shows how this technique was applied for a typical spectrum analyser output.

2.8 Optical resonators

Much of the work presented in this thesis involves optical resonators. These resonators fulfilled a number of purposes in the experiments, including spectral and spatial modecleaning, and power enhancement to improve the effective non-linearity of non-linear systems. In this Section we first provide a basic introduction to modelling of open quantum systems. This will allow us to effectively model all of the systems involving resonators used in the work presented in this thesis. We then model a passive resonator, demonstrating its spectral and spatial modecleaning properties. Since a crucial aspect of optical resonators is the interference of the internal and external fields, precise control of the length of the resonator is important. Our model allows us to describe how error signals are generated that allow active control of the resonator length.

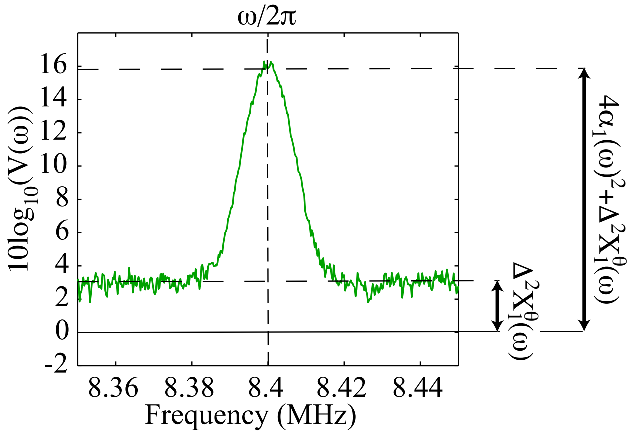

Figure 2.8: Typical spectrum observed with a spectrum analyser for a frequency domain quadrature operator with $\omega/2\pi$=8.4 MHz. The part of the spectrum at frequencies away from ω gives a measure of $\Delta^2\hat{X}_1^\theta(\omega)$, and the part near ω gives $4\alpha_1(\omega)^2 + \Delta^2\hat{X}_1^\theta(\omega)$.

2.8.1 Modelling of optical resonators

Modelling open quantum systems

In this thesis the approach taken to modelling systems involving optical resonators is to first define a Hamiltonian for the system. This Hamiltonian can be used to predict equations of motion for the time domain operators of relevance, or in other words to determine the *quantum Langevin equations* for the system. We separate these equations into pairs of time domain amplitude and phase quadrature operator equations. Taking the Fourier transform results in the corresponding frequency domain quadrature operators. Here we will briefly describe the second stage of this process, transforming the Hamiltonian of the system into an equation of motion, before we consider the specific case of a passive optical resonator.

Within a closed system with Hamiltonian $H_{\rm rev}$, the equation of motion of a system operator $\tilde{a}_{\rm sys}(t)$ is given simply by

$$\dot{\tilde{a}}_{\rm sys}(t) = i\left(\Omega\tilde{a}_{\rm sys}(t) - \frac{1}{\hbar}\left[\tilde{a}_{\rm sys}(t), H_{\rm rev}\right]\right), \tag{2.98}$$

where we have chosen a frame rotating at frequency Ω. In open systems however, fields from the environment interact with the system, and the equation of motion becomes more complex. Gardiner and Collett [78] showed that, assuming the coupling of the system to the environment γ is independent of frequency[7], if the environment interacts irreversibly with the system operator of interest $\tilde{a}_{\rm sys}(t)$ its effect on the equation of motion of the operator can be modelled by adding a correction term to Eq. (2.98). The modified equation of motion is then

$$\begin{aligned}\dot{\tilde{a}}_{\rm sys}(t) &= i\left(\Omega\tilde{a}_{\rm sys}(t) - \frac{1}{\hbar}\left[\tilde{a}_{\rm sys}(t), H_{\rm rev}\right]\right) \qquad (2.99)\\ &- \left[\tilde{a}_{\rm sys}(t), \tilde{a}^\dagger(t)\right]\left(\gamma\tilde{a}(t) + \sqrt{2\gamma}\,\delta a_{\rm env}(t)\right) + \left(\gamma\tilde{a}^\dagger(t) + \sqrt{2\gamma}\,\delta a_{\rm env}^\dagger(t)\right)\left[\tilde{a}_{\rm sys}(t), \tilde{a}(t)\right]\end{aligned}$$

where $\tilde{a}_{\rm env}(t)$ is the time domain annihilation operator describing the environment, and $\tilde{a}(t)$ is the system operator coupled to the environment. This equation is known as the *quantum Langevin*

---

[7] This assumption is known as the *first Markov approximation*

equation.

Modelling a passive optical resonator

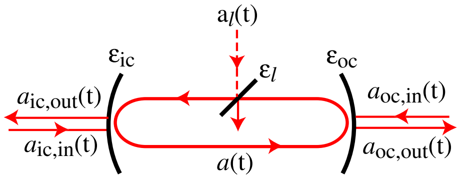

Figure 2.9: A model of a passive optical resonator, including input fields from the input and output couplers, input field fluctuations due to loss in the resonator, and output fields exiting the input and output couplers.

The Hamiltonian of a lossless passive optical resonator $H_{\rm resonator}$ is identical to that of a simple harmonic oscillator

$$H_{\rm resonator} = \Omega' \hbar \left(\tilde{a}^\dagger(t)\tilde{a}(t) + \frac{1}{2} \right), \tag{2.100}$$

where $\tilde{a}$ is the intra-cavity resonator mode, Ω' is the frequency of the oscillator, or in other words the resonance frequency of the resonator, and the $1/2$ term is the oscillators ground state energy. In practice however, an optical resonator is not lossless, and interacts with the environment in a number of ways. The resonator mirrors, which we term here the input (sub-script ic) and output (subscript oc) couplers, have some transmission $\epsilon_{\rm ic}$ and $\epsilon_{\rm oc}$, and the intra-cavity mode experiences some round trip loss $1 - \epsilon_l$, which we denote here by a sub-script l. Each of these properties couples a mode of the environment into the resonator (denoted here by $\tilde{a}_{\rm ic,in}(t)$, $\tilde{a}_{\rm oc,in}(t)$, and $\tilde{a}_l(t)$, respectively), and couples out some of the resonator mode. This coupling is shown schematically in Fig. 2.9. The equation of motion for the resonator mode $\tilde{a}(t)$ can then be written as in Eq. (2.99) with a correction term for each of the environmental modes. After some work we obtain

$$\dot{\tilde{a}}(t) = -(\gamma + i\Delta)\tilde{a}(t) - \sqrt{2\gamma_{\rm ic}}\,\tilde{a}_{\rm ic,in}(t) - \sqrt{2\gamma_{\rm oc}}\,\tilde{a}_{\rm oc,in}(t) - \sqrt{2\gamma_l}\,\tilde{a}_l(t), \tag{2.101}$$

where $\Delta = \Omega' - \Omega$ is the detuning between the resonator and the pump field; $\gamma_{\rm ic}$, $\gamma_{\rm oc}$, and γ_l are the resonator decay rates due to the input coupler, output coupler, and loss respectively; and $\gamma = \gamma_{\rm ic} + \gamma_{\rm oc} + \gamma_l$ is the overall resonator decay rate. The decay rates $\gamma_{\rm ic}$, $\gamma_{\rm oc}$, and γ_l are given by the respective mirror transmissivity and the resonator round trip time τ,

$$\begin{aligned} \gamma_{\rm ic} &= \epsilon_{\rm ic}/2\tau && (2.102)\\ \gamma_{\rm oc} &= \epsilon_{\rm oc}/2\tau && (2.103)\\ \gamma_l &= (1-\epsilon_l)/2\tau. && (2.104) \end{aligned}$$

Assuming $\Delta = 0$ so that the laser carrier frequency is perfectly resonant, and taking the Fourier transform gives

$$\begin{aligned} \mathbb{F}\left(\dot{\tilde{a}}(t)\right) &= i\omega\hat{a}(\omega) && (2.105)\\ &= -\gamma\hat{a}(\omega) - \sqrt{2\gamma_{\rm ic}}\,\hat{a}_{\rm ic,in}(\omega) - \sqrt{2\gamma_{\rm oc}}\,\hat{a}_{\rm oc,in}(\omega) - \sqrt{2\gamma_l}\,\hat{a}_l(\omega), && (2.106) \end{aligned}$$

where we have used the Fourier transform property $\mathbb{F}(\dot{g}(t)) = i\omega\mathbb{F}(g(t))$. Rearranging Eqs. (2.105) and (2.106) give the frequency domain annihilation operators of the field inside the resonator

$$\hat{a}(\omega) = \frac{-1}{\gamma + i\omega}\left(\sqrt{2\gamma_{\rm ic}}\,\hat{a}_{\rm ic,in}(\omega) + \sqrt{2\gamma_{\rm oc}}\,\hat{a}_{\rm oc,in}(\omega) + \sqrt{2\gamma_l}\,\hat{a}_l(\omega)\right). \tag{2.107}$$

To obtain the measurable fields $\tilde{a}_{\rm ic,out}$ and $\tilde{a}_{\rm oc,out}$ exiting the resonators input and output couplers we require the input and output coupler boundary conditions[78]

$$\tilde{a}_{m,\rm out}(t) = \sqrt{2\gamma_m}\,\tilde{a}(t) + \tilde{a}_{m,\rm in}(t), \tag{2.108}$$

where $m \in \{\rm ic, oc\}$. Taking the Fourier transform we obtain the frequency domain boundary conditions

$$\hat{a}_{m,\rm out}(\omega) = \sqrt{2\gamma_m}\,\hat{a}(\omega) + \hat{a}_{m,\rm in}(\omega). \tag{2.109}$$

Finally, substituting Eq. (2.107) into Eq. (2.109) above, we obtain the frequency domain annihilation operators of the fields exiting the input and output couplers

$$\hat{a}_{m,\rm out}(\omega) = \frac{(\gamma + i\omega - 2\gamma_m)\,\hat{a}_{m,\rm in}(\omega) - 2\sqrt{\gamma_m\gamma_n}\,\hat{a}_{n,\rm in}(\omega) - 2\sqrt{\gamma_m\gamma_l}\,\hat{a}_l(\omega)}{\gamma + i\omega}, \tag{2.110}$$

where $\{m, n\} \in \{\rm ic, oc\}$.

Now that we have the annihilation operators of the fields exiting a general passive resonator, we will consider a specific example of relevance to this thesis. That of a resonator with equal input and output coupler decay rates $\gamma_{\rm ic} = \gamma_{\rm oc}$, with a bright field impinging on the input coupler, and the fields entering the resonator through the output coupler and through loss being in vacuum states. At frequencies much lower than the total resonator decay rate $\omega \ll \gamma$ the field exiting the output coupler is given by

$$\hat{a}_{\rm oc,out}(\omega) = \frac{1}{\gamma}\left((\gamma_l - \gamma)\,\hat{a}_{\rm ic,in}(\omega) + \gamma_l\hat{a}_{\rm oc,in}(\omega) - 2\sqrt{(\gamma - \gamma_l)\,\gamma_l}\,\hat{a}_l(\omega)\right). \tag{2.111}$$

If the resonator decay rate due to loss is low compared to its input coupler decay rate $\gamma_l \ll \gamma_{\rm ic}$, $\gamma_{\rm ic} \sim \gamma_{\rm oc} + \gamma_l$ and the resonator is impedance matched[8], with the input field transmitted perfectly through the output coupler $\hat{a}_{\rm oc,out}(\omega) = \hat{a}_{\rm ic,in}(\omega)$. At frequencies much higher than the total resonator decay rate $\omega \gg \gamma$, however, we find that the fields incident on the input and output couplers do not interact with the resonator, but rather reflect straight off the input and output couplers. In this case the field exiting the output coupler is given simply by $\hat{a}_{\rm oc,out}(\omega) = \hat{a}_{\rm oc,in}(\omega)$. Given that the field entering through the output coupler is a vacuum state, we see that the resonator is acting to filter out the fluctuations on the input state with frequencies $\omega > \gamma$. In fact, it is acting as a low pass filter on the input state, with $\omega = \gamma$ defining the 3 dB point. Such a resonator is used in Section 3.2 to reduce the high frequency spectral noise of our laser.

2.8.2 Error signals to control the length of optical resonators

In the previous Section we derived the annihilation operators for the fields reflected off, and transmitted through, an optical resonator when the the laser carrier frequency is perfectly resonant ($\Delta = 0$). We showed that on transmission an optical resonator can act as a low pass frequency

---

[8] In general a resonator is impedance matched if the input coupler decay rate is equal to the sum of all other resonator decay rates $\gamma_{\rm ic} = \gamma_{\rm oc} + \gamma_l$.

filter with a cut-off frequency of γ. In this Section we will describe how an error signal can be derived to hold the laser carrier field on resonance.

Let us first consider the frequency response of the mean power and phase delay of the fields reflected off and transmitted through the resonator. Using Eq. (2.110) and again assuming that $\gamma_{\rm ic} = \gamma_{\rm oc}$, and that the fields introduced due to loss and the output coupler are in vacuum states, we find that the mean intensities $P_{\rm ic,out}(\omega)$ and $P_{\rm oc,out}(\omega)$ as a function of frequency are given by

$$\begin{aligned} P_{\rm ic,out}(\omega) &= \hbar\Omega\left\langle \hat{a}^\dagger_{\rm ic,out}(\omega)\hat{a}_{\rm ic,out}(\omega)\right\rangle = P_{\rm ic,in}(\omega)\frac{\gamma_l^2+\omega^2}{\gamma^2+\omega^2} && (2.112)\\ P_{\rm oc,out}(\omega) &= \hbar\Omega\left\langle \hat{a}^\dagger_{\rm oc,out}(\omega)\hat{a}_{\rm oc,out}(\omega)\right\rangle = P_{\rm ic,in}(\omega)\frac{(\gamma-\gamma_l)^2}{\gamma^2+\omega^2}, && (2.113)\end{aligned}$$

where we have assumed that $\hat{a}_{\rm ic,in}(\omega)$ is bright ($\alpha_{\rm ic,in}(\omega) \gg 1$) and have therefore neglected any terms not containing $\alpha_{\rm ic,in}$. In this case, the mean resonator phase delay $\langle\phi_m(\omega)\rangle$ can be calculated as

$$\langle\phi_m(\omega)\rangle = \sin^{-1}\left(\frac{\langle\Im\{\hat{a}_{m,\rm out}(\omega)\}\rangle}{\sqrt{P_{m,\rm out}(\omega)}}\right), \tag{2.114}$$

where again $m \in \{\rm ic, oc\}$. The mean phase delays for the fields exiting the input and output couplers are then found to be

$$\begin{aligned} \langle\phi_{\rm ic}(\omega)\rangle &= \sin^{-1}\left(\frac{\omega}{\sqrt{\gamma^2+\omega^2}}\cdot\frac{\gamma-\gamma_l}{\sqrt{\gamma_l^2+\omega^2}}\right) && (2.115)\\ \langle\phi_{\rm oc}(\omega)\rangle &= \sin^{-1}\left(\frac{\omega}{\sqrt{\gamma^2+\omega^2}}\right). && (2.116)\end{aligned}$$

The intensity and phase responses of an impedance matched resonator and a lossy resonator are shown in Fig. 2.10. Unsurprisingly, the maximum intensity is transmitted when the field is resonant ($\omega = 0$), notice, further, that at $\omega = 0$ no phase delay is experienced by the fields reflected off and transmitted through the resonator, $\langle\phi_m(0)\rangle = 0$. In both cases the phase varies linearly with ω around $\omega = 0$, but as $\omega/\gamma \to \pm\infty$ it asymptotes to $\langle\phi_m(\omega)\rangle = 0$ for the reflected field, and $\langle\phi_m(\omega)\rangle = \pm\pi/2$ for the transmitted field. As we will see shortly, this behavior allows the generation of error signals to control the length of the resonator.

Phase modulation error signal: Pound-Drever-Hall technique

The most commonly used method to generate a high precision resonator locking error signal is the Pound-Drever-Hall (PDH) technique [79]. The input field to the resonator is phase modulated at frequency $\omega_{\rm PDH}$. We will assume that $\omega_{\rm PDH} \gg \gamma$ since this is the regime of relevance for the work later in this thesis[9]. In this case we see from Fig. 2.10 that when the carrier is near resonance both the phase and intensity of the sidebands are independent of the resonance condition. The sidebands are so far from resonance that they simply reflect off the input coupler. As can be seen in Fig. 2.11, the carrier however, experiences a linear phase delay as the resonance condition varies. This is very similar to the sideband modulation locking technique described in Section 2.5.2, which was used

---

[9] In theory, PDH locking will work for any $\omega_{\rm PDH} \neq 0$, and indeed the optimum error signal is generated when $\omega_{\rm PDH} = \gamma$, we avoid this regime for technical reasons.

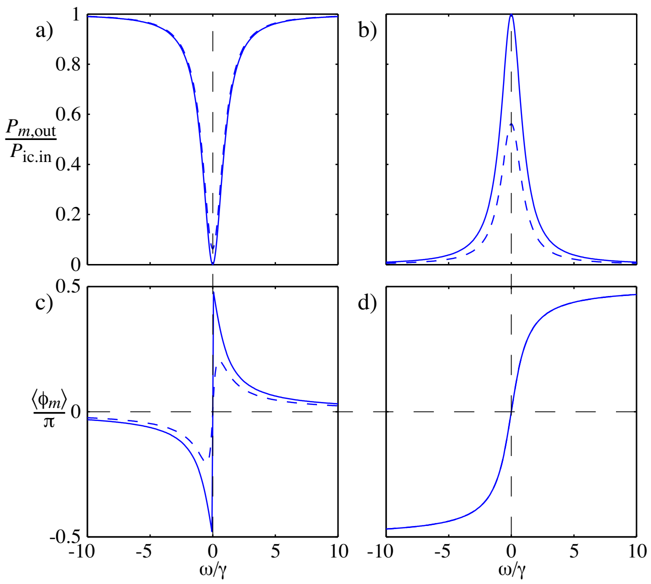

Figure 2.10: Phase and intensity response of a passive resonator with $\gamma_{\mathrm{ic}} = \gamma_{\mathrm{oc}}$. a) $P_{\mathrm{ic,out}}(\omega)$ b) $P_{\mathrm{oc,out}}(\omega)$, c) $\langle\phi_{\mathrm{ic}}(\omega)\rangle$, and d) $\langle\phi_{\mathrm{oc}}(\omega)\rangle$. The solid curves are for an impedance matched resonator such that $\gamma_l \ll \gamma$, the dashed curves are for a resonator with $\gamma_l = \gamma/4$.

to generate a relative phase error signal for the input fields to a beam splitter. The carrier rotation again transforms some component of the input phase modulation into an amplitude modulation (see Fig. 2.11 e)). An error signal can then be generated by detecting the reflected field[10], mixing down the resulting photocurrent at frequency ω_{PDH}, and low pass filtering to remove terms with frequency of ω_{PDH} and higher. Neglecting quantum noise, the resulting PDH error signal E_{PDH} is then given simply by

$$
\begin{aligned}
E_{\mathrm{PDH}} &= -g_D \xi P_{\mathrm{ic,out}}(\omega) \sin\langle\phi_{\mathrm{ic}}(\omega)\rangle && (2.117)\\
&\approx -g_D \xi P_{\mathrm{ic,out}}(\omega)\,\langle\phi_{\mathrm{ic}}(\omega)\rangle \qquad \text{for } \theta \approx 0, && (2.118)
\end{aligned}
$$

where again g_D is the gain of the detection process, and ξ is the modulation depth. This error signal is zeroed at $\langle\phi_{\mathrm{ic}}(\omega)\rangle = 0$ and therefore around the resonance frequency, and is linear around that frequency. Throughout this thesis, an adaption of this technique is used, with the phase modulation introduced within the resonator via an electro-optic modulation of the refractive index of a crystal. The resulting error signal is, to within a weighting factor, identical to that given above. This weighting factor arises because in this case the sidebands do not simply reflect of the input coupler, they exit the input and output couplers with a ratio governed by the input and output coupler transmissivities. This technique, therefore, enhances the error signal that can be obtained by detecting the field transmitted through the resonator.

---

[10] or indeed the transmitted field, although in this case with $\omega_{\mathrm{PDH}} \gg \gamma$ the detected error signal is significantly smaller.

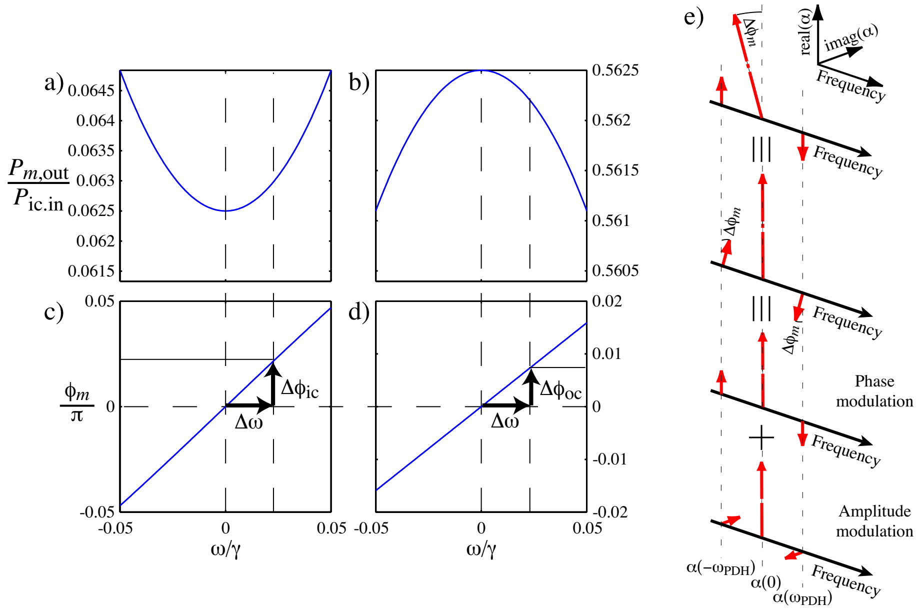

Figure 2.11: Phase and intensity response of a passive resonator around the resonance frequency with $\gamma_l = \gamma/4$ and $\gamma_{\mathrm{ic}} = \gamma_{\mathrm{oc}}$; and the effect of this response on an input phase modulation. a) $P_{\mathrm{ic,out}}(\omega)$ b) $P_{\mathrm{oc,out}}(\omega)$, c) $\langle\phi_{\mathrm{ic}}(\omega)\rangle$, and d) $\langle\phi_{\mathrm{oc}}(\omega)\rangle$. e) effect of the resonator response on an input phase modulation.

Spatial mode error signal: Tilt-locking

An alternative technique that can be used to derive a high precision resonator error signal is tilt locking[80, 28]. This technique is based on spatial mode interference between the TEM_{00} and TEM_{01} transverse field modes. The input field to the resonator is misaligned via a tilt around the resonator waist[11]. To first order, this misaligned field can be approximated by a sum of the resonator TEM_{00} and TEM_{01} modes, with a $\pi/2$ phase shift between them [81]. Assuming that the TEM_{00} mode is near resonance, the TEM_{01} mode will typically be far off resonance as a result of the Gouy phase shift between the modes[82]. The TEM_{01} mode will then reflect directly from the resonator in an analogous manner to the sidebands in PDH locking. The reflected TEM_{00} mode, however, will experience a phase shift dictated by Eq. (2.115).

The transverse electric field distribution of the TEM_{00} and TEM_{01} modes are shown in Fig. 2.12 a) and b). Notice that the TEM_{01} mode has two lobes with a π phase shift between them. This phase shift means that if the TEM_{00} and TEM_{01} fields are interfered in phase, The TEM_{00} field constructively interferes with one TEM_{01} lobe, and destructively interferes with the other. This results in a shift in the transverse position of the power in the combined mode in favour of the lobe with constructive interference. When the TEM_{00} mode is on resonance, it is reflected with no phase shift, and therefore, since when the input field is tilted the TEM_{00} and TEM_{01} components are orthogonal, there is no shift in the transverse position of the power in the reflected mode. When the TEM_{00} mode moves off resonance however, the two modes become non-orthogonal, and the power in the reflected field shifts in favour of one of the TEM_{01} lobes. This effect is shown in Fig. 2.12 c) and d). If this reflected field is then detected on a split detector as shown in Fig. 2.12 e), the difference of the power on the two halves of the detector can be used

---

[11] that is, a tilt around the point within the resonator where the transverse beam size is minimised.

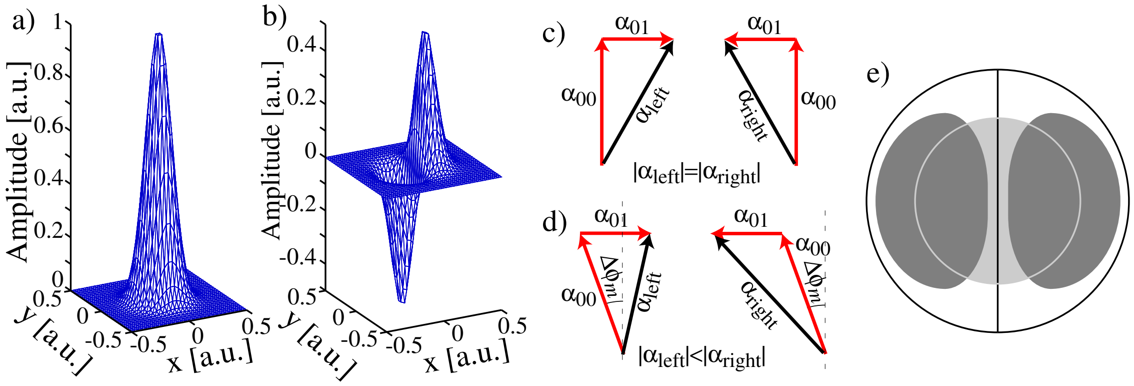

Figure 2.12: a) and b) electric field spatial distribution of the TEM$_{00}$ and TEM$_{01}$ Hermite-Gaussian modes,respectively, showing the π phase shift between the lobes of the TEM$_{01}$ mode. c) and d) the interference of the TEM$_{00}$ and TEM$_{01}$ modes when the TEM00 mode is on, and slightly off, resonance, respectively. e) intensity distribution of the TEM$_{00}$ (light grey) and TEM$_{01}$ (dark grey) modes on a split detector.

as an error signal.

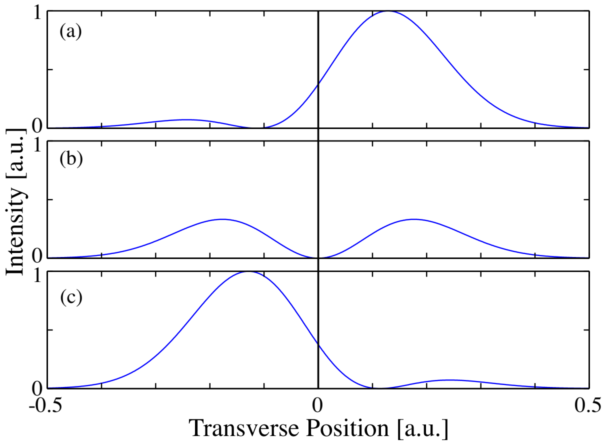

Figure 2.13: Interference between the TEM$_{00}$ and π/2 phase advanced TEM$_{10}$ Hermite-Gaussian modes reflected from an impedance matched resonator for a TEM$_{00}$ mode with a phase change of (a) -π/1500, (b) 0, and (c) π/1500 rad in one resonator cycle.

The transverse intensity profile of a tilted field reflected from an impedance matched resonator, on resonance, and with a $\pm\pi/1500$ phase change during one resonator cycle, is shown in Fig. 2.13. On resonance the TEM$_{00}$ mode is fully transmitted so that the reflected intensity distribution is just that of the TEM$_{01}$ mode. It is therefore symmetric over the split detector so that the difference between the intensities of the two halves of the detector is zero. Slightly off-resonance, however, the intensity distribution shifts towards one or the other side of the detector.

This Tilt error signal requires no modulation or demodulation. For this reason it is much cheaper, and in general, easier to perform than PDH locking. The spectrum of the transmitted field is also cleaner, with no modulation spikes. This can be a significant advantage, especially for applications such as squeezing where minimisation of spectral noise is critical. Tilt locking requires a system with better mechanical stability than PDH locking, since any drift in the beam path before the split detector will result in an offset in the observed error signal. As a result of these mechanical drifts, Tilt locking requires more maintenance than PDH locking. A typical trace of the power transmitted through a resonator as its length is scanned over a free-spectral range is shown in Fig. 2.14 a) with corresponding PDH and Tilt locking error signals in Fig. 2.14 b) and c). We see that both error signals are linear near resonance, and zeroed at resonance. The Tilt locking technique provides a significantly broader error signal, and also generates a large error signal that can be used to lock the TEM_{01} to resonance which can be useful for some applications.

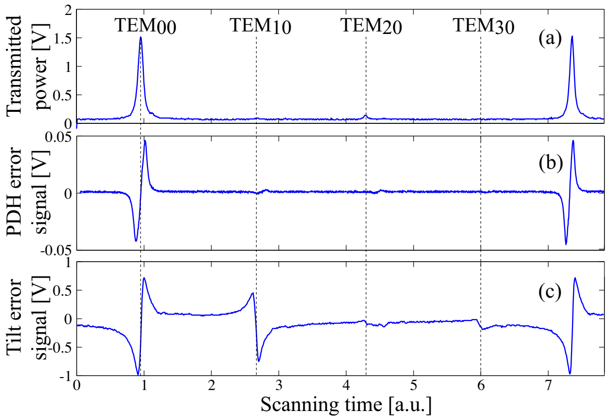

Figure 2.14: (a) Transmitted power through an optical resonator. The various misalignment and mismatch modes are indicated by dotted lines. (b) Error signals generated via PDH locking technique and, (c) via tilt locking technique.

2.9 Feedback control of resonance and interference

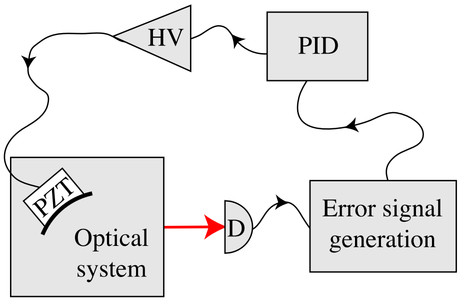

Figure 2.15: A schematic of a typical control system. PZT: Piezo-electric-crystal, PID: proportional, integral, differential servo, HV: high voltage amplifier, D: detector.

We now have a variety of methods to generate error signals that monitor the length of a resonator and the relative phase between the inputs to a beam splitter. This Section discusses how we use those error signals to control an experiment. A typical control scheme is shown in Fig. 2.15. It consists of the experiment we wish to control, stages for detection and generation of an error signal, then filters and amplifiers for the error signal, and finally actuation back onto the experiment. We have discussed the detection of optical fields and generation of error signals in previous Sections. The filters and amplifiers used for the work presented in this thesis will not be treated here, although schematics of the electronic circuits can be found in Appendix B. In this Section we treat the actuation stage. The main form of actuation used throughout the work presented here was via piezo-electric-crystals (PZTs) that lengthen and shrink in response to an applied voltage. By attaching mirrors to these PZTs we may actively control the length of an optical beam path. The maximum expansion achievable from a typical PZT is around 10 μm, which is several optical wavelengths and is therefore sufficient for our purposes. We also use temperature actuation via resistors and peltier elements. The bandwidth of such actuation depends strongly on the geometry and thermal conductivity of the object undergoing heating. Typically, however, temperature control is limited to frequencies below 100 mHz, which is much lower than PZT control and we will therefore not consider it further here.

2.9.1 Limitations to the control bandwidth

Time delay in control electronics

The ideal control scheme takes an error signal and applies it directly, and without phase delay, to the system to control the variable that the error signal is monitoring. However, in a real control system a time delay $t_{\rm control}$ is unavoidable. This delay results in a phase delay $\phi_{\rm control}$ on the feedback given by

$$\phi_{\rm control} = \omega t_{\rm control}, \tag{2.119}$$

where ω is the frequency of the perturbation that we wish to control. In general, the control system phase delay depends on the particulars of the filtering and amplifying electronics, and can be a complex function of frequency. Here, however, we will treat it simply as the time delay dictated by Eq. (2.119). The total phase delay of the control system is then given by

$$\phi_{\rm total} = \phi_{\rm control} + \phi_{\rm PZT} = \omega t_{\rm control} + \phi_{\rm PZT}, \tag{2.120}$$

where $\phi_{\rm PZT}$ is the phase delay related to the PZT actuator. Once the total phase delay reaches $\phi_{\rm total} = \pi$ rad control is not possible since a perturbation of the experiment will then be amplified by the control system rather than deamplified. This will clearly cause the system to become highly unstable, and is the reason why spectral filtering is required in the control scheme of Fig. 2.15. We see that the time delay in the control system ultimately limits the frequencies at which the system can be controlled. As we will see in the following Section, the phase delay related to PZT actuations has a strong frequency dependence and can also limit the control bandwidth.

Resonance frequency of a PZT

An ideal PZT configuration consists of a PZT with a mirror attached to one side and a large counterweight attached to the other. This can be modelled as a mass $m_{\rm m}$ on a spring the other end of which is attached to an infinite mass, as shown in fig 2.16 [83]. The equation of motion of the mirror is then given by

$$F_{\rm m}(t) = m_{\rm m}\ddot{x}_{\rm m}(t) - \gamma_{\rm PZT}\dot{x}_{\rm m}(t) + k_{\rm PZT}\left(x_{\rm m}(t) - x_{\rm m,0}\right) \tag{2.121}$$

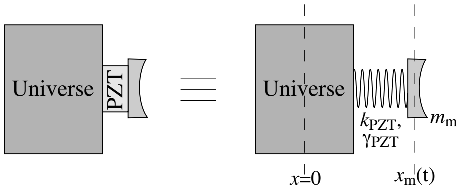

Figure 2.16: An ideal PZT modelled in terms of masses connected by springs.

where $F_{\mathrm{m}}(t)$ is a driving force applied to the mirror, $x_{\mathrm{m}}(t)$ is the position of the mirror relative to the infinite mass, $x_{\mathrm{m},0}$ is the rest position of the mirror, k_{PZT} is the spring constant of the PZT, and γ_{PZT} is the PZT damping co-efficient. This equation can solved for $x_{\mathrm{m}}(\omega)$ in a similar manner to the equation for the internal resonator field in Section 2.8.1, by taking the Fourier transform and using the property that $\mathbb{F}(\dot{g}(t)) = i\omega\mathbb{F}(g(t))$. Doing this we obtain the mirror displacement for a given driving force $x_{F,\mathrm{m}}(\omega)$ as a function of frequency

$$x_{F,\mathrm{m}}(\omega) = \frac{x_{\mathrm{m}}(\omega)}{F_{\mathrm{m}}(\omega)} = \frac{\mathbb{F}\left(x_{\mathrm{m}}(t)\right)}{\mathbb{F}\left(F_{\mathrm{m}}(t)\right)} = \frac{1}{k_{\mathrm{PZT}} - i\omega\gamma_{\mathrm{PZT}} - \omega_{\mathrm{m}}^2}. \tag{2.122}$$

The amplitude A_{PZT} and phase ϕ_{PZT} response of the system can then be calculated as

$$A_{\mathrm{PZT}} = |x_{F,\mathrm{m}}(\omega)| \tag{2.123}$$

$$\phi_{\mathrm{PZT}} = \sin^{-1}\left(\frac{\Im\left(x_{F,\mathrm{m}}(\omega)\right)}{|x_{F,\mathrm{m}}(\omega)|}\right). \tag{2.124}$$

These response functions are shown as a function of frequency by the solid lines in Fig. 2.17, for a PZT and mirror configuration with the properties $k_{\mathrm{PZT}} = 9 \cdot 10^8$ Kg/s^2, $m_{\mathrm{m}} = 50$ g, and $\gamma_{\mathrm{PZT}} = 1000$ Kg/s. We see that this ideal PZT configuration has a resonance frequency that is dictated by the PZT spring constant and the mass that the PZT is acting on. Notice that around the resonance frequency the phase delay increases rapidly. This phase response limits the control system bandwidth to below the resonance frequency of the PZT, which is typically around 20 kHz.

Counterweighting

The PZT configuration analysed above was ideal in the sense that the PZT was assumed to be attached to an infinite mass. Clearly this is not the case in a real system. To see what the effect of a non-infinite counterweight is we model the system as shown in Fig. 2.18. In this case, the mirror and PZT are connected via a spring to a counterweight of finite mass m_{c} which is then connected via another spring to an infinite mass. The coupled equations of motion for the two masses in this configuration are then given by

$$F_{\mathrm{m}}(t) = m_{\mathrm{m}}\ddot{x}_{\mathrm{m}}(t) - \gamma_{\mathrm{PZT}}\dot{x}_{\mathrm{m}}(t) + k_{\mathrm{PZT}}\left((x_{\mathrm{m}}(t) - x_{\mathrm{m},0}) - (x_{\mathrm{c}}(t) - x_{\mathrm{c},0})\right) \tag{2.125}$$

$$\begin{aligned} F_{\mathrm{c}}(t) &= m_{\mathrm{c}}\ddot{x}_{\mathrm{c}}(t) - \gamma_{\mathrm{c}}\dot{x}_{\mathrm{c}}(t) - \gamma_{\mathrm{PZT}}\dot{x}_{\mathrm{c}}(t) + k_{\mathrm{c}}\left(x_{\mathrm{c}}(t) - x_{\mathrm{c},0}\right) \\ &\quad -k_{\mathrm{PZT}}\left((x_{\mathrm{m}}(t) - x_{\mathrm{m},0}) - (x_{\mathrm{c}}(t) - x_{\mathrm{c},0})\right) = 0, \end{aligned} \tag{2.126}$$

where $F_{\mathrm{c}}(t)$ is the driving force exerted on the counterweight which we take here as zero, $x_{\mathrm{c}}(t)$ is the position of the counter weight relative to the infinite mass, $x_{\mathrm{c},0}$ is the rest position of the

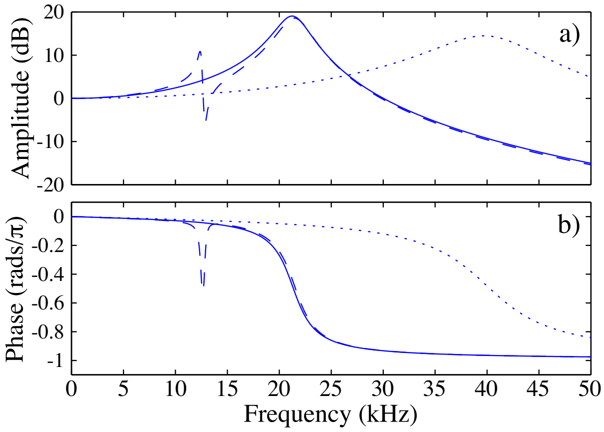

Figure 2.17: Frequency response of a PZT showing the effects of preloading and imperfect counterweighting. a) displays the amplitude and b) the phase response. The solid lines represent an ideal PZT with $k_{\mathrm{PZT}} = 9 \cdot 10^8$ Kg/s^2, $m_{\mathrm{m}} = 50$ g, and $\gamma_{\mathrm{PZT}} = 1000$ Kg/s. The dashed lines represent the same PZT but with non-ideal counterweighting, with $m_{\mathrm{c}} = 4$ Kg, $k_{\mathrm{c}} = 2.5 \cdot 10^{10}$ Kg/s^2, and $\gamma_{\mathrm{c}} = 7000$ Kg/s. Finally, the dotted lines represent the ideal PZT with pre-loading, $k_{\mathrm{preload}} = 2.3 \cdot 10^9$ Kg/s^2, and $\gamma_{\mathrm{preload}} = 2000$ Kg/s.

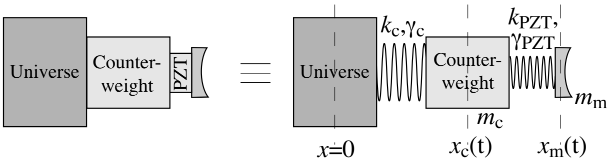

Figure 2.18: PZT and counterweight interaction modelled by masses connected with springs.

counterweight, and γ_{c} and k_{c} are respectively the damping co-efficient and spring constant of the spring between the counterweight and the infinite mass. This coupled set of equations can be solved for $x_{\mathrm{m}}(\omega)$ in a similar manner to that above, and yields the frequency dependent mirror displacement for a given driving force

$$x_{F,\mathrm{m}}(\omega) = \left[-\omega^2 m_{\mathrm{m}} - i\omega\gamma_{\mathrm{PZT}} + k_{\mathrm{PZT}} \left(\frac{-\omega^2 m_{\mathrm{c}} - i\omega\left(\gamma_{\mathrm{c}} + \gamma_{\mathrm{PZT}}\right) + k_{\mathrm{c}}}{-\omega^2 m_{\mathrm{c}} - i\omega\left(\gamma_{\mathrm{c}} + \gamma_{\mathrm{PZT}}\right) + k_{\mathrm{c}} + k_{\mathrm{PZT}}} \right) \right]^{-1}, \tag{2.127}$$

where the amplitude and phase response can be calculated in the same manner as the previous case. Taking the same parameters for the PZT and mirror as before, and choosing $m_{\mathrm{c}} = 4$ Kg, $k_{\mathrm{c}} = 2.5 \cdot 10^{10}$ Kg/s^2, and $\gamma_{\mathrm{c}} = 7000$ Kg/s, we obtain the phase and amplitude responses shown by the dashed lines in Fig. 2.17. We see that the response is almost identical to the previous case where the counterweight was assumed to have infinite mass, and has an identical resonance frequency. However, a spurious resonance has appeared around 12.5 kHz. Depending on the magnitude of other control system phase delays, the phase delay corresponding to this resonance could limit the control bandwidth.

2.9.2 Using preloading to improve the control bandwidth

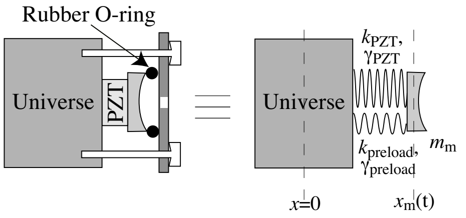

Figure 2.19: PZT preloading modelled in terms of masses connected by springs.

It is possible to show from Eq. (2.122) that the resonance frequency of the PZT goes as $\sqrt{k_\mathrm{PZT}}$. Therefore, increasing the PZT spring constant will increase the resonance frequency, enhancing our control bandwidth. One technique that can be used to increase the PZT resonance frequency is preloading. The PZT and mirror assembly are clamped to increase the tension over the PZT, with a rubber O-ring between the clamp and the mirror as shown in Fig. 2.19. This can be modelled simply by adding a second spring, representing the O-ring, between the mirror and the counterweight. Assuming again that we have a counterweight of infinite mass the equation of motion for the mirror becomes

$$F_\mathrm{m}(t) = m_\mathrm{m}\ddot{x}_\mathrm{m}(t) - (\gamma_\mathrm{PZT} + \gamma_\mathrm{preload})\,\dot{x}_\mathrm{m}(t) + (k_\mathrm{PZT} + k_\mathrm{preload})\,(x_\mathrm{m}(t) - x_{\mathrm{m},0})\,, \tag{2.128}$$

where γ_preload and k_preload are respectively the damping co-efficient and spring constant of the O-ring. We see that the effect of the pre-loading is simply to increase the spring constant and damping co-efficient of the PZT. Of course, both the damping co-efficient and the spring constant of the O-ring depend on the tension of the clamping, and so can be varied by tightening the clamping screws. The dotted lines in Fig. 2.17 show the amplitude and phase response of the ideal PZT configuration modelled previously with the addition of pre-loading, where the parameters of the O-ring were set to $k_\mathrm{preload} = 2.3 \cdot 10^9$ Kg/s^2, and $\gamma_\mathrm{preload} = 2000$ Kg/s. Clearly, pre-loading has the potential to increase the control bandwidth of the system.

2.9.3 Experimental characterisation of control bandwidth

We characterised the amplitude and phase response of various PZT configurations by building a two mirror optical resonator with one of the mirrors attached to a PZT. In all cases a small aluminium mount was superglued to the PZT, the mirror sat in that mount and was attached with three small screws. We modulated the length of the resonator at 29.7 MHz via the electro-optic effect. This modulation was used to generate a PDH error signal which monitored the length of the resonator. The resonator length was manually controlled so that an optical field at 1064 nm was on resonance. The output of a network analyser, which was a sinusoidal signal that swept between 100 Hz and 50 kHz, was connected to the PZT. This signal caused the PZT to oscillate, and the amplitude and phase of the oscillation as a function of frequency could be monitored via the resonator error signal.

In the first PZT configuration analysed the PZT was simply superglued to a small counterweight. The amplitude and phase responses for this configuration are shown in Fig. 2.20 a). We see that both spectra are extremely noisy. The most likely cause for this noise was that with such a small counterweight many system resonances become significant in the frequency response. These

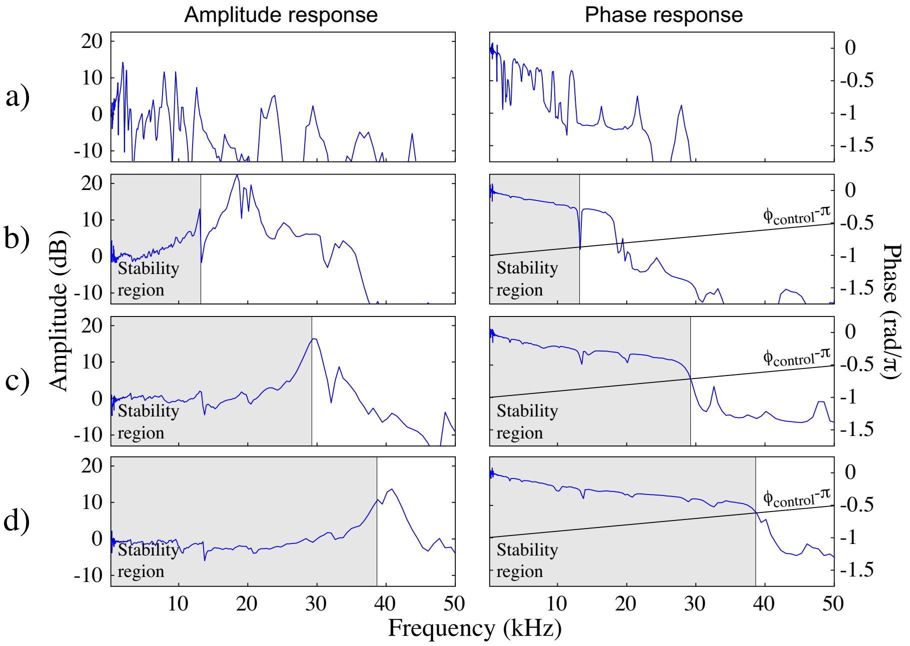

Figure 2.20: Experimental determined amplitude and phase response of a PZT a) with small counterweight b) with large counter weight, c) with large counter weight and low tension pre-loading, and d) with large counter weight and high tension pre-loading.

spurious resonances can be caused by any joint between two surfaces. For example there would be a resonance between the counterweight and the optical mount that it was placed in, and a variety of resonances between the optical mount and the optical table. With the extreme variability of both the amplitude and phase response, it would be impossible to actively control the length of the resonator with this configuration.

Increasing the mass of the counterweight by a factor of twenty we observed the amplitude and phase responses shown in Fig. 2.20 b). All bar one of the previously observed spurious resonances disappeared, with the remaining resonance probably the result of one of the joints between the PZT and the mirror, which would be independent of the counterweight mass. These spectra are in good qualitative agreement with the calculated spectra shown in Fig. 2.17. We see that the PZT has a resonance at around 20 kHz. For the sake of comparison, we assume here that the time delay associated with the control electronics is $t_{\mathrm{control}} = 5\ \mu$s. It is then possible to define a maximum bandwidth for the control system from the phase response of the PZT. This bandwidth is shown in Fig. 2.20 b). We see that for this PZT configuration the bandwidth is limited by the remaining spurious resonance at 13 kHz.

To improve the control bandwidth we implemented a pre-loading scheme similar to that depicted in Fig. 2.19. An aluminium plate with a hole for the optical field was connected to the inside surface of the resonator mirror. Screws with rubber O-ring washers[12] were then used to clamp the plate to the counterweight. Tightening the screws increased the tension on the PZT, and also reduced the effect of resonances at joints between the aluminium plate and the counterweight. We analysed the effect of the preloading for two levels of tension, and the results are shown in

---

[12] We also tested teflon washers but found that they introduced several spurious resonances and were therefore not optimum.

Fig. 2.20 c) and d). We see that the resonance frequency of the PZT is increased, and the spurious resonance at 13 kHz is damped out. This damping of the spurious resonance supports our earlier conjecture that it occurs at a joint between the mirror and the PZT. We found that the PZT resonance frequency could be increased up to around 41 kHz, and this combined with the damping of the 13 kHz resonance resulted in a control bandwidth as high as 38 kHz. This was not necessarily the limit to the bandwidth achievable using preloading. Rather than push the configuration to its limits we stopped increasing the tension due concerns about possible damage to the resonator mirror.

2.10 The second order optical nonlinearity

The processes studied throughout the history of optics are almost entirely linear[13]. Linear processes are independent of the intensity of the light, do not affect its frequency, and obey the principle of superposition which states that the linear combination of any two solutions of an optics problem is itself a solution. With the invention of the laser in 1960[40] came light fields with much greater intensity than was previous available. These fields provide access to highly non-linear processes that are not constrained by the properties of linear processes given above. Provided that the frequency of the light is far detuned from the atomic resonances of the media, the critical parameter of a di-electric medium with regard to these non-linear processes is its atomic polarisation $\mathcal{P}$. This atomic polarisation is the overall effect of the dipole moments of each of the atoms constituting the medium. When an electromagnetic field propagates through the medium it effects these dipole moments and induces a macro-scopic atomic polarisation. In a linear medium, this polarisation oscillates at the frequency of the electromagnetic field, and can re-radiate back into the field. In a non-linear medium it can oscillate at harmonics of the original field frequency. The relationship between the atomic polarisation and the electromagnetic field can be expressed as the power series

$$\mathcal{P} = \epsilon_0 \left(\chi E + \chi^{(2)} E^2 + \chi^{(3)} E^3 + \dots \right), \tag{2.129}$$

where ϵ_0 is the permittivity of free space, E is the applied electric field, χ is the linear susceptibility of the medium and $\chi^{(i)}$ is the i^{th} order nonlinear susceptibility of the medium. For low electromagnetic field intensities $\mathcal{P}$ is purely linear, as the intensity increases the higher order terms in Eq. (2.129) become more significant and $\mathcal{P}$ becomes increasingly non-linear. This non-linearity gives rise to many interesting phenomena. Here we will focus on the second order (or $\chi^{(2)}$) nonlinearity. In the following Sections we will see how this nonlinearity can be used to facilitate second harmonic generation, and optical parametric amplification, and to generate squeezed states of light.

2.10.1 Second order nonlinear optical processes

Second order non-linear optical processes are the optical processes that rely on the second order nonlinear susceptibility $\chi^{(2)}$. They can be broadly described as the non-linear optical processes that involve the interaction of three photons, or in other words are three-wave mixing processes. A summary of these processes is given in Fig. 2.21, and an excellent treatment can be found in the nonlinear optics text by Boyd[84]. There are two kinds of second order non-linear optical processes: upconversion processes that take two low energy photons and combine them to form one

---

[13] The discussion in this Section follows that given in the thesis of Ping Koy Lam[75]

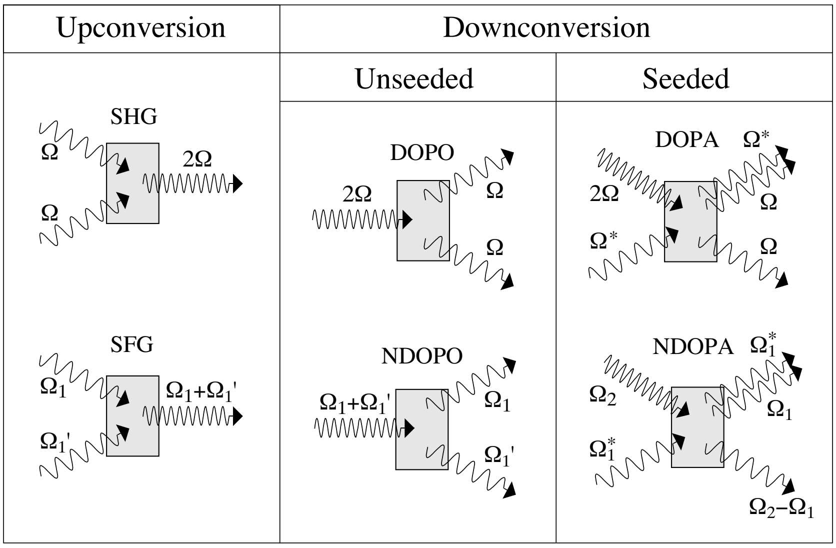

Figure 2.21: A summary of second order non-linear optical processes. Left hand side: diagrammatic representation of upconversion processes. SHG: second harmonic generation, SFG: sum frequency generation. Right hand side: diagrammatic representation of downconversion processes. DOPO: degenerate optical parametric oscillation, NDOPO: non-degenerate optical parametric oscillation. Typically a threshold power must be exceeded before downconversion processes will proceed. This threshold is unnecessary if the process is seeded. In this case the processes in the right hand column can occur, where the seed field is labeled *. DOPA: degenerate optical parametric amplification, NDOPA: non-degenerate optical parametric amplification. [Diagram adapted from Fig. 4.1 in [75].]

photon of higher energy, and downconversion processes where a single high energy photon is split into two photons of lower energy. The generic upconversion process is sum frequency generation (SFG) where two photons with respective frequencies Ω_1 and $\Omega_1^{'}$ are combined to produce one photon of energy $\Omega_1 + \Omega_1^{'}$. If the original photons have equal frequency ($\Omega_1 = \Omega_1^{'}$), the process is termed second harmonic generation (SHG). Downconversion processes are complementary to upconversion, with the reverse processes to SFG and SHG being non-degenerate (NDOPO) and degenerate (DOPO) optical parametric oscillation, respectively. Downconversion processes are differentiated from upconversion however, since typically a threshold power must be exceeded before they will proceed. Seeding the process with a field at the frequency of one of the output fields eliminates this threshold, and the corresponding processes are then termed non-degenerate (NDOPA) and degenerate (DOPA) optical parametric amplification.

2.10.2 Conservation laws and the phase matching condition

Both energy and momentum must be conserved by all physical processes. In the case of second order nonlinear processes these conservation laws impose restrictions on the regime in which the processes are effective. The condition for energy conservation can be written in terms of the frequencies of the lower energy photons Ω_1 and $\Omega_1^{'}$, and that of the higher energy photon Ω_2

$$\Omega_2 = \Omega_1 + \Omega_1^{'}. \tag{2.130}$$

For momentum to be conserved the photon wavevectors $\vec{k}_i$ must satisfy

$$\vec{k}_2 = \vec{k}_1 + \vec{k}_1^{\prime}, \tag{2.131}$$

where $|\vec{k}_i| = k_i = n_i\Omega_i/c$, n_i is the refractive index of the nonlinear medium as experienced by photon i, Ω_i is the frequency of photon i, and c is the speed of light in vacuum. Clearly this condition imposes a restriction on the refractive index of the atomic medium. Henceforth we restrict our analysis to the case of relevance to this thesis where fields 1 and $1^{\prime}$ are degenerate, and therefore $\Omega_1 = \Omega_1^{\prime} = \Omega_2/2$ and $n_1 = n_1^{\prime}$. We term the fields at Ω_1 and Ω_2 the *fundamental* and *second harmonic* fields, respectively. Assuming that the fundamental and second harmonic fields are co-propagating the condition for momentum conservation becomes

$$n_1 = n_2. \tag{2.132}$$

So that the fields must propagate at the same speed through the medium. The result is that the atomic polarisation modes generated in the nonlinear medium at the fundamental and second harmonic frequencies remain in phase with the fields at the same frequencies throughout propagation in the medium. The condition for momentum conservation in second order non-linear optical processes is therefore commonly termed the *phase matching condition*. In the absence of atomic transitions dielectric media have normal dispersion[14], meaning that their refractive index increases with optical frequency. The phase matching condition is therefore not naturally satisfied. Phase matching can be achieved in a birefringent medium, in which the refractive indices vary depending on the orientation of the optical polarisation relative to the optical axis. There are two methods commonly used to achieve phase matching: 'Type I' and 'Type II' phase matching[15]. Here we will consider only 'Type I' phase matching. In this case the second harmonic field is polarised along the fast axis of the birefringent medium, and the fundamental field along its slow axis. It is then be possible to cancel the dispersion using the media birefringence. This cancellation can be achieved by either angle or temperature tuning the media. When the polarisation of one field is parallel to the optical axis (z), and the other field is free to propagate along any direction of the xy-plane the phase matching is said to be *noncritical*. The nonlinear media used throughout the experiments presented in this thesis was Magnesium Oxide doped Lithium Niobate (MgO:LiNbO$_3$). MgO:LiNbO$_3$'s refractive index is strongly depend on temperature, and temperature tuning was used to achieve noncritical phase matching.

Unlike the condition for energy conservation, momentum conservation between the optical fields is not required to be exactly satisfied in non-linear optical processes. If it is not satisfied exactly the efficiency of the non-linear process is degraded and some momentum is imparted onto the atomic polarisation, so that, of course, the overall momentum is conserved. When the fundamental and second harmonic fields are co-propagating the magnitude of the momentum (or phase) mismatch Δk is given by

$$\Delta k = k_2 - 2k_1. \tag{2.133}$$

The phase mismatch for MgO:LiNbO$_3$ as a function of temperature and wavelength can be ob-

---

[14] Near an atomic transition a media may have anomalous dispersion, where the refractive index decreases with increasing frequency.

[15] Note that it is also possible to avoid the phase matching condition entirely by periodically poling the non-linear medium so that the propagating fields experiences a phase flip when the phases of the atomic polarisation and the optical fields begin to drift apart. This methods is termed 'quasi-phase matching'.

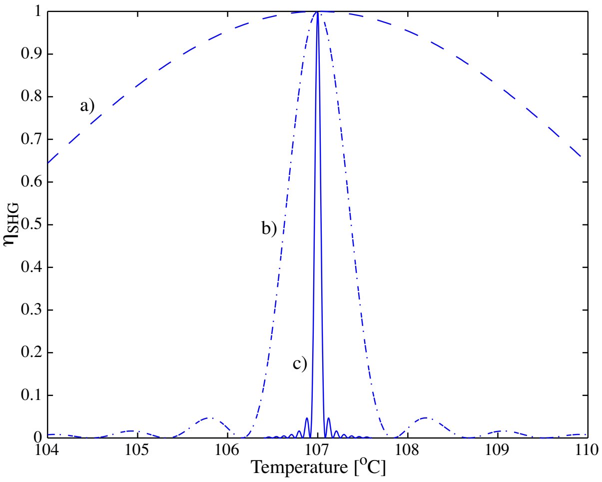

Figure 2.22: The effect of phase mismatch on the efficiency of ideal single-pass second harmonic generation using MgO:LiNbO$_3$ for a range of interaction lengths. a) $z = 0.1$ cm, b) $z = 1$ cm, and c) $z = 10$ cm.

tained from the corresponding Sellmeier equation[85]

$$\Delta k = -8666\,\mathrm{cm}^{-1} \times \left(1 - \frac{\lambda_0}{\lambda}\right) + 7.49\,\mathrm{cm}^{-1}\mathrm{K}^{-1} \times (T - T_0)\,, \tag{2.134}$$

where $\lambda_0 = 1064$ nm and $T_0 = 107$°C. The effect of phase mismatch on the non-linear interaction strength can be see by considering the conversion efficiency of ideal single-pass second harmonic generation η_{SHG}[84]

$$\eta_{\mathrm{SHG}} = \mathrm{sinc}^2\left(\frac{\Delta k z}{2}\right), \tag{2.135}$$

where z is the interaction length within the nonlinear medium. This sinc^2 functionality is analogous to that of Young's single slit experiment, where a square near-field transverse field distribution is transformed to a sinc^2 in the far-field. In our case, the interaction length within the nonlinear medium can be thought of as the slit. Fig. 2.22 plots η_{SHG} as a function of temperature and for several interaction lengths, when the nonlinear medium used is MgO:LiNbO$_3$. We see that for a fundamental wavelength of $\lambda = 1064$ nm, as was the case for our experiments, the optimum nonlinearity occurs at 107 °C, independent of the interaction length z. Since observation of high levels of nonlinearity requires that the phase matching condition be maintained over the entire interaction length, we find that as the interaction length increases the temperature range for good nonlinearity reduces. In a real system however, high conversion efficiencies are hard to achieve with a short interaction length. In practice the interaction length is chosen to maximise the conversion efficiency, and highly accurate temperature controllers are used to maintain the correct crystal temperature.

2.10.3 Equations of motion

Let us now consider the equations of motion for the fundamental and second harmonic fields when coupled through second order non-linear processes. In Chapter 3 we will use the solutions of these equations to model second harmonic generation and degenerate optical parametric amplification.

We saw in Section 2.8.1 that the equations of motion of open quantum systems can be determined from their reversible Hamiltonian. The reversible Hamiltonian describing degenerate second order nonlinear processes $H_{\chi^{(2)}}$ is [69]

$$H_{\chi^{(2)}} = \hbar\Omega_1 \tilde{a}_1^\dagger(t)\tilde{a}_1(t) + \hbar\Omega_2 \tilde{a}_2^\dagger(t)\tilde{a}_2(t) + \frac{i\hbar\Lambda}{2}\left(\tilde{a}_1^\dagger(t)^2\tilde{a}_2(t) - \tilde{a}_1(t)^2\tilde{a}_2^\dagger(t)\right), \tag{2.136}$$

where $\hbar\Omega_1\tilde{a}_1^\dagger(t)\tilde{a}_1(t)$ and $\hbar\Omega_2\tilde{a}_1^\dagger(t)\tilde{a}_2(t)$ are the energies of the fundamental and second harmonic fields respectively, $\tilde{a}_1^\dagger(t)^2\tilde{a}_2(t) - \tilde{a}_1(t)^2\tilde{a}_2^\dagger(t)$ describes the interaction between the fields, and Λ is the interaction strength which is a function of the second order nonlinear susceptibility $\chi^{(2)}$ and experimental parameters such as the phase mismatch and beam focussing.

High field intensities are required before the effects of optical non-linearities can be observed. Two methods are commonly used to achieve this high field intensity: the input fields can be pulsed, or the non-linear medium can be placed within an optical resonator. Here, we place our MgO:LiNbO$_3$ inside an optical resonator for the fundamental field. When the fundamental field is on resonance its intra-resonator field intensity is strongly enhanced. The system then interacts with the environment through intra-resonator losses, and the transmissivities of the input and output couplers in a manner identical to the passive resonator described in Section 2.8.1. Using the formalism introduced in Section 2.8.1, we can transform the Hamiltonian $H_{\chi^{(2)}}$ into equations of motion for the fundamental and second harmonic fields inside the resonator

$$\dot{\tilde{a}}_1(t) = -\gamma_1\tilde{a}_1(t) + \Lambda\tilde{a}_1^\dagger(t)\tilde{a}_2(t) - \sqrt{2\gamma_{\mathrm{ic},1}}\,\tilde{a}_{\mathrm{ic,in1}}(t) - \sqrt{2\gamma_{\mathrm{oc},1}}\,\tilde{a}_{\mathrm{oc,in1}}(t) - \sqrt{2\gamma_{l,1}}\,\tilde{a}_{l,1}(t) \tag{2.137}$$

$$\dot{\tilde{a}}_2(t) = -\gamma_2\tilde{a}_2(t) - \frac{\Lambda}{2}\tilde{a}_1(t)^2 - \sqrt{2\gamma_{\mathrm{ic},2}}\,\tilde{a}_{\mathrm{ic,in2}}(t) - \sqrt{2\gamma_{\mathrm{oc},2}}\,\tilde{a}_{\mathrm{oc,in2}}(t) - \sqrt{2\gamma_{l,2}}\,\tilde{a}_{l,2}(t), \tag{2.138}$$

where the subscripts 'ic', 'oc' and 'l' label terms relating to the input coupler, output coupler, and loss, respectively, and we have assumed that the fundamental field is on resonance. Assuming that the resonator for the fundamental field has much higher finesse than that for the second harmonic field ($\gamma_1 \ll \gamma_2$), the evolution of the second harmonic field will occur rapidly compared to the fundamental field. In this case at time scales relevant to $\tilde{a}_1(t)$ we can assume $\dot{\tilde{a}}_2(t) = 0$ [86, 87]. Rearranging Eq. (2.138), we see that the intra-resonator second harmonic field is then given by

$$\tilde{a}_2(t) = \frac{1}{\gamma_2}\left[-\frac{\Lambda}{2}\tilde{a}_1(t)^2 + \sqrt{2\gamma_{\mathrm{ic},2}}\,\tilde{a}_{\mathrm{ic,in2}}(t) + \sqrt{2\gamma_{\mathrm{oc},2}}\,\tilde{a}_{\mathrm{oc,in2}}(t) + \sqrt{2\gamma_{l,2}}\,\tilde{a}_{l,2}(t)\right]. \tag{2.139}$$

Substituting this expression into Eq. (2.137) the equation of motion for the intra-resonator fundamental field becomes

$$\dot{\tilde{a}}_1(t) = -\gamma_1\tilde{a}_1(t) - \frac{\Lambda}{\gamma_2}\tilde{a}_1^\dagger(t)\left[\frac{\Lambda}{2}\tilde{a}_1(t)^2 + \tilde{a}_{\mathrm{in2}}(t)\right] - \tilde{a}_{\mathrm{in1}}(t), \tag{2.140}$$

where $\tilde{a}_{\mathrm{in},1}(t)$ and $\tilde{a}_{\mathrm{in},2}(t)$ are

$$\begin{aligned} \tilde{a}_{\mathrm{in1}}(t) &= \sqrt{2\gamma_{\mathrm{ic},1}}\,\tilde{a}_{\mathrm{ic,in1}}(t) + \sqrt{2\gamma_{\mathrm{oc},1}}\,\tilde{a}_{\mathrm{oc,in1}}(t) + \sqrt{2\gamma_{l,1}}\,\tilde{a}_{l,1}(t) & (2.141)\\ \tilde{a}_{\mathrm{in2}}(t) &= \sqrt{2\gamma_{\mathrm{ic},2}}\,\tilde{a}_{\mathrm{ic,in2}}(t) + \sqrt{2\gamma_{\mathrm{oc},2}}\,\tilde{a}_{\mathrm{oc,in2}}(t) + \sqrt{2\gamma_{l,2}}\,\tilde{a}_{l,2}(t). & (2.142) \end{aligned}$$

The classical behavior of this equation of motion can be analysed by replacing each operator by its expectation value $\tilde{a}(t) \to \alpha(t)$. We then obtain the expression

$$\dot{\alpha}_1(t) = -\gamma_{\mathrm{II}}\alpha_1(t)^3 - \left(2\sqrt{\gamma_{\mathrm{II}}}\,\alpha_{\mathrm{ic,in2}}(t) + \gamma_1\right)\alpha_1(t) - \alpha_{\mathrm{in1}}(t), \tag{2.143}$$

where we have assumed that the second harmonic input field enters through the input coupler ($\alpha_{\mathrm{oc,in2}}(t) = 0$), and that $\gamma_2 = \gamma_{\mathrm{ic},2}$ which is reasonable for the extremely weak second harmonic resonators used throughout the work presented here; and

$$\gamma_{\mathrm{II}} = \frac{\Lambda^2}{2\gamma_2} \tag{2.144}$$

is the two-photon decay rate. Setting $\dot{\alpha}_1(t) = 0$ and choosing $\tilde{a}_{\mathrm{in1}}(t)$ to be real and positive, Eq. (2.143) can be solved to yield the steady state solution for $\alpha_1(t)$

$$\alpha_1(t) = \frac{\gamma_1 + 2\sqrt{\gamma_{\mathrm{II}}}\,\alpha_{\mathrm{ic,in2}}(t) - K^2}{\sqrt{3\gamma_{\mathrm{II}}}\,K}, \tag{2.145}$$

where K is given by

$$K = 2^{-\frac{1}{3}}\left[\sqrt{3^3\gamma_{\mathrm{II}}\alpha_{\mathrm{in1}}(t)^2 + 4\left(\gamma_1 + 2\sqrt{\gamma_{\mathrm{II}}}\,\alpha_{\mathrm{ic,in2}}(t)\right)^3} - 3\sqrt{3\gamma_{\mathrm{II}}}\,\alpha_{\mathrm{in1}}(t)\right]^{\frac{1}{3}}. \tag{2.146}$$

Eq. (2.139) provides $\alpha_2(t)$

$$\alpha_2(t) = \frac{1}{\gamma_2}\left[-\frac{\Lambda}{2}\alpha_1(t)^2 + \alpha_{\mathrm{in2}}(t)\right], \tag{2.147}$$

and the classical fundamental and second harmonic steady state output fields can be calculated using the resonator boundary conditions given in Eq. (2.108).

The quantum mechanical behavior can be obtained via a similar method as that performed for a passive optical resonator in Section 2.8.1. In this case however, we must expand each of the operators in Eq. (2.140) in terms of its expectation value and fluctuations, $\tilde{a}(t) = \alpha(t) + \delta\tilde{a}(t)$, assuming that $|\alpha_1(t)| = \alpha_1(t) \gg \{|\Delta\tilde{a}_1(t)|, |\Delta\tilde{a}_{\mathrm{in2}}(t)|\}$ we can linearise the equation neglecting the higher order terms in $\delta\tilde{a}_1(t)$ and $\delta\tilde{a}_{\mathrm{in2}}(t)$. The resulting expression for $\delta\dot{\tilde{a}}_1(t)$ can be rewritten as an expression for each of the time domain amplitude and phase quadrature operators using the relations $\delta\dot{\tilde{X}}^+(t) = \delta\dot{\tilde{a}}_1^\dagger(t) + \delta\dot{\tilde{a}}_1(t)$ and $\delta\dot{\tilde{X}}^-(t) = i(\delta\dot{\tilde{a}}_1^\dagger(t) - \delta\dot{\tilde{a}}_1(t))$. Taking the Fourier transform of these time domain quadrature operator equations of motion provides expressions for the frequency domain intra-resonator quadrature operators $\hat{X}_1^\pm(\omega)$.

$$\hat{X}_1^\pm(\omega) = -\frac{\sqrt{2\gamma_{\mathrm{ic},1}}\hat{X}^\pm_{\mathrm{ic,in1}}(\omega) - \sqrt{2\gamma_{\mathrm{oc},1}}\hat{X}^\pm_{\mathrm{oc,in1}}(\omega) - \sqrt{2\gamma_{l,1}}\hat{X}^\pm_{l,1}(\omega) - 2\sqrt{\gamma_{\mathrm{II}}}\,\alpha_1(t)\hat{X}^\pm_{\mathrm{ic,in2}}(\omega)}{i\omega + \gamma_1 + \Upsilon^\pm}, \tag{2.148}$$

where $\Upsilon^\pm$ are defined as

$$\Upsilon^\pm = 2\gamma_{\mathrm{II}}\alpha_1(t)^2 \pm \left(\gamma_{\mathrm{II}}\alpha_1(t)^2 + 2\sqrt{\gamma_{\mathrm{II}}}\,\alpha_{\mathrm{ic,in2}}(t)\right). \tag{2.149}$$

The boundary conditions given in Eq. (2.109) can then be used to obtain expressions for the frequency domain quadrature operators of the fields exiting the resonator. Notice that the frequency domain operators for the intra-resonator fundamental field depend not only on the input fields at the fundamental wavelength, but also on those at the second harmonic wavelength. This dependence on $\hat{X}^\pm_{\mathrm{ic,in2}}(\omega)$ varies proportionally with the intra-resonator fundamental field amplitude $\alpha_1(t)$. Therefore, the coupling can be eliminated by ensuring this field amplitude is low, $\alpha_1(t) \ll 1/2\sqrt{\gamma_{\mathrm{II}}}$.

2.11 Summary

This Chapter introduced the quantum optical techniques used throughout the work presented in this thesis. These techniques include those used to model quantum states, quantum optical experiments, and the detection of quantum states; and those used in the laboratory to monitor and control our experiments.

To summarise, we introduced the relevant quantum states of light, and discussed how they could be represented using Wigner functions and Ball and Stick diagrams. We discussed the quantum optical sideband states, and demonstrated that an optical modulation performs the function of the Displacement operator on such states. We introduced the beam splitter, showing how it can be used to model inefficient processes, and how error signals can be generated to control the relative phase of the beam splitter inputs. We demonstrated how the quantum state of the sidebands of an optical field can be probed using direct detection and homodyne detection. We modelled optical resonators, and discussed methods used to control their length. The limitations of, and methods used to improve, the frequency bandwidths of control loops in an experiment were discussed. Finally, we introduced the second order optical nonlinearity that we make use of to produce the second harmonic of our laser field and to generate squeezed states of light.

Chapter 3

Generation of quadrature squeezing

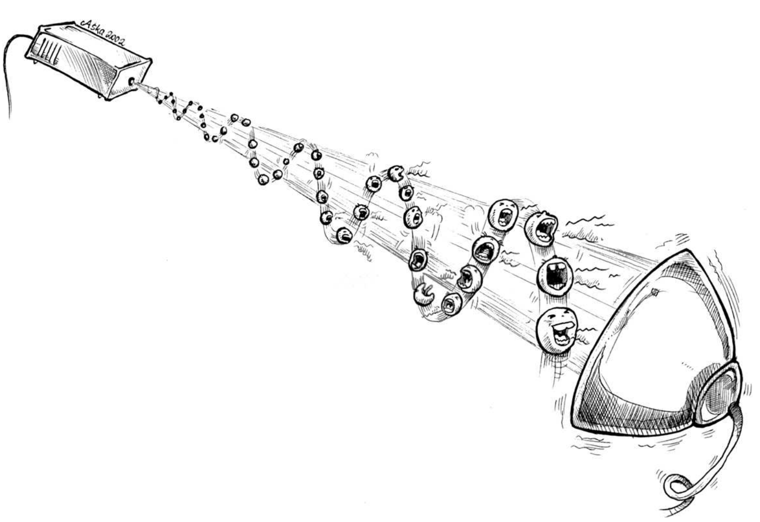

'The origin of quantum noise' - Aśka Dolińska 2002

In this Chapter we discuss in detail the experimental system that enabled generation of the squeezed optical fields used throughout the work presented in this thesis. The core components of this system are a pair of optical parametric amplifiers that rely on the second order non-linearity of Magnesium Oxide doped Lithium Niobate. The development of these optical parametric amplifiers relied on expertise developed over several Ph.D.'s at the A.N.U. quantum optics group [75, 76]; and their design was based on the pioneering work of Schiller, Mlynek and co-workers at Universität Konstanz [53, 63] who demonstrated as much as 6.2 dB of squeezing in a stably controlled 1064 nm optical field. We analyse several optical parametric amplifier configurations based on this design, and discuss some of the significant noise sources that degrade the level of squeezing observed on the output field. We experimentally characterise the level of squeezing exhibited by the output fields, measuring an optimum 4.4 dB below the quantum noise limit. Finally, we suppress the relaxation oscillation noise of our laser by placing the OPAs within a Mach-Zehnder interferometer; demonstrating stably locked vacuum squeezing at frequencies as low as 210 kHz.

Part of the work presented in this Chapter has been published in the journal articles:

- D. A. Shaddock, B. C. Buchler, W. P. Bowen, M. B. Gray, and P. K. Lam. *Modulation-free control of a continuous-wave second-harmonic generator.* Journal of Optics A: Pure and Applied Optics **2**, pp. 400 (2000).
- M. J. Lawrence, W. P. Bowen, H.-A. Bachor, R. L. Byer, and M. M. Fejer. *Squeezed Singly Resonant Second Harmonic Generation in Periodically Poled Lithium Niobate.* Journal of

the Optical Society of America B **19**, pp.1592 (2002).

- W. P. Bowen, R. Schnabel, N. Treps, H.-A. Bachor, and P. K. Lam. *Recovery of continuous wave squeezing squeezing at low frequencies.* Journal of Optics B: Quantum and Semi-Classical Optics **4**, pp. 421 (2002).
- R. Schnabel, W. P. Bowen, N. Treps, B. C. Buchler, T. C. Ralph, P. K. Lam, and H.-A. Bachor. *Optical experiments beyond the quantum limit: squeezing, entanglement, and teleportation.* Optics and Spectroscopy **94**, pp. 711 (2003).

3.1 The laser

The majority of the work present in this thesis utilised an Innolight Mephisto Nd:YAG laser producing radiation at 1064 nm. The laser had a nonplanar ring geometry (NPRO), which provided an output field of extremely stable frequency with a FWHM linewidth in the low kHz (see Fig. 3.1). Single mode operation of the laser was ensured via the Faraday effect. The laser output field was a diffraction limited, low noise, single frequency mode 1.5 W beam [88, 89]. The frequency of the laser field could be controlled at low frequencies via Peltier elements that heated or cooled the laser crystal and therefore changed the length of the resonator, and at high frequency via a PZT actuator that mechanically stressed the laser crystal, changing its refractive index. The PZT tuning range was limited to 80 MHz, which corresponds to 4 % of the free spectral range (FSR) of the laser. To achieve the desired frequency tuning range and control bandwidth when locking the laser to an optical resonator, a combination of temperature and PZT actuation was used. The resonant relaxation oscillation (RRO) of the laser, which couples noise into its power spectrum, had a peak at around 750 kHz. This can be thought of as the atomic cycling frequency from the ground state of the Nd:YAG energy level system to the laser level. Measurements of the FSR, RRO, and linewidth of a typical Innolight Mephisto Nd:YAG laser are shown in Fig. 3.1.

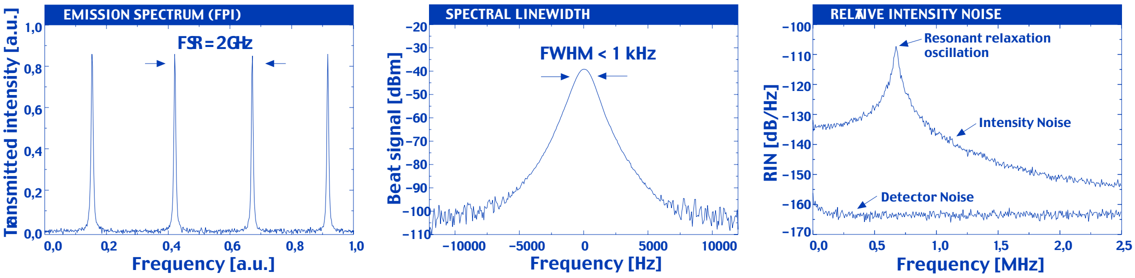

Figure 3.1: Measurements of the FSR, RRO, and linewidth of a typical Innolight Mephisto Nd:YAG laser [obtained from the Innolight Mephisto technical data sheet, http://www.innolight.de/products/mephisto/INNOLIGHT_Mephisto.pdf].

The laser output at 1064 nm was passed through an optical isolator to prevent feedback, and was collimated to a width of 1 mm. The Rayleigh length of the beam was then $\sim$ 3 m, so that its width remained at $\sim$ 1 mm over the length of our optical table. 1.2 W of light at 1064 nm was then available to perform our experiments. Prior to any optical resonators in the experiment the field was focussed or *mode-matched* into a spatial mode identical to the resonator mode. The output fields were then recollimated at 1 mm width. This recollimation allowed for convenient mode-matching of the interferometer stages of the experiment.

3.2 Spectral and spatial mode cleaning resonator

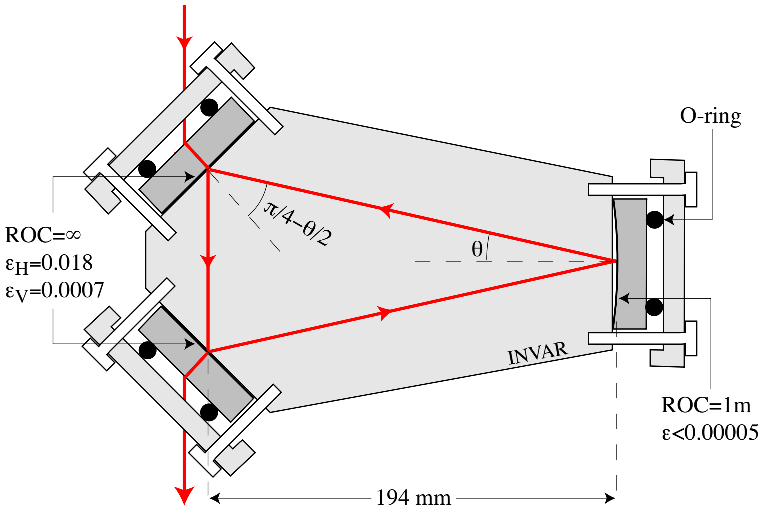

Figure 3.2: Schematic of the mode cleaner used to improve the spatial and spectral mode quality of the 1064 nm laser beam, $\theta = 4.41°$, ROC: radius of curvature, ϵ: transmission of the respective resonator mirror, sub-scripts H and V label the horizontally and vertically polarised modes, respectively.

Sixty percent of the laser power was used to pump a second harmonic generator, which is the subject of Section 3.3. The experiments presented in this thesis were very sensitive to spectral noise and spatial mode-matching inefficiencies. To minimise problems related to these effects the remaining laser field was passed through a high-finesse optical resonator, or *mode cleaner*, before being used to generate squeezed and entangled states; to control optical resonators and interferometers; and for homodyne local oscillators to characterise optical states. This mode cleaner was based on a design developed in the Ginzton Labs, Stanford [90], and a schematic diagram is given in Fig. 3.2. It was a ring resonator consisting of two identical closely spaced flat $\lesssim 45°$ angled input/output coupling mirrors, and a 1 m radius of curvature mirror coated for high reflection at normal incidence (transmissivity: $\epsilon_{\text{curv}} < 0.00005$); and had a total resonator length of 42 cm. All three mirrors were dielectrically coated by Research-Electro-Optics (REO) with tolerances of 10-100 parts-per-million. In general the reflectivity and phase response of an angled dielectric mirror depends on the polarisation of the input field. Two mode cleaner operation regimes could then be accessed. For a vertically polarised input field the input and output mirrors had transmissivity $\epsilon_{\text{V}} = 0.0007$. Assuming no intra-resonator loss, these transmissivities lead to a predicted resonator finesse of 4300. In contrast we observed a finesse of 2000, this provided an estimate of the round-trip resonator loss of $(1 - \epsilon_l) = 0.0017$. The total resonator decay rate was then $\gamma_{\text{V}} = (2\epsilon_{\text{V}} + \epsilon_{\text{curv}} + (1 - \epsilon_l))/2\tau = 1.1 \times 10^6$ rad. In Section 2.8.1 we found that a resonator with $\epsilon_{\text{ic}} = \epsilon_{\text{oc}}$ acts as a low pass filter on the fluctuations of the input field, with 3 dB point defined by the total resonator decay rate γ. Therefore, in this mode cleaner operation regime, the fluctuations of the input field were significantly attenuated at frequencies above $\gamma_{\text{V}}/2\pi = 0.18$ MHz. When the mode cleaner input field was horizontally polarised the input and output coupler mirror transmissivities were specified to be $\epsilon_{\text{H}} = 0.018$. Assuming a round-trip resonator loss of $(1 - \epsilon_l) = 0.0017$, the finesse was then predicted to be 165, which compared well with the observed finesse of 170. The resulting resonator decay rate was $\gamma_{\text{H}} = 13.5 \times 10^6$ rad. Therefore in this case the resonator 3 dB point was $\gamma_{\text{H}}/2\pi = 2.1$ MHz, and fluctuations on the input field

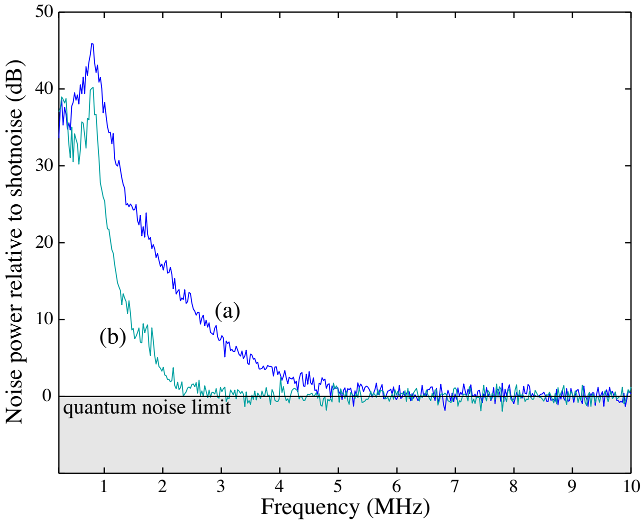

Figure 3.3: Frequency spectra of the field transmitted through the mode cleaner in low (a) and high (b) finesse modes, normalised to the quantum noise limit.

above that frequency were attenuated.

Frequency spectra for the intensity noise of a 25 mW laser field after transmission through the mode cleaner for both its low and high finesse modes are shown in Fig. 3.3. We see that at frequencies below 5 MHz the intensity noise of the high finesse output was attenuated significantly more than that of the low finesse output. In the experiments presented in this thesis we utilised the low finesse mode to maximise the power transmitted through the resonator. The mode cleaner then acted primarily to ensure that the laser field was in a pure TEM_{00} mode, and that the alignment of the 1064 nm beam used in our experiments did not drift. Fig. 3.3 shows that a 25 mW beam transmitted through the mode cleaner was quantum noise limited at around 6 MHz. The frequency of our laser source was locked to the mode cleaner using both temperature and PZT control. The error signal for this control system was generated using the tilt locking technique introduced in Section 2.8.2 [28, 80].

3.3 Second harmonic generation

Throughout the work presented in this thesis the second harmonic of our 1064 nm laser field was used as a pump source for a pair of optical parametric amplifiers (OPAs). Our primary objective was to design a second harmonic generator with high efficiency to provide an intense source of 532 nm light. It is possible to generate squeezed light via second harmonic generation[91], and these techniques were investigated during the course of my PhD[26]. However, they were found to be less effective than OPA based techniques, and will not be discussed further here. We limit our treatment to the classical behaviour of second harmonic generation.

The experimental configuration used to generate an intense second harmonic field is shown in Fig. 3.4. It consisted of an input/output coupler and a hemilithic MgO:LiNbO_3 crystal of dimension $\{x, y, z\} = \{5\,\text{mm}, 7.5\,\text{mm}, 2.5\,\text{mm}\}$ where z is the crystal optical axis and the field propagates along y. The MgO:LiNbO_3 crystal was polished and coated by PMS Optik GmbH. One end had a 10 mm radius of curvature and was coated for high reflection at 1064 and 532 nm, and the other was flat and anti-reflection coated at both 1064 and 532 nm. The temperature of

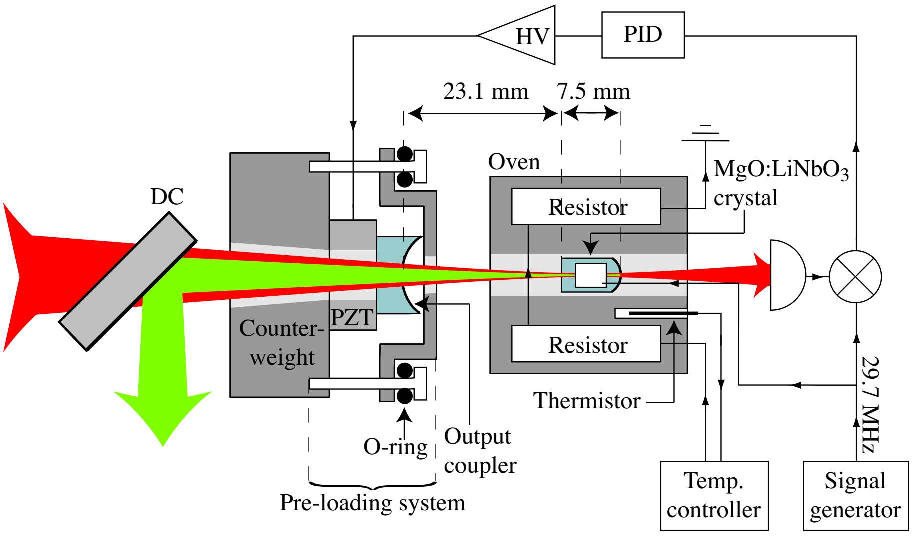

Figure 3.4: Second harmonic generator configuration, HV: high voltage amplifier, PID: proportional, integral, differential servo, DC: dichroic mirror, PZT: piezo-electric crystal, $\otimes$: RF mixer.

the crystal was controlled so that the phase matching condition was satisfied. It was mounted in an aluminium oven, a thermistor monitored the temperature of the oven and a home-built temperature servo then controlled it to a setpoint by applying current to resistors within the oven. The input/output coupling mirror had a radius of curvature of 25 mm, and was anti-reflection coated for 532 nm, $\epsilon_{\mathrm{ic},2} = 0.94$. The transmissivity if the output coupler for the fundamental field was chosen to maximise the SHGs conversion efficiency for 700 mW of input 1064 nm field. It was attached to a PZT so that the length of the resonator could be controlled, and a pre-loading system as described in Section 2.9.2 was used to enhance the PZT bandwidth to 40 kHz. 23 mm separated the MgO:LiNbO$_3$ crystal and the output coupler, this created a mode for the resonant 1064 nm light with a 27 μm waist at the center of the MgO:LiNbO$_3$ crystal. A 29.7 MHz electro-optic modulation was applied to the MgO:LiNbO$_3$ crystal, this caused a refractive index modulation of the crystal, and therefore a phase modulation on the intra-resonator field. Detecting the transmitted field and de-modulating (mixing down) at 29.7 MHz provided a Pound-Drever-Hall (PDH) type error signal [79] (see Section 2.8.2) which was used to control the length of the SHG resonator. The second harmonic output field exited the resonator through the output coupler and was separated from the input fundamental field with a dichroic mirror. A summary of the parameters characterising our SHG is given in Table 3.1.

The conversion efficiency of external resonator second harmonic generation η_{SHG} is given as a function of fundamental input power by

$$\eta_{\mathrm{SHG}} = \frac{P_{\mathrm{ic,out2}}}{P_{\mathrm{ic,in1}}} = \frac{\hbar\Omega_2 \left|\alpha_{\mathrm{ic,out2}}\right|^2}{P_{\mathrm{ic,in1}}} = \frac{\hbar\Omega_2 \Lambda^2 \alpha_1^2}{2\gamma_2 P_{\mathrm{ic,in1}}}, \tag{3.1}$$

where we have related the coherent amplitude of the second harmonic output field $\alpha_{\mathrm{ic,out2}}$ to that of the fundamental intra-resonator field α_1 via Eq. (2.147) and the boundary conditions in Eq. (2.108). For second harmonic generation α_1 is given by Eq. (2.145) with no second harmonic input power ($\alpha_{\mathrm{ic,in2}} = 0$). The conversion efficiency can then be predicted given knowledge of the nonlinear interaction strength Λ. The nonlinear interaction strength depends on experimen-

	SHG	OPAs
Fundamental input coupler transmissivity, $\epsilon_{\rm ic,1}$	0.08	0.0005
Fundamental output coupler transmissivity, $\epsilon_{\rm oc,1}$	0.0005	0.04
Intra-resonator loss, $1-\epsilon_{l,1}$	0.0065	0.0065
Second harmonic input coupler transmissivity, $\epsilon_{\rm ic,2}$	0.94	0.94
Single pass resonator optical path length, L	4 cm	4 cm
Non-linear interaction strength, Λ	3100 $\rm s^{-\frac{1}{2}}$	3100 $\rm s^{-\frac{1}{2}}$
Fundamental input power, $P_{\rm ic,in1}$	700 mW	10-60 mW
Second harmonic input power, $P_{\rm ic,in2}$	0 mW	135 mW

Table 3.1: Summary of the parameters characterising the SHG and OPAs developed for the work presented in this thesis. $P_i = \hbar\Omega_i\alpha_i^\dagger\alpha_i$ is the intensity of field i, and L is the single-pass optical path length within the resonator. $\gamma_{\rm ic,1} = \epsilon_{\rm ic,1}/2\tau$, $\gamma_{\rm oc,1} = \epsilon_{\rm oc,1}/2\tau$, $\gamma_{\rm ic,2} = \epsilon_{\rm ic,2}/2\tau$, and $\gamma_{l,1} = (1-\epsilon_{l,1})/2\tau$, where the resonator round trip time is given by $\tau = 2L/c$.

tal parameters such as beam focussing, crystal imperfections, and temperature variation over the interaction region, and is typically quite difficult to characterise. It is related to the threshold second harmonic pump power required to generate a bright coherent field in an optical parametric oscillator (see Eq. 3.2), and one of the most accurate characterisation techniques is to determine that threshold. However, since second harmonic power is required for this measurement, it was not possible before the SHG was set up. In a similar system to ours Λ had been determined to be 6000 $\rm s^{-\frac{1}{2}}$[92], and this value was used to estimate the optimum value of input coupling for our SHG. The predicted conversion efficiency as a function of input fundamental intensity is shown in Fig. 3.5 a) for a range of input coupler transmissivities. For 700 mW of input power the optimum conversion efficiency was predicted to occur for $\epsilon_{\rm ic,1} = 0.08$, and a corresponding input coupler was therefore chosen. With this input coupler the SHG provided 370 mW of 532 nm light with 53 % conversion efficiency.

Using the second harmonic field we could determine the non-linear interaction strength Λ for our experiment. It is related to the operation threshold of optical parametric oscillation via[1]

$$\Lambda = \frac{\gamma_1\gamma_2}{\sqrt{2\gamma_{\rm ic,2}}\left|\alpha^\circ_{\rm ic,in2}\right|}, \tag{3.2}$$

where $\alpha^\circ_{\rm ic,in2}$ is the coherent amplitude of the second harmonic input field at threshold. We set up an optical parametric oscillator in an identical configuration to the SHG, but with fundamental input coupler transmissivity of $\epsilon_{\rm ic,1} = 0.04$, and determined the optical parametric oscillation threshold to occur at $P^\circ_{\rm ic,in2} = \hbar\Omega_2|\alpha^\circ_{\rm ic,in2}|^2 = 270$ mW. We therefore predict an interaction strength of $\Lambda = 3100\,\rm s^{-\frac{1}{2}}$, close to half that measured in [92]. The corresponding SHG conversion efficiencies are shown as a function of fundamental power in Fig. 3.5 b). We see that although the second harmonic power available was sufficient for the experiments reported here, in hindsight a fundamental input coupler transmissivity of $\epsilon_{\rm ic,1} = 0.04$ may have provided higher conversion efficiency.

---

[1] This can be shown quite easily from Eq. (2.140).

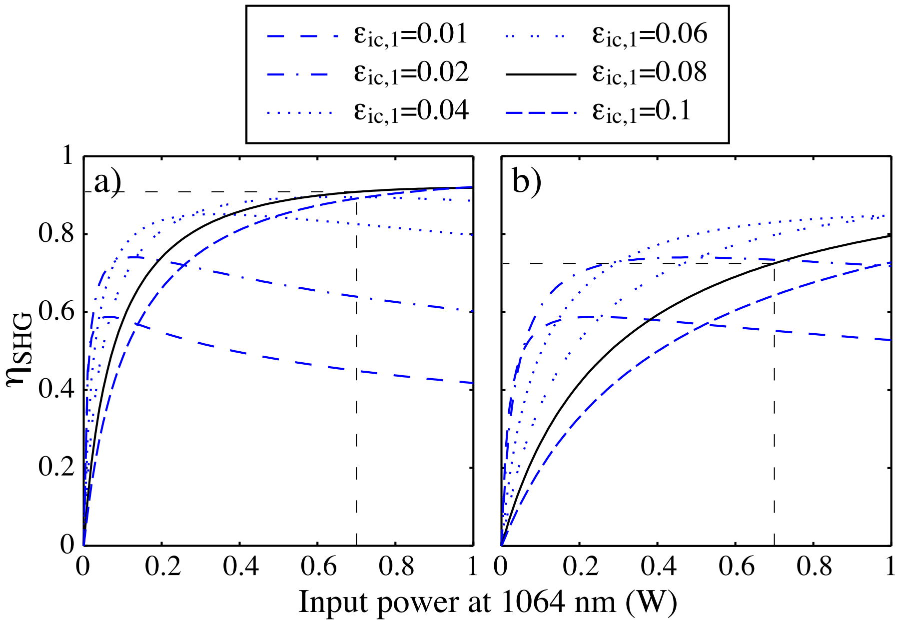

Figure 3.5: Conversion efficiency of second harmonic generator as a function of power and input coupler reflectivity, a) using the interaction strength $\Lambda = 6000\,\mathrm{s}^{-\frac{1}{2}}$ as reported in [92], and b) using $\Lambda = 3100\,\mathrm{s}^{-\frac{1}{2}}$ as measured *a posteriori* from our experiment. Parameters used: $\epsilon_{l,1} = 0.0065$, $\epsilon_{\mathrm{oc},1} = 0.0005$, $\epsilon_2 = 0.94$, $\mathrm{L}_{\mathrm{SHG}} = 4$ cm.

3.4 Optical parametric amplification

The second harmonic field was used to pump a pair of degenerate OPAs which were seeded with a field at the fundamental frequency. The design of the OPAs was identical to that of the SHG shown in Fig. 3.4, with the exception that the OPA output coupler transmissivities for the fundamental field were $\epsilon_{\mathrm{oc},1} = 0.04$. This output coupler transmissivity was found to provide the optimum balance between OPA escape efficiency and the threshold for OPO operation which, as we will see later, dictates the level of squeezing on the OPA output fields. A summary of the experimental parameters relevant to the OPAs can be found in Table 3.1.

An alternative OPA configuration used in some experiments requiring a pair of squeezed beams [93] is to utilise a single ring OPA. In this case both directional modes in the OPA can be squeezed directly, resulting in two squeezed output fields. We chose not to use that approach here. It requires a more complex resonator design with more intra-resonator surfaces, angled curved mirrors, and a longer round trip time. Correspondingly, the round trip loss is higher, the output beam shape is distorted, and the squeezing bandwidth is reduced. These problems can be overcome, and highly squeezed fields can be generated from these resonators [93], but with a significantly higher level of engineering required. Furthermore, both directional modes in a ring resonator must be pumped, so that for a given level of amplification, a doubling of the intra-resonator second harmonic pump power is required. This doubling can increase the effect of green-induced infrared absorption (GRIIRA), a non-linear intra-resonator loss factor proportional to the second harmonic pump power[94]. GRIIRA is one of the most significant limiting factors in a number of existing squeezing experiments using ring resonators [93]. On the other hand, we will see in Section 3.7, that ring resonator configurations could provide an excellent source of low frequency squeezing.

3.4.1 Classical behaviour

Before analysing the predicted squeezing of the output field from an OPA, let us examine its classical behaviour. The coherent amplitude of the fundamental field exiting the output coupler of an OPA $\alpha_{\rm oc,out1}$ may be calculated quite generally from Eq. (2.145) for the steady state intra-resonator field, using the boundary conditions given in Eqs. (2.108). The resulting expression, however, is rather complicated. Here, to enable an intuitive understanding we consider an idealised OPA with negligible decay rates due to intra-resonator losses and the input coupler ($\{\gamma_{l,1}, \gamma_{\rm ic,1}\} \ll \gamma_{\rm oc,1} \approx \gamma_1$), and no second harmonic pump depletion[2]. This idealised OPA can be seeded through either the front (through the output coupler) or the back (through the back of the MgO:LiNbO$_3$ crystal). In our experiment, we seeded our OPAs through the back, and we consider that situation here. A detailed comparison of the two seeding methods is given in Section 3.5. Using Eqs. (2.108), (2.144), (2.145), and (3.2), the coherent amplitude of the output field $\alpha^{\rm ideal,back}_{\rm oc,out1}$ is found to be

$$\alpha^{\rm ideal,back}_{\rm oc,out1} = -\frac{\sqrt{2\gamma_{\rm ic,1}}\alpha_{\rm ic,in1}}{\gamma_1}\left(\frac{1}{1-\alpha_{\rm ic,in2}/|\alpha^{\circ}_{\rm ic,in2}|}\right), \tag{3.3}$$

where $|\alpha_{\rm ic,in2}| < |\alpha^{\circ}_{\rm ic,in2}|$. We see that the phase relationship between the coherent amplitudes of the second harmonic pump field and the seed field dictates the amplification of the OPA. If the pump and seed fields are in phase, the pump coherent amplitude $\alpha_{\rm ic,in2}$ is real and positive, and as $|\alpha_{\rm ic,in2}| \to |\alpha^{\circ}_{\rm ic,in2}|$, $|\alpha^{\rm ideal,back}_{\rm oc,out1}| \to \infty$. Therefore in this regime the OPA acts to amplify the seed field, transferring power from the pump field. Of course, infinite power is not truly achievable from an OPA, at some stage the pump field will be depleted and the amplification will clamp, an analysis including pump depletion is given in Section 3.5. If the seed and pump fields are π out of phase $\alpha_{\rm ic,in2}$ is real and negative, and as $|\alpha_{\rm ic,in2}| \to |\alpha^{\circ}_{\rm ic,in2}|$, $|\alpha^{\rm ideal,back}_{\rm oc,out1}| \to \sqrt{2\gamma_{\rm ic,1}}|\alpha_{\rm ic,in1}|/2\gamma_1$. So that the OPA then acts to deamplify the seed field, transferring power into the pump field.

Regenerative gain

The amplification of an OPA is characterised by its the regenerative gain G_R, which is defined as the ratio of the fundamental output power with and without the second harmonic pump field

$$G_R = \frac{P_{\rm oc,out1}}{P^{\rm no\ 532}_{\rm oc,out1}} = \left|\frac{\alpha_{\rm oc,out1}}{\alpha^{\rm no\ 532}_{\rm oc,out1}}\right|^2, \tag{3.4}$$

where the super-script 'no 532' labels the fundamental output field obtained when no second harmonic pump field is used ($\alpha_{\rm ic,in2} = 0$). Neglecting pump depletion and the resonator decay rates due to losses and the input coupler this can be calculated simply for our OPA, and is given by

$$G^{\rm ideal}_{R,\rm back} = \frac{1}{\left|1-\alpha_{\rm ic,in2}/|\alpha^{\circ}_{\rm ic,in2}|\right|^2}. \tag{3.5}$$

The curves in Fig. 3.6 show the regenerative gain of our ideal OPA operating in the amplification and deamplification regimes. We see that in the amplification regime as the second harmonic power approaches the threshold for OPO operation the regenerative gain increases towards infinity.

---

[2] It can be shown that when the OPA is not operating near threshold there is negligible second harmonic pump depletion if $|\alpha_{\rm ic,in2}| \gg |\alpha_{\rm in1}|$.

On the other hand, in the deamplification regime as the OPO threshold is approached the regenerative gain clamps at $G^{\rm ideal}_{R,\rm back} = 1/4$. As a consequence, any noise entering the OPA through the back surface of the MgO:LiNbO$_3$ crystal can be deamplifed by a maximum factor of only 1/4. Of course, since the noise is attenuated by a factor governed by the transmissivity of the MgO:LiNbO$_3$ crystal back surface while entering the OPA, this does not place a fundamental limit on the squeezing achievable with optical parametric amplification.

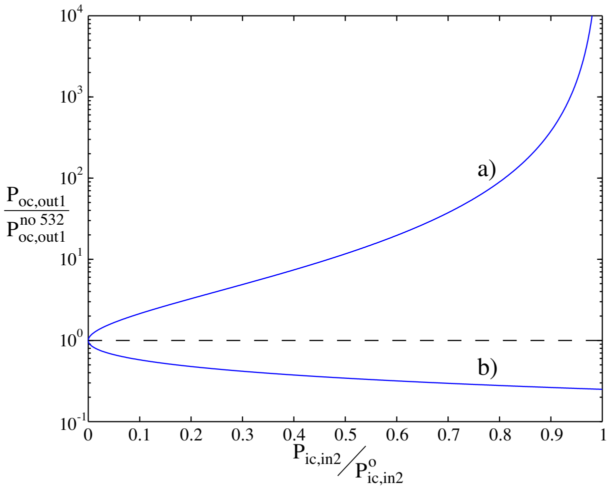

Figure 3.6: Regenerative gain of an optical parametric amplifier. a) predicted amplification and b) predicted deamplification of a back seeded OPA with $\epsilon_{\rm ic,1} = \epsilon_{l,1} = 0$, neglecting pump depletion.

3.4.2 Squeezing of the output coupled field

The fluctuations of the output coupled field may be directly obtained from Eq. (2.148) for the intra-resonator noise properties for a resonator with a second order non-linear element inside. Using the boundary conditions given in Eq. (2.109), the resulting fluctuations are given quite generally by

$$\begin{aligned}\hat{X}^{\pm}_{\rm oc,out1}(\omega) &= \left(1 - \frac{2\gamma_{\rm oc,1}}{i\omega + \gamma_1 + \Upsilon^{\pm}}\right)\hat{X}^{\pm}_{\rm oc,in1}(\omega) \\ &\quad - \frac{\sqrt{2\gamma_{\rm oc,1}}}{i\omega + \gamma_1 + \Upsilon^{\pm}}\left(2\sqrt{\gamma_{\rm II}}\alpha_1(t)\hat{X}^{\pm}_{\rm ic,in2}(\omega) + \sqrt{2\gamma_{\rm ic,1}}\hat{X}^{\pm}_{\rm ic,in1}(\omega) + \sqrt{2\gamma_{l,1}}\hat{X}^{\pm}_{l,1}(\omega)\right),\end{aligned} \tag{3.6}$$

where $\Upsilon^{\pm}$ are defined in Eq. (2.149). The frequency spectra obtained when the output field is analysed in a homodyne detector are equal to the variances of these fluctuations $\Delta^2\hat{X}^{\pm}_{\rm oc,out1}(\omega) = \langle\delta\hat{X}^{\pm}_{\rm oc,out1}(\omega)^*\delta\hat{X}^{\pm}_{\rm oc,out1}(\omega)\rangle$, which are given by the relatively complicated expression

$$\begin{aligned}\Delta^2\hat{X}^{\pm}_{\rm oc,out1}(\omega) &= \frac{4\gamma_{\rm oc1}\left[2\gamma_{\rm II}\alpha_1(t)^2\Delta^2\hat{X}^{\pm}_{\rm ic,in2}(\omega) + \gamma_{\rm ic,1}\Delta^2\hat{X}^{\pm}_{\rm ic,in1}(\omega) + \gamma_{l,1}\right]}{\omega^2 + (\gamma_1 + \Upsilon^{\pm})^2} \\ &\quad + \left[\frac{(2\gamma_{\rm oc,1} - \gamma_1 - \Upsilon^{\pm})^2 + \omega^2}{\omega^2 + (\gamma_1 + \Upsilon^{\pm})^2}\right]\Delta^2\hat{X}^{\pm}_{\rm oc,in1}(\omega),\end{aligned} \tag{3.7}$$

where we have assumed that the fields entering the resonator as a result of losses are vacuum ($\Delta^2\hat{X}^{\pm}_{l1}(\omega) = 1$). We see that at $\omega = 0$, if the resonator is impedance matched (i.e. if $\gamma_{\rm oc,1} =$

$\gamma_{\rm ic,1}+\gamma_{l,1}+\Upsilon^{\pm}$) the noise contribution from the field incident on the output coupler is eliminated. In this regime, so long as the fluctuations coupling in from the pump field and through losses and the input coupling are small, squeezing will be evident on the output field.

To gain a clearer understanding of the process of squeezing via optical parametric amplification let us, for the moment, assume that all of the input fields are in coherent or vacuum states, and neglect pump depletion. The quadrature variances of the output field are then given by the simplified expression

$$\Delta^2\hat{X}^{\pm}_{\rm oc,out1}(\omega) = 1 \pm \eta_{\rm esc}\frac{4\alpha_{\rm ic,in2}/|\alpha^{\circ}_{\rm ic,in2}|}{(\omega/\gamma_1)^2+\left(1\mp\alpha_{\rm ic,in2}/|\alpha^{\circ}_{\rm ic,in2}|\right)^2}, \tag{3.8}$$

where the OPA escape efficiency is given by $\eta_{\rm esc}=\gamma_{\rm oc,1}/\gamma_1$, and to derive this expression we have used Eqs. (2.108), (2.144), (3.2), and (3.7). In the deamplification regime the second harmonic pump field is π out of phase with the fundamental seed, so that the coherent amplitude of the pump field $\alpha_{\rm ic,in2}$ is real and negative. We see that in this regime for all non-zero pump powers and all sideband frequencies, the amplitude quadrature of the output field is squeezed. As ω increases the level of squeezing drops with $\Delta^2\hat{X}^{+}_{\rm oc,out1}(\omega)\rightarrow 1$ as $\omega\rightarrow\infty$, and as the pump power approaches the threshold power ($|\alpha_{\rm ic,in2}|\rightarrow|\alpha^{\circ}_{\rm ic,in2}|$) the squeezing improves. At $\omega=0$, and at threshold, we reach the optimum squeezing of $\Delta^2\hat{X}^{+}_{\rm oc,out1}(\omega)\rightarrow 1-\eta_{\rm esc}$, so that the level of squeezing is ultimately limited by the escape efficiency of the OPA. In the amplification regime ($\alpha_{\rm ic,in2}$ real and positive) equivalent behaviour is observed with the squeezing improving at low frequencies and near threshold. Here however, the squeezing is observed on the phase quadrature of the output field, and the amplitude quadrature is anti-squeezed. Again, the optimum squeezing is $\Delta^2\hat{X}^{-}_{\rm oc,out1}(\omega)=1-\eta_{\rm esc}$, limited only by the escape efficiency of the OPA, and occurs at threshold with $\omega=0$. Fig. 3.13 show the predicted squeezed quadrature variance as a function of pump power for both amplification regimes.

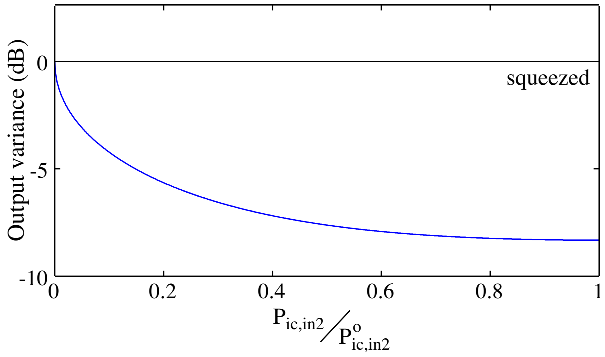

Figure 3.7: Squeezing from an optical parametric amplifier as a function of pump power. The plot shows the predicted amplitude (phase) quadrature variance of the output field at $\omega=0$ when the OPA is operating to deamplify (amplify) the seed field. Pump depletion is neglected, and all input fields are assumed to be in coherent or vacuum states. The calculation was performed with the experimental parameters in Table 3.1.

Squeezing spectra

In practice, due to low frequency noise sources such as laser relaxation oscillation noise, locking noise, and acoustic noise, we do not observe squeezing at $\omega=0$. We are therefore interested

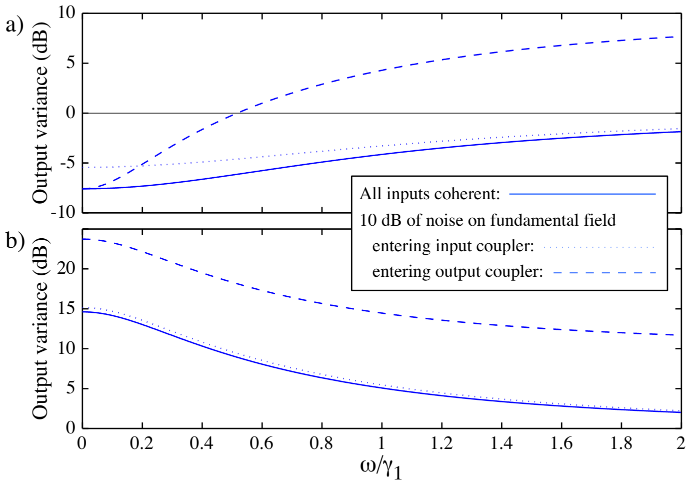

Figure 3.8: a) Amplitude and b) phase quadrature spectra for the field exiting an optical parametric amplifier operating at half threshold in the deamplification regime. The solid curves show the predicted spectra for our experimental parameters with vacuum or coherent input fields. The dotted and dashed curved show the resulting spectra when the fields entering the input and output couplers, respectively, are 10 dB above the quantum noise limit. Parameters used: $\epsilon_{\text{ic},1} = 0.0005$, $\epsilon_{\text{oc},1} = 0.04$, $\epsilon_{l,1} = 0.0065$, $\epsilon_2 = 0.94$, $L = 4$ cm, $\Lambda = 3100\,\text{s}^{-\frac{1}{2}}$, and $P_{\text{in}1} = 10$ mW.

in the predicted frequency spectra of the squeezing, which is contained in Eq. (3.7). Fig. 3.8 shows such spectra for an OPA operating in the deamplification regime, and at half threshold ($P_{\text{ic,in}2} = P^{\circ}_{\text{ic,in}2}/2$). The effects of non-quantum noise limited fundamental fields entering the OPA through its input and output couplers are also displayed. We see that so long as the fundamental field entering through the output coupler is quantum noise limited, the level of squeezing on the output field is more-or-less constant at frequencies below the resonator decay rate γ_1. For our OPAs $\gamma_1/2\pi \approx 14$ MHz. Since the dominant noise sources in our experiment all occur at frequencies below 2 MHz, we expect to observe reasonable levels of squeezing between $\omega/2\pi = 2$ and 14 MHz.

3.4.3 Generation of squeezed fields

Fig. 3.9 shows a detailed schematic of the experimental configuration we used to generate a pair of squeezed fields. Each of our OPAs was pumped with a second harmonic field through its output coupler, and seeded through the back of its MgO:LiNbO$_3$ crystal. The OPA lengths were controlled using a similar method to that used for the SHG resonator. An electro-optic modulation at 30.5 MHz was applied to the MgO:LiNbO$_3$ crystal resulting in a phase modulation of the intra-resonator field. We detected the field exiting the back surface of the MgO:LiNbO$_3$ crystal. Demodulating (or mixing-down) the resulting photocurrent at 30.5 MHz resulted in an error signal for the resonator length, after amplification and filtering this error signal was applied to a PZT mounted between the output coupler mount and the output coupler. As we have just seen, an OPA acts to either amplify or deamplify its seed field depending on the relative phase between the

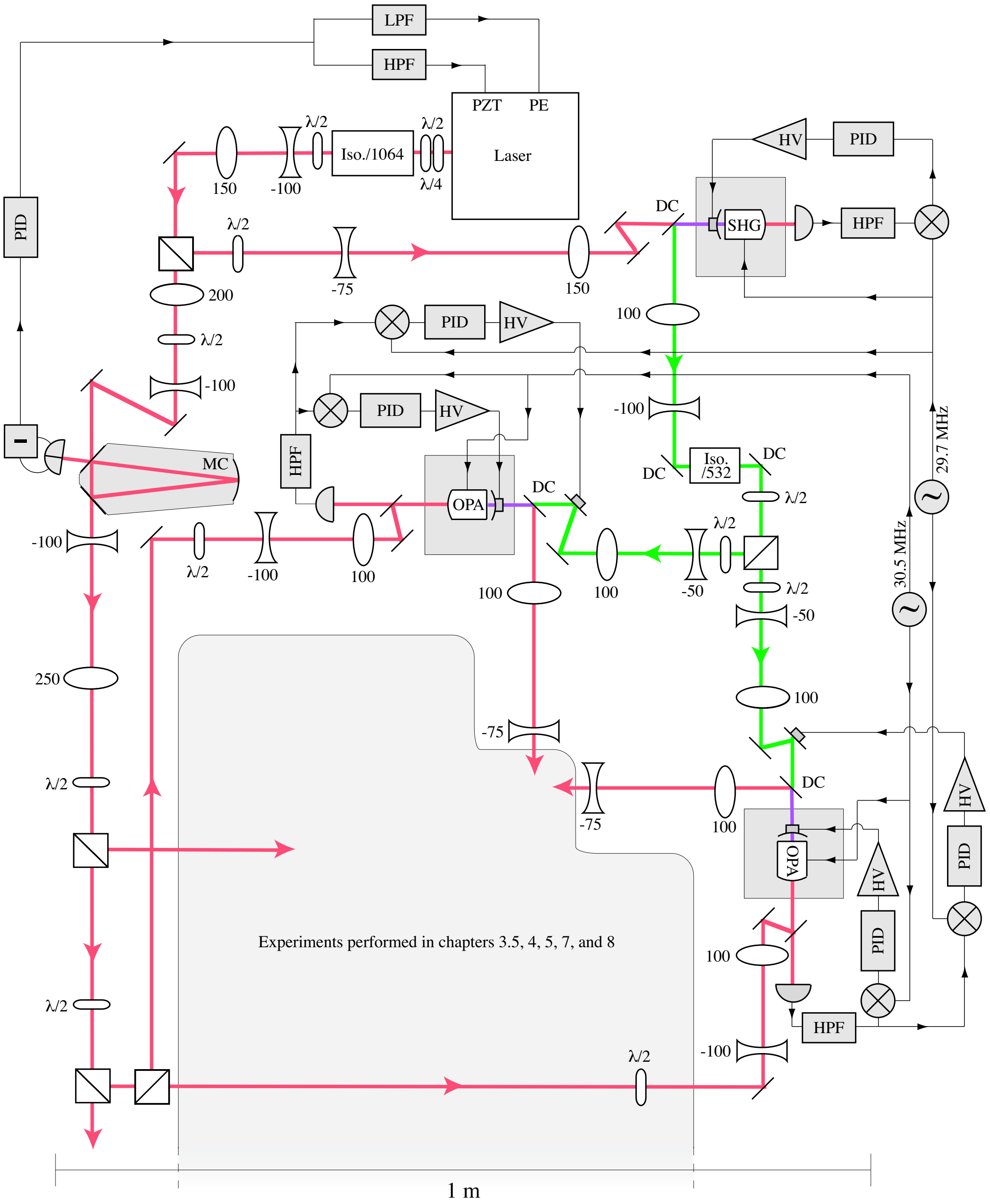

Figure 3.9: Detailed schematic of system used to generate a pair of squeezed fields. HV: high voltage amplifier, PID: proportional, integral, differential servo, DC: dichroic mirror, PZT: piezo-electric crystal, PE: Peltier element, $\otimes$: RF mixer, $\lambda/2$ ($\lambda/4$) half (quarter) wave plate, Iso.: optical isolator, LPF: low pass filter, HPF: high pass filter, MC: mode cleaner.

seed and pump fields. Since our SHG was controlled via an intra-resonator phase modulation at 29.7 MHZ the output second harmonic field was phase modulated at that frequency. This resulted in a modulation of the amplification of each OPA. Demodulating the photocurrent obtained from the field exiting the back of each OPA at 29.7 MHz resulted in an error signal that could be used to lock the OPA to amplification or to deamplification. The output field of interest was the fundamental field exiting the front of the OPA (i.e. through the output coupler). When our OPAs were locked to amplification we typically observed a regenerative gain for this field of ~ 20, and when locked to deamplification the regenerative gain was ~ 0.3. The ratio of pump power to the threshold power for OPO operation depended on a number of experimental parameters such as pump alignment and OPA temperature that varied somewhat from day to day. Usually the pump power was roughly 50 % of the threshold power.

3.4.4 Characterisation of the squeezed fields

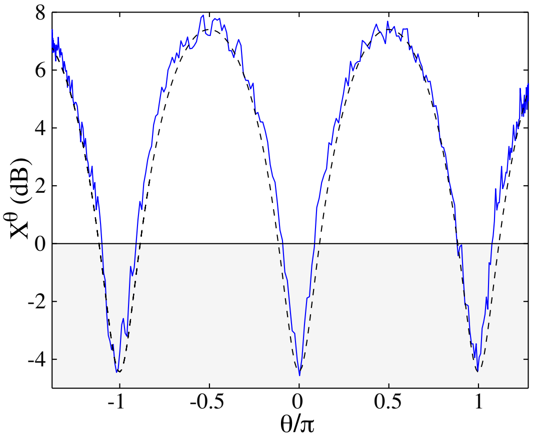

Figure 3.10: Squeezing trace observed at 6 MHz for the output of one OPA in a homodyne detector with swept local oscillator phase. RBW: 200 kHz.

We analysed the OPA output fields in a homodyne detector as described in Section 2.7.2. Each field was interfered with a bright local oscillator field on a 50/50 beam splitter, with interference visibility measured as described in Section 2.6.3 to be $\sim$ 96.5 %. The two beam splitter output fields were detected on a pair of ETX500 photodiodes with quantum efficiencies measured to be $\sim$ 93 %. The difference of the two resulting photocurrents yielded a quadrature of the OPA output field, with the specific quadrature controlled by the relative phase between the OPA output field and the local oscillator. Scanning this phase swept through all quadratures of the OPA output field. The difference photocurrent generated with the relative phase scanned was analysed in a Hewlett Packard E4405B spectrum analyser. The quantum noise limit could be determined by blocking the OPA output field so that only vacuum fluctuations were observed by the homodyne detector. This allowed normalisation of the spectra observed for the OPA output fields. Setting the spectrum analyser to zero span at 6 MHz, with a resolution bandwidth of 200 kHz, we observed squeezing traces of the form shown in Fig. 3.10. This 'MacDonald sign' shape is characteristic of squeezing experiments. The peak of the MacDonald sign give the variance of the anti-squeezed quadrature of the OPA output field, and the minimum gives the variance of its squeezed quadrature. Since the OPA was locked to deamplification, and therefore amplitude squeezing; the amplitude and phase quadrature variances of the detected field can be determined from Fig. 3.10. We find $\Delta^2\hat{X}^+ = 0.36$ and $\Delta^2\hat{X}^- = 5.5$, respectively.

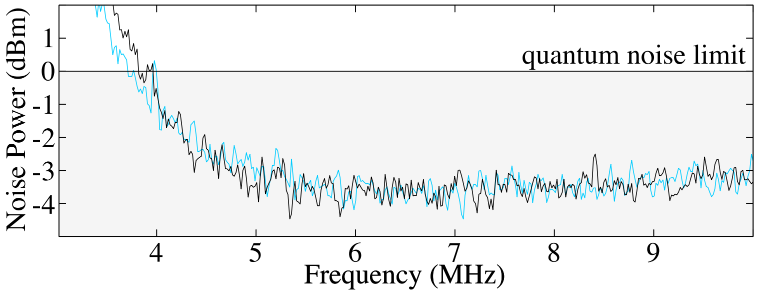

Figure 3.11: Squeezing spectra observed from the two OPAs, normalised to the quantum noise limit.

The homodyne detector could be locked to observe either the amplitude or phase quadrature of each OPA output field (see Section 2.5.2). Locking to the amplitude quadrature we observed the squeezing spectra shown in Fig. 3.11. We see that both OPAs produced almost identical squeezing spectra, with squeezing at sideband frequencies from $\omega/2\pi = 3.5$ MHz to 10 MHz. At frequencies below 6 MHz the squeezing was degraded by the resonant relaxation oscillation noise of our laser.

3.5 Regimes of optical parametric amplification

The experimental results presented in the previous section were obtained with our OPA's back seeded and locked to deamplification. In this section we consider other operation regimes[3]. Four operation regimes were possible for our OPAs; they could be operated to amplify or deamplify the seed field, and could be seeded through either the back end of the MgO:LiNbO$_3$ crystal or through the output coupling mirror. We analyse the coherent amplitude and noise properties of the fundamental field exiting the output coupler for each of these four regimes.

3.5.1 Classical behaviour of a front seeded optical parametric amplifier

The classical behaviour of a back seeded OPA is discussed in some detail in Section 3.4.1. To perform a comparison between front and back seeded regimes, we must perform the same analysis for a front seeded OPA. Again, for clarity, we assume that the resonator decay rates due to intra-resonator losses and the input coupler are negligible ($\{\gamma_{l,1}, \gamma_{\rm ic,1}\} \ll \gamma_{\rm oc,1} \approx \gamma_1$), and that no pump depletion occurs. The coherent amplitude of the output field from a front seeded OPA is then given by

$$\alpha_{\rm oc,out1}^{\rm ideal,front} = -\alpha_{\rm oc,in1}\left(\frac{1+\alpha_{\rm ic,in2}/|\alpha^{\circ}_{\rm ic,in2}|}{1-\alpha_{\rm ic,in2}/|\alpha^{\circ}_{\rm ic,in2}|}\right), \tag{3.9}$$

where we have again used Eqs. (2.108), (2.144), (2.145), and (3.2), and $|\alpha_{\rm ic,in2}| < |\alpha^{\circ}_{\rm ic,in2}|$. Similarly to the back seeded case, we see that if the pump and seed fields are in phase ($\alpha_{\rm ic,in2}$ real and positive) the OPA acts to amplify the seed; and if they are π out of phase ($\alpha_{\rm ic,in2}$ real and negative) it acts to de-amplifies the seed. In the amplification regime $|\alpha_{\rm oc,out1}^{\rm ideal,front}| \rightarrow \infty$ as $|\alpha_{\rm ic,in2}| \rightarrow |\alpha^{\circ}_{\rm ic,in2}|$, in qualitative agreement with the back seeded case. In the de-amplification regime, however, the deamplification is not clamped, with $|\alpha_{\rm oc,out1}^{\rm ideal,back}| \rightarrow 0$ as $|\alpha_{\rm ic,in2}| \rightarrow |\alpha^{\circ}_{\rm ic,in2}|$.

---

[3] The work presented in this Section was motivated, in part, by detailed discussions with Kirk McKenzie.

So that, in contrast to the back seeded case, the seed field can be perfectly deamplified. Noise entering the OPA through its output coupler can, therefore, in the ideal case be perfectly de-amplified.

Optical parametric amplification is the result of both the non-linear gain of the system; and the impedance matching of the resonator, which is a function of the non-linear decay rate. The impedance matching condition is satisfied when the resonator decay rate due to the input coupler is equal to the sum of all other resonator decay rates. As a consequence the fields reflected directly from, and output coupled through, the input coupler are balanced so that no power is reflected from the resonator. The signature of impedance matching is therefore that the power entering the resonator is completely transmitted and/or absorbed. We see that this signature is apparent for the front seeded OPA in the deamplification regime, and occurs at the threshold for OPO operation (i.e. when $\alpha_{\mathrm{ic,in2}} = |\alpha^{\circ}_{\mathrm{ic,in2}}|$, $\alpha^{\mathrm{ideal,front}}_{\mathrm{oc,out1}} = 0$). Notice that for a conventional linear resonator with $\{\gamma_{l,1}, \gamma_{\mathrm{ic},1}\} \ll \gamma_{\mathrm{oc},1} \approx \gamma_1$ impedance matching is not possible. It is achieved for our OPA due to the non-linear decay rate γ_{II} (see Section 2.10) which, in the deamplification regime increases the decay rate for the fundamental field. The existence of squeezing on the output light field for both front and back seeded OPA operation can be understood simply in terms of this unusual type of impedance matching. Normally, to achieve impedance matching losses must be introduced in the system, these losses couple vacuum fields to the output state that prevent the observation of squeezing. For an OPA, however, the field incident on the output coupler is, ideally, impedance matched and is entirely transmitted through, or absorbed inside, the resonator. In this case, since no additional loss has been introduced to the system no vacuum fields are introduced as a result of the impedance matching of the incident field, so that in theory perfect squeezing of the OPA output field may be achieved.

We can calculate the regenerative gain of a front seeded OPA using Eq. (3.4). For our idealised OPA it is given by

$$G^{\mathrm{ideal}}_{R,\mathrm{front}} = \left| \frac{1 + \alpha_{\mathrm{ic,in2}}/|\alpha^{\circ}_{\mathrm{ic,in2}}|}{1 - \alpha_{\mathrm{ic,in2}}/|\alpha^{\circ}_{\mathrm{ic,in2}}|} \right|^2 . \tag{3.10}$$

A direct comparison of the classical behaviour of the four OPA operation regimes is then possible. Such a comparison is shown in Fig. 3.12. The dot-dashed curves in Fig. 3.12 a) and c) show the regenerative gain of an ideal OPA operating as an amplifier and seeded from the back and front, respectively. We see that in both cases as the pump power approaches the threshold for OPO operation the regenerative gain increases towards infinity. The dot-dashed curves in Fig. 3.12 b) and d) show the same calculations but with the OPA acting to deamplify the seed. In this case as the OPO threshold is approached for the front seeded OPA the regenerative gain approaches zero and therefore the seed can be completely deamplified. On the other hand, as discussed previously, when the OPA is back seeded the deamplification clamps at $G^{\mathrm{ideal}}_{R,\mathrm{back}} = 1/4$. This can be shown to be a direct result of the fact that at the OPO threshold the OPA is impedance matched for a fundamental field incident on the front of the resonator.

In the previous analysis we have assumed an ideal OPA with all input fields being in coherent or vacuum states, and without pump depletion. Of course, in an experimental situation these ideal circumstances cannot always be achieved. The classical behaviour of a non-ideal OPA with our experimental parameters for all four operation regimes is shown by the solid lines in Fig. 3.12. In this case depletion of the pump field restrains the amplification possible so that the output power no longer approaches infinity as the pump power approaches the OPO threshold. Since intra-resonator losses are now present, the impedance matching point for the front seeded deamplification regime now occurs before the threshold for OPO action.

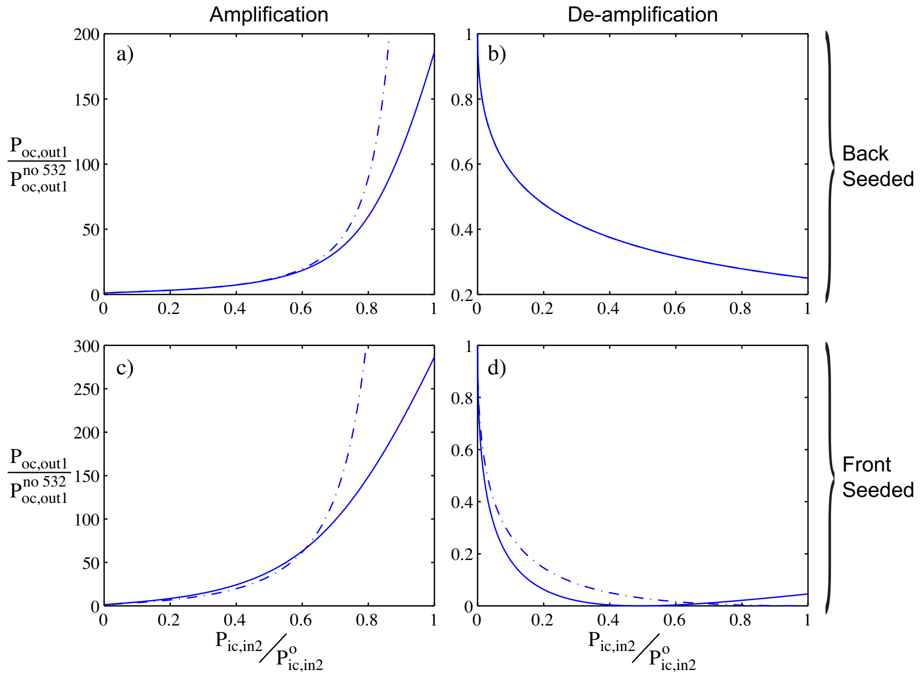

Figure 3.12: Regenerative gain for each optical parametric amplification regime. a) and b) predicted amplification and deamplification respectively of the OPA when seeded from the back with $P_{\rm ic,in1} = 10$ mW. c) and d) predicted amplification and deamplification respectively of the OPA when seeded from the front with $P_{\rm ic,in1} = 0.74$ mW so that the intra-resonator power is the same as in the previous case. The solid curves show the predicted regenerative gain for our experimental parameters, $\epsilon_{\rm ic,1} = 0.0005$, $\epsilon_{\rm oc,1} = 0.04$, $\epsilon_{l,1} = 0.0065$, $\epsilon_2 = 0.94$, $L = 4$ cm, and $\Lambda = 3100\,{\rm s}^{-\frac{1}{2}}$. The dot-dashed curves show the ideal case where the resonator decay rate is dictated solely by the output coupling so that $\epsilon_{\rm ic,1} = \epsilon_{l,1} = 0$.

3.5.2 Noise properties of the output fields

Let us now consider the predicted squeezing from each regime of OPA operation. We saw earlier that, assuming no pump depletion, the predicted squeezing spectra were equivalent for the amplification and de-amplification regimes. We will see here that when pump depletion is included in the analysis this equivalence is broken. The solid curves in Fig. 3.13 show the predicted level of squeezing at $\omega = 0$ calculated from Eq. (3.7), assuming that all input fields are in vacuum or coherent states, and including the effect of pump depletion. Fig. 3.13 a) and c) show the amplitude and phase quadrature variances with the OPA operating in the deamplification regime. In this case energy is being transferred from the seed field to the pump field. Since the seed is much less intense than the pump, the total power in the pump field does not change significantly. We therefore find that pump depletion is an insignificant effect in this regime. On the other hand, in the amplification regime energy is transferred from the pump to the seed. Since the regenerative gain of this process becomes very high at $|\alpha_{\rm ic,in2}| \approx |\alpha^{\rm o}_{\rm ic,in2}|$, the pump field can be significantly depleted. Correspondingly, in this process we find that pump fluctuations can be transferred onto the output fundamental field. As can be seen in Fig. 3.13 b), this effect degrades the level of squeezing observable in the amplification regime at pump powers near threshold.

In an experimental situation, the OPA input fields often carry classical noise, the effect of this noise on the output field is shown by the broken curves in Fig. 3.13. We see that in both amplification and deamplification operation regimes noise entering through the input coupler degrades the squeezing by a level more or less independent of the pump power. The effect of noise entering through the output coupler, however, has a strong dependence on the pump power. At the resonator impedance matching point none of this noise is reflected, and it therefore does not degrade the observed squeezing, but at other pump powers it degrades the squeezing more than the noise entering through the input coupler. Noise coupling into the output from the pump field is, in the deamplification regime, entirely insignificant. In contrast, we see from Fig 3.13 b) that in the amplification regime this noise significantly degrades the level of squeezing on the output field for pump powers higher than $P^{\rm o}_{\rm ic,in2}/5$.

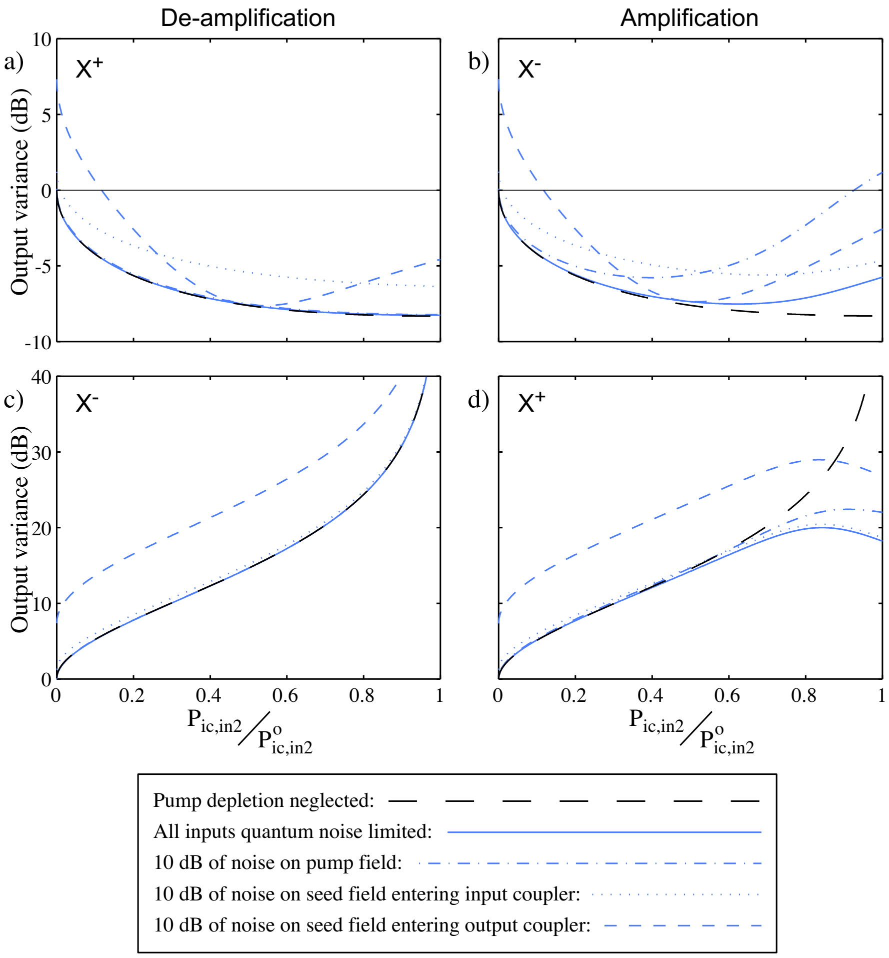

Figure 3.13: Predicted squeezing for each optical parametric amplifier regime as a function of pump power. a) and c) [d) and b)] show the amplitude and phase quadrature variances of the output field at $\omega = 0$ when the OPA is operating in the deamplification [amplification] regime. Calculations of the effect of various noise sources, and of neglecting pump depletion are shown. All calculations were performed for our experimental parameters with $\epsilon_{\rm ic,1} = 0.0005$, $\epsilon_{\rm oc,1} = 0.04$, $\epsilon_{l,1} = 0.0065$, $\epsilon_2 = 0.94$, $L = 4$ cm, $\Lambda = 3100\ {\rm s}^{-\frac{1}{2}}$, and $P_{\rm ic,in1} = 10$ mW.

The predicted behaviour of our OPAs in each of the four possible regimes of operation is summarised in Table 3.2. The four regimes are: amplification and front seeded; amplification and back seeded; deamplification and front seeded; and deamplification and back seeded. We have seen that when the OPA is operating to amplify the seed, noise on the pump field couples significantly into the output state, furthermore from Fig. 3.8 we see that at sideband frequencies $\sim \gamma_1$ when the

OPA is front seeded, noise on the seed field significantly degrades the level of squeezing on the output state. For the majority of this thesis we therefore chose to operate both of our OPAs in the deamplification and back seeded regime. If low frequency squeezing, as investigated in Section 3.7, is desired from a single OPA, however, it could be worth considering operating in the deamplification and front seeded regime. In this case, the resonant relaxation oscillation of the laser could be suppressed by a level equal to the regenerative gain of the OPA.

Amplification regime	Input regime	G_R	Squeezed variance at $\omega = 0$			Squeezed variance at $\omega = \gamma_1/2$		
			coherent or vacua inputs	10 dB noise on seed	10 dB noise on pump	coherent or vacua inputs	10 dB noise on seed	10 dB noise on pump
amp	front	39.1	0.184	0.184	0.276	0.247	0.949	0.333
amp	back	11.2	0.184	0.295	0.276	0.247	0.350	0.333
deamp	front	~ 0	0.174	0.175	0.177	0.239	0.944	0.242
deamp	back	0.34	0.174	0.286	0.177	0.239	0.342	0.242

Table 3.2: An analysis of the four regimes of optical parametric amplification. All calculations were performed at half OPO threshold $P_{\mathrm{ic,in2}} = P^{\circ}_{\mathrm{ic,in2}}/2$. Parameters used: $\epsilon_{\mathrm{ic},1} = 0.0005$, $\epsilon_{\mathrm{oc},1} = 0.04$, $\epsilon_{l,1} = 0.0065$, $\epsilon_2 = 0.94$, $L = 4$ cm, $\Lambda = 3100\ \mathrm{s}^{-\frac{1}{2}}$, and $P_{\mathrm{in1}} = 10$ mW.

3.6 Optical parametric amplifiers as unitary squeezers

One further analysis of the output field from our OPAs is useful to our understanding of their behaviour. Consider again the situation where the decay rates due to loss and the input coupler transmissivity are insignificant compared to the output coupler decay rate ($\gamma_1 \approx \gamma_{\mathrm{oc},1} \gg \{\gamma_{\mathrm{ic},1}, \gamma_{l,1}\}$) and that depletion of the second harmonic pump field is negligible; and further that the frequency of interest is well within the OPA bandwidth $\omega \ll \gamma_1$. The amplitude and phase quadratures of the output field in Eq. (3.7) then reduce to the simple form

$$\hat{X}^{+}_{\mathrm{oc,out1}} = \sqrt{G^{\mathrm{ideal}}_{R,\mathrm{front}}}\,\hat{X}^{+}_{\mathrm{oc,in1}} \tag{3.11}$$

$$\hat{X}^{-}_{\mathrm{oc,out1}} = \frac{1}{\sqrt{G^{\mathrm{ideal}}_{R,\mathrm{front}}}}\hat{X}^{-}_{\mathrm{oc,in1}}, \tag{3.12}$$

where $G^{\mathrm{ideal}}_{R,\mathrm{front}}$ is the front seeded regenerative gain of the OPA given in Eq. (3.10), and we have used Eqs. (2.144) and (3.2). We see that in this ideal case, the OPA operates as a perfect squeezer on the input field $\hat{a}_{\mathrm{oc,in1}}$, with the squeeze factor r (see Eq. (2.15)) directly related to the regenerative gain of the OPA. We saw in Section 2.2 that a squeezed vacuum state has pair-wise photon statistics. In the OPA these pair-wise statistics arise because photons at the second harmonic frequency Ω_2 are transformed into pairs of photons at frequencies $\Omega_1 \pm \omega$. So, the photons in the sideband ω of this idealised OPA output state will always exist in pairs. Any inefficiencies during the detection process, and in output coupling as a result of non-negligible input coupler or loss related decay rates, will reduce some of these photon pairs into individual photons or vacuum and therefore degrade the level of squeezing observed from the OPA.

3.7 Recovery of low frequency squeezing

Before continuing with the main theme of this thesis, I will briefly discuss a technique developed during the course of my PhD that can be used to circumvent noise carried by the laser field, and therefore produce squeezing at low frequencies[27].

3.7.1 Introduction

In almost all experiments to date, and in those presented thus far in this thesis, the squeezing has been observed at frequencies above 1 MHz, at lower frequencies most laser sources are classically noisy. Many interesting spatial and interferometric signals occur in the Hz to kHz regime[95, 96], to accurately study these dynamics squeezing should be available at lower frequencies. Two experiments using pulsed laser light have produced squeezing in the kHz regime[97, 98]. Both experiments ultimately produced a squeezed vacuum state and therefore avoided the classical noise evident on their laser sources. The feasibility of these states in real measurement technology is limited due to both their pulsed nature and their extremely low power. Their pulsed nature severely limits their application to devices that involve resonators or have peak power limitations (e.g. optical damage) such as advanced gravitational wave detectors [96]. The utilisation of squeezed states in measurement technology requires that their phase be accurately controlled. Typically this is achieved using the techniques described in Section 2.5.2, which utilise either the carrier power of the squeezed state, or a bright sideband that has a controlled phase relationship with the squeezed quadrature. Since squeezed vacuum states arise from vacuum noise, neither of these techniques is usually available. Active control of the phase of squeezed vacuum states is therefore generally very difficult to achieve[62].

In this Section we describe a experimental technique that allows the production of a squeezed vacuum exhibiting squeezing in the kHz regime[27]. This technique allowed the production of bright sidebands on the squeezed vacuum. These sidebands acted as a phase reference that allowed the phase of the vacuum to be stably locked in a downstream homodyne detector. Squeezed state enhancement of an interferometer configuration compatible with current gravitational wave detectors has recently been demonstrated[99]. This work was performed in the MHz regime, however, and therefore cannot be directly applied to existing gravitational wave detectors. In reality squeezing will not be useful for gravitational wave detection until it reaches frequencies around 10 kHz, the work presented here produced a squeezed vacuum at frequencies as low as 210 kHz, an order of magnitude lower than was achievable without using the technique. It therefore represents a significant step in the right direction. Since the squeezed field had a wavelength of 1064 nm it is directly compatible with present day gravitational wave detection systems. The frequency of our squeezing was limited from below by noise introduced inside the OPAs. A simple extension of this technique is possible that should eliminate these technical issues and produce squeezing at much lower frequencies.

3.7.2 Theoretical Background

Noise cancellation schemes have been proposed to enhance squeezing utilising Kerr non-linearity in fibers [100] and second harmonic generation [101]. The scheme presented here is similar to that of [100] but uses optical parametric processes. A single optical field at 1064 nm was split on a 50/50 beam splitter and used to seed our pair of OPAs, which were locked to deamplify the seed and therefore produced amplitude squeezed output fields. These output fields were then recombined in phase on another 50/50 beam splitter as shown in Fig. 3.14. Since second harmonic pump depletion is not relevant when our OPAs are locked to deamplification, we neglect it here

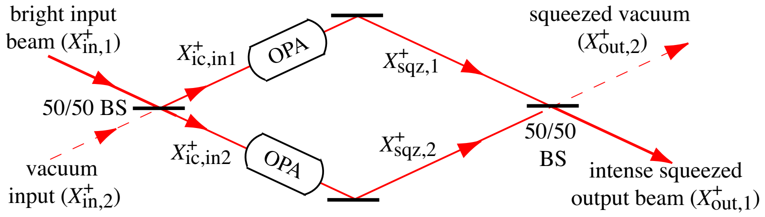

Figure 3.14: Squeezed vacuum production via classical noise cancellation using two OPAs.

for simplicity. From Eq. (3.6) we find that the frequency domain amplitude quadrature operators for the fields exiting our two OPAs $\hat{X}^+_{\rm sqz,\mathit{j}}$ are given by

$$\hat{X}^+_{\rm sqz,\mathit{j}} = \hat{X}^+_{\rm oc,in,\mathit{j}}\left(1-\frac{2\gamma_{\rm oc}}{i\omega+\Upsilon^++\gamma}\right)-\frac{\sqrt{2\gamma_{\rm oc}}}{i\omega+\Upsilon^++\gamma}\left(\sqrt{2\gamma_{\rm ic}}\hat{X}^+_{\rm ic,in\mathit{j}}+\sqrt{2\gamma_l}\hat{X}^+_{l,j}\right), \quad (3.13)$$

where since all of the fields involved are now at the fundamental frequency we have omitted the subscript ‘1’, and now use the subscripts $j \in \{1,2\}$ to distinguish the fields related to each of the OPAs (see Fig. 3.14).

The amplitude quadrature operators for the output fields of a 50/50 beam splitter with one intense $\hat{X}^+_{in,1}$ and one vacuum $\hat{X}^+_{\rm in,2}$ input field can be expressed as $\hat{X}^+_{\rm ic,1} = (\hat{X}^+_{\rm in,1}+\hat{X}^+_{\rm in,2})/\sqrt{2}$ and $\hat{X}^+_{\rm ic,2} = (\hat{X}^+_{\rm in,1}-\hat{X}^+_{\rm in,2})/\sqrt{2}$ (see Section 2.5). Substituting these expressions as the seed fields in Eqs. (3.13) we obtain

$$\hat{X}^+_{\rm sqz,\mathit{j}} = \hat{X}^+_{\rm oc,\mathit{j}}\left(1-\frac{2\gamma_{\rm oc}}{i\omega+\Upsilon^++\gamma}\right)-\frac{\sqrt{2\gamma_{\rm oc}}}{i\omega+\Upsilon^++\gamma}\left(\sqrt{\gamma_{\rm ic}}\left(\hat{X}^+_{\rm in,1}-(\text{-}1)^j\hat{X}^+_{\rm in,2}\right)+\sqrt{2\gamma_l}\hat{X}^+_{l,j}\right). \quad (3.14)$$

The interference of these two fields, each output from one of our OPAs, in phase on a 50/50 beam splitter yields an intense squeezed beam, and a squeezed vacuum, which have amplitude quadrature operators $\hat{X}^+_{\rm out,1}$ and $\hat{X}^+_{\rm out,2}$ respectively, given by

$$\begin{aligned}\hat{X}^+_{\rm out,\mathit{j}} &= \frac{1}{\sqrt{2}}\left(1-\frac{2\gamma_{\rm oc}}{i\omega+\Upsilon^++\gamma}\right)\left(\hat{X}^+_{\rm oc,1}-(\text{-}1)^j\hat{X}^+_{\rm oc,2}\right)\\ &\quad -\frac{\sqrt{\gamma_{\rm oc}}}{i\omega+\Upsilon^++\gamma}\left(2\sqrt{\gamma_{\rm ic}}\hat{X}^+_{\rm in,\mathit{j}}+\sqrt{2\gamma_l}(\hat{X}^+_{l,1}-(\text{-}1)^j\hat{X}^+_{l,2})\right). \quad (3.15)\end{aligned}$$

Note that interfering the beams with a $\pi/2$ phase shift would have produced an Einstein-Podolsky-Rosen entangled pair [102], a detailed analysis of this process is provided in the following Chapter. Assuming that the fields entering through the output coupler and through loss are in vacuum states we obtain the amplitude quadrature variances of the output beams $\Delta^2\hat{X}^+_{\rm out,\mathit{j}}$

$$\Delta^2\hat{X}^+_{\rm out,\mathit{j}} = \frac{4\gamma_{\rm oc}(\gamma_{\rm ic}\Delta^2\hat{X}^+_{\rm in,\mathit{j}}+\gamma_l)+\omega^2+(2\gamma_{\rm oc}-\Upsilon^+-\gamma)^2}{\omega^2+(\Upsilon^++\gamma)^2} \quad (3.16)$$

These spectral noise distributions are identical to those that would be produced from two independent OPAs, one seeded with the intense input beam ($\hat{X}^+_{\rm in,1}$), and the other with the vacuum field entering at the first beam splitter ($\hat{X}^+_{\rm in,2}$) (c.f. Eqs. (3.13)). Unlike the case for a single vacuum seeded OPA [62] however, the resonance frequency of each OPA can be conveniently locked to the frequency of the seed beam and the vacuum squeezed output can be produced with bright sidebands far outside the frequency range for squeezing. These sidebands are produced by applying anti-correlated phase modulation to the intra-resonator fields of the OPAs, and allow the quadrature of the squeezed vacuum to be locked in downstream applications.

In theory none of the laser noise is carried through onto $\Delta^2\hat{X}^+_{\mathrm{out},2}$. In reality however, the two OPAs will not have identical non-linearity, bandwidth, or consequently de-amplification. This will cause classical noise from the intense input beam to couple into the vacuum output. By varying the input beam splitter ratio it is possible to completely compensate for these differences over some frequency range. In our experiment we balanced the intensity of the seed beams such that the intensity of the (ideally) squeezed vacuum output of the system ($\hat{X}^+_{\mathrm{out},2}$) was minimised. This suppressed the classical noise from the seed beam ($\hat{X}^+_{\mathrm{in},1}$) at $\omega = 0$. Since Eqs. (3.15) are slowly varying with ω while $\omega \ll \gamma + \Upsilon^+$ the classical noise was also suppressed throughout this frequency range. The suppression is only limited by inefficiencies in the mode-matching between the OPA output beams.

3.7.3 Experiment

To experimentally generate a locked squeezed vacuum, we locked our pair of OPAs to de-amplify their respective seed beams and therefore produced amplitude squeezed output fields. As shown in Fig. 3.9, a fundamental field was split on a polarising beam splitter, with each beam splitter output field used to seed one of the OPAs. This process coupled a vacuum field into the system, which was ultimately the field on which low frequency squeezing was produced. The seed power to the OPAs was adjusted so that the OPA output fields were of equal intensity. We combined these output fields on a 50/50 beam splitter as shown in Fig. 3.14 and observed a visibility between them of 98.6 %. Detecting one output of this second beam splitter, and utilising the sideband locking technique described in Section 2.5.2, we were able to lock the relative phase of the input beams producing either an intense (1.2 mW), or a weak (0.9 μW) squeezed beam at the other output. This beam was analysed in a homodyne detector that was locked so that the phase modulation from the OPAs was not observed. Since the OPA outputs were amplitude squeezed, this setup naturally provided a measurement of the maximally squeezed quadrature independent of the relative phase of the squeezed beams incident on the 50/50 beam splitter. A homodyne visibility of 96 % was observed for the intense squeezed beam. The majority of the power of the weak squeezed beam came from the residual non-mode-matched part of the input beams and had a non-Gaussian transverse modeshape; consequently, the homodyne visibility observed for this beam was only 28 %. The squeezed vacuum, however, arose from the mode-matched part of this beam and therefore had the same homodyne visibility as the intense squeezed beam. The low visibility of the residual power caused the classical noise that it carried to be poorly detected. This effect and the 50/50 beam splitter visibility together led to a predicted optical suppression of approximately 29 dB. The classical noise from the homodyne local oscillator was electronically suppressed by 64 dB and was insignificant for our measurements.

Fig. 3.15 shows the observed squeezing traces for intense and vacuum squeezed beams. Both the OPA resonators and the homodyne detector were phase locked. The intense squeezed beam was degraded by the resonant relaxation oscillation of the laser and squeezing was only observed above 1.9 MHz. The squeezed vacuum however was observed to be squeezed from 220 kHz to the end of our measurement range at 2.1 MHz, excluding frequencies between 640 kHz and 870 kHz where our optical suppression was not high enough to suppress the laser relaxation oscillation. The signal at 810 kHz was the beat between the SHG and OPA locking frequencies. The low frequency degradation observed in our squeezed vacuum was caused by uncorrelated acoustic and locking

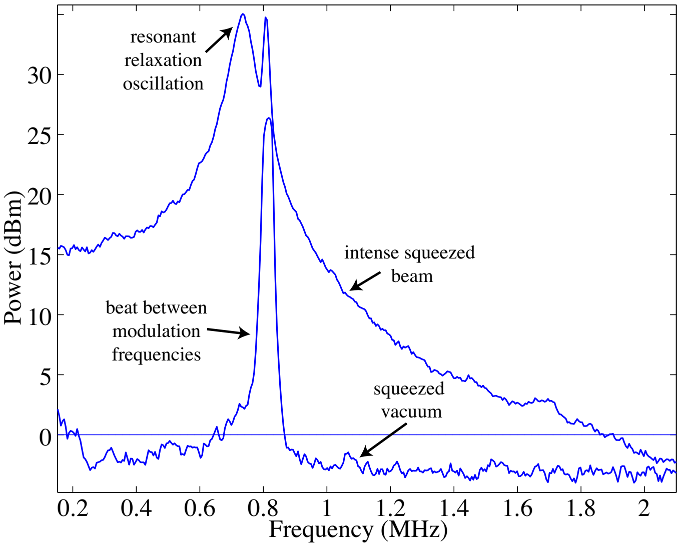

Figure 3.15: Squeezing observed on the intense squeezed output (upper trace) and on the squeezed vacuum output (lower trace).

noise introduced within the OPAs. Further improvement to the squeezing spectra could only be achieved by either reducing this noise, or by classically correlating it. Employing a ring OPA as shown in Fig. 3.16 accomplishes the second of these alternatives. A squeezed output is produced by each of the two directional modes in the OPA. In this configuration the noise introduced in the resonator is common mode and cancels on the vacuum output of a 50/50 beam splitter.

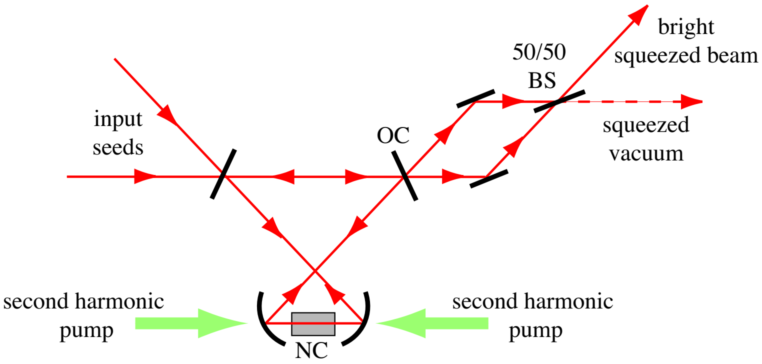

Figure 3.16: Proposed scheme to cancel classical noise. OC: output coupler, BS: beam splitter, NC: nonlinear crystal.

To summarise, this Section discussed the production of a locked continuous wave squeezed vacuum at 1064 nm using a pair of OPAs inside a Mach-Zehnder interferometer. By phase modulating the OPAs we produced phase sidebands that act as a phase reference allowing the quadrature of the squeezing to be locked in downstream applications. We used these sidebands to lock a homodyne detector and measured stably locked vacuum squeezing down to 220 kHz. In an extension of this work, an alternative OPA configuration could be developed that should allow the production of vacuum squeezing at significantly lower frequencies. Furthermore, our noise cancellation technique is compatible with existing techniques such as spectrally filtering the OPA seeds in a high finesse mode cleaner, or using a servo controlled laser intensity noise eater.

3.8 Summary

This Chapter detailed the experimental configuration used to generate the squeezed states used throughout the work present in this thesis. We described the process of second harmonic generation, and performed a detailed analysis of both the coherent amplitude and fluctuations of the output field from an optical parametric amplifier. We demonstrated that for our OPA configuration, the optimum squeezing is produced in the deamplification regime with the OPA seeded from the back. We experimentally generated and characterised squeezed states using a pair of MgO:$LiNbO_3$ based optical parametric amplifiers, observing as much as 4.5 dB of squeezing relative to the vacuum noise level. The frequency spectra over which this squeezing was observed was limited from below by our laser resonant relation oscillation which peaked at 750 kHz. Combining the two squeezed beams in phase on a 50/50 beam splitter eliminated this noise on the dim output field, and squeezing was then observed down to frequencies as low as 210 kHz.

Part II

Quantum communication protocols

Overview

Since the birth of quantum mechanics at the beginning of the twentieth century, it has revolutionised not only the way that scientists and philosophers view the universe, but also the technology utilised in our day-to-day lives. Over the last two decades a new field has emerged from quantum mechanics - the field of *quantum information science*. This field has been fuelled by the realisation that some tasks in information science can be solved faster using quantum computation techniques, than they could be in a conventional computer. The first indication that this was the case came from David Deutsch [103] in 1985. His results can be described in terms of a coin toss, where the coin used is either fair with a head on one side and a tail on the other, or phony with the same image on both sides. To determine whether the coin is fair or phony a conventional computer requires a minimum of two operations, whereas a quantum computer requires only one. Of course, a speed enhancement of a factor of two is in practise insignificant, given the extreme complexity of quantum computers. In 1994, however, Peter Shor made a remarkable discovery. He showed that a quantum computer has the power to solve a NP (non-polynomial) problem in conventional information science in polynomial time [7]. Shors algorithm factorised semi-prime numbers. It has serious implications to present-day cryptographic schemes which rely on the extremely long time required to factorise large semi-prime numbers in conventional computers; and also demonstrated the significance of quantum mechanics to information science.

Experiments then began to demonstrate information protocols in quantum mechanical regimes [5]. The vast majority of these protocols are facilitated by *entanglement*, one of the quintessential properties of quantum mechanics. Entanglement was first discussed by Einstein [16] and Schrödinger [104] in 1935, and implications of its existence have intrigued philosophers and scientists alike for almost a century. In Chapter 4 we generate and characterise entanglement between the amplitude and phase quadratures of a pair of optical fields[30, 31, 105]. This entanglement is directly analogous to that originally discussed by Einstein[16] and Schrödinger[104]. We use our entanglement to perform a demonstration of the EPR paradox, which caused Einstein to describe entanglement by 'spooky interactions at a distance'. The efficacy of quantum information protocols utilising entanglement depends strongly on the specific properties of the entangled state utilised. We fully characterise our entangled state, and introduce a new characterisation technique, the *photon number diagram*.

One of the primary goals of the present day quantum optics community is to produce a large scale quantum computer[10]. By utilising Shors protocol [7] and other similar protocols (see for example [8, 106]) these computers are expected to significantly enhance the speed at which some computing problems can be solved. To date, experimental realisations of such computers have been restricted to proof-of-principle demonstrations [5]. An outstanding issue in quantum computation is whether the resources required to scale these demonstrations up to useful sizes scale linearly or exponentially with the size of the computer. Recently, Knill, Laflamme, and Milburn [17] showed that in a discrete variable quantum computer, *quantum teleportation* within the quantum gates that make up the computer can allow linear resource scaling. Furthermore, quantum teleportation can be used as a quantum data-bus, transferring data from one part of a quantum computer to another, or indeed between the nodes of a network of quantum computers [9, 10, 107, 108, 109, 110]. Quantum teleportation, which relies on entanglement, can be described as the transfer of quantum states through classical channels, and is the subject of Chapter 5 of this thesis. Therein, we demonstrate continuous variable quantum teleportation of the sideband amplitude and phase quadratures of an optical field[32, 111].

The possible realisation of quantum computers with the potential to break present-day cryptography techniques necessitates the investigation of alternative cryptography techniques that do not rely on semi-prime number encoding. One such technique, quantum cryptography[112], relies on the laws of quantum mechanics to guarantee the security of the transmission. In Chapter 6 we investigate a hierarchical quantum cryptography scheme, *quantum secret sharing* [113]. This scheme allows an encoded secret quantum state to be distributed to a set of players each of whom cannot be fully trusted. To recover the secret state a subset of the players must collaborate. In the advent that the secret state appears partially lost due to malicious players or faulty communication channels, the secret can, in the ideal case, still be perfectly recovered. We propose an experimentally viable scheme to perform continuous variable quantum secret sharing using the entanglement produced in Chapter 4.

Chapter 4

Generation and characterisation of quadrature entanglement

Entanglement is one of the defining features of quantum mechanics, with Einstein describing it as 'spooky interactions at a distance'. With the recent advent of quantum information science many potential applications of entanglement have been discovered. In this Chapter we experimentally generate a quadrature entangled state using the pair of squeezed beams produced in Chapter 3. Each of the potential applications of entanglement require that the entanglement is well characterised. We characterise the correlation matrix of our entangled state within a set of reasonable assumptions, and the strength of the entanglement is gauged based on the inseparability of the state and the EPR paradox. Introducing controlled decoherence to the state caused qualitative differences between these two methods of gauging the entanglement. We introduce a new intuitive and physically relevant representation of quadrature entanglement in terms of sideband photon numbers. Our entanglement can then be represented on a three dimensional photon number diagram. The efficacy of quantum information protocols can be directly displayed as contours on this diagram.

The work presented in this Chapter has been published in the journal articles:

- W. P. Bowen, R. Schnabel, P. K. Lam, and T. C. Ralph. *An experimental investigation of criteria for continuous variable entanglement.* Physical Review Letters **90**, 043601 (2003).
- W. P. Bowen, P. K. Lam, T. C. Ralph. *Biased EPR entanglement and its application to teleportation.* Journal of Modern Optics **50**, pp. 801, (2003).
- W. P. Bowen, R. Schnabel, P. K. Lam, and T. C. Ralph. *A characterization of continuous variable entanglement.* Physical Review A **69**, 012304 (2004).

4.1 Introduction

Entanglement is one of the most intriguing features of quantum mechanics. It was first discussed by Einstein, Podolsky, and Rosen in 1935 [16] who used the concept to propose that either quantum mechanics was incomplete or local realism was false. Shortly thereafter, Schrödinger coined the term 'entanglement', and an intense investigation of this counter-intuitive phenomena began. The first experimental evidence for entanglement came from an experiment by Bleuler and Bradt in 1948 [114] who examined the fields emitted from a positron annihilation. A conclusive test of the non-local behaviour of entanglement would wait, however, until in 1964 Bell proposed his famous inequality distinguishing local hidden variable models from the quantum mechanical model [66].

Shortly thereafter, Kasday *et al.*[67] demonstrated that positron decay violated Bells inequality, and in doing so verified the quantum mechanical model. Verifications of the quantum mechanical model were then performed in various other systems [115, 116, 117, 118], with perhaps the most rigorous test reported in a series of articles by Aspect *et al.* [119, 120, 121], who utilised polarisation entangled photon pairs. Until recently the study of entanglement was based purely on our desire to more fully understand the physical world. Entanglement has now been shown to be an enabling technology in quantum information protocols such as quantum teleportation [122], dense coding [123, 124] and quantum computation [10], which has stimulated further investigation into its properties. Through an intense scientific and engineering effort optical fields have proved to be an exquisite medium for entanglement[125, 102, 126, 127, 128, 129, 105, 31]. Optical field entanglement has been studied both in the discrete variable regime where correlations are observed between pairs of photons[125], and in the continuous variable regime where the correlations are between field quadratures[31, 102, 105, 126, 127, 128, 129]. This Chapter describes the methods we used to generate and characterise Gaussian continuous variable entanglement between the amplitude and phase quadratures of a pair of light beams[31, 105]; henceforth termed *quadrature entanglement*. The signature of this type of entanglement is strong correlations between the amplitude and phase quadratures of a pair of beams.

This Chapter focusses particularly on techniques that can be used to accurately and completely characterise the entanglement. This is of particular relevance since quantum information protocols vary in their requirements for a good entangled state, so that the specific properties of the entangled state utilised play a highly significant role in the success of the protocol. It is well known that Gaussian entanglement can be fully characterised by the coherent amplitudes of the entangled beams and a matrix containing the correlations between each of the variables of interest (in our case the amplitude and phase quadratures of both entangled beams), termed the *correlation matrix*. To our knowledge all previous of experiments on continuous variable entanglement [102, 126, 127, 128, 129] have not performed this characterisation. Although the coherent amplitudes of the entangled beams and the correlation matrix together provide a complete characterisation of quadrature entanglement, they do not directly yield a measure for the strength of the entanglement. In past experiments the strength of an entangled resource has been characterised in the spirit of either the Schrödinger [105, 127, 128, 129] or Heisenberg pictures [102, 105, 126, 127], and the characterisations lead to qualitatively different results. In the Schrödinger picture, a necessary and sufficient criterion for the entanglement of a pair of sub-systems is that the state describing the entire system is *inseparable*. That is, it is not possible to factor the wavefunction of the entire system into a product of separate contributions from each sub-system. Given that an observable signature of the mathematical criterion for wave-function entanglement can be identified, one can define the *degree of inseparability* for the state, and use it to characterise the strength of the entanglement. In the Heisenberg picture, a sufficient criterion for entanglement is that correlations between conjugate observables of two sub-systems allow the statistical inference of either observable in one sub-system, upon a measurement in the other, to be smaller than the standard quantum limit. That is, the presence of non-classical correlations. This approach was originally proposed by Einstein, Podolsky and Rosen [16] and has since been termed the *EPR paradox*. Similarly to the Schrödinger picture we can define the *degree of EPR paradox* for a given entangled state, and use it to characterise the strength of the entanglement. For pure states the Schrödinger and Heisenberg approaches return qualitatively equivalent results suggesting consistency of the two methods. However, when decoherence is present, causing the state to become impure, differences can occur. For quadrature entanglement wave-function inseparability may be identified using the *inseparability criterion* proposed by Duan *et al.* [130] (see also [131, 132, 133]). We use this criterion to define the degree of inseparability of our entanglement. To define the degree of EPR paradox we use the criterion for demonstration of the EPR paradox as quantified by Reid and Drummond [134, 135], and refer to this as the *EPR paradox criterion*. By introducing decoherence in the form of optical loss to both of our entangled beams we observe qualitative differences between the degree of inseparability and the degree of EPR paradox.

Finally, we characterise our entanglement in terms of mean sideband photon numbers [105]. We find that the mean number of photons per bandwidth per time in the sidebands of an entangled state can be broken into four categories: the mean number of photons required to maintain the entanglement, to produce any bias that exists between the amplitude and phase quadratures of the beams, to produce the impurity of the state, and to produce any impurity bias between the amplitude and phase quadratures. For our entanglement, these four mean photon numbers provide an equivalent but perhaps more intuitive characterisation to the correlation matrix. We attach less significance to the mean photon numbers resulting from impurity than those required to maintain and bias the entanglement, and sum them to give the total mean photon number per bandwidth per time due to impurity. Our entanglement could then be represented on a three dimensional photon number diagram. On a plane of this diagram, we directly assess the level of success achievable for quantum teleportation, demonstration of the EPR paradox, and high and low photon number dense coding when utilising our entanglement. The photon number diagram can also be used to assess the effect of techniques such as distillation[136, 137, 138] and purification[139, 140, 141], that can be used to improve the quality of an entangled state. As an example we analyse a simple feedforward scheme to reduce the number of photons in an entangled state as a result of impurity, whilst maintaining the entanglement strength. We show that this technique can improve the channel capacity of dense coding protocols.

4.2 Production of continuous variable entanglement

Several techniques may be used to generate quadrature entanglement. It was first generated by Ou *et al.* in 1992 [102, 126] using a non-degenerate optical parametric amplifier, and more recently using the Kerr non-linearity in fibers [127], and interfering the outputs of two below threshold optical parametric amplifiers [93, 105, 129]. Ultimately all of these techniques yield Gaussian continuous variable entanglement of a form that can be modelled simply and, as we will see in Section 4.3, quite generally, by combining two quadrature squeezed beams with orthogonal squeezing on a 50/50 beam splitter. Indeed, it is this technique that we adopted to experimentally generate quadrature entanglement. In general, the two beam splitter outputs $\tilde{a}_x(t)$ and $\tilde{a}_y(t)$ are of the form

$$\tilde{a}_x(t) = \frac{e^{i\phi_x}}{\sqrt{2}}\left(\tilde{a}_{\rm sqz,1}(t) + e^{i\theta}\tilde{a}_{\rm sqz,2}(t)\right) \tag{4.1}$$

$$\tilde{a}_y(t) = \frac{e^{i\phi_y}}{\sqrt{2}}\left(\tilde{a}_{\rm sqz,1}(t) - e^{i\theta}\tilde{a}_{\rm sqz,2}(t)\right), \tag{4.2}$$

where $\tilde{a}_{\rm sqz,1}(t)$ and $\tilde{a}_{\rm sqz,2}(t)$ are the annihilation operators of the input squeezed beams, θ defines the relative phase between them, ϕ_x and ϕ_y are phase shifts that rotate the operators such that $\alpha_x(t)$ and $\alpha_y(t)$ are real, and throughout the remainder of this thesis the sub-scripts x and y denote the beams being interrogated for entanglement. To avoid frequency dependent noise sources present on our optical fields we examine our entangled states henceforth in the frequency domain. Throughout this thesis we have take the time domain coherent amplitude of the our optical fields to be real, but this property does not carry over to the frequency domain. We denote the real and imaginary parts of the frequency domain coherent amplitude respectively as $\alpha^+ = \Re\{\alpha(\omega)\} = \langle \hat{X}^+ \rangle/2$ and $\alpha^- = \Im\{\alpha(\omega)\} = \langle \hat{X}^- \rangle/2$. We take the input beams to be amplitude squeezed states ($\Delta^2 \hat{X}^+_{\mathrm{sqz},1} < 1$ and $\Delta^2 \hat{X}^+_{\mathrm{sqz},2} < 1$) with equal intensities ($\alpha_{\mathrm{sqz},1}(t) = \alpha_{\mathrm{sqz},2}(t)$), and set $\theta = \pi/2$ so that the squeezed quadratures are orthogonal at the beam splitter. The frequency domain amplitude and phase quadratures of the output beams x and y can then be expressed as

$$\hat{X}^{\pm}_x = \frac{1}{2}\left(\pm\hat{X}^+_{\mathrm{sqz},1} + \hat{X}^+_{\mathrm{sqz},2} + \hat{X}^-_{\mathrm{sqz},1} \mp \hat{X}^-_{\mathrm{sqz},2}\right) \tag{4.3}$$

$$\hat{X}^{\pm}_y = \frac{1}{2}\left(\hat{X}^+_{\mathrm{sqz},1} \pm \hat{X}^+_{\mathrm{sqz},2} \mp \hat{X}^-_{\mathrm{sqz},1} + \hat{X}^-_{\mathrm{sqz},2}\right). \tag{4.4}$$

We see that as the squeezing of the input beams approaches perfect ($\{\Delta^2\hat{X}^+_{\mathrm{sqz},1}, \Delta^2\hat{X}^+_{\mathrm{sqz},2}\} \to 0$) the quadrature noise operators of beams x and y approach

$$\delta\hat{X}^{\pm}_x \to \frac{1}{2}\left(\delta\hat{X}^-_{\mathrm{sqz},1} \mp \delta\hat{X}^-_{\mathrm{sqz},2}\right) \tag{4.5}$$

$$\delta\hat{X}^{\pm}_y \to \mp\frac{1}{2}\left(\delta\hat{X}^-_{\mathrm{sqz},1} \mp \delta\hat{X}^-_{\mathrm{sqz},2}\right), \tag{4.6}$$

so that

$$\left\langle\left(\delta\hat{X}^+_x + \delta\hat{X}^+_y\right)^2\right\rangle \to 0 \tag{4.7}$$

$$\left\langle\left(\delta\hat{X}^-_x - \delta\hat{X}^-_y\right)^2\right\rangle \to 0. \tag{4.8}$$

Therefore in this limit an amplitude quadrature measurement on beam x would provide an exact prediction of the amplitude quadrature of beam y; and similarly a phase quadrature measurement on beam x would provide an exact prediction of the phase quadrature of beam y. This is a demonstration of the EPR paradox in exactly the manner proposed in the seminal paper of Einstein *et al.* [16]. Analysis of the entanglement in the physically realistic regime where $\{\Delta^2\hat{X}^+_{\mathrm{sqz},1}, \Delta^2\hat{X}^+_{\mathrm{sqz},2}\} \neq 0$ is more complex, and is the topic of the following Section.

4.3 Characterisation of continuous variable entanglement

Characterisation of continuous variable entanglement is, in many ways, a more complex enterprise than its discrete variable counterpart. Discrete variable entanglement can be fully characterised by a density matrix of finite dimension (usually 4×4). In contrast, complete characterisation of continuous variable entanglement requires a density matrix of infinite size. This problem has received considerable interest in the quantum optics community with, as of now, no consensus on the most appropriate characterisation method (see for example [130, 131, 132, 133, 134, 135, 141, 142, 143]). However, experimental realisations of continuous variable entanglement have, to date, been limited to a sub-class of states - those with Gaussian statistics - for which well defined characterisation techniques do exist. In this Section we introduce the characterisation techniques used for our entanglement, and discuss a new interpretation separating the mean number of photons per bandwidth per time in the entangled state into components required to maintain and bias the entangled state, and to produce and bias the impurity present in the state [30, 105].

4.3.1 Gaussian entanglement and the correlation matrix

Any Gaussian continuous variable bi-partite state can be fully characterised by its amplitude and phase quadrature coherent amplitudes $\alpha_x^\pm$, $\alpha_y^\pm$, and the correlation (or covariance) matrix[69]. In general $\alpha_x^\pm$ and $\alpha_y^\pm$ are easily characterised, and do not contribute to the strength of entanglement exhibited by the state. In our experiment the entangled state was produced from two squeezed vacuum states[1], so that the amplitude and phase quadrature coherent amplitudes of beams x and y were all zero, $\alpha_x^\pm = \alpha_y^\pm = 0$. We will therefore focus on the correlation matrix here. The correlation matrix CM is given by

$$CM = \begin{pmatrix} C_{xx}^{++} & C_{xx}^{+-} & C_{xy}^{++} & C_{xy}^{+-} \\ C_{xx}^{-+} & C_{xx}^{--} & C_{xy}^{-+} & C_{xy}^{--} \\ C_{yx}^{++} & C_{yx}^{+-} & C_{yy}^{++} & C_{yy}^{+-} \\ C_{yx}^{-+} & C_{yx}^{--} & C_{yy}^{-+} & C_{yy}^{--} \end{pmatrix}. \tag{4.9}$$

Each term in this matrix is the correlation co-efficient between two of the variables $\hat{X}_x^+$, $\hat{X}_x^-$, $\hat{X}_y^+$, and $\hat{X}_y^-$; defined as

$$\begin{aligned} C_{mn}^{kl} &= \frac{1}{2}\left\langle \hat{X}_m^k \hat{X}_n^l + X_n^l \hat{X}_m^k \right\rangle - \left\langle \hat{X}_m^k \right\rangle \left\langle \hat{X}_n^l \right\rangle && (4.10) \\ &= \frac{1}{2}\left\langle \delta\hat{X}_m^k \delta\hat{X}_n^l + \delta\hat{X}_n^l \delta\hat{X}_m^k \right\rangle, && (4.11) \end{aligned}$$

with $\{k, l\} \in \{+, -\}$, $\{m, n\} \in \{x, y\}$. The symmetry in the form of C_{mn}^{kl} dictates that in general $C_{mn}^{kl} = C_{nm}^{lk}$. The correlation matrix is therefore fully specified by ten independent co-efficients.

The entangled beams analysed here and utilised in the following Chapters were generated in a symmetric manner by interfering two amplitude squeezed beams with $\pi/2$ phase shift on a 50/50 beam splitter (as discussed in the previous Section), and encountered identical loss before detection. Furthermore, the squeezed beams themselves were produced in an identical manner in identical OPAs, with no cross quadrature correlations present either within each beam individually or between the beams. When applied to Eqs. (4.3) and (4.4) these symmetries dictate that the amplitude (phase) quadrature variances of beams x and y are equal, $\Delta^2\hat{X}^\pm = \Delta^2\hat{X}_x^\pm = \Delta^2\hat{X}_y^\pm$, so that $C_{mm}^{\pm\pm} = \Delta^2\hat{X}^\pm$; and that the beams exhibit no cross-quadrature correlations. That is, that $C_{mn}^{\pm\mp} = 0$. The correlation matrix is then given by

$$CM = \begin{pmatrix} C_{xx}^{++} & 0 & C_{xy}^{++} & 0 \\ 0 & C_{xx}^{--} & 0 & C_{xy}^{--} \\ C_{xy}^{++} & 0 & C_{xx}^{++} & 0 \\ 0 & C_{xy}^{--} & 0 & C_{xx}^{--} \end{pmatrix}, \tag{4.12}$$

where complete specification now only requires characterisation of $\Delta^2!\hat{X}^+$, $\Delta^2\hat{X}^-$, $\langle\delta\hat{X}_x^+\delta\hat{X}_y^+ + \delta\hat{X}_y^+\delta\hat{X}_x^+\rangle$, and $\langle\delta\hat{X}_x^-\delta\hat{X}_y^- + \delta\hat{X}_y^-\delta\hat{X}_x^-\rangle$. Specification of these four parameters is equivalent to characterisation of the variance of the squeezed and anti-squeezed quadratures of the pair of squeezed beams produced by re-combining the entangled beams losslessly and in-phase on a 50/50 beam splitter.

---

[1] From a time domain perspective these states were amplitude squeezed, however since our analysis was performed in the frequency domain, a frequency domain perspective with optical sideband states is more appropriate here. Since no modulation was present at our analysis frequencies, the sideband states were indeed squeezed vacuum.

4.3.2 The inseparability criterion

Specification of the correlation matrix, although it does offer a complete description of the entanglement, does not immediately provide a measure of whether beams x and y are entangled, or how strongly they are entangled. We use two criteria, both of which can be inferred from the correlation matrix, to measure those properties. In this Section we discuss the inseparability criterion recently proposed by Duan *et al.* [130] (see also [131, 132, 133]) which provides a necessary and sufficient condition for Gaussian entanglement; and in the Section following we introduce the EPR paradox criterion proposed by Reid and Drummond [134, 135] which has been used to characterise entanglement in past experiments. It should be noted that strictly speaking, a good measure of entanglement should satisfy the conditions given in [144, 145], and stated explicitly later in this Chapter. Neither the inseparability or EPR criteria have been shown to satisfy these conditions, and indeed, to our knowledge no such measure exists presently for continuous variable entanglement. However, both criteria considered here have strong physical significance, have a straight forward dependance on the strength of the quantum resources used to generate the entanglement, and are commonly used to gauge the strength of entanglement in experiments. Throughout this thesis we, therefore, refer to both criteria as measures of the strength of entanglement.

To derive their criterion, Duan *et. al*[130] showed that through local linear unitary Bogoliubov operations any bi-partite Gaussian state can be transformed so that its correlation matrix has the standard form

$$CM_s = \begin{pmatrix} C_{xx}^{++} & 0 & C_{xy}^{++} & 0 \\ 0 & C_{xx}^{--} & 0 & C_{xy}^{--} \\ C_{xy}^{++} & 0 & C_{yy}^{++} & 0 \\ 0 & C_{xy}^{--} & 0 & C_{yy}^{--} \end{pmatrix}, \tag{4.13}$$

where the values of $C_{nm}^{\pm\pm}$ are restricted by the conditions

$$\frac{C_{xx}^{++} - 1}{C_{yy}^{++} - 1} = \frac{C_{xx}^{--} - 1}{C_{yy}^{--} - 1}, \tag{4.14}$$

and

$$\sqrt{(C_{xx}^{++} - 1)(C_{yy}^{++} - 1)} - |C_{xy}^{++}| = \sqrt{(C_{xx}^{--} - 1)(C_{yy}^{--} - 1)} - |C_{xy}^{--}|. \tag{4.15}$$

Given that the state is in this form, they showed, by identifying separability with positivity of the P-representation[2] of the state, that the inseparability criterion

$$\Delta^2 \hat{X}_I^+ + \Delta^2 \hat{X}_I^- < 2\left(k^2 + \frac{1}{k^2}\right), \tag{4.16}$$

is a necessary and sufficient condition for the presence of entanglement, where $\Delta^2 \hat{X}_I^\pm$ are the measurable correlations

$$\Delta^2 \hat{X}_I^\pm = \left\langle \left(k\delta\hat{X}_x^\pm - \frac{C_{xy}^{\pm\pm}}{|C_{xy}^{\pm\pm}|}\frac{\delta\hat{X}_y^\pm}{k} \right)^2 \right\rangle, \tag{4.17}$$

---

[2] The P-representation is directly related to the Wigner function of Section 2.2.1 by a Gaussian convolution.

and k is a parameter that compensates for bias between sub-systems x and y and is given by

$$k = \left(\frac{C_{yy}^{++} - 1}{C_{xx}^{++} - 1} \right)^{\frac{1}{4}} = \left(\frac{C_{yy}^{--} - 1}{C_{xx}^{--} - 1} \right)^{\frac{1}{4}}. \tag{4.18}$$

In fact, Duan *et. al* showed that if the state under interrogation is separable satisfaction of Criterion (4.16) is impossible for any arbitrary k. From an experimental perspective k can then be thought of as a variable parameter. Satisfaction of the criterion for any k is a sufficient condition for entanglement.

A comparison of the form of the correlation matrix describing our entanglement (Eq. (4.12)) with Duan *et al.*'s standard form (Eqs. (4.13), (4.14), and (4.15)) reveals that, in general, we cannot directly apply the inseparability criterion of Eq. (4.16). Of course, after a complete characterisation of the correlation matrix it can be taken into the standard form, and the inseparability criterion can then be applied. However, we will see in the following analysis that if a product form of the criterion is taken, it becomes valid for a wider range of correlation matrices and indeed is then directly applicable to our entanglement. Let us consider the effect that Restrictions (4.14) and (4.15) have on $\Delta^2\hat{X}_I^{\pm}$. Expanding $\Delta^2\hat{X}_I^{\pm}$ we find

$$\begin{aligned} \Delta^2\hat{X}_I^{\pm} &= k^2\Delta^2X_x^{\pm} + \frac{\Delta^2X_y^{\pm}}{k^2} - 2\frac{C_{xy}^{\pm\pm}}{|C_{xy}^{\pm\pm}|}\left\langle \delta X_x^{\pm}\delta X_y^{\pm} \right\rangle && (4.19) \\ &= \sqrt{\frac{C_{yy}^{\pm\pm} - 1}{C_{xx}^{\pm\pm} - 1}}C_{xx}^{\pm\pm} + \sqrt{\frac{C_{xx}^{\pm\pm} - 1}{C_{yy}^{\pm\pm} - 1}}C_{yy}^{\pm\pm} - 2\left|C_{xy}^{\pm\pm}\right| && (4.20) \\ &= 2\left[\sqrt{\left(C_{xx}^{\pm\pm} - 1\right)\left(C_{yy}^{\pm\pm} - 1\right)} - \left|C_{xy}^{\pm\pm}\right|\right] + \sqrt{\frac{C_{xx}^{\pm\pm} - 1}{C_{yy}^{\pm\pm} - 1}} + \sqrt{\frac{C_{yy}^{\pm\pm} - 1}{C_{xx}^{\pm\pm} - 1}}. && (4.21) \end{aligned}$$

A comparison of Eqs. (4.21) with Restrictions (4.14) and (4.15) reveals that transforming a general bi-partite Gaussian state into the standard form for which the inseparability criteria of Eq. (4.16) is valid equates $\Delta^2\hat{X}_I^{+}$ and $\Delta^2\hat{X}_I^{-}$ ($\Delta^2\hat{X}_I^{+} = \Delta^2\hat{X}_I^{-}$). The inseparability criteria can therefore be equivalently written in the product form

$$\sqrt{\Delta^2\hat{X}_I^{+}\Delta^2\hat{X}_I^{-}} < \left(k^2 + \frac{1}{k^2}\right). \tag{4.22}$$

In this form however, the criterion is insensitive to equal local unitary squeezing operations on beams x and y. We can see this by making the substitutions $\delta\hat{X}_x^{+} = \sqrt{G}\delta\hat{Y}_x^{+}$, $\delta\hat{X}_y^{+} = \sqrt{G}\delta\hat{Y}_y^{+}$, $\delta\hat{X}_x^{-} = \delta\hat{Y}_x^{-}/\sqrt{G}$, and $\delta\hat{X}_y^{-} = \delta\hat{Y}_y^{-}/\sqrt{G}$; where G can be thought of as the gain of a unitary squeezing operation as discussed in Section 3.6, and the state described by the operators $\hat{Y}_x^{\pm}$ and $\hat{Y}_y^{\pm}$ is therefore unitarily related to the original entangled state. We can then see from Eqs. (4.17) that

$$\Delta^2\hat{X}_I^{+}\Delta^2\hat{X}_I^{-} = \Delta^2\hat{Y}_I^{+}\Delta^2\hat{Y}_I^{-}. \tag{4.23}$$

Therefore, if Eq. (4.22) is true for a particular state, then it is identically true for any state achieved by applying equal unitary squeezing operations to the sub-states x and y. This was not the case for the sum criterion of Eq. (4.16), where it was necessary that Restrictions (4.14) and (4.15) forbade such operations. The product form of the inseparability criterion is therefore valid for a wider set of correlations matrices. This can be seen explicitly by substituting $\delta\hat{X}_x^{+} \rightarrow \sqrt{G}\delta\hat{X}_x^{+}$, $\delta\hat{X}_y^{+} \rightarrow \sqrt{G}\delta\hat{X}_y^{+}$, $\delta\hat{X}_x^{-} \rightarrow \delta\hat{X}_x^{-}/\sqrt{G}$, and $\delta\hat{X}_y^{-} \rightarrow \delta\hat{X}_y^{-}/\sqrt{G}$ in Restrictions (4.14) and (4.15).

As we have seen, this has no effect on the product inseparability criterion. The gain G of the unitary squeezing operation can then be arbitrarily chosen so that one of the restrictions is satisfied. Here we choose the gain so that Restriction (4.15) is true. Although the exact solution for the gain can be easily calculated, it is rather complicated and, as we will see later[3], is not required in our case. We therefore omit it here. Choosing the correct gain, the product version of the inseparability criterion only requires the one restriction,

$$C_{yy}^{++}C_{xx}^{--} - C_{xx}^{++}C_{yy}^{--} = G\left(C_{yy}^{++} - C_{xx}^{++}\right) + \left(C_{xx}^{--} - C_{yy}^{--}\right)/G, \tag{4.24}$$

to be valid. This restriction is obtained directly from substitution of $\delta\hat{X}_x^+ \rightarrow \sqrt{G}\delta\hat{X}_x^+$, $\delta\hat{X}_y^+ \rightarrow \sqrt{G}\delta\hat{X}_y^+$, $\delta\hat{X}_x^- \rightarrow \delta\hat{X}_x^-/\sqrt{G}$, and $\delta\hat{X}_y^- \rightarrow \delta\hat{X}_y^-/\sqrt{G}$ in Restriction (4.14). Since for our entanglement $C_{xx}^{++} = C_{yy}^{++}$ and $C_{xx}^{--} = C_{yy}^{--}$ (see Eq. (4.12)), we see that this less stringent restriction is satisfied for arbitrary gain G. The correlation matrix given in Eq. (4.12) describing our entanglement is of the same form as that in Eq. (4.13), therefore the product form of the inseparability criterion is directly valid. To provide a direct measure of the strength of the entanglement we define the *degree of inseparability*

$$\mathcal{I} = \frac{\sqrt{\Delta^2\hat{X}_I^+\Delta^2\hat{X}_I^-}}{k^2 + 1/k^2}, \tag{4.25}$$

normalised such that beams x and y are entangled if $\mathcal{I} < 1$, where it should be noted that k is now given by

$$k = \left(\frac{GC_{yy}^{++} - 1}{GC_{xx}^{++} - 1}\right)^{\frac{1}{4}} = \left(\frac{C_{yy}^{--}/G - 1}{C_{xx}^{--}/G - 1}\right)^{\frac{1}{4}}. \tag{4.26}$$

For entanglement produced as described in Section 4.2 the expression for $\mathcal{I}$ becomes considerably simpler. The entangled beams are produced on a 50/50 beam splitter, furthermore, prior to detection they encounter only linear optics and incur equal loss. There is, therefore, symmetry between the quadratures of beams x and y, so that $C_{xx}^{\pm\pm} = C_{yy}^{\pm\pm}$. In this case we see from Eq. (4.26) that $k = 1$ independent of the gain G. Eq. (4.25) can then be written

$$\mathcal{I} = \sqrt{\Delta^2\hat{X}_{x\pm y}^+\Delta^2\hat{X}_{x\pm y}^-}, \tag{4.27}$$

where $\Delta^2\hat{O}_{x\pm y}$ is the minimum of the variance of the sum or difference of the operator $\hat{O}$ between beams x and y normalised to the two beam quantum noise limit, $\Delta^2\hat{O}_{x\pm y} = \min\langle(\delta\hat{O}_x \pm \delta\hat{O}_y)^2\rangle/2$. This measure of entanglement in terms of the product of sum and difference variances between the beams has been used previously in the literature [146, 147].

We are interested in the effect of decoherence in the form of optical loss on the EPR paradox and inseparability criteria, and the photon number diagram. It can be shown from Eqs. (4.3), (4.4) and (4.27) that for entanglement generated from a pair of uncorrelated squeezed beams as detailed in Section 4.2, and with equal optical loss for beams x and y, $\mathcal{I}$ can be expressed as a function of the overall detection efficiency η as

$$\mathcal{I} = \eta\Delta^2\hat{X}_{\text{sqz,ave}}^+ + (1-\eta), \tag{4.28}$$

---

[3] From the omission of G in Eq. 4.27.

where we define the average of the input beam squeezing as $\Delta^2\hat{X}^{+}_{\rm sqz,ave} = (\Delta^2\hat{X}^{+}_{\rm sqz,1}+\Delta^2\hat{X}^{+}_{\rm sqz,2})/2$. We see that so long as the average squeezing of the two beams used to generate the entanglement is below one ($\Delta^2\hat{X}^{+}_{\rm sqz,ave} < 1$), then $\mathcal{I} < 1$. So beams x and y are entangled for any level of input squeezing. Notice that even as η approaches zero, for any level of squeezing $\mathcal{I}$ remains below unity. We see that the entanglement is robust against losses at least in the sense that loss alone cannot transform an inseparable state to a separable one.

4.3.3 The EPR paradox criterion

The concept of entanglement was first introduced by Einstein, Podolsky, and Rosen in 1935 [16]. They demonstrated than an apparent violation of the Heisenberg uncertainty principle could be achieved between the position and momentum observables of a pair of particles[4]. This apparent violation has since been termed the *EPR paradox*. Demonstration of the EPR paradox relies on quantum correlations between a pair of non-commuting observables, so that measurement of either observable in sub-system x allows the inference of that variable in sub-system y to better than the quantum noise limit. Between the amplitude and phase quadratures of a pair of optical beams this is quantified by the product of conditional variances [134, 135], we therefore define the *degree of EPR paradox* $\mathcal{E}$

$$\mathcal{E} = \Delta^2\hat{X}^{+}_{x|y}\Delta^2\hat{X}^{-}_{x|y}, \tag{4.29}$$

where the EPR paradox is demonstrated for $\mathcal{E} < 1$ and the quadrature conditional variances $\Delta^2\hat{X}^{\pm}_{x|y}$ are given by

$$\begin{aligned}\Delta^2\hat{X}^{\pm}_{x|y} &= \Delta^2\hat{X}^{\pm}_{x} - \frac{\left|\langle \delta X^{\pm}_{x}\delta X^{\pm}_{y}\rangle\right|^2}{\Delta^2\hat{X}^{\pm}_{y}} && (4.30)\\ &= C^{\pm\pm}_{xx} - \frac{\left|C^{\pm\pm}_{xy}\right|^2}{C^{\pm\pm}_{xx}} && (4.31)\\ &= \min_{g^{\pm}}\left\langle\left(\delta X^{\pm}_{x} - g^{\pm}\delta X^{\pm}_{y}\right)^2\right\rangle, && (4.32)\end{aligned}$$

where $g^{\pm}$ are experimentally adjustable variables. Satisfaction of the EPR paradox criterion between two beams is a sufficient but not necessary condition for their entanglement. This criterion has been used to characterise the strength of entanglement in several previous experiments [102, 126, 127, 128].

It is relatively easy to show that for pure input squeezed states ($\{\Delta^2\hat{X}^{+}_{\rm sqz,1}\cdot\Delta^2\hat{X}^{-}_{\rm sqz,1}, \Delta^2\hat{X}^{+}_{\rm sqz,2}\cdot\Delta^2\hat{X}^{-}_{\rm sqz,2}\} = 1$) and equal optical loss for beams x and y, the dependence of $\mathcal{E}$ on detection efficiency is given by

$$\mathcal{E} = 4\left(1-\eta+\frac{2\eta-1}{\eta(\Delta^2\hat{X}^{+}_{\rm sqz,ave}+1/\Delta^2\hat{X}^{+}_{\rm sqz,ave}-2)+2}\right)^2. \tag{4.33}$$

Notice that when $\eta = 0.5$, $\mathcal{E} = 1$, independent of the level of squeezing. This defines a boundary such that if $\eta > 0.5$ the EPR paradox criterion is satisfied for any level of squeezing, and if $\eta < 0.5$ it can never be satisfied. This is a striking contrast to the inseparability criterion which, as we showed earlier, is satisfied for any level of squeezing and any detection efficiency. The

---

[4] Of course, there is no real violation since the position and momentum inferences cannot be made simultaneously.

reason for this difference is that the inseparability criterion is independent of the purity of the entanglement (ie. independent of $\Delta^2\hat{X}^+_{\rm sqz,1}\cdot\Delta^2\hat{X}^-_{\rm sqz,1}$ and $\Delta^2\hat{X}^+_{\rm sqz,2}\cdot\Delta^2\hat{X}^-_{\rm sqz,2}$), a property that the EPR paradox criterion is very sensitive to. Optical loss changes the purity of the entanglement and therefore effects the EPR paradox and inseparability criteria differently. However, if $\eta = 1$ the measured entangled state is pure, and both criteria are monotonically increasing functions of $\Delta^2\hat{X}^+_{\rm sqz,ave}$ in the range $0 < \Delta^2\hat{X}^+_{\rm sqz,ave} < 1$, with $\mathcal{E} = \mathcal{I} = 1$ at $\Delta^2\hat{X}^+_{\rm sqz,ave} = 1$. Therefore, in the limit of pure measured entanglement, the inseparability and EPR paradox criteria become qualitatively equivalent.

4.3.4 The photon number diagram

Many applications have been proposed for quadrature entanglement in the field of quantum information [5, 15]. For almost all of these applications, a pure entangled state is desired[5]. Due to the unavoidable losses in any real system however, a perfectly pure entangled state is unachievable. It is therefore essential to characterise the effect of impurity on the outcome of any application of entanglement. We have seen already, that impurity has different effects on the degrees of inseparability and EPR paradox. It may not be such a surprise therefore, that the effect of impurity varies from application to application. To illustrate the point we consider two well known potential applications related to quantum information, unity gain quantum teleportation [93, 148, 149, 150] which will be analysed in more detail in the following Chapter, and dense coding [124, 151]. We analyse the performance of these applications as a function of the purity of the entanglement and its strength inferred from the inseparability criterion.

A nice feature of some discrete variable measures of an entanglement resource, such as Von Neumann entropy[144] and relative entropy[152], is that they vary proportionally with the size of the resource. That is, if the number of entangled photon pairs doubles the value of the measure doubles. This is not the case for the inseparability criterion. In fact, as the strength of the entanglement increases, the inseparability criterion approaches zero. Alternatively, in a manner analogous to discrete variable entanglement measures, we can examine the average number of photons per bandwidth per time required to generate the entanglement resource [30]. The average number of photons per bandwidth per time in the sideband ω of an optical field is given by

$$\begin{aligned}\bar{n}(\omega) &= \left\langle \hat{a}^\dagger(\omega)\hat{a}(\omega)\right\rangle \\ &= \frac{1}{4}\Big\langle\big(\hat{X}^+ - i\hat{X}^-\big)\big(\hat{X}^+ + i\hat{X}^-\big)\Big\rangle \\ &= \frac{1}{4}\Big(\Big\langle\big(\hat{X}^+\big)^2\Big\rangle + \Big\langle\big(\hat{X}^-\big)^2\Big\rangle + i\left\langle\hat{X}^+\hat{X}^- - \hat{X}^-\hat{X}^+\right\rangle\Big) \\ &= \left|\alpha^+\right|^2 + \left|\alpha^-\right|^2 + \frac{1}{4}\Big(\Delta^2\hat{X}^+ + \Delta^2\hat{X}^- - 2\Big). \qquad (4.34)\end{aligned}$$

We see that with only vacuum in the sideband $\Delta^2\hat{X}^+ = \Delta^2\hat{X}^- = 1$ and $\alpha^\pm = 0$, so no photons are present. If the state is squeezed, however, then $\Delta^2\hat{X}^+ + \Delta^2\hat{X}^- > 2$ always, and therefore $\bar{n} > 0$ (see also Section 2.2). As the squeezing improves the average number of photons in the state increases. Since entanglement may be generated by interfering a pair of squeezed beams we can see that to maintain an entangled resource of a given strength (or a given $\mathcal{I}$) will also require some non-zero average number of photons. The mean number of photons in an entangled state

---

[5] The exception is quantum cryptography and related applications, where impurity can be useful to obscure a state from observation by an eavesdropper [113]. This will be discussed further in Chapter 6

$\bar{n}_{\rm total}$ is just the sum of the number in beams x and y

$$\begin{aligned}\bar{n}_{\rm total} &= \bar{n}_x + \bar{n}_y & (4.35)\\ &= \frac{1}{4}\left(\Delta^2\hat{X}_x^+ + \Delta^2\hat{X}_x^- + \Delta^2\hat{X}_y^+ + \Delta^2\hat{X}_y^-\right) - 1, & (4.36)\end{aligned}$$

where since the coherent amplitudes $\alpha_x^\pm$ and $\alpha_y^\pm$ have no relevance to the correlation matrix characterising our entanglement, and are easily accounted for, we have neglect contributions from them setting $\alpha_x^\pm = \alpha_y^\pm = 0$. As stated earlier, some fraction of $\bar{n}_{\rm total}$ is required to maintain the strength of the entanglement. A contribution is also made by the impurity of the squeezed beams used to generate the entanglement; and by the decoherence experienced by the state after production. Of course, the photons in a quadrature entangled state are indistinguishable from one another so that a definite separation of photons into distinct categories is not possible. This separation is possible however, when only the average number of photons within a quadrature entangled state per bandwidth per time is considered. The strength of the entanglement ($\mathcal{I}$) dictates a minimum average number of photons $\bar{n}_{\rm min}$ per bandwidth per time that are required to maintain the entanglement. The remaining photons can (on average) be separated into photons that are present due to bias between the amplitude and phase quadratures of the entangled beams $\bar{n}_{\rm bias}$, and excess photons that are the result the impurity of the entanglement $\bar{n}_{\rm excess}$.

For entanglement that is symmetric between beams x and y such as is relevant to this thesis, the average number of excess photons per bandwidth per time $\bar{n}_{\rm excess}$ can be found by considering the lossless interference of the two entangled beams in phase on a 50/50 beam splitter. In this case the output beams (labelled with the sub-scripts 'out1' and 'out2' here) would exhibit squeezing with squeezed quadrature variances of $\Delta^2\hat{X}^+_{\rm sqz,out1} = \Delta^2\hat{X}^+_{x\pm y}$ and $\Delta^2\hat{X}^-_{\rm sqz,out2} = \Delta^2\hat{X}^-_{x\pm y}$, respectively. From Eq. (4.27) we see that the strength of our entanglement, $\mathcal{I}$, depends only on the squeezing of these output beams. Any impurity in the entanglement causes the output beams to be non-minimum uncertainty ($\{\Delta^2\hat{X}^+_{\rm sqz,out1}\Delta^2\hat{X}^-_{\rm sqz,out1}, \Delta^2\hat{X}^+_{\rm sqz,out2}\Delta^2\hat{X}^-_{\rm sqz,out2}\} > 1$). To determine the average number of photons in the entangled state due to impurity, $\bar{n}_{\rm excess}$, we can simply compare the mean number of photons in the entangled state $\bar{n}_{\rm total}$ to the number that would be in the state if it was perfectly pure, $\bar{n}_{\rm pure}$,

$$\begin{aligned}\bar{n}_{\rm excess} &= \bar{n}_{\rm total} - \bar{n}_{\rm pure} & (4.37)\\ &= \bar{n}_x + \bar{n}_y - \bar{n}_{\rm pure}. & (4.38)\end{aligned}$$

$\bar{n}_{\rm pure}$ can be thought of as the average number of photons per bandwidth per time required to generate two pure squeezed beams with the same level of squeezing as the two output beams. When $\mathcal{I} \geq 1$ no entanglement is present between beams x and y, and no squeezing is required. We therefore find $\bar{n}_{\rm min} = 0$ and $\bar{n}_{\rm total} = \bar{n}_{\rm excess} + \bar{n}_{\rm bias}$. For the remainder of this Chapter (and indeed this thesis) we only consider the more interesting situation when entanglement is present, restricting ourselves to $\mathcal{I} < 1$. In this case since the two output beams have squeezed quadrature variances of $\Delta^2\hat{X}^+_{x\pm y}$ and $\Delta^2\hat{X}^-_{x\pm y}$ respectively, $\bar{n}_{\rm pure}$ is given by

$$\bar{n}_{\rm pure} = \frac{1}{4}\left(\Delta^2\hat{X}^+_{x\pm y} + \frac{1}{\Delta^2\hat{X}^+_{x\pm y}} + \Delta^2\hat{X}^-_{x\pm y} + \frac{1}{\Delta^2\hat{X}^-_{x\pm y}}\right) - 1. \qquad (4.39)$$

$\bar{n}_{\rm excess}$ can then be directly obtained from Eq. (4.38).

$\bar{n}_{\rm pure}$ can be separated into a component due to bias in the entanglement $\bar{n}_{\rm bias}$ and a component required to maintain the entanglement $\bar{n}_{\rm min}$

$$\bar{n}_{\rm pure} = \bar{n}_{\rm min} + \bar{n}_{\rm bias}. \tag{4.40}$$

$\bar{n}_{\rm min}$, since it is directly related to the strength of the entanglement $\mathcal{I}$, should be independent of local reversible operations performed individually on beams x and y. The photons resulting from bias between the amplitude and phase quadratures of the entangled state, however, may be completely eliminated by performing equal local squeezing operations on beams x and y [30]. After performing these operations $\bar{n}_{\rm pure}$ becomes

$$\bar{n}'_{\rm pure} = \frac{1}{4}\left(g^2\Delta^2\hat{X}^+_{x\pm y} + \frac{1}{g^2\Delta^2\hat{X}^+_{x\pm y}} + \frac{\Delta^2\hat{X}^-_{x\pm y}}{g^2} + \frac{g^2}{\Delta^2\hat{X}^-_{x\pm y}}\right) - 1, \tag{4.41}$$

where g is the gain of the squeezing operations. It is relatively easy to show that $\bar{n}'_{\rm pure}$ is minimised, and therefore $\bar{n}_{\rm bias}$ is eliminated, when $g^2 = \sqrt{\Delta^2\hat{X}^-_{x\pm y}/\Delta^2\hat{X}^+_{x\pm y}}$, and we find that

$$\begin{aligned}\bar{n}_{\rm min} &= \frac{1}{2}\left(\sqrt{\Delta^2\hat{X}^+_{x\pm y}\Delta^2\hat{X}^-_{x\pm y}} + \frac{1}{\sqrt{\Delta^2\hat{X}^+_{x\pm y}\Delta^2\hat{X}^-_{x\pm y}}}\right) - 1\\ &= \frac{1}{2}\left(\mathcal{I} + \frac{1}{\mathcal{I}}\right) - 1,\end{aligned} \tag{4.42}$$

where $\bar{n}_{\rm min}$ is the minimum mean number of photons per bandwidth per time required to generate entanglement of a given strength $\mathcal{I}$. We see that $\bar{n}_{\rm min}$ is completely determined by $\mathcal{I}$ and is monotonically increasing as $\mathcal{I} \rightarrow 0$. The average number of photons present in the entanglement per bandwidth per time as a result of bias can then also be determined $\bar{n}_{\rm bias} = \bar{n}_{\rm pure} - \bar{n}_{\rm min}$.

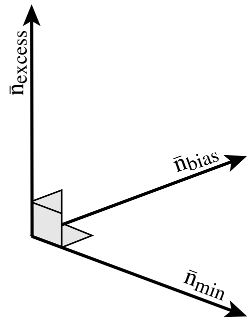

Figure 4.1: Axes of the photon number diagram representation of entanglement.

We can now separate the average photon number per bandwidth per time in a quadrature entangled state into three categories; photons required to maintain the entanglement $\bar{n}_{\rm min}$, photons produced by bias between the amplitude and phase quadratures $\bar{n}_{\rm bias}$, and excess photons resulting from impurity $\bar{n}_{\rm excess}$. All three average photon numbers can be calculated from measurements of $\Delta^2\hat{X}^\pm_x$, $\Delta^2\hat{X}^\pm_y$, and $\Delta^2\hat{X}^\pm_{x\pm y}$. An entangled state can then be conveniently and intuitively analysed on a three dimensional diagram as shown in Fig. 4.1, with $\bar{n}_{\rm min}$, $\bar{n}_{\rm bias}$, and $\bar{n}_{\rm excess}$ forming each of the axes. Note that, in a manner analogous to that performed for $\bar{n}_{\rm pure}$ above, $\bar{n}_{\rm excess}$ may be broken into two parts: the average number of photons required to produce the impurity of the entanglement, and the average number of photons generated by bias between the amplitude and phase quadratures caused by the impurity of the state. We do not perform this separation explicitly here, since the exact distribution of excess photons is of much less significance than that for the photons necessary to generate the entanglement. Including this extra parameter, and assuming the entanglement is of the same form as is discussed earlier, the correlation matrix of Section 4.3.1 can be fully characterised by these photon number parameters.

An analogy can be made between the $\bar{n}_{\rm min}$-$\bar{n}_{\rm excess}$ plane of the photon number diagram and the tangle/linear entropy analysis often performed for discrete variable entanglement[153]. In both cases the entanglement is represented on a plane with one axis representing the strength of the entanglement ($\bar{n}_{\rm min}$ for continuous variables, and the tangle for discrete variables), and the other axis representing the purity of the state ($\bar{n}_{\rm excess}$ for continuous variables and the linear entropy for discrete variables). Unlike the discrete variable case where the region of the tangle-linear entropy plane occupied by physical states is bounded, the set of continuous variable entangled states spans the entire $\bar{n}_{\rm min}$-$\bar{n}_{\rm excess}$ plane. The difference occurs because the discrete quantum states analysed on the tangle-linear entropy plane involve a finite and fixed number of photons. This restriction limits both the strength of the entanglement (the tangle) and the purity (the linear entropy). Continuous variable entangled states have no such limitation.

$\bar{n}_{\rm min}$ as a measure of entanglement

As an aside, it is interesting to consider whether $\bar{n}_{\rm min}$ is a good measure of entanglement. Formally, a good measure of the entanglement of the state ρ, $E(\rho)$, must satisfy the following criteria[144, 145]:

1. $E(\rho) = 0$ if and only if ρ is separable,
2. $E(\rho)$ is left invariant under local unitary operations,
3. $E(\rho)$ is non-increasing under local general measurements and classical communication,
4. Given two separate entangled states ρ_1 and ρ_2 such that $\rho = \rho_1 \otimes \rho_2$, $E(\rho) = E(\rho_1) + E(\rho_2)$.

Duan *et al.* demonstrated that $\mathcal{I} = 1$ if and only if the state under interrogation is separable. It is clear then that $\bar{n}_{\rm min} = 0$ if and only if the state under interrogation is separable, and therefore Criterion 1. is true for $\bar{n}_{\rm min}$. Furthermore, since characterisation of $\mathcal{I}$ requires that the states correlation matrix be taken into a standard form, both $\mathcal{I}$ and $\bar{n}_{\rm min}$ are invariant under local unitary operations so that Criterion 2. is true, also. As yet we have no conclusion about the validity of Criterion 3. for $\bar{n}_{\rm min}$. It seems likely that it is valid since an increase in $\bar{n}_{\rm min}$ is equivalent to an increase in the quantum correlation between fields x and y, which should not be possible through local general measurements and classical communication. Finally, given two separate entangled states the minimum average number of photons per bandwidth per time required to generate both states is simply the sum of the minimum average number of photons per bandwidth per time required to generate each state, $\bar{n}_{\rm min} = \bar{n}_{\rm min,1} + \bar{n}_{\rm min,2}$, so that Criterion 4. is valid. We see therefore that $\bar{n}_{\rm min}$ satisfies three of the four criteria for a good entanglement measure, and although we have not shown so here, we believe it is likely to satisfy the remaining criterion. $\bar{n}_{\rm min}$ is a particularly elegant measure of entanglement due to its physical significance.

Entanglement criteria and the photon number diagram

We can represent the degrees of inseparability and EPR paradox on the photon number diagram. As can be seen from Eq. (4.42), for entanglement symmetric between beams x and y the degree inseparability can be expressed solely as a function of $\bar{n}_{\rm min}$

$$\mathcal{I} = \bar{n}_{\rm min} + 1 - \sqrt{(\bar{n}_{\rm min}+1)^2 - 1}. \tag{4.43}$$

The same is not true for the EPR paradox criterion. This result is unsurprising, we have already found that the EPR paradox is sensitive to the purity of the entangled state which can be expressed in terms of $\bar{n}_{\rm excess}$. The degree of EPR paradox can be obtained from the amplitude and phase quadrature conditional variances between beams x and y (see Eq. (4.29)). We see from Eq. (4.30) that the amplitude and phase quadrature conditional variances are defined by $\Delta^2\hat{X}_x^{\pm}$, $\Delta^2\hat{X}_y^{\pm}$, and $\left|\left\langle \delta X_x^{\pm}\delta X_y^{\pm}\right\rangle\right|$. For simplicity here we assume the entanglement is symmetric between amplitude and phase quadratures. This assumption is true for the entanglement analysed in this thesis at sideband frequencies above around 5 MHz, and has the consequence that there are no photons in the entangled state due to bias $\bar{n}_{\rm bias} = 0$. We then find that

$$\Delta^2\hat{X} = \Delta^2\hat{X}_x^{+} = \Delta^2\hat{X}_x^{-} = \Delta^2\hat{X}_y^{+} = \Delta^2\hat{X}_y^{-} = \bar{n}_{\rm total} + 1, \tag{4.44}$$

and can express $\left|\left\langle \delta X_x^{\pm}\delta X_y^{\pm}\right\rangle\right|$ in terms of $\bar{n}_{\rm min}$ and $\bar{n}_{\rm excess}$ as

$$\left|\left\langle \delta X_x^{\pm}\delta X_y^{\pm}\right\rangle\right| = \bar{n}_{\rm excess} + \sqrt{(\bar{n}_{\rm min})^2 - 1}. \tag{4.45}$$

The degree of EPR paradox can then also be written in terms of $\bar{n}_{\rm min}$ and $\bar{n}_{\rm excess}$

$$\mathcal{E} = \left(\frac{2\bar{n}_{\rm excess}\left(\bar{n}_{\rm min} + 1 - \sqrt{(\bar{n}_{\rm min}+1)^2 - 1}\right) + 1}{\bar{n}_{\rm excess} + \bar{n}_{\rm min} + 1}\right)^2. \tag{4.46}$$

Since we have assumed that $\bar{n}_{\rm bias} = 0$, the degree of EPR paradox can be represented as contours on the $\bar{n}_{\rm min}$-$\bar{n}_{\rm excess}$ plane of the photon number diagram. This representation is shown in Fig. 4.14 a), the curvature of the contours demonstrates again the sensitivity of the EPR paradox to impurity.

It is interesting to note that in the extrema of $\bar{n}_{\rm excess} \rightarrow 0$ and $\bar{n}_{\rm excess} \rightarrow \infty$, the degree of EPR paradox becomes a function of only $\bar{n}_{\rm min}$, and can be written in terms of the degree of inseparability as

$$\begin{aligned} \mathcal{E}_{\bar{n}_{\rm excess}\rightarrow 0} &= \frac{4\mathcal{I}^2}{(\mathcal{I}^2+1)^2} && (4.47)\\ \mathcal{E}_{\bar{n}_{\rm excess}\rightarrow \infty} &= 4\mathcal{I}^2. && (4.48) \end{aligned}$$

We see again that for pure entanglement ($\bar{n}_{\rm excess} = 0$) $\mathcal{I} < 1$ implies $\mathcal{E} < 1$. In contrast, for extremely impure entanglement ($\bar{n}_{\rm excess} \rightarrow \infty$), we see that to observe the EPR paradox requires $\mathcal{I} < 0.5$. This result has the consequence that if the squeezed beams used to generate the entanglement have squeezed variances $\{\Delta^2\hat{X}^{+}_{\rm sqz,1}, \Delta^2\hat{X}^{+}_{\rm sqz,2}\} < 0.5$, then no matter how large the anti-squeezed variances, the EPR paradox can be demonstrated.

Quantum teleportation and the photon number diagram

Quantum information protocols are also representable on the photon number diagram. In this Chapter we consider two well-known examples, quantum teleportation and dense coding.

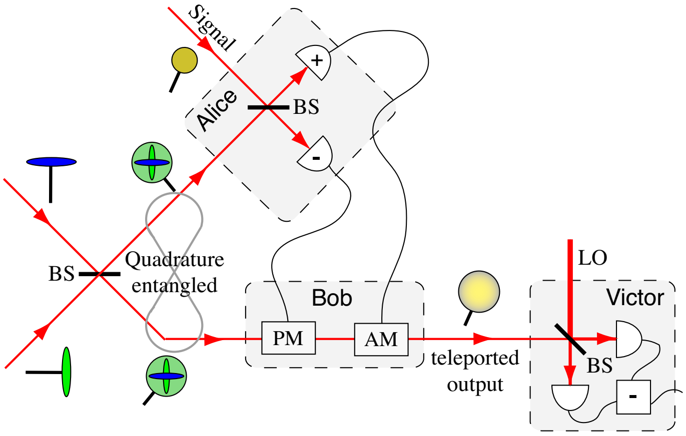

Figure 4.2: Schematic of a quantum teleportation experiment, detectors labelled with the symbols + and - are amplitude and phase detectors respectively, BS: beam splitter, AM: amplitude modulator, PM: phase modulator, LO: local oscillator.

The uncertainty principle of quantum mechanics fundamentally limits both the ability to measure and to reconstruct quantum states. Since quantum teleportation requires both measurement of the original state, and then reconstruction at a distant location, it was therefore thought that teleportation was also fundamentally limited by the uncertainty principle. In 1993, however, Bennett *et. al* [122] discovered that by using entangled photon pairs in the measurement and reconstruction processes perfect teleportation could be facilitated. Their proposal has been generalised to the continuous variable regime [148, 149], and a schematic of the continuous variable scheme is shown in Fig. 4.2. A detailed analysis of quantum teleportation is given in Chapter 5. Here, we restrict ourselves to the unity gain regime where the coherent amplitudes of the input and output states are equal, and characterise the protocol using only the most well known measure, the fidelity of teleportation. Fidelity measures the state-overlap between the teleporter input $|\psi_{\rm in}\rangle$ and output $\hat{\rho}_{\rm out}$ states, and is given by

$$\mathcal{F} = \langle\psi_{\rm in}|\hat{\rho}_{\rm out}|\psi_{\rm in}\rangle. \tag{4.49}$$

$\mathcal{F} = 1$ implies perfect overlap between the input and output states and therefore perfect teleportation, without entanglement the fidelity is limited to $\mathcal{F} \leq 0.5$, and $\mathcal{F} = 0$ if the input and output states are orthogonal. Again assuming that the entanglement is unbiased ($\bar{n}_{\rm bias} = 0$), the fidelity of unity gain coherent state teleportation using quadrature entanglement [148, 149] may be expressed as

$$\mathcal{F} = \frac{1}{1+\mathcal{I}}. \tag{4.50}$$

We see that the success of the teleportation protocol depends only on the degree of inseparability. This results in vertical efficacy contours for teleportation when represented on the photon number diagram, as can be seen in Fig. 4.14 b). The shading in Fig. 4.14 b) indicates the area of the photon number diagram for which the more stringent *no cloning* teleportation limit is left unsatisfied [154, 155]. Note that, if the teleportation protocol was operated at non-unity gain, the protocol would become sensitive to impurity and the teleportation efficacy contours would be curved. Although the non-unity gain regime is significant for quantum information protocols such as optimum entanglement swapping and is the focus of much of the discussion in Chapter 5, we will not consider it here.

Dense coding and the photon number diagram

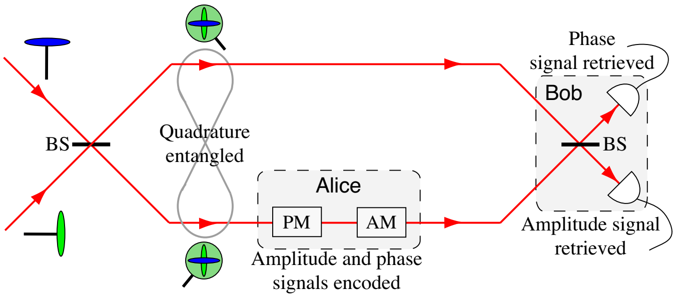

Figure 4.3: Schematic of a dense coding experiment, BS: beam splitter, AM: amplitude modulator, PM: phase modulator.

Dense coding was first proposed by Bennett *et. al* [123] in 1992, when they showed that by utilising shared entanglement between the sending (Alice) and receiving (Bob) stations, a single communication channel can achieve a higher information transfer rate than is physically possible using the same resources (i.e. the same number of photons) but without entanglement.

An upper bound to the information transfer rate of a bandwidth limited Gaussian information channel is given by the Shannon capacity C [156]

$$C = \frac{\log_2(1+\mathrm{SNR})}{2}, \tag{4.51}$$

where $\mathrm{SNR} = \Delta^2\hat{S}/\Delta^2\hat{N}$ is the signal to noise ratio of the channel, with $\Delta^2\hat{S}$ and $\Delta^2\hat{N}$ being the variance of the signal and noise respectively. Dense coding in the continuous variable regime was first proposed by Braunstein and Kimble in 2000 [151], and a detailed discussion may be found in [124]. A schematic diagram of the proposal of Braunstein and Kimble is given in Fig. 4.3.

In this thesis we restrict ourselves to the comparison of the channel capacities achievable using a squeezed state and using a dense coding protocol based on quadrature entanglement. To obtain a fair comparison of the two schemes we define the total average number of photons allowed in the beam encoded with information $\bar{n}_{\rm encoding}$. In both the squeezed state and entangled state based schemes some of these photons must be used to generate the quantum state, and the remaining photons can be used to encode signals. For the squeezed state scheme the number of photons in the squeezed state is given by

$$\bar{n}_{\rm sqz} = \frac{1}{4}\left(\Delta^2\hat{X}_{\rm sqz} + \frac{1}{\Delta^2\hat{X}_{\rm sqz}} - 2\right), \tag{4.52}$$

where $\Delta^2\hat{X}_{\rm sqz}$ is the variance of the squeezed quadrature. The remaining $\bar{n}_{\rm encoding} - \bar{n}_{\rm sqz}$ photons are used to encode signals on the squeezed quadrature of the beam. This results in a channel with signal variance given by $\Delta^2\hat{S}_{\rm sqz} = 4(\bar{n}_{\rm encoding} - \bar{n}_{\rm sqz})$, and noise variance given by $\Delta^2\hat{N}_{\rm sqz} = \Delta^2\hat{X}_{\rm sqz}$. The squeezed state channel capacity is then

$$C_{\rm sqz} = \log_2\left(1 + \frac{4(\bar{n}_{\rm encoding} - \bar{n}_{\rm sqz})}{\Delta^2\hat{X}_{\rm sqz}}\right). \tag{4.53}$$

Optimising the ratio of the mean number of photons per bandwidth per time used to generate squeezing and the mean number of photons per bandwidth per time used to encode the signal we arrive at the optimum squeezed state channel capacity [124]

$$C_{\rm sqz,opt} = \log_2\left(1 + 2\bar{n}_{\rm encoding}\right). \tag{4.54}$$

Let us now consider the dense coding scheme. Again, we make the assumption that the entanglement is symmetric between the amplitude and phase quadratures. In this case we can use the amplitude and phase quadratures as independent channels, and find that the noise variance of each channel is given by $\Delta^2\hat{N}_{\rm EPR} = \mathcal{I} = \Delta^2\hat{X}^+_{x\pm y} = \Delta^2\hat{X}^-_{x\pm y}$. $\bar{n}_{\rm total}$ as defined previously is the average number of photons per bandwidth per time in the entangled state before encoding of any signals. These photons are split evenly between the two entangled beams, therefore on average $\bar{n}_{\rm encoding} - \bar{n}_{\rm total}/2$ photons per bandwidth per time are available for encoding. The amplitude and phase quadrature signal variances are both then given by $\Delta^2\hat{\mathcal{S}}_{\rm EPR} = \bar{n}_{\rm encoding} - \bar{n}_{\rm total}/2$, which is attenuated by a factor of four when compared to the squeezed state signal variance. This attenuation is the result of two effects, a factor of two arises because the signal photons must be shared between the amplitude and phase quadratures of the entangled beam, and another factor of two is due to the 50/50 beam splitter required before measurement. We then obtain the entangled state channel capacity

$$C_{\rm EPR} = \log_2\left(1 + \frac{\Delta^2\hat{\mathcal{S}}_{\rm EPR}}{\mathcal{I}}\right) \tag{4.55}$$

$$= \log_2\left(1 + \frac{\bar{n}_{\rm encoding} - \left(\bar{n}_{\rm min} + \bar{n}_{\rm excess}\right)/2}{\bar{n}_{\rm min} + 1 - \sqrt{\left(\bar{n}_{\rm min}+1\right)^2 - 1}}\right). \tag{4.56}$$

When the average number of photons available to the dense coding protocol is large ($\bar{n}_{\rm encoding} \to \infty$), the dense coding channel capacity becomes independent of the number of photons present due to impurity in the entanglement. This is shown in Fig. 4.14 d) which plots contours of the ratio $C_{\rm EPR}/C_{\rm sqz}$ for large $\bar{n}_{\rm encoding}$. We see that in this limit the dense coding channel capacity exceeds the optimum achievable squeezed state channel capacity for $\bar{n}_{\rm min} > 0.25$. When the average number of photons available to the dense coding protocol is small however, the dense coding channel capacity can be extremely sensitive to impurity. This is perhaps not a surprise, since every photon that exists in the entangled state is one less that may be used to encode signals. Clearly, in the limit that $\bar{n}_{\rm encoding} = (\bar{n}_{\rm min} + \bar{n}_{\rm excess})/2$, no photons remain to encode signals, and therefore $C_{\rm EPR} = 0$. The ratio $C_{\rm EPR}/C_{\rm sqz}$ for small $\bar{n}_{\rm encoding}$ is shown as a function of $\bar{n}_{\rm min}$ and $\bar{n}_{\rm excess}$ in Fig. 4.14 c), and indeed the contours are strongly curved.

4.4 Experiment

The previous Section described methods presently available to characterise continuous variable entangled states. In particular we discussed the correlation matrix which can be used to fully characterise Gaussian entanglement, the inseparability and EPR paradox criteria, and a new representation the photon number diagram. In this Section we describe the methods used in our experiment to generate a pair of entangled beams. We then present experimental results for each entanglement characterisation technique over the frequency range from 2.5 to 10 MHz. We examine the effect of loss on the inseparability and EPR paradox criteria demonstrating qualitative differences, and use the photon number diagram to predict the efficacy of our entanglement in the quantum information protocols introduced earlier.

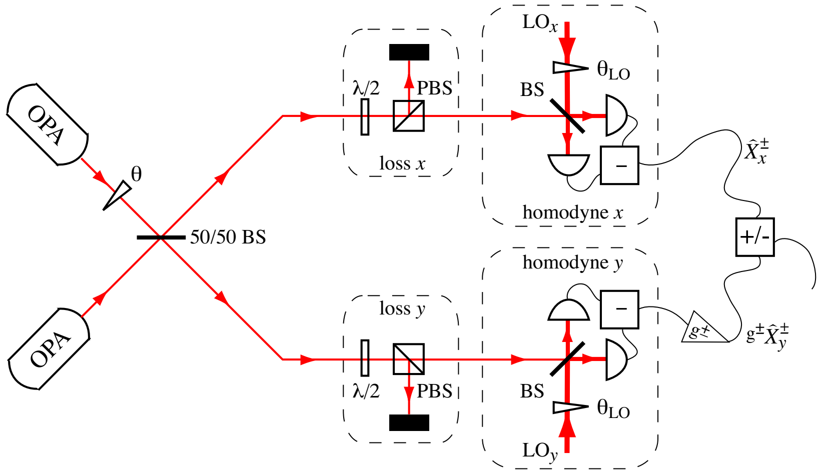

Figure 4.4: The apparatus used to generate and characterise quadrature entangled beams. x and y respectively label the entangled beams, BS: beam splitter, PBS: polarising beam splitter, $\lambda/2$: half-wave plate, θ: phase shift between squeezed beams, LO$_x$ and LO$_y$ homodyne local oscillator beams for homodynes x and y, $\theta_{\rm LO}$: phase of homodyne local oscillator beams.

4.4.1 Generation and measurement of entanglement

We generated quadrature entanglement by combining our two amplitude squeezed beams with relative phase of $\pi/2$ on a 50/50 beam splitter as discussed in Section 4.2 and shown in Fig. 4.4. A visibility of 98.7±0.3 % was observed for the process, and the relative phase was controlled at $\pi/2$ by actively balancing the power in the two entangled beams. Each entangled beam was interrogated in a balanced homodyne detector that could be locked to detect either its phase or amplitude quadrature. The efficiency of the detection process was approximately 86 %, with loss contributed equally by the homodyne visibility and the photo-detector efficiency. Measured spectra of the amplitude and phase quadrature variances of the two entangled beams are shown in Fig. 4.5. Both spectra are greater that the quantum noise limit over the entire range of measurement, a necessary prerequisite for entanglement. Due to the symmetric arrangement of our experiment the spectra are identical, so that the assumption of symmetry made in Sections 4.3.4, 4.3.4, and 4.3.4 seem reasonable.

We analysed the correlations between beams x and y by measuring the amplitude and phase quadrature sum and difference variances $\Delta^2\hat{X}^{\pm}_{x\pm y}$. The gain between the two homodyne detectors was verified to be unity by encoding large correlated phase modulations on beams x and y, throughout the experiment these modulations were suppressed on subtraction by greater than 30 dB. Spectra for $\Delta^2\hat{X}^{\pm}_{x\pm y}$ were then obtained by taking the minimum of the sum and difference variances between homodynes x and y with both homodynes locked to either the amplitude or phase quadratures. These spectra were normalised to the vacuum noise scaled by the combined power of the two homodyne local oscillators and the two entangled beams, and are shown in Fig. 4.6. At frequencies above 5 MHz both the amplitude and phase quadrature sum and difference variances are identical and well below the level expected between a pair of coherent states of the same power. At lower frequencies however, the symmetry between the amplitude and phase quadratures is broken. This effect is due to the relaxation oscillation of the laser which is common mode, and therefore correlated, between the entangled beams. As shown in Section 4.2 the am-

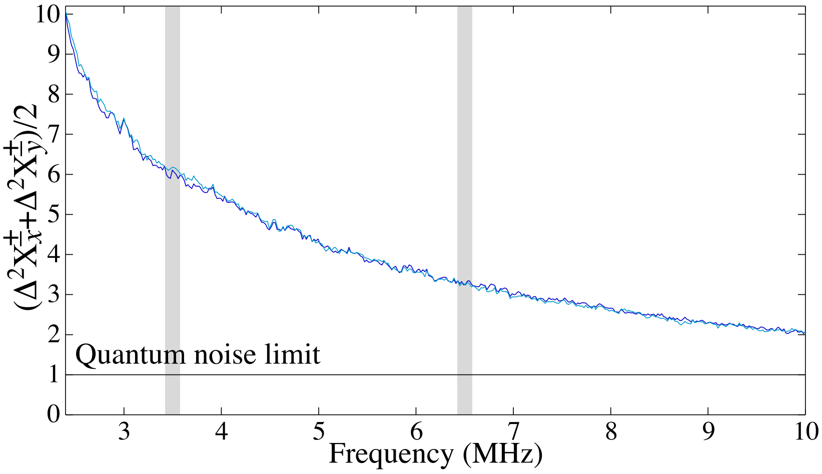

Figure 4.5: Frequency spectra of the average amplitude ($\Delta^2\hat{X}^+$) and phase ($\Delta^2\hat{X}^-$) quadrature variances of the individual entangled beams normalised to the quantum noise limit. The shaded frequency bands indicate the frequency ranges over which the correlation matrix is characterised.

plitude quadratures of our entangled beams were anti-correlated, and the phase quadratures were correlated. $\Delta^2\hat{X}^+_{x\pm y}$ was therefore obtained by summing the amplitude quadrature photo-currents from homodynes x and y, and the contribution from the relaxation oscillation was therefore also summed. $\Delta^2\hat{X}^-_{x\pm y}$ on the other hand was obtained by subtracting the phase quadrature photo-currents from the homodynes, and so the contributions from the relaxation oscillation cancelled. We see then that with decreasing frequency $\Delta^2\hat{X}^+_{x\pm y}$ degrades quickly, whereas $\Delta^2\hat{X}^-_{x\pm y}$ remains roughly constant. The slight degradation of $\Delta^2\hat{X}^-_{x\pm y}$ at frequencies below 4 MHz can be attributed to small differences in the response of the two homodyne detectors so that the relaxation oscillation was not quite perfectly cancelled.

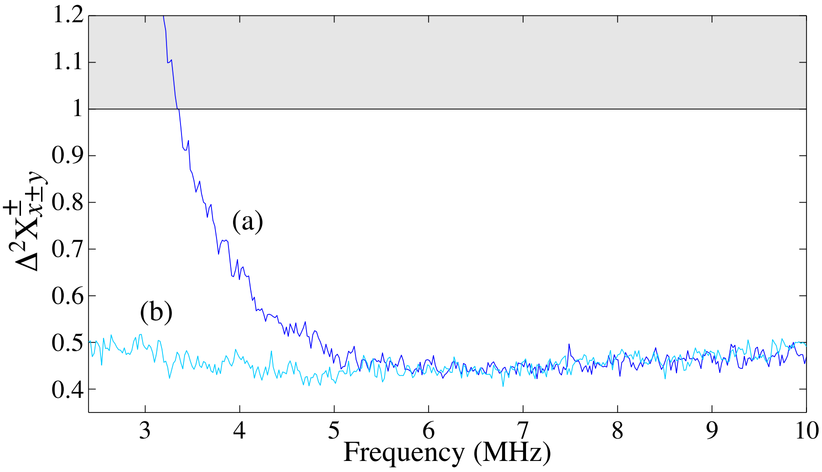

Figure 4.6: Frequency spectra of the amplitude and phase quadrature sum and difference variances between quadrature entangled beams x and y. (a) $\Delta^2\hat{X}^+_{x\pm y}$ and (b) $\Delta^2\hat{X}^-_{x\pm y}$.

4.4.2 Characterisation of the correlation matrix

As discussed in Section 4.3.1, the correlation matrix provides a complete characterisation of Gaussian entanglement. Given the assumptions that entangled beams x and y are interchangeable and that there are no cross-quadrature correlations the correlation matrix is completely specified through measurements of $C_{xx}^{\pm\pm} = \Delta^2\hat{X}^{\pm}$ and $C_{xy}^{\pm\pm} = \frac{1}{2}\langle\delta\hat{X}_x^{\pm}\delta\hat{X}_y^{\pm} + \delta\hat{X}_y^{\pm}\delta\hat{X}_x^{\pm}\rangle$. Measurements of $C_{xx}^{\pm\pm}$ for our entanglement are presented in Fig. 4.5. To obtain $C_{xy}^{\pm\pm}$ we expand $\Delta^2\hat{X}_{x\pm y}^{\pm}$

$$\begin{aligned}
\Delta^2\hat{X}_{x\pm y}^{\pm} &= \frac{\left\langle\left(\delta\hat{X}_x^{\pm} \pm \delta\hat{X}_y^{\pm}\right)^2\right\rangle}{2} &(4.57)\\
&= \frac{\Delta^2\hat{X}_x^{\pm} + \Delta^2\hat{X}_y^{\pm}}{2} \pm \left\langle\delta\hat{X}_x^{\pm}\delta\hat{X}_y^{\pm}\right\rangle &(4.58)\\
&= \Delta^2\hat{X}^{\pm} \pm \frac{1}{2}\left\langle\delta\hat{X}_x^{\pm}\delta\hat{X}_y^{\pm} + \delta\hat{X}_y^{\pm}\delta\hat{X}_x^{\pm}\right\rangle &(4.59)\\
&= C_{xx}^{\pm\pm} \pm C_{xy}^{\pm\pm}. &(4.60)
\end{aligned}$$

So $C_{xy}^{\pm\pm}$ can be obtained from our measurements of the average amplitude and phase quadrature variances, and the amplitude and phase quadrature sum and difference variances, $C_{xy}^{\pm\pm} = \pm\Delta^2\hat{X}_{x\pm y}^{\pm} \mp \Delta^2\hat{X}^{\pm}$. Fig. 4.7 shows the resulting spectra. We see that C_{xy}^{++} is negative, and C_{xy}^{--} is positive, throughout the range of the measurement. This is a characterisation of the correlation and anti-correlation of the phase and amplitude quadratures, respectively, between beams x and y.

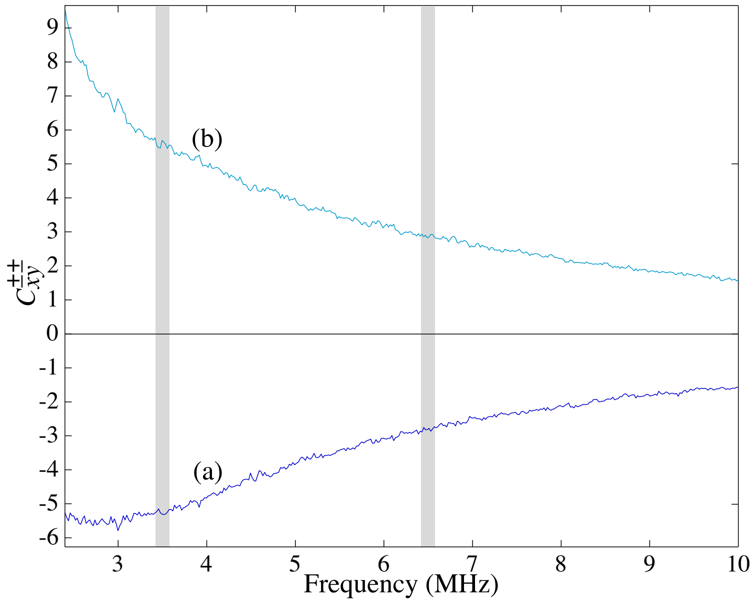

Figure 4.7: Frequency spectra of the same-quadrature correlation matrix elements between beams x and y. (a) C_{xy}^{++}, (b) C_{xy}^{--}. The shaded frequency bands indicate the frequency ranges over which the correlation matrix is characterised.

For every sideband frequency, assuming that entangled beams x and y are interchangeable and that there are no cross-quadrature correlations, a correlation matrix describing our entanglement can be constructed from the curves in Figs. 4.5 and 4.7. Here, as illustrated by the shaded frequency bands in the figures, we take two examples, the correlation matrices of the sidebands at

3.5 and 6.5 MHz. Extracting the data directly from the figures we obtain the correlation matrices

$$CM_{3.5\ \mathrm{MHz}} = \begin{pmatrix} 6.2 & (0) & 5.3 & (0) \\ (0) & 6.1 & (0) & 5.7 \\ 5.3 & (0) & 6.2 & (0) \\ (0) & 5.7 & (0) & 6.1 \end{pmatrix}, \tag{4.61}$$

and

$$CM_{6.5\ \mathrm{MHz}} = \begin{pmatrix} 3.3 & (0) & 2.9 & (0) \\ (0) & 3.3 & (0) & 2.9 \\ 2.9 & (0) & 3.3 & (0) \\ (0) & 2.9 & (0) & 3.3 \end{pmatrix}, \tag{4.62}$$

where all experimentally determined values have an associated statistical error of ± 0.05. The bracketed values are fixed as a result of the symmetry assumptions made in Section 4.3.1 and are therefore not experimentally determined. We can now examine whether the inseparability criterion originally proposed by Duan *et al.* (Eq. (4.16)), and the product inseparability criterion of Eq. (4.25) can be used to directly analyse the strength of our entanglement. The correlation matrix given here is of the form required for both criteria (see Eq. (4.13)). It remains, solely, to determine whether the restrictions imposed by each criteria are satisfied. For the original criterion to be valid Eqs. (4.14) and (4.15) must be true. Since our entangled beams x and y are interchangeable $C_{xx}^{\pm\pm} = C_{yy}^{\pm\pm}$, so that Eq. (4.14) is always true. Eq. (4.15) on the other hand, is true at 6.5 MHz, but not at the lower frequency of 3.5 MHz. The original inseparability criterion can therefore be used to characterise the strength of our entanglement at 6.5 MHz, but not at 3.5 MHz. For the product criterion to be valid, Eq. (4.24) must be satisfied. Since $C_{xx}^{\pm\pm} = C_{yy}^{\pm\pm}$ for our entanglement at all frequencies, we see that indeed the product criterion is valid for all sideband frequencies. Of course, once the correlation matrix describing the entanglement is fully characterised, it can be transformed into Duan *et al.*'s standard form, and subsequently either inseparability criterion can be used. This, however, involves many more measurements on the entangled state than are required to simply determine the product form of the criterion. Therefore, if a characterisation of the inseparability of the entanglement is all that is required, the product form is preferable.

4.4.3 Characterisation of the inseparability and EPR paradox criteria

We directly determine a spectrum for the degree of inseparability of our entanglement from the amplitude and phase quadrature sum and difference variance spectra in Fig. 4.6, using the product measure given in Eq. (4.27). This spectrum is shown in Fig. 4.8. We see that beams x and y were entangled at frequencies within our measurement range higher than 2.8 MHz. As with the other spectra presented in this Chapter, the strength of the entanglement is degraded at low frequencies as a result of the relaxation oscillation of our laser, and at high frequencies due to the bandwidth of the OPA resonators. The optimum degree of inseparability was achieved at 6.5 MHz, where we observed $\Delta^2\hat{X}_{x\pm y}^{\pm} = 0.44 \pm 0.01$ for both the amplitude and phase quadratures. This resulted in a degree of inseparability of $\mathcal{I} = 0.44 \pm 0.01$.

Characterisation of the EPR paradox criterion requires measurements of the amplitude and phase quadrature conditional variances between beams x and y. As can be seen from Eq. (4.31), these variances can be inferred from the correlation matrix elements $C_{xx}^{\pm\pm}$, and $C_{xy}^{\pm\pm}$. However, since these conditional variances were easily measurable from our experimental setup, we measured them directly. The conditional variance measures the uncertainty of one variable ($\hat{X}_x^+$ say)

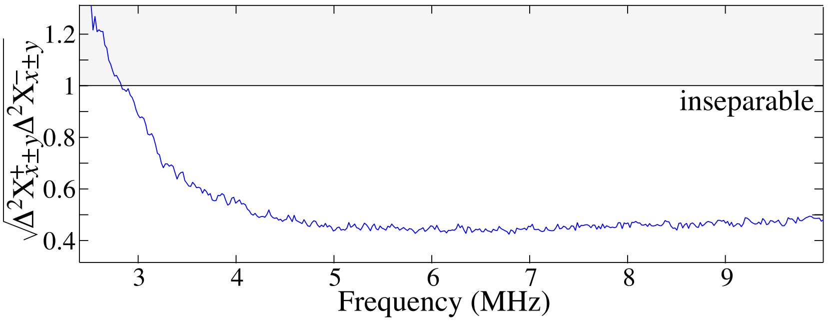

Figure 4.8: Frequency spectrum of the degree of inseparability $\mathcal{I}$ between the amplitude and phase quadratures of our quadrature entangled state.

given knowledge of another variable ($\hat{X}^+_y$ say). We characterise it here in a similar manner to that used to characterise the sum and difference variances. This time, however, rather than being fixed to unity, the gain between the two homodyne photocurrents was optimised to minimise the measured variances; and the normalisation was performed with respect to vacuum fluctuations scaled by only one homodyne local oscillator and entangled beam. The resulting amplitude and phase quadrature conditional variance spectra are shown in Fig. 4.9. We see that both $\Delta^2\hat{X}^\pm_{x|y}$ are below unity for the majority of our measurement range. This implies that a measurement performed on beam y will prepare beam x in a squeezed state, and therefore that non-classical correlations exist between the two beams. At 6.5 MHz we obtained the conditional variances $\Delta^2\hat{X}^+_{x|y} = 0.77 \pm 0.01$ and $\Delta^2\hat{X}^-_{x|y} = 0.76 \pm 0.01$. Notice that again, the amplitude quadrature spectrum is strongly degraded at low frequencies due to the relaxation oscillation of our laser, whereas the phase quadrature is unaffected by it.

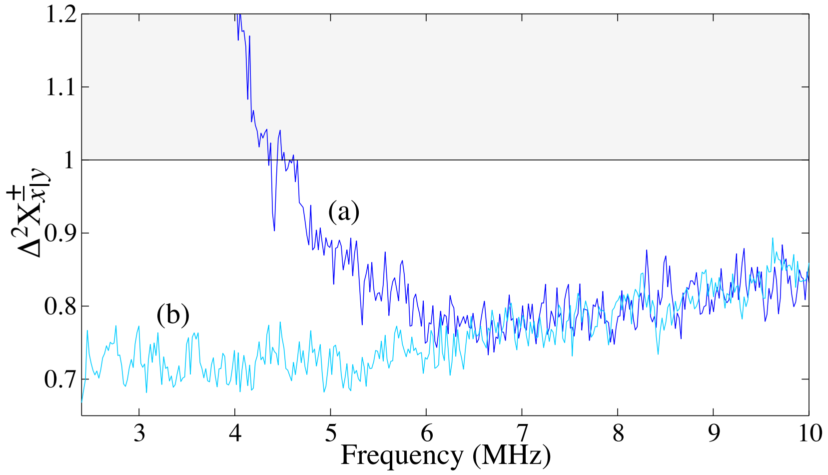

Figure 4.9: Conditional variance of the amplitude (a) and phase (b) quadratures of beam x given a measurement of that quadrature on beam y.

Taking the product of the amplitude and phase quadrature conditional variances yields the degree of EPR paradox. Fig. 4.10 presents the resulting frequency spectrum. We observe an optimum of $\mathcal{E} = 0.58 \pm 0.02 < 1$, which is well within the regime for observation of the EPR paradox.

We know from the discussion in Section 4.3 that the degree of EPR paradox $\mathcal{E}$ is highly sensitive to entanglement impurity, whereas the degree of inseparability $\mathcal{I}$ is independent of impurity.

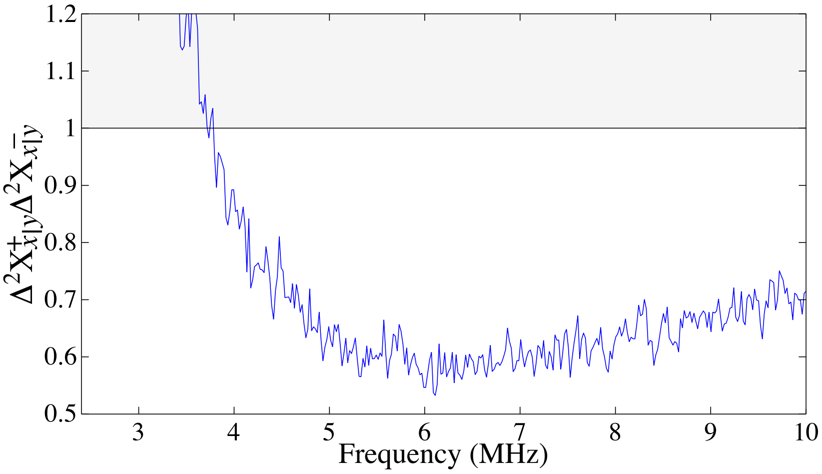

Figure 4.10: Frequency spectrum of the degree of EPR paradox between the amplitude and phase quadratures of our entangled state.

We interrogate this qualitative difference by introducing equal loss to the two entangled beams. Each entangled beam was passed through a waveplate and polarising beam splitter before detection as shown in Fig. 4.4. Rotating the waveplate allowed us to vary the amount of loss introduced. We characterised both the degree of EPR paradox and the degree of inseparability at 6.5 MHz for a number of loss settings (waveplate settings). For each measurement the spectrum analyser was set to zero span and averaged over ten consecutive traces. Fig. 4.11 summarises these measurements. We see that the experimental dependences on loss for both $\mathcal{E}$ and $\mathcal{I}$ agree very well with the theoretical curves obtained from Eqs. (4.28) and (4.33). As discussed in [130], no matter what the loss, the inseparability criterion always holds. We find however, that the EPR paradox criterion fails for loss greater than 0.48. In fact as observed earlier, it is impossible for the EPR paradox criterion to hold for loss greater than or equal to 0.5. The error bars on the plots can be attributed to uncertainty in the loss introduced, small fluctuations in the local oscillator powers and, for the EPR paradox criterion, error in the optimisation of the electronic gain.

4.4.4 Representation of results on the photon number diagram

The photon number diagram introduced in Section 4.3.4 provides a physically intuitive representation of continuous variable entanglement. The measured spectra for $\Delta^2\hat{X}^{\pm}$ and $\Delta^2\hat{X}^{\pm}_{x\pm y}$ shown in Figs. 4.5 and 4.6 may be translated into the three axes of this diagram ($\bar{n}_{\rm min}$, $\bar{n}_{\rm excess}$, and $\bar{n}_{\rm bias}$) using Eqs. (4.38), (4.39), (4.40), and (4.42). The resulting spectra are shown in Fig. 4.12. At low frequencies there is no entanglement, and from Fig. 4.12 (a) we see that correspondingly no photons are required to maintain the entanglement ($\bar{n}_{\rm min} = 0$), with increasing frequency the average number of photons required increases, peaking at $\bar{n}_{\rm min} = 0.35$ around 6.5 MHz, before dropping off as the frequency moves above the bandwidth of our OPAs. From Fig. 4.12 (b) we see that over the majority of the measured spectrum on average very few photons are present in the entanglement as a result of bias between the amplitude and phase quadratures. Photons resulting from bias only become significant at frequencies below 5 MHz. This bias is a direct consequence of the differing sensitivity of $\Delta^2\hat{X}^{+}_{x\pm y}$ and $\Delta^2\hat{X}^{-}_{x\pm y}$ to our lasers relaxation oscillation. Fig. 4.12 (c) shows that throughout the spectrum of our measurement the majority of the photons present in our entanglement are there as a result of impurity. In fact from the fit to the degree of EPR paradox in Fig. 4.11 we see that at 6.5 MHz the most significant contribution to the impurity of our entangled

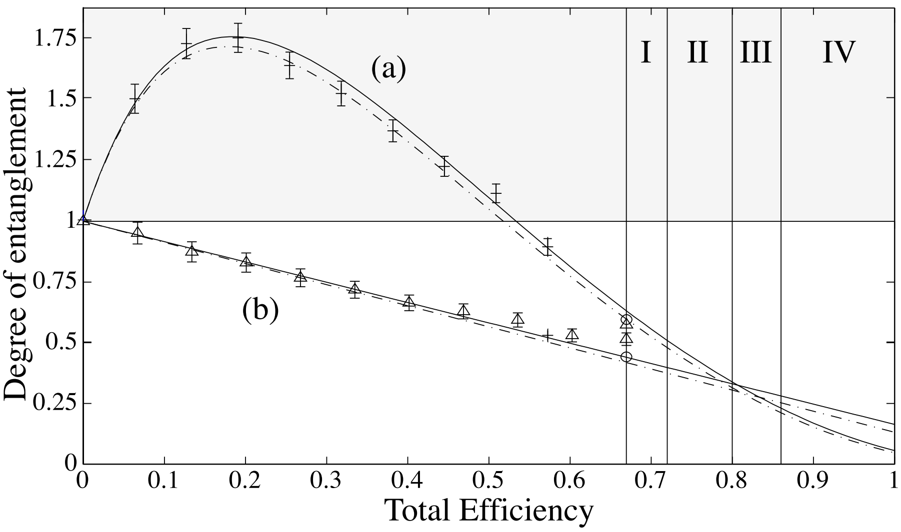

Figure 4.11: Comparison of (a) EPR and (b) inseparability criteria with varied detection efficiency. The symbols $+$, $\triangle$, and $\bigcirc$ label three separate experimental runs. For $+$ a systematic error was introduced by the detection darknoise when optimising the EPR paradox criterion gain. The solid fit in (a) includes this, the dashed fit is the result expected if the error was eliminated, and agrees well with runs $\triangle$ and $\bigcirc$. The solid line in (b) is a theoretical fit, the dashed line is the result predicted by the fit in (a). There were four sources of unavoidable loss in our system, I: Detection loss, II: Homodyne loss, III: optical loss and IV: OPA escape loss.

state is optical loss. Therefore even relatively small levels of loss (such as 33%) facilitate a significant transfer of mean photons per bandwidth per time from $\bar{n}_{\rm min}$ to $\bar{n}_{\rm excess}$. If additional sources of phase noise are present in the process used to generate squeezing, the average number of photons present due to impurity can become extremely large. The **X** in Fig. 4.17 shows $\bar{n}_{\rm min}$ and $\bar{n}_{\rm excess}$ for the entanglement generated by Siliberhorn *et. al* [127]. Their entanglement was produced via the Kerr non-linearity in optical fibres, with additional phase noise introduced via guided-acoustic-wave Brillouin scattering [157, 97]. Consequently, an average of around 100 photon per bandwidth per time were present due to impurity, compared with an average of 0.45 photons per bandwidth per time required to maintain the entanglement. The spectra of $\bar{n}_{\rm min}$, $\bar{n}_{\rm excess}$, and $\bar{n}_{\rm bias}$ obtained for our entanglement are mapped onto the photon number diagram in Fig. 4.13.

The photon number diagram can be used to analyse the efficacy of an entangled state in quantum information protocols. As discussed in Section 4.3.4, Fig. 4.14 shows efficacy contours of the degree of EPR paradox, quantum teleportation, and high and low photon number dense coding, on the $\bar{n}_{\rm min}$-$\bar{n}_{\rm excess}$ plane of the photon number diagram assuming that $\bar{n}_{\rm bias} = 0$. Since $\bar{n}_{\rm bias} \approx 0$ for our entangled state over most of the measured spectrum, we project the curve shown in Fig. 4.13 onto the $\bar{n}_{\rm bias} = 0$ plane and display it on Fig. 4.14. We can then obtain estimates of the optimum efficacy that could be achieved with our entangled state in various quantum information protocols, and estimates of the frequencies at which the optima occur. From Fig. 4.14 (a) we find that the optimum expected degree of EPR paradox for our entanglement is roughly $\mathcal{E} = 0.68$ and occurs around 6.6 MHz. In Section 4.4.3 we experimentally obtained a value of $\mathcal{E} = 0.58 \pm 0.02$ which is significantly lower. This difference is evident because the experiment was operating more effectively when the measurements of the degree of EPR paradox were made. Indeed this can be seen in Fig. 4.11, where the degree of inseparability predicted from our the degree of EPR paradox results is somewhat better than the result we obtained directly. Due to sensitivity of the degree of

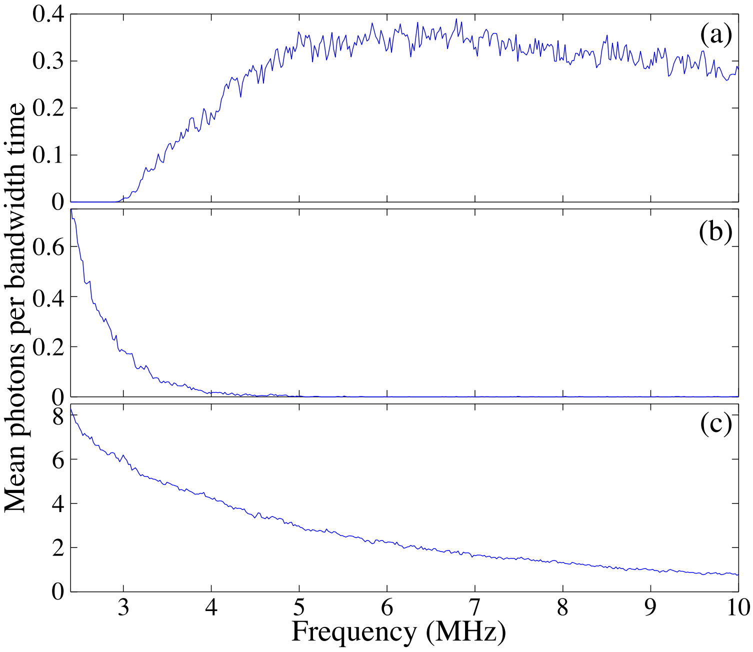

Figure 4.12: Frequency spectra of the axes of the photon number plot. (a) $\bar{n}_{\mathrm{min}}$, (b) $\bar{n}_{\mathrm{bias}}$, and (c) $\bar{n}_{\mathrm{excess}}$

EPR paradox to loss and impurity, this difference explains the discrepancy. From Fig. 4.14 (b) we see that the optimum teleportation fidelity achievable with our entanglement is approximately $\mathcal{F} = 0.695$ and would be observed near 6.2 MHz. The entangled state analysed here was used to perform quantum teleportation in Chapter 5, due to non-ideal effects such as optical loss and detector darknoise an optimum fidelity of $\mathcal{F} = 0.64 \pm 0.02$ was observed [111]. Fig. 4.14 (c) and (d) show dense coding contours on the photon number diagram. The low photon number efficacy contours for dense coding shown in Fig. 4.14(c) have an extremely strong dependence on the average number of excess photons carried by the entanglement, accordingly the optimum ratio of dense coding to squeezed state channel capacities would occur at 10 MHz where our entanglement is most pure, in our case this never exceeds unity. However, as discussed in Section 4.3.4, increasing the total average number of photons allowed in the sidebands ($\bar{n}_{\mathrm{encoding}}$) causes the dense coding protocol to become independent of $\bar{n}_{\mathrm{excess}}$. We find that when a large number of photons per bandwidth per time are available to encode signals ($\bar{n}_{\mathrm{encoding}} \gg \bar{n}_{\mathrm{excess}}$) the optimum achievable ratio of channel capacities is $C_{\mathrm{EPR}}/C_{\mathrm{sqz}} \approx 1.02$ and occurs near 6.3 MHz. So that in the large photon number limit dense coding using the entangled state characterised in this Chapter could yield a channel capacity marginally better than that achievable with optimal squeezed state encoding.

4.5 A simple scheme to reduce $\bar{n}_{\mathrm{excess}}$ with minimum effect on $\bar{n}_{\mathrm{min}}$

The photon number diagram can be a useful tool not only to diagnose the efficacy of a given entanglement resource in quantum information protocols, but also the effect of techniques available to improve the quality of the entanglement such as entanglement distillation [136, 137, 138] and purification [139, 140, 141]. As an example we will consider a simple scheme to reduce the average number of photons in an entangled state as a result of impurity, and will again assume that the entanglement is interchangeable and symmetric between the amplitude and phase quadratures.

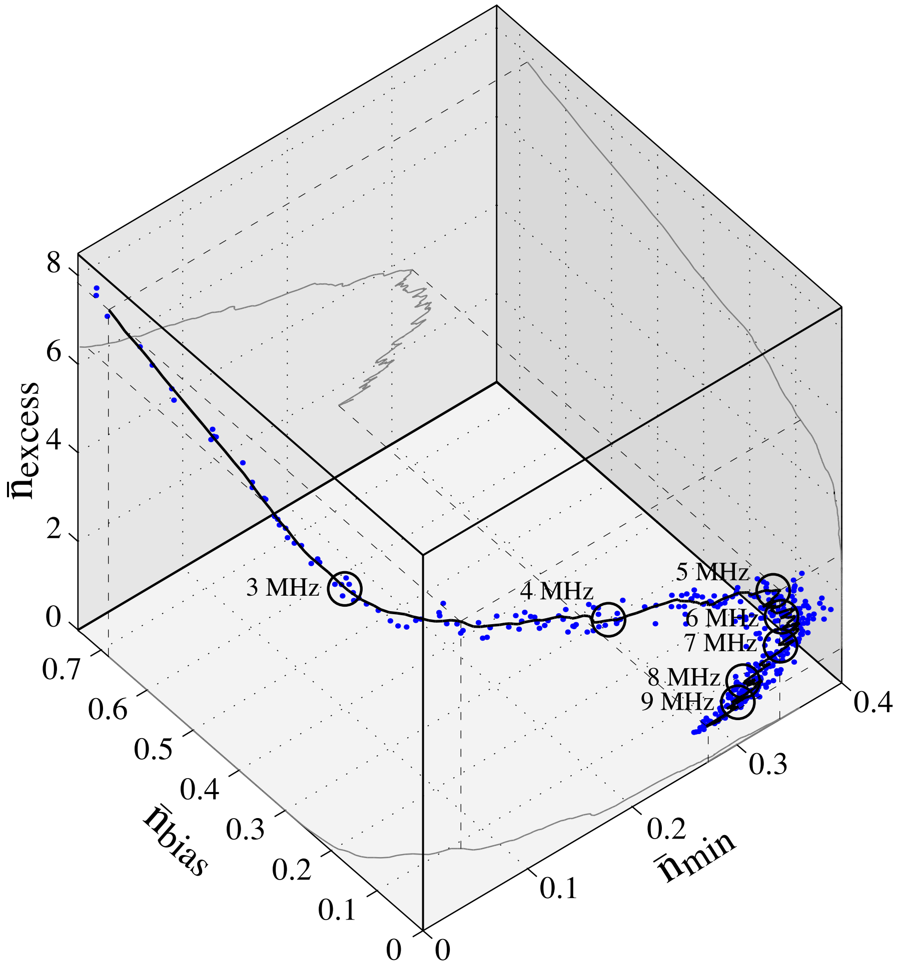

Figure 4.13: Representation of the quadrature entangled state on the photon number diagram.

This sort of scheme is somewhat analogous to entanglement purification which identifies and removes photons present in an entangled state that do not contribute to the entanglement. Ideally our scheme when represented on the photon number diagram would eliminate all photons present due to impurity $\bar{n}_{\rm excess}$, without affecting the photons required to maintain the entanglement or those due to bias $(\bar{n}_{\rm min}, \bar{n}_{\rm bias}, \bar{n}_{\rm excess}) \longrightarrow (\bar{n}_{\rm min}, \bar{n}_{\rm bias}, 0)$. In practice this ideal situation is not possible and some reduction of entanglement strength during the process is inevitable. Since some quantum information protocols are highly sensitive to impurity (see Fig. 4.14), however, a less strong but more pure entangled state may still be preferable over a stronger, less pure one.

Let us initially consider the paths mapped out on the photon number diagram when an entangled state is exposed to optical loss. These paths are obtained by considering the effect of loss on Eqs. (4.3) and (4.4); calculating the individual variances of the quadratures of the entangled beams $\Delta^2\hat{X}_x^\pm$ and $\Delta^2\hat{X}_y^\pm$; and their sum and difference variances $\Delta^2\hat{X}_{x\pm y}^\pm$;[6] and applying these variances to Eqs. (4.38), (4.39) and (4.42). Several such paths are shown in Fig. 4.15 a) and b). Notice that for the relatively pure entangled states shown in Fig. 4.15 b), $\bar{n}_{\rm excess}$ actually increases with in-

---

[6] $\Delta^2\hat{X}_x^\pm$, $\Delta^2\hat{X}_y^\pm$, and $\Delta^2\hat{X}_{x\pm y}^\pm$ as a function of detection efficiency ϵ are given by Eqs. (4.65) and Eqs. (4.66) with $g_a = g_b = 0$.

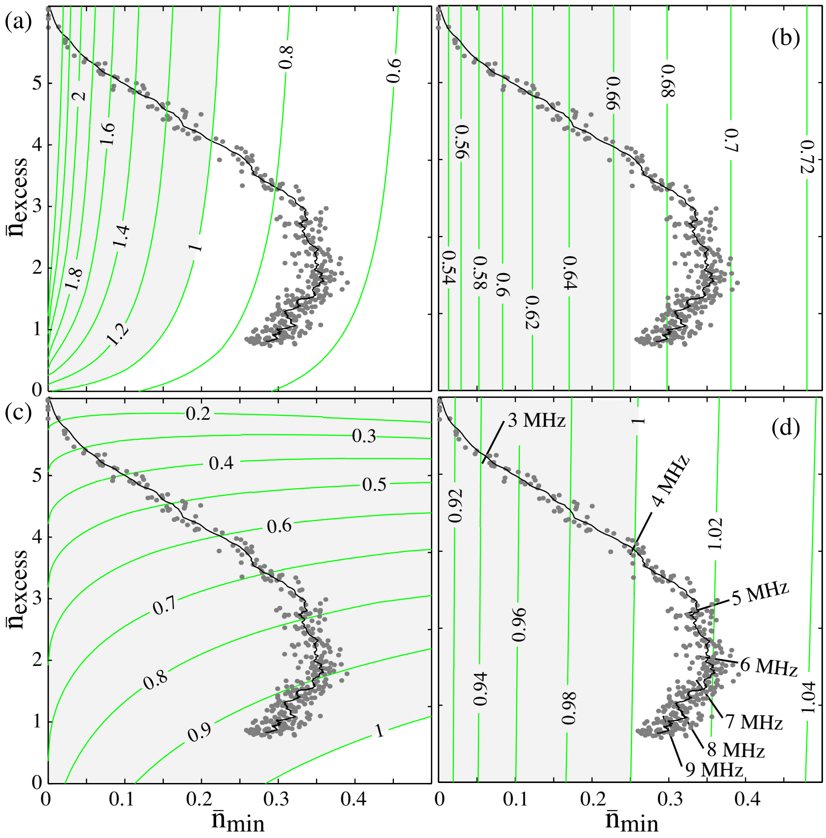

Figure 4.14: Two dimensional slice of the photon number diagram for $\bar{n}_{\text{bias}} = 0$. The contours on the plots are (a) the degree of EPR paradox, (b) the fidelity of quantum teleportation, (c) and (d) ratio of dense-coding channel capacity to optimum squeezed channel capacity for $\bar{n}_{\text{encoding}} = 3.375$ and $\bar{n}_{\text{encoding}} = 125$, respectively.

creasing loss. It is this relationship between purity and loss that causes the sensitivity of the degree EPR paradox to loss shown in Fig. 4.11. Clearly however, as the loss approaches 100 % the entangled state approaches an independent pair of vacuum states and $(\bar{n}_{\text{min}}, \bar{n}_{\text{bias}}, \bar{n}_{\text{excess}}) \rightarrow (0, 0, 0)$. So that in most cases $\bar{n}_{\text{excess}}$ decreases with increasing loss, and in some sense optical loss achieves our goal of reducing $\bar{n}_{\text{excess}}$. We can analyse the affect of optical loss on each of the protocols discussed in this Chapter simply by superimposing the efficacy contours of the protocol over the optical loss paths in the photon number diagram. Unsurprisingly, we find then that optical loss always degrades quantum teleportation and the degree of EPR paradox. In a dense coding protocol however, if the entangled state is highly impure and very few photons are available to encode signals the dense coding channel capacity can be worse than the channel capacity achievable using a vacuum state. Attenuating the entangled state will then enhance its channel capacity and the efficacy of the dense coding protocol. This attenuation will only improve the dense coding protocol whilst in the classical regime where $C_{\text{EPR}}/C_{\text{sqz}} < 1$, when $C_{\text{EPR}}/C_{\text{sqz}} > 1$ attenuation will only reduce C_{EPR}. So optical loss can not improve the efficacy of a dense coding protocol operating in the quantum regime.

Clearly, since the degree of inseparability of an entangled state is very sensitive to loss, simply adding loss is not a particularly effective technique. A much more sensible approach would be to use the light tapped off from the entangled state when loss is introduced to gain some information

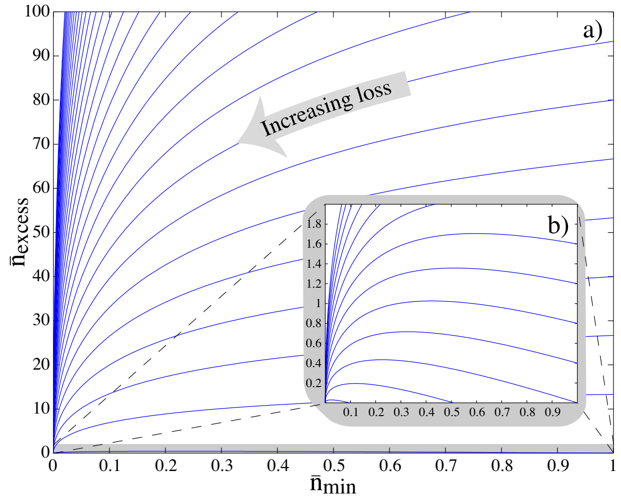

Figure 4.15: Paths mapped out onto the photon number diagram when loss is introduced to the entanglement, a) paths obtained over a broad area of the photon number diagram, b) paths obtained when the entanglement is relatively pure.

about the entangled state. A scheme to do this is shown in Fig. 4.16. A part of each entangled beam (dictated by the beam splitter ratio ϵ), is tapped off and then split in two. Amplitude and phase quadrature measurements are performed. The resulting photocurrents are correlated to the amplitude and phase quadratures of both entangled beams, and can be fed forward and applied to the entangled beams to reduce the impurity of the entanglement. Assuming that the entanglement is interchangeable and symmetric between the amplitude and phase quadratures, the variances of each entangled beam individually after the feedforward are given by

$$\Delta^2\hat{X}^{\pm}_{x,\text{feed}} = \Delta^2\hat{X}^{\pm}_{y,\text{feed}} \tag{4.63}$$

$$\begin{aligned} &= K_-^2\left(\Delta^2\hat{X}^{+}_{\text{sqz},1}+\Delta^2\hat{X}^{+}_{\text{sqz},2}\right)+K_+^2\left(\Delta^2\hat{X}^{-}_{\text{sqz},1}+\Delta^2\hat{X}^{-}_{\text{sqz},2}\right)\\ &\quad+\left(\sqrt{1-\epsilon}+g_b\sqrt{\frac{\epsilon}{2}}\right)^2+\frac{g_b^2}{2}+\frac{g_a^2}{2}\left(1+\epsilon\right), \end{aligned} \tag{4.64}$$

where the constants K_- and K_+ are

$$K_\pm=\frac{1}{2}\left(\sqrt{\epsilon}-\sqrt{\frac{1-\epsilon}{2}}\left(g_b\pm g_a\right)\right), \tag{4.65}$$

ϵ is the tap-off beam splitter ratio, and g_a and g_b are the feedforward gains for the signals encoded across the entangled beams and on the entangled beam they were obtained from, respectively. Likewise, the sum and difference variances are given by

$$\Delta^2\hat{X}^{\pm}_{x\pm y,\text{feed}}=4K_-^2\left(\Delta^2\hat{X}^{+}_{\text{sqz},1}+\Delta^2\hat{X}^{+}_{\text{sqz},2}\right)+2\left(\sqrt{1-\epsilon}+\sqrt{\frac{\epsilon}{2}}\left(g_b-g_a\right)\right)^2+\left(g_b-g_a\right)^2. \tag{4.66}$$

The effect of this feedforward technique on $\bar{n}_{\text{min}}$ and $\bar{n}_{\text{excess}}$ can be obtained, as above, by inserting $\Delta^2\hat{X}^{\pm}_{x,\text{feed}}$, $\Delta^2\hat{X}^{\pm}_{y,\text{feed}}$ and $\Delta^2\hat{X}^{\pm}_{x\pm y,\text{feed}}$ into Eqs. (4.38), (4.39) and (4.42). For each level of purity $\bar{n}_{\text{excess}}$ the beam splitter ratio ϵ and the feedforward gains g_a and g_b can be used to optimise $\bar{n}_{\text{min}}$,

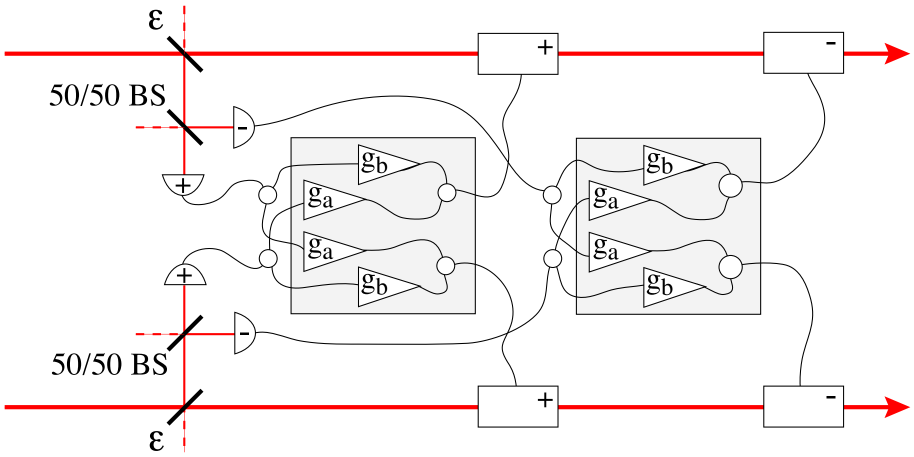

Figure 4.16: Schematic of a simple experiment to reduce $\bar{n}_{\text{excess}}$. BS: beam splitter, g_a and g_b: gains introduced to the detected signals before they are encoded on the entangled beams, detectors (modulators) labelled with the symbols + and - are amplitude and phase detectors (modulators) respectively.

this yields optimum paths on the photon number diagram for reducing $\bar{n}_{\text{excess}}$ whilst degrading $\bar{n}_{\text{min}}$ as little as possible. Some selected paths are displayed in Fig. 4.17, super-imposed on the photon number plot are efficacy contours for a dense coding protocol with $\bar{n}_{\text{encoding}} = 50$. We find again that neither quantum teleportation nor the degree of EPR paradox can be improved using this technique. In contrast to the optical loss paths discussed earlier however, $\bar{n}_{\text{excess}}$ can be very significantly reduced with very little change in $\bar{n}_{\text{min}}$. We can see from Fig. 4.17 that applying this feedforward technique before a dense coding protocol can facilitate the transition from $C_{\text{EPR}}/C_{\text{sqz}} < 1$ to $C_{\text{EPR}}/C_{\text{sqz}} > 1$. The **X** on Fig. 4.17 plots the ($\bar{n}_{\text{min}}$, $\bar{n}_{\text{excess}}$) co-ordinates of the Kerr-fiber soliton entangled pair recently generated by Silberhorn et. al [127]. Due to guided-acoustic-wave Brillouin scattering [157, 97] entanglement generated using Kerr-fiber soliton technology is inherently highly impure. This places significant limitations on the usefulness of this entanglement for protocols such as dense coding in which the number of photons used in the protocol is critical. We see that by using this simple feedforward procedure the purity of the entanglement of Silberhorn et. al [127] could be significantly improved. For the example considered here of dense coding with $\bar{n}_{\text{encoding}} = 50$ our feedforward protocol can improve the efficacy $C_{\text{EPR}}/C_{\text{sqz}}$ of the protocol from 0.23 to 1.01, and in the process takes $(\bar{n}_{\text{min}}, \bar{n}_{\text{excess}})$ from $(0.45, 98)$ to $(0.35, 8)$.

4.6 Conclusion

In conclusion, we have generated a strongly quadrature entangled state from the amplitude squeezed beams produced in Chapter 3. The correlation matrix of the state was characterised. We gauged the strength of the entanglement in the spirit of the Schrödinger picture by measuring the degree of inseparability, and in the spirit of the Heisenberg picture by measuring the degree of EPR paradox, with optimum results of $\mathcal{I} = 0.44 \pm 0.01$ and $\mathcal{E} = 0.58 \pm 0.02$, respectively. Through the introduction of controlled loss to each entangled beam, qualitative differences between the behavior of the degree of inseparability and the degree of EPR paradox were demonstrated. We proposed a photon number diagram to analyse the entanglement in a physically meaningful manner, and characterised the entanglement using this technique. On this diagram the average number of photons per bandwidth per time in the entangled state is separated into components required to

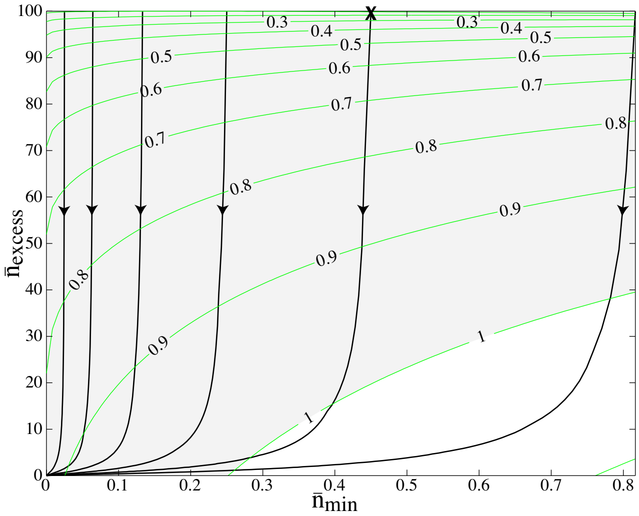

Figure 4.17: Optimum paths for the feedforward technique to reduce $\bar{n}_{\rm excess}$ represented on the photon number diagram. The contours represent the efficacy of a dense coding protocol using the entanglement for $\bar{n}_{\rm encoding} = 50$. **X** labels the ($\bar{n}_{\rm min}$, $\bar{n}_{\rm excess}$) co-ordinates of the experiment reported in [127].

maintain the strength of the entanglement, the bias between the amplitude and phase quadratures of the state, and the states impurity. We calculated efficacy contours for the degree of EPR paradox, quantum teleportation and dense coding protocols on the photon number diagram, and used them to predict the level of success achievable for each protocol using our entanglement. Finally, as a demonstration of the usefulness of the photon number diagram we investigated a simple feedforward scheme to reduce the mean number of photons per bandwidth per time in the entangled state present as a result of impurity. We found that this scheme could improve the channel capacity of a dense coding protocol from well below to above the optimum squeezed state channel capacity.

Chapter 5

Quantum teleportation

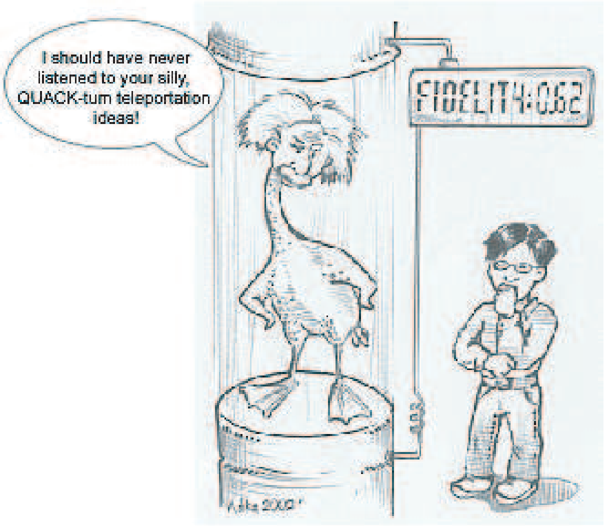

'Quack-tum teleportation' - Aśka Dolińska 2002

This Chapter investigates continuous variable quantum teleportation. Quantum teleportation can be thought of as the disembodied transportation of a quantum state from one place to another, and in our case the quantum state considered is the sideband state of an optical field. Some time is spent discussing methods that can be used to characterise this kind of teleportation. A new measure is introduced that is optimally designed to judge the success of teleportation when the output is an amplified or de-amplified version of the original state. This measure has particular relevance to entanglement swapping, where the teleportation protocol is used to teleport one half of an entangled state. We use the quadrature entanglement generated in the previous Chapter to experimentally implement quantum teleportation of a range of optical sideband states. Several regimes of teleportation are experimentally analysed, and the success of the protocol is characterised with each of the measures discussed.

A number of publications have resulted from the work presented in this Chapter:

- P. K. Lam, W. P. Bowen, and T. C. Ralph. *Quantum Teleportation with Einstein-Podolsky-Rosen Optical Entanglement.* The Physicist **39**, no. 3, pp. 72 (2002).
- W. P. Bowen, N. Treps, B. C. Buchler, R. Schnabel, T. C. Ralph, H.-A. Bachor, T. Symul, and P. K. Lam. *Experimental investigation of continuous variable quantum teleportation.* Physical Review A **67**, 032302 (2003).

- W. P. Bowen, P. K. Lam, T. C. Ralph. *Biased EPR entanglement and its application to teleportation.* Journal of Modern Optics **50**, pp. 801 (2003).
- W. P. Bowen, N. Treps, B. C. Buchler, R. Schnabel, T. C. Ralph, T. Symul and P. K. Lam. *Unity and non-unity gain quantum teleportation.* IEEE Journal of Selected Topics in Quantum Electronics 9, pp. 1519 (2003).

5.1 Introduction

Quantum teleportation was first proposed by Bennett *et al.* [122] in the discrete variable regime of single photon polarisation states. They showed that, by utilising entanglement, it was possible to perform a perfect quantum reconstruction of a state from classical destructive measurements. This technique in now of significant relevance to quantum information systems in terms of both communicating [158] and processing [159] quantum information. The first experimental demonstrations of quantum teleportation were performed in 1997 on the polarisation state of single photons [160]. Quantum teleportation has now been generalised to many other regimes, and has been demonstrated using liquid NMR ensembles [161], and optical field states [93, 111, 162]. Here we consider teleportation of the quadrature amplitudes of a light field [148, 150, 163]. This continuous variable optical teleportation has some significant advantages over its discrete variable counterpart. Much of the technology required is the same as that used in present-day communication systems, and the states are the encoded sidebands of an optical field. There is, therefore, a much higher bandwidth associated with the process than is achievable in the discrete variable regime. Low loss optics, and highly efficient detectors are also available; and the experimentally challenging Bell state measurements required for efficiencies above 25 % in most discrete variable teleportation experiments are not necessary.

Since the first demonstration of optical field state teleportation by Furusawa *et al.* [93], there has been considerable discussion about how continuous variable quantum teleportation may be performed using different systems [148, 163, 164, 165, 166]; applied to different input states [18, 167]; generalised to multi-party situations [168]; and comprehensively characterised [154, 169]. Given this intense interest, it is somewhat surprising that further continuous variable teleportation experiments have only been performed very recently. Zhang *et al.* [162] performed a detailed analysis and presented new results from the Furusawa et al. setup; and this Chapter presents results from a new teleportation experiment[111]. We summarise some of the discussion about how best to characterise continuous variable teleportation, and divide the process into two regimes: unity gain, and non-unity gain. We discuss each regime, and introduce a new measure for the non-unity gain regime, the gain normalised conditional variance product. A necessary and sufficient analysis of continuous variable entanglement swapping is given to emphasise the importance of the non-unity gain regime, and to demonstrate the significance of the gain normalised conditional variance product.

The teleportation protocol demonstrated here was, in many ways, very similar to the one used by Furusawa *et. al* [93]. It consisted of three parts: measurement (Alice), reconstruction (Bob), and generation and verification (Victor). There were some notable differences, however, in both the methods of input state measurement and of output state verification. In our experiment the input and output states were both analysed by Victor in the same homodyne detector, and in a location spatially separated from Alice and Bob. This spatial separation is in line with the original concept of quantum teleportation, and is important to ensure that Alice and Bob obtain no information about how Victor encodes the input state. If they do obtain information about the encoding they can use it to artificially improve the quality of Bob's reconstructed state. Our experiment is based on a Nd:YAG laser that produces two squeezed beams in two independently pumped optical parametric amplifiers (OPAs). As discussed in Chapter 3, using independent OPAs reduces the degradation of squeezing caused by green-induced-infrared-absorption which is presently one of the limiting factors in the Furusawa *et al.* teleportation setup. We use a more compact configuration for Alice's measurements which relies on only two detectors and one electronic locking loop, as opposed to the four detectors, two local oscillators, and two locking loops used in the Furusawa *et al.* experiment. The use of two independent modulators each for encoding of Victor's input state and Bob's reconstructed output state allows the phase space of the input state to be completely spanned, and the amplitude and phase quadrature teleportation gains to be accurately experimentally verified. The fidelity especially, is extremely sensitive to gain, so that in our experiment *a posteriori* verification of the applied gain was essential to confirm any fidelity results.

We analysed the efficacy of our experiment using three measures: fidelity $\mathcal{F}$; a T-V diagram of the signal transfer T_q and conditional variance product V_q between the input and output states; and the gain normalised conditional variance product $\mathcal{M}$. In the unity gain teleportation regime we used the fidelity, $\mathcal{F}$, between the input and output states to characterise the teleportation protocol, and observed an optimum of $\mathcal{F} = 0.64 \pm 0.02$ where $\mathcal{F} \leq 0.5$ when only classical resources are used. The fidelity degrades quickly as the teleportation gain moves away from unity, however, and is not an appropriate measure of non-unity gain teleportation. Instead, we use the signal transfer T_q and conditional variance V_q between the input and output states, in a manner analogous to QND analysis [148]. This enables a more detailed two dimensional characterisation of the performance of our teleporter. T_q and V_q both have physical significance. $T_q > 1$ ensured that Bob's output state contains more information about the input state than any other possible reconstruction, and $T_q = 1$ therefore defines an 'information cloning' limit. $V_q < 1$ is necessary to enable Bob to reconstruct non-classical features of the input state such as squeezing. We observe an optimum signal transfer of $T_q = 1.06 \pm 0.02 > 1$; and observe $V_q = 0.96 \pm 0.10 < 1$ and $T_q = 1.04 \pm 0.03 > 1$ simultaneously, at unity teleportation gain this would imply a fidelity surpassing the no-cloning limit. We analyse the gain normalised conditional variance product $\mathcal{M}$ introduced herein and demonstrate $\mathcal{M} < 1$ for a gain bandwidth from $g_{\min} = 0.58$ to $g_{\max} = 1.21$, with an optimum of $\mathcal{M} = 0.22 \pm 0.2$. Our teleportation protocol could be used to successfully perform entanglement swapping throughout this bandwidth.

5.2 Continuous variable teleportation protocol

Quantum teleportation is usually described as the disembodied transportation of a quantum state from one place (Alice) to another (Bob). Or in other words, it is a process that allows Bob to reconstruct a quantum state from measurements performed by Alice at time t_0, using only classical communication and local operations after time t_0 (see Fig. 5.1). The concept of quantum teleportation was first proposed [122] and demonstrated [160, 170] in the discrete variable regime of single, or few, photons. It has since then been generalised to the continuous variable regime [148, 150, 163], which is the setting of the majority of this thesis. In our work, as in that of Ref. [93], the teleported states are the sideband amplitude ($\hat{X}^+$) and phase ($\hat{X}^-$) quadratures of a bright optical beam. The uncertainty relation of Eq. (2.9) between these quadratures forbids the simultaneous exact knowledge of the amplitude and phase of an optical field and thus prevents perfect duplication or *quantum cloning*.

Until the proposal of Bennett *et. al* [122], uncertainty products were thought to fundamentally limit the quality of any teleportation protocol. Bennett proved that in the discrete regime this was not the case, by utilising shared entanglement between Alice and Bob. Since then many other

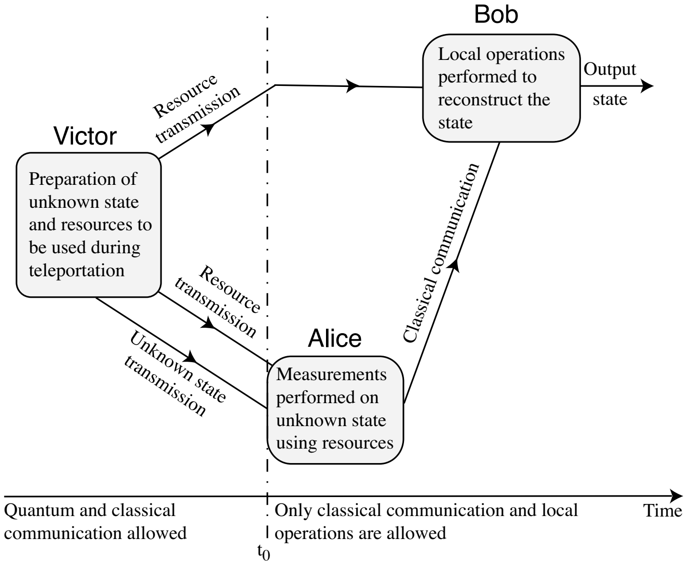

Figure 5.1: Time line for a quantum teleportation experiment.

teleportation protocols have been proposed (see for example [148, 149, 164, 171, 108, 172, 173, 174]), all of which rely on shared entanglement. In continuous variable quadrature teleportation protocols [148, 150, 163], Alice and Bob share a quadrature entangled pair, which in this work we restrict to be Gaussian. We generate Gaussian quadrature entanglement by combining two equally amplitude squeezed beams with a $\pi/2$ phase shift on a 50/50 beam splitter as discussed in Chapter 4. The outputs of this beam splitter are quadrature entangled, with the entanglement evidenced through strong amplitude/amplitude and phase/phase quadrature correlations between the beams. One of these entangled beams is sent to Alice and the other to Bob, as shown in Fig. 5.2. Victor provides an unknown input state to Alice who then interferes it with her entangled beam

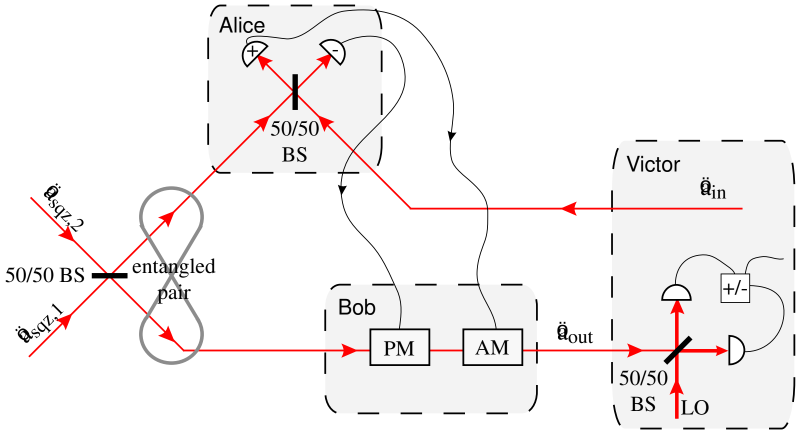

Figure 5.2: A continuous variable quantum teleportation protocol, AM: amplitude modulator, PM: phase modulator, BS: beam splitter.

and performs an amplitude quadrature measurement on one of the outputs and a phase quadrature measurement on the other. The measurement results are sent through classical communication to Bob, who encodes them using amplitude and phase modulators on his entangled beam. The frequency domain amplitude and phase quadratures of the output state produced can be written

$$\hat{X}^+_{\mathrm{out}} = g^+\hat{X}^+_{\mathrm{in}} + \frac{(1+g^+)}{\sqrt{2}}\hat{X}^+_{\mathrm{sqz},1} + \frac{(1-g^+)}{\sqrt{2}}\hat{X}^-_{\mathrm{sqz},2} \tag{5.1}$$

$$\hat{X}^-_{\mathrm{out}} = g^-\hat{X}^-_{\mathrm{in}} + \frac{(1+g^-)}{\sqrt{2}}\hat{X}^+_{\mathrm{sqz},2} + \frac{(1-g^-)}{\sqrt{2}}\hat{X}^-_{\mathrm{sqz},1}, \tag{5.2}$$

where the sub-scripts 'in' and 'out' label the input and output states respectively, $g^\pm = \langle\hat{X}^\pm_{\mathrm{out}}\rangle/\langle\hat{X}^\pm_{\mathrm{in}}\rangle = \alpha^\pm_{\mathrm{out}}/\alpha^\pm_{\mathrm{in}}$ are the amplitude and phase quadrature teleportation gains, and the sub-scripts 'sqz,1' and 'sqz,2' label the squeezed beams used to generate our quadrature entanglement. Assuming that the entanglement used in the teleportation protocol is produced by two equally amplitude squeezed beams with $\Delta^2\hat{X}_{\mathrm{sqz}} = \Delta^2\hat{X}^+_{\mathrm{sqz},1} = \Delta^2\hat{X}^+_{\mathrm{sqz},2} < 1$ and $\Delta^2\hat{X}_{\mathrm{anti}} = \Delta^2\hat{X}^-_{\mathrm{sqz},1} = \Delta^2\hat{X}^-_{\mathrm{sqz},2} > 1$, the quadrature variances of the output state are

$$\Delta^2\hat{X}^\pm_{\mathrm{out}} = g^{\pm2}\Delta^2\hat{X}^\pm_{\mathrm{in}} + \frac{(1+g^\pm)^2}{2}\Delta^2\hat{X}_{\mathrm{sqz}} + \frac{(1-g^\pm)^2}{2}\Delta^2\hat{X}_{\mathrm{anti}}. \tag{5.3}$$

We then see that for unity gain teleportation ($g^\pm = 1$), as $\Delta^2\hat{X}_{\mathrm{sqz}} \rightarrow 0$, the amplitude and phase quadratures of the output state approach those of the input ($\hat{X}^\pm_{\mathrm{out}} \rightarrow \hat{X}^\pm_{\mathrm{in}}$). So that, at least in the limit of perfect squeezing, perfect teleportation of the amplitude and phase quadratures of an optical field can be achieved. Of course, unity gain is not necessarily the only interesting operation point of a teleporter. In the following Section we discuss methods to characterise the success of teleportation in both the unity gain regime, and in other regimes.

5.3 Characterisation of teleportation

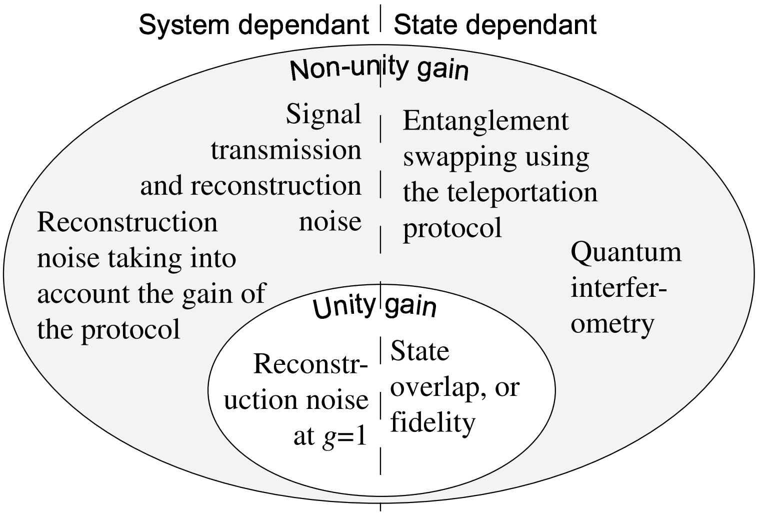

Figure 5.3: Approaches to characterisation of quantum teleportation.

There is some debate in the quantum optics community about specifically what constitutes continuous variable quantum teleportation [148, 154, 155, 169, 175, 176]. One approach is to restrict quantum teleportation to systems that produce output states identical to their input states but with noise convolution, i.e. for all operators involved $\hat{X}_{\mathrm{out}} = \hat{X}_{\mathrm{in}} + \hat{X}_{\mathrm{noise}}$ [154, 175]. We term this *unity gain* teleportation. The interesting aspect of quantum teleportation is that classical communication can be used to transmit quantum information. This can also be demonstrated in situations where the unity gain condition is not true, i.e. when $\hat{X}_{\rm out} = g\hat{X}_{\rm in} + \hat{X}_{\rm noise}$. Indeed under certain conditions optimum transmission of quantum information occurs for non-unity gain. We term this class of teleportation protocols *non-unity gain* teleportation.

A number of methods have been proposed to measure the success of quantum teleportation in both unity gain, and non-unity gain situations [148, 154, 176, 177]. These measures typically adopt either a *system dependent* or *state dependent* approach, as shown in Fig. 5.3. System dependent measures such as those introduced by Grangier and Grosshans [155] and Ralph and Lam [148] characterise the effect of the system on the input state, such as what noise it introduces, in a manner independent of the form of the input state. While state dependent measures such as the fidelity [177], quantum interferometry [176], and entanglement swapping [18] formulate relationships between the input and output states that cannot be satisfied through any classical means, and vary according to the form of the input state as well as the quality of teleportation. The transfer function approach of system dependent measures is perhaps more useful for characterisation of quantum communication networks; and the state dependent approach more relevant when fragile quantum states are being teleported. Ultimately, however, these two approaches should yield equivalent results.

5.3.1 Fidelity

The most well known and widely used measure of the success of a teleportation protocol is the *fidelity* of teleportation [177], which is state dependent. Fidelity measures the state-overlap between the input $|\psi_{\rm in}\rangle$ and output $\hat{\rho}_{\rm out}$ states, and is given by

$$\mathcal{F} = \langle\psi_{\rm in}|\hat{\rho}_{\rm out}|\psi_{\rm in}\rangle. \tag{5.4}$$

$\mathcal{F} = 1$ indicates that the output state is a perfect reconstruction of the input, and $\mathcal{F} = 0$ if the input and output states are orthogonal. The maximum fidelity achievable classically lies somewhere between these bounds and depends strongly on the input state. For pure input states the fidelity can be written in terms of the overlap of the Wigner functions (see Section 2.2.1) of the input and output states, which we label $W_{\rm in}(\hat{X}^+, \hat{X}^-)$ and $W_{\rm out}(\hat{X}^+, \hat{X}^-)$ respectively, here

$$\mathcal{F} = 2\pi \int_{-\infty}^{\infty}\int_{-\infty}^{\infty} W_{\rm in}(X^+, X^-) W_{\rm out}(X^+, X^-) dX^+ dX^-, \tag{5.5}$$

If the input state is coherent, and the entanglement resource and all other noise sources are Gaussian, the fidelity is given by

$$\mathcal{F} = \frac{2e^{-k^+ - k^-}}{\sqrt{(1 + \Delta^2\hat{X}^+_{\rm out})(1 + \Delta^2\hat{X}^-_{\rm out})}}, \tag{5.6}$$

where $k^\pm = {\alpha^\pm_{\rm in}}^2(1 - g^\pm)^2/(1 + \Delta^2\hat{X}^\pm_{\rm out})$. If the input state is selected from a sufficiently broad Gaussian distribution of coherent states (i.e, a set having a range of coherent amplitudes $\Delta\alpha^\pm_{\rm in} \gg 1$) in a manner unknown to Bob, the generally accepted classical limit to fidelity is $\mathcal{F}_{\rm class} = 1/2$. This classical limit is determined by considering the optimal teleportation protocol without the availability of an entanglement resource when a weighted average of the fidelity over the input state distribution is made. There is some debate however, about whether the *no-cloning limit* is more appropriate [154] since in the original teleportation paper of Bennett *et. al* they state “Of course Alices original $|\phi\rangle$ [$|\psi_{\rm in}\rangle$ here] is destroyed in the process, as it must be to obey the no-cloning theorem” [122]. For a sufficiently broad distribution of coherent states the no-cloning limit occurs at $\mathcal{F}_{\mathrm{no-cloning}} = 2/3$. Achieving $\mathcal{F} = 2/3$ ensures that Bob's reconstruction of the input state is better than any other possible reconstruction. There is, therefore, significance in experimentally surpassing both $\mathcal{F} = 1/2$ and $\mathcal{F} = 2/3$.

Notice that the fidelity of Eq. (5.6) has an exponential dependence on k^+ and k^-. The condition $\Delta\alpha_{\mathrm{in}}^{\pm} \gg 1$ (and therefore for some input states $\alpha_{\mathrm{in}}^{\pm} \gg 1$) for validity of $\mathcal{F}_{\mathrm{class}}$ and $\mathcal{F}_{\mathrm{no-cloning}}$, then results in a very strong dependence of the fidelity on gain. The optimum fidelity occurs at $g^{\pm} \approx 1$, and for the ideal case of an infinitely broad set of input states ($\Delta\alpha_{\mathrm{in}}^{\pm} \to \infty$), at $g^{\pm} = 1$. In a physically realistic situation however, there will be some error associated with $g^{\pm}$. The effect of this error on the fidelity as a function of the input coherent amplitude is shown in Fig. 5.4. No matter how small the gain error, as α_{in} increases the fidelity falls away towards zero. This puts an upper limit on the breadth of the distribution of states that the teleporter can handle and causes the values of $\mathcal{F}_{\mathrm{class}}$ and $\mathcal{F}_{\mathrm{no-cloning}}$ to become somewhat higher than the limits given above [178, 179]. In experiments to date, these issues have been avoided by strictly defining the fidelity as valid only when $g^{\pm} = 1$. In that case $k^{\pm} = 0$, and the fidelity becomes independent of α_{in}. Given this definition of fidelity, it is critical to experimentally verify $g^{\pm}$.

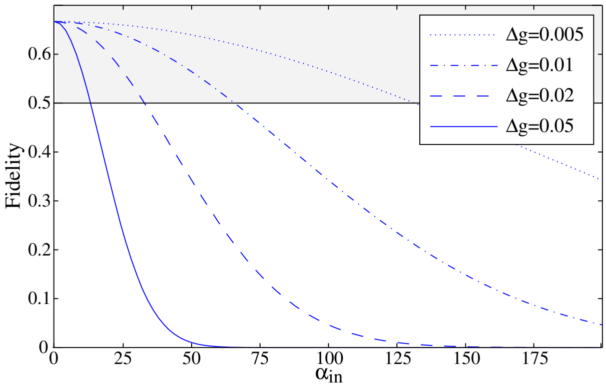

Figure 5.4: Fidelity as a function of coherent amplitude α_{in} for a range of teleportation gain errors $\Delta g = g - 1$, with 3 dB of squeezing ($\Delta^2\hat{X}_{\mathrm{sqz}} = 0.5$).

5.3.2 The conditional variance product and signal transfer

From a system dependent perspective, the ideal way to characterise a teleportation protocol is to identify exactly the transfer function of the protocol between the input and output states. This approach is relatively easy for protocols utilising Gaussian entanglement, which is the only form of continuous variable entanglement presently experimentally available. For the continuous variable quadrature teleportation discussed in this Chapter, only two variables for each quadrature need to be characterised to completely define the transfer function of the system. They are the teleportation gain, and the amount of noise (or degradation) introduced during the teleportation process. All that remains to be done is then to define bounds on the system that are impossible to exceed classically.

The first such approach was the work of Ralph and Lam [148]. They proposed a characterisation in terms of the conditional variance between the input and output states $\Delta^2\hat{X}^{\pm}_{\mathrm{in|out}} = \Delta^2\hat{X}^{\pm}_{\mathrm{out}} - |\langle\delta\hat{X}^{\pm}_{\mathrm{in}}\delta\hat{X}^{\pm}_{\mathrm{out}}\rangle|^2/\Delta^2\hat{X}^{\pm}_{\mathrm{in}}$, and the signal transfer from the input to the output state $T^{\pm} = \mathrm{SNR}^{\pm}_{\mathrm{out}}/\mathrm{SNR}^{\pm}_{\mathrm{in}}$ where $\mathrm{SNR}^{\pm} = (2\alpha^{\pm})^2/\Delta^2\hat{X}^{\pm}$ are conventional signal-to-noise ratios[1]. The conditional variance measures the noise introduced during the protocol, and the signal transfer is related to the gain of teleportation.

---

[1] The factor of two in the expression for the signal to noise ratio come from the definition $\hat{a} = \alpha + (\delta\hat{X}^{+} + i\delta\hat{X}^{-})/2$

Ralph and Lam demonstrated limits to both the joint signal transfer, and the joint conditional variance of the amplitude and phase quadratures that, in a teleportation protocol, can only be overcome by utilising entanglement. Alice's measurement is limited by the generalised uncertainty principle $\Delta^2\hat{M}^+\Delta^2\hat{M}^- \geq 1$ [180], where $\Delta^2\hat{M}^\pm$ are the measurement penalties, which holds for simultaneous measurements of conjugate quadrature amplitudes. In the absence of entanglement this places a strict limit on Bob's reconstruction accuracy which, in terms of quadrature signal transfer coefficients $T^\pm$, can be expressed as

$$T_q = T^+ + T^- - T^+T^- \left(1 - \frac{1}{\Delta^2\hat{X}^+_{\rm in}\Delta^2\hat{X}^-_{\rm in}}\right) \leq 1. \tag{5.7}$$

For minimum uncertainty input states ($\Delta^2\hat{X}^+_{\rm in}\Delta^2\hat{X}^-_{\rm in} = 1$), this expression reduces to $T_q = T^+ + T^-$. Perfect signal transfer would give $T_q = 2$.

Bob's reconstruction must be carried out on an optical field, the fluctuations of which obey the uncertainty principle. In the absence of entanglement, these intrinsic fluctuations remain present on any reconstructed field. Therefore, since the amplitude and phase conditional variances $\Delta^2\hat{X}^\pm_{\rm in|out}$ measure the noise added during the teleportation process, they must satisfy $\Delta^2\hat{X}^+_{\rm in|out}\Delta^2\hat{X}^-_{\rm in|out} \geq 1$. This can be written in terms of the quadrature variances of the input and output states and the teleportation gain as

$$V_q = \Delta^2\hat{X}^+_{\rm in|out}\Delta^2\hat{X}^-_{\rm in|out} = \left(\Delta^2\hat{X}^+_{\rm out} - g^{+2}\Delta^2\hat{X}^+_{\rm in}\right)\left(\Delta^2\hat{X}^-_{\rm out} - g^{-2}\Delta^2\hat{X}^-_{\rm in}\right) \geq 1 \tag{5.8}$$

A teleportation protocol that introduced no reconstruction noise would give $V_q = 0$. In the original paper of Ralph and Lam [148] they propose $\Delta^2\hat{X}^+_{\rm in|out} + \Delta^2\hat{X}^-_{\rm in|out} \geq 2$ as the conditional variance limit. For cases where the quadratures are symmetric, such as those considered by them [148, 18], both limits are equivalent. The product limit, however, is significantly more immune to asymmetry in the teleportation gain and provides a more rigorous bound in situations when the entanglement used in the protocol is asymmetric, we therefore prefer it here.

The criteria of Eqs. (5.7) and (5.8) enable teleportation results to be represented on a T-V graph similar to those used to characterise quantum non-demolition experiments [181]. The T-V graph is two dimensional, and therefore conveys more information about the teleportation process than single dimensional measures such as fidelity. It tracks the quantum correlation and signal transfer in non-unity gain situations, and identifies two particularly interesting regimes that are not evident from a fidelity analysis; the situation where the output state has minimum additional noise ($\min_g\{V_q\}$) which occurs in the regime of $g \leq 1$, and the situation when the input signals are transferred to the output state optimally ($\max_g\{T_q\}$) which occurs in the regime of $g \geq 1$.

Both the T_q and V_q limits have independent physical significance. If a signal has some inherent signal-to-noise ratio, and the noise is truly an unknown quantity, then even in a classical world, that signal-to-noise ratio can in no way be *a posteriori* enhanced. In the case of the teleportation protocol discussed here, Bob receives two signals, the amplitude and phase quadratures of a light field, with a total possible signal transfer of $T_{q,\rm max} = 2$. If Bob receives $T_{q,\rm Bob} = \xi$, then the most signal any other party can receive is $T_{q,\rm other} = 2 - \xi$. Therefore, if Bob surpasses $T_q = 1$ then he has received over half of the signal from Alice, and this forbids any others parties from doing so. This is an 'information cloning' limit that is particularly relevant in light of recent proposals for quantum cryptography [182]. Furthermore, if Bob passes the T_q limit at unity gain ($g^\pm = 1$), then Bob has beaten the no-cloning limit and has $\mathcal{F} \geq 2/3$. Surpassing the V_q limit is a necessary pre-requisite for reconstruction of non-classical features of the input state such as squeezing. The T-V measure coincides with the teleportation no-cloning limit when both $T_q = V_q = 1$. Clearly it is desirable that the T_q and V_q limits are simultaneously exceeded.

Information cloning and eavesdropper attacks

Consider that an eavesdropper (Eve) performs an attack on Bob's entangled beam utilising a beam splitter tap off, whilst allowing Alice to make full used of her entangled beam. As discussed above, Bob can guarantee that the signal transfer to his output state is better than to Eve's if he finds $T_q \geq 1$. Alice then, obliviously, performs her measurements and transmits the results to Bob - a transmission intercepted by Eve. Bob and Eve both then attempt to reconstruct the input state from Alice's measurements and their part of the entanglement. Fig. 5.5 a) shows Bob's T-V analysis of the teleportation protocol for various entanglement strengths with Eve tapping off 50 % of his entanglement. In this special case, we find that $T_q \leq 1$ for all entanglement strengths ($\Delta^2\hat{X}_{\rm sqz}$) and all teleportation gains g, with the equality $T_q = 1$ achievable for any entanglement strength at some gain. In fact, Bob is able to map out the entire physically realistic region of the T-V diagram with $T_q \leq 1$. Since the arrangement is symmetric, Eve obtains the same result. This special case defines the transition point between Bob successfully surpassing the information cloning limit, and Eve surpassing it.

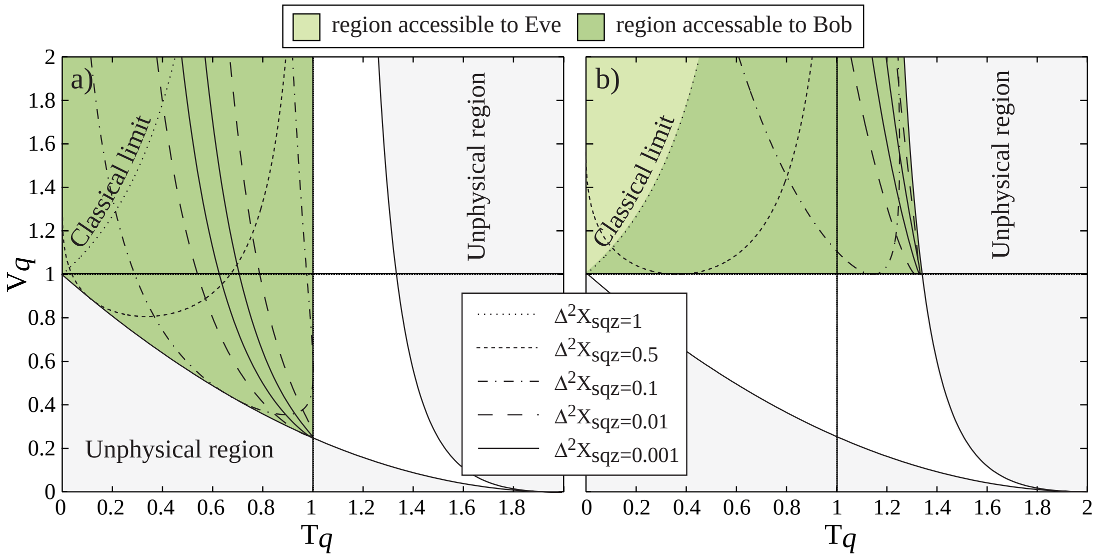

Figure 5.5: T-V diagram representation of teleportation with 50% loss introduced to a) Bob's or b) Alices entangled beam. The lines show the results of the protocol utilising various squeezing strengths as a function of teleportation gain. In a) Bob and Eve have identical accessible regions. In b) Eve can only access a small portion of the region accessible to Bob, as indicated by the shading.

It is interesting to consider the complimentary situation where Eve taps off a part of Alice's entanglement. In this case Eve can, again, use Alice's measurement results to attempt to reconstruct the input state. This time, however, the situation is not symmetric for Bob and Eve, and we find that Bob can surpass the information cloning limit. The conditional variance between his output state and the input is, however, limited to $V_q \geq 1$. For this situation we see from Fig. 5.5 b) that Bob can obtain results throughout the physically realistic region of the T-V diagram with $V_q \geq 1$. If Eve attempts to reconstruct the input state, however, she is restricted to the classical region of the T-V diagram.

5.3.3 A gain normalised conditional variance product

In their paper [155], Grangier and Grosshans discuss in some detail both the fidelity, and signal transfer and conditional variance, measures for teleportation. They restrict teleportation to occur only in the unity gain regime. In this case, the signal transfer and conditional variance criteria of Eqs. (5.7) and (5.8) become equivalent and Grosshans and Grangier propose that both are good measures of teleportation. One advantage that both their measure and fidelity have over the T-V diagram is that they provide a single number for the quality of the teleportation protocol. Although this does provide less information about the operation of the protocol, it allows different teleportation schemes to be directly compared. It is interesting to consider whether a single number can be used to characterise teleportation in the non-unity gain regime. In the following Section we will briefly reproduce Grosshans and Grangier's main results and generalise them to the non-unity gain regime.

Grosshans and Grangier quite generally denote the joint measurements $M^{\pm}$ performed by Alice on the input state as

$$M^{\pm} = \Lambda^{\pm}\hat{X}^{\pm}_{\text{in}} + \hat{N}^{\pm}_{\text{Alice}}, \tag{5.9}$$

where $\Lambda^{\pm}$ are amplitude and phase quadrature gains related to the detection, and $\hat{N}^{\pm}_{\text{Alice}}$ is the noise introduced during the measurement. Both $M^{\pm}$ are detected photocurrents so that $[M^{+}, M^{-}] = 0$. Given that the measurement noise is uncorrelated to the input state, one can easily obtain the Heisenberg uncertainty product

$$\Delta^2\hat{N}^{+}_{\text{Alice}}\Delta^2\hat{N}^{-}_{\text{Alice}} \geq |\Lambda^{+}\Lambda^{-}|^2, \tag{5.10}$$

and the signal transfer co-efficients from the input state to Alice's photo-currents are

$$T^{\pm}_{\text{Alice}} = \frac{\Lambda^{\pm 2}\Delta^2\hat{X}^{\pm}_{\text{in}}}{\Lambda^{\pm 2}\Delta^2\hat{X}^{\pm}_{\text{in}} + \Delta^2\hat{N}^{\pm}_{\text{Alice}}}. \tag{5.11}$$

Notice that $T^{\pm}_{\text{Alice}} \leq 1$ always, so that as stated earlier, T_q is bounded from above by two. Using the Heisenberg uncertainty product of Eq. (5.10) it is then possible to derive the same signal transfer bound as given in Eq. (5.7). Of course, Bob still has to reconstruct the input state on his output optical field. The output quadrature operators can be expressed quite generally as

$$\begin{aligned}
\hat{X}^{\pm}_{\text{out}} &= \Pi^{\pm}M^{\pm} + \hat{N}^{\pm}_{\text{Bob}} && (5.12)\\
&= \Pi^{\pm}\Lambda^{\pm}\hat{X}^{\pm}_{\text{in}} + \Pi^{\pm}\hat{N}^{\pm}_{\text{Alice}} + \hat{N}^{\pm}_{\text{Bob}} && (5.13)\\
&= g^{\pm}\hat{X}^{\pm}_{\text{in}} + \hat{N}^{\pm}_{\text{total}}, && (5.14)
\end{aligned}$$

where $\hat{N}^{\pm}_{\text{Bob}}$ are quadrature operators describing Bob's initial optical field, $\Pi^{\pm}$ are the amplitude and phase feedforward gains applied to Alice's measurements, and the teleportation gains $g^{\pm} = \Pi^{\pm}\Lambda^{\pm}$. $\hat{N}^{\pm}_{\text{total}} = \Pi^{\pm}\hat{N}^{\pm}_{\text{Alice}} + \hat{N}^{\pm}_{\text{Bob}}$ describe the total noise added to the amplitude and phase quadratures during the teleportation process, and for each quadrature the total noise variance is equal to the condition variance between the input and output states, $\Delta^2\hat{N}^{\pm}_{\text{total}} = \Delta^2\hat{X}^{\pm}_{\text{in}|\text{out}}$. Grosshans and Grangier observe that this output form dictates the Heisenberg uncertainty product

$$V_q = \Delta^2\hat{X}^{+}_{\text{in}|\text{out}}\Delta^2\hat{X}^{-}_{\text{in}|\text{out}} \geq (g^{+}g^{-} - 1)^2. \tag{5.15}$$

This implies that unless $g^{+}g^{-} = 1$ the output state must be degraded by some noise. They then restrict their analysis to the unity gain case ($g^+ = g^- = 1$) and, like Ralph and Lam [148], derive $V_q < 1$ as a classical limit for unity gain teleportation.

In this Section we wish to extend Grosshans and Grangier's analysis to provide a measure of non-unity gain teleportation based on V_q. Since $[\hat{N}^+_{\text{Bob}}, \hat{N}^-_{\text{Bob}}] = 2i$,

$$\Delta^2\hat{N}^+_{\text{Bob}}\Delta^2\hat{N}^-_{\text{Bob}} \geq 1. \tag{5.16}$$

In general, the noise introduced by Alice and Bob can be broken down into a part due to classical sources such as for example electrical pick-up (sub-script c), and a part due to quantum fluctuations (sub-script q) that are uncorrelated with each other, $\hat{N}^\pm_{\text{Bob}} = \hat{N}^\pm_{\text{Bob},c} + \hat{N}^\pm_{\text{Bob},q}$ and $\hat{N}^\pm_{\text{Alice}} = \hat{N}^\pm_{\text{Alice},c} + \hat{N}^\pm_{\text{Alice},q}$. Since we are interested in the lower bounds of V_q achievable without entanglement we neglect the classical noise term here, setting $\hat{N}^\pm_{\text{Bob}} = \hat{N}^\pm_{\text{Bob},q}$ and $\hat{N}^\pm_{\text{Alice}} = \hat{N}^\pm_{\text{Alice},q}$. In that case, if the noise introduced by Alice and Bob is separable (i.e. not entangled)

$$\begin{aligned} V_q &= \left({\Pi^+}^2\Delta^2\hat{N}^+_{\text{Alice}} + \Delta^2\hat{N}^+_{\text{Bob}}\right)\left({\Pi^-}^2\Delta^2\hat{N}^-_{\text{Alice}} + \Delta^2\hat{N}^-_{\text{Bob}}\right) && (5.17) \\ &= {\Pi^+}^2{\Pi^-}^2\Delta^2\hat{N}_{\text{Alice}}{}^+\Delta^2\hat{N}^-_{\text{Alice}} + \Delta^2\hat{N}^+_{\text{Bob}}\Delta^2\hat{N}^-_{\text{Bob}} \\ &\qquad + {\Pi^+}^2\Delta^2\hat{N}^+_{\text{Alice}}\Delta^2\hat{N}^-_{\text{Bob}} + {\Pi^-}^2\Delta^2\hat{N}^-_{\text{Alice}}\Delta^2\hat{N}^+_{\text{Bob}} && (5.18) \\ &\geq |g^+g^-| + 1 + {\Pi^+}^2\Delta^2\hat{N}^+_{\text{Alice}}\Delta^2\hat{N}^-_{\text{Bob}} + \frac{(\Lambda^+\Lambda^-\Pi^-)^2}{\Delta^2\hat{N}^+_{\text{Alice}}\Delta^2\hat{N}^-_{\text{Bob}}}. && (5.19) \end{aligned}$$

Some simple calculus shows that the right-hand-side of Inequality (5.19) is minimised when $\Delta^2\hat{N}^+_{\text{Alice}}\Delta^2\hat{N}^-_{\text{Bob}} = |\Lambda^+\Lambda^-\Pi^-/\Pi^+|$, and we find that

$$V_q \geq \left(|g^+g^-| + 1\right)^2. \tag{5.20}$$

For $g^+ = g^- = 0$ this classical limit is equivalent to that given in Eq. (5.8), and for non-zero gain it is stronger. We define the non-unity gain teleportation measure $\mathcal{M}$

$$\mathcal{M} = \frac{V_q}{(|g^+g^-| + 1)^2}, \tag{5.21}$$

where $\mathcal{M} < 1$ can only be achieved if the noise introduced by Alice and Bob is entangled. It is relatively easy to show that $\mathcal{M} = 1$ is achievable in the teleportation protocol discussed here, using no shared entanglement and for any teleportation gain. For non-unity gain ($g^+ \neq 1$ and/or $g^- \neq 1$) however, to observe $\mathcal{M} < 1$ Alice and Bob must both utilise local squeezing resources in their measurement and reconstruction processes.

Eq. (5.15) defines the minimum amount of noise added to the reconstructed state as a function of teleportation gain. This relationship dictates minimum physically achievable values for $\mathcal{M}$ as a function of gain.

$$\mathcal{M}_{\text{min}} = \frac{(g^+g^- - 1)^2}{(|g^+g^-| + 1)^2}. \tag{5.22}$$

Fig. 5.6 shows $\mathcal{M}$ as a function of gain for the teleportation protocol discussed in Section 5.2, with a range of utilised squeezing strengths. The optimum of $\mathcal{M}$ always occurs at $g = \sqrt{g^+g^-} = 1$, and improves as the strength of the entanglement used in the protocol increases (as $\Delta^2\hat{X}_{\text{sqz}} \rightarrow 0$). Notice that $\mathcal{M} = 0$ is only possible at $g = 1$, so that at $g \neq 1$ the output state, no matter what entanglement strength is utilised, will incur some reconstruction noise. It is interesting, however, that for all entanglement strengths $\mathcal{M}$ is less than unity for a wide range of gains. Some algebra shows that the gain extremema g_{min} and g_{max} for which $\mathcal{M} < 1$ are given by

$$g_{\text{max/min}} = \frac{\Delta^2\hat{X}_{\text{anti}} - \Delta^2\hat{X}_{\text{sqz}}}{\Delta^2\hat{X}_{\text{anti}} + \Delta^2\hat{X}_{\text{sqz}} - 2} \pm \sqrt{\left(\frac{\Delta^2\hat{X}_{\text{anti}} - \Delta^2\hat{X}_{\text{sqz}}}{\Delta^2\hat{X}_{\text{anti}} + \Delta^2\hat{X}_{\text{sqz}} - 2}\right)^2 - 1}. \tag{5.23}$$

Perhaps contrary to intuition, as the entanglement strength increases (as $\Delta^2\hat{X}_{\text{sqz}} \to 0$) the range of gain over which $\mathcal{M} < 1$ is satisfied decreases. In fact, if a teleportation protocol is intended to operate with a specific gain, a generally non-ideal entanglement strength ($\Delta^2\hat{X}_{\text{sqz,opt}} \neq 0$) exists for maximum efficacy of the protocol. If $g = 1$ then $\Delta^2\hat{X}_{\text{sqz,opt}} = 0$, but as $g \to 0$ or $g \to \infty$, $\Delta^2\hat{X}_{\text{sqz,opt}} \to 1$.

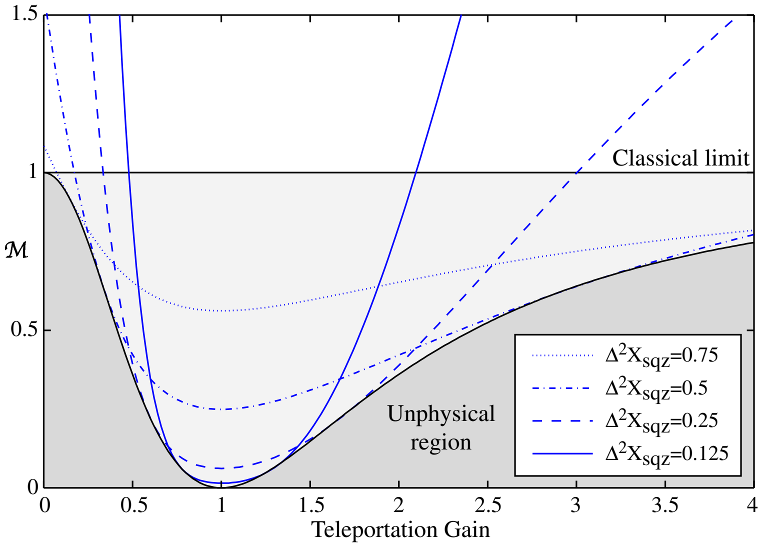

Figure 5.6: $\mathcal{M}$ as a function of teleportation gain for pure teleporter input squeezing ($\Delta^2\hat{X}_{\text{sqz}}\Delta^2\hat{X}_{\text{anti}} = 1$) with a range of strengths. The unphysical region here is defined by Eq. (5.22).

5.3.4 A comparison of fidelity, the T-V diagram, and the gain normalised conditional variance product

It is interesting to compare T-V based measures of teleportation with state dependent measures such as fidelity. The gain normalised conditional variance product $\mathcal{M}$ introduced in the previous Section can be directly compared to fidelity. It can be seen from Eq. (5.21) that $\mathcal{M}$, and in particular its gain bandwidth, is independent of the coherent amplitude α of the input state. This is not the case for fidelity, and as discussed earlier, it is this dependence that restricts the fidelity to $g = 1$. Fig. 5.7 shows the fidelity of teleportation for $\Delta^2\hat{X}_{\text{sqz}} = 0.125$ and a range of coherent amplitudes. The gain bandwidth of fidelity clearly depends very strongly on the input coherent amplitude, and in the limit of $\alpha \to \infty$ the gain bandwidth approaches zero, centered around $g = 1$.

Fig. 5.8 shows a similar result obtained through plotting fidelity contours directly on the T-V diagram. Here we show the fidelity contours at $\mathcal{F} = 1/2$ and $\mathcal{F} = 2/3$ for a range of input coherent amplitudes. From Fig. 5.8 a) we see that with no coherent amplitude the fidelity can be greater than $1/2$, or even $2/3$, for a large area of the T-V diagram, even in the purely classical region in the top left corner of the diagram. As the input coherent amplitude increases through Fig. 5.8 b), c) and d) the area of the T-V diagram in which $\mathcal{F} > 1/2$ or $\mathcal{F} > 2/3$ collapses down

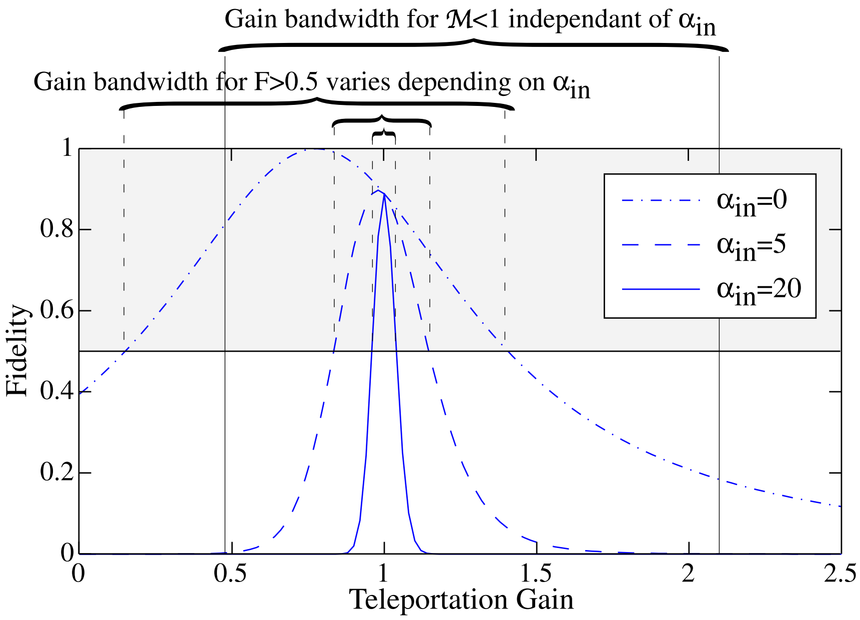

Figure 5.7: Fidelity as a function of teleportation gain for $\Delta^2\hat{X}_{\rm sqz} = 0.125$, $\Delta^2\hat{X}_{\rm anti} = \Delta^2\hat{X}_{\rm sqz}{}^{-1}$, and a range of input coherent amplitudes $\alpha_{\rm in}$.

to the line defining $g = 1$. We see that for large input coherent amplitudes $\mathcal{F} > 1/2$ can not be achieved in the classical region of the T-V diagram, and $\mathcal{F} > 2/3$ can only be achieved if both $V_q < 1$ and $T_q > 1$. Of course, if we restrict ourselves to the unity gain line then this is true for all coherent amplitudes.

The distinction between fidelity and the conditional variance product based approaches is in some sense unsurprising. The T-V diagram and $\mathcal{M}$ are explicitly designed to be state independent, whilst fidelity is almost as explicitly state dependent. There are some consequences of this distinction regarding the experimental verification of the teleportation process. Characterisation of T-V and $\mathcal{M}$ makes use of known test states to determine the transfer function of the teleporter. Provided the teleporter is not biased towards the test states, their particular form is irrelevant. On the other hand, characterisation of fidelity uses a set of states representative of the assumed ensemble of unknown input states. In particular, for validity of the coherent state teleportation limits $\mathcal{F}_{\rm class} = 1/2$ and $\mathcal{F}_{\rm no-cloning} = 2/3$, the test states must have a sufficiently large range of coherent amplitudes to represent a broad distribution. The fidelity is then highly gain dependent, as we have seen from Figs. 5.7 and 5.8. In this sense fidelity is a stronger test of quantum teleportation since it requires both high precision quantum and classical control. On the other hand, it becomes essential to accurately characterise the teleportation gain.

5.3.5 Entanglement swapping

To illustrate why non-unity gain teleportation is of interest we will consider the example of continuous variable entanglement swapping. Entanglement swapping utilising a continuous variable teleportation protocol was first introduced by Polkinghorne and Ralph [18]. They showed that in a polarisation teleportation protocol, effectively comprising of two quadrature teleporters, if the input is one of a pair of polarisation entangled photons, then the output and the other polarisation entangled photon can violate a Clauser-Horne-type Inequality [183]. An interesting result of their work was that when weak continuous variable entanglement was used in the teleportation protocol,

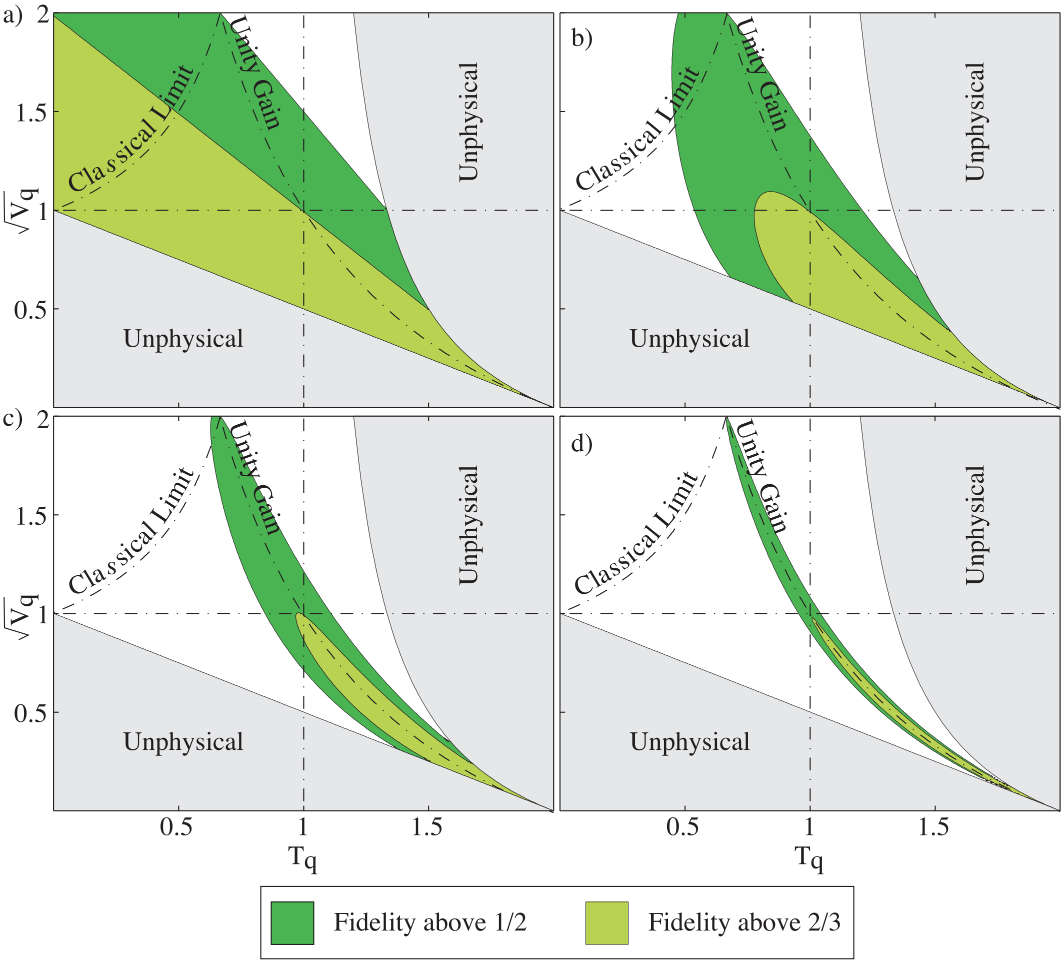

Figure 5.8: Fidelity contours for $\mathcal{F} = 1/2$ and $\mathcal{F} = 2/3$ and several coherent amplitudes, represented on the T-V diagram. a) $\alpha_{\text{in}} = 0$, b) $\alpha_{\text{in}} = 2$, c) $\alpha_{\text{in}} = 5$, and d) $\alpha_{\text{in}} = 15$.

entanglement swapping could only be achieved for teleportation gain less than unity ($g^{\pm} < 1$). In this Section we consider entanglement swapping of quadrature entanglement using a quadrature teleportation protocol. This type of entanglement swapping has been considered previously by Tan [146], by van Loock and Braunstein [184], and more recently by Zhang *et. al* [185].

Tan [146] considered entanglement swapping using a unity gain teleportation protocol ($g = 1$). He defined successful entanglement swapping to occur when the inequality $\langle(\delta\hat{X}_x^+ - \delta\hat{X}_y^+)^2\rangle + \langle(\delta\hat{X}_x^- + \delta\hat{X}_y^-)^2\rangle \geq 4$ is violated, where the sub-scripts x and y label the two sub-systems that the entanglement is being interrogated over. This is a sufficient criterion for the inseparability of sub-systems x and y. Tan then showed that entanglement swapping occurs successfully if the squeezed beams used to generate the entanglement both used in, and input to, the teleportation protocol have at least 3 dB of squeezing. van Loock and Braunstein considered a more complex system, where the output entanglement from the entanglement swapping protocol is used to teleport a coherent state [184]. They allowed non-unity gain in the entanglement swapping teleporter, but not in the coherent state teleporter, and characterised the success of entanglement swapping by the fidelity of the coherent state teleportation as defined in Eq. (5.6). Violation of the criterion $\mathcal{F} \leq 0.5$ is however, equivalent to violation of the criterion used by Tan, the significant difference between the two papers was the use of non-unity gain teleportation by van Loock and Braunstein. With this extra degree of freedom van Loock and Braunstein showed that entanglement swapping could be performed for any non-zero input squeezing. Zhang *et. al* [185] performed a similar analysis to that of van Loock and Braunstein but proposed an alternative experimental configuration.

The entanglement swapping protocols discussed above characterised success with sufficient but not necessary conditions for entanglement. Some situations in which the entanglement swapping was successful were therefore not identified. Here, we will consider entanglement swapping in more detail, using the inseparability criterion proposed by Duan *et al.* [130] and introduced in Chapter 4 to characterise the success of the process. The inseparability criterion relies on the identification of separability with positivity of the P-function, and is a necessary and sufficient criterion for the presence of entanglement. Eq. (4.25) defines the *degree of inseparability* of the quadrature amplitudes of a pair of beams, where they are entangled if $\mathcal{I} < 1$. Here, we optimise the gain k in Eq. (4.25) to minimise $\mathcal{I}$. Note that if k is restricted to unity this criterion becomes equivalent to the entanglement criterion used by Tan [146]. We use the degree of inseparability to characterise the strength of quadrature entanglement between a pair of optical beams before one is sent through a teleporter $\mathcal{I}_{\rm initial}$, and afterwards $\mathcal{I}_{\rm final}$.

We utilise the teleportation protocol given in Fig. 5.2, with the output defined by Eqs. (5.1) and (5.2). The second quadrature entangled pair required for entanglement swapping can be produced identically to the one used for teleportation, by combining two amplitude squeezed beams on a 50/50 beam splitter. The entangled pair can then be described by the quadrature operators $\hat{Y}_x^{\pm}$ and $\hat{Y}_y^{\pm}$

$$\hat{Y}_x^{\pm} = \frac{\hat{Y}^{\pm}_{\rm sqz,1} + \hat{Y}^{\mp}_{\rm sqz,2}}{\sqrt{2}} \tag{5.24}$$

$$\hat{Y}_y^{\pm} = \frac{\hat{Y}^{\pm}_{\rm sqz,1} - \hat{Y}^{\mp}_{\rm sqz,2}}{\sqrt{2}}, \tag{5.25}$$

where $\hat{Y}^{\pm}_{\rm sqz,1}$ and $\hat{Y}^{\pm}_{\rm sqz,2}$ are quadrature operators describing the amplitude squeezed beams used to generate the entanglement. We replace the operators describing the teleporter input state in Eqs. (5.1) and (5.2) with those from entangled beam x

$$\hat{X}^{\pm}_{\rm in} = \hat{Y}^{\pm}_x = \frac{\hat{Y}^{\pm}_{\rm sqz,1} + \hat{Y}^{\mp}_{\rm sqz,2}}{\sqrt{2}}. \tag{5.26}$$

We then determine $\mathcal{I}_{\rm final}$ between the quadratures of the output from the teleportation protocol $\hat{X}^{\pm}_{\rm out}$ and those from the second entangled beam $\hat{Y}^{\pm}_y$. For simplicity, here we assume that the input entangled state is symmetric and pure so that $\Delta^2\hat{Y}_{\rm sqz} = \Delta^2\hat{Y}^{+}_{\rm sqz,1} = \Delta^2\hat{Y}^{+}_{\rm sqz,2} < 1$ and $\Delta^2\hat{Y}_{\rm anti} = \Delta^2\hat{Y}^{-}_{\rm sqz,1} = \Delta^2\hat{Y}^{-}_{\rm sqz,2} = 1/\Delta^2\hat{Y}_{\rm sqz} > 1$. $\mathcal{I}_{\rm final}$ as a function of the teleportation gain $g = g^+ = g^-$ is shown in Fig. 5.9. Fig. 5.9 a) shows $\mathcal{I}_{\rm final}$ for $\mathcal{I}_{\rm initial} = 0.5$, ($\Delta^2\hat{Y}_{\rm sqz} = 0.5$) and for a range of teleportation efficacies (or in other words, a range of $\Delta^2\hat{X}_{\rm sqz}$). The degree of inseparability is, of course, degraded by the entanglement swapping procedure. We see, however, that the procedure is successful ($\mathcal{I}_{\rm final} < 1$) over a wide range of teleportation gains, and that, unlike the analysis of [18], it is always successful for $g = 1$. This difference is due to the more stringent nature of Clauser-Horne-type inequalities compared to tests of the presence of entanglement. Interestingly, optimal entanglement swapping ($\min_g\{\mathcal{I}_{\rm final}\}$) occurs at teleportation gain $g_{\rm opt}$ below unity in all cases except for the unphysical situations when $\Delta^2\hat{X}_{\rm sqz} \to 0$ or $\Delta^2\hat{Y}_{\rm sqz} \to 0$.

$$g_{\rm opt} = 1 - \frac{2(\Delta^2\hat{X}_{\rm sqz} + \Delta^2\hat{Y}_{\rm sqz})}{\Delta^2\hat{X}_{\rm sqz} + \Delta^2\hat{X}^{-1}_{\rm sqz}o + \Delta^2\hat{Y}_{\rm sqz} + \Delta^2\hat{Y}^{-1}_{\rm sqz}} \tag{5.27}$$

It can be shown that at this optimal point $k = 1$ so that the inseparability criterion of Eq. (4.25) becomes equivalent to the criteria of Tan [146] and van Loock and Braunstein [184]. Unsurprisingly then, the optimum gain for entanglement swapping derived here is in agreement with that of van Loock and Braunstein [184]. For $g \neq g_{\rm opt}$ however, it is no longer true that $k = 1$, so that the gain bandwidth for successful entanglement swapping we present here is wider than what could be obtained using the schemes of Tan, or van Loock and Braunstein.

Fig. 5.9 b) shows the same result as Fig. 5.9 a) but with stronger initial entanglement ($\mathcal{I}_{\rm initial} = 0.1$). Unsurprisingly, in this case the optimal final degree of inseparability is better than the previous example, and the optimal gain is closer to unity. Notice however that, for a given $\Delta^2\hat{X}_{\rm sqz}$, the gain bandwidth for successful entanglement swapping is the same in both Fig. 5.9 a) and b). Calculation of this gain bandwidth yields the same bandwidth as is given in Eq. (5.23) for $\mathcal{M} < 1$. We see that the entanglement swapping gain bandwidth only depends on the variances of the squeezed beams used in the teleportation protocol, and is independent of the strength of the input entanglement. The fact that the gain bandwidth for entanglement swapping corresponds exactly to that for $\mathcal{M}$ is a clear indication of the relevance of $\mathcal{M}$ as a measure for non-unity gain teleportation. In fact, if the input entanglement is perfect ($\Delta^2\hat{Y}_{\rm sqz} \rightarrow 0$), the degree of inseparability for the entanglement swapping protocol discussed here becomes equivalent to $\mathcal{M}$

$$\mathcal{I}_{\Delta^2\hat{Y}_{\rm sqz}\rightarrow 0} = \sqrt{\mathcal{M}} \tag{5.28}$$

5.4 Experiment

This Section describes our experimental teleportation protocol. In the following part we describe the teleportation protocol itself, and in Section 5.4.2 we analyse the protocol in terms of fidelity, signal transfer and conditional variance, and the gain normalised conditional variance. Finally, in Section 5.4.3 we discuss some of the experimental loopholes associated with quantum teleportation.

5.4.1 Teleportation apparatus

Fig. 5.10 illustrates the optical (Fig. 5.10 a)) and electrical (Fig. 5.10 b)) configuration for our teleportation protocol. The apparatus consisted of three distinct parts: measurement (Alice), reconstruction (Bob), and generation and verification (Victor). At the generation stage Victor generated the input signal by independently amplitude and phase modulating an optical beam at 8.4 MHz. This produced a coherent state at 8.4 MHz with a coherent amplitude unknown to either Alice or Bob. He could then measure the Wigner function of this input state in a homodyne detector. Assuming that the input state is Gaussian however, Victor need only characterise the amplitude and phase quadratures to completely define the state. We make that assumption here, we lock Victor's homodyne to the amplitude quadrature using a PDH-type error signal, and to the phase quadrature by balancing the power to the two detectors incorporated in the homodyne detector (see Fig. 5.10 b)). Victor then shared this fully characterised input state with Alice. Alice interfered it with one of our entangled beams with $\pi/2$ phase shift on a 50/50 beam splitter. The absolute intensities of the entangled beam and the input signal beam were arranged to be identical. Alice then detected the two beam splitter outputs with identical detectors, the detector darknoise was 10 dB below the quantum noise of the input beam. The sum of the two output photocurrents gave a measure of the amplitude quadrature of the signal, degraded by the amplitude quadrature of the

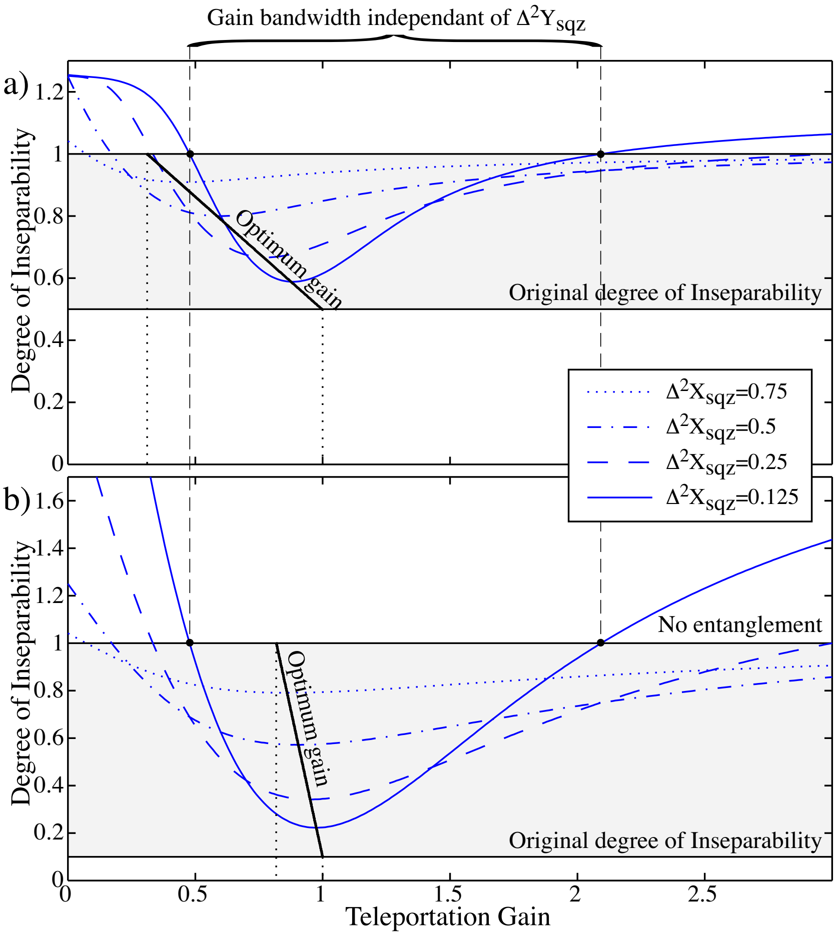

Figure 5.9: Degree of entanglement between a pair of entangled beams after one is teleported as a function of the teleportation gain. a) $\Delta^2\hat{Y}_{\rm sqz} = 0.5$, b) $\Delta^2\hat{Y}_{\rm sqz} = 0.1$.

entangled beam; and likewise, the difference photocurrent measured the phase quadrature of the signal, degraded by the phase quadrature of the entangled beam. Notice that it is this mixing of the fluctuations from the signal and the entanglement that allows quantum teleportation to be performed successfully. If Alice gains information about the quantum fluctuations of the input state through her measurements, then the Heisenberg uncertainty principle dictates that Bob's reconstruction must be degraded. The stronger the entanglement used in the protocol, the better the signal quadratures can be shrouded and therefore, the smaller the degradation required of Bob's reconstruction.

Alice sent her two photocurrents to Bob. Bob could then, if he wanted, simply encode those photocurrents using an amplitude and a phase modulator on his entangled beam. Typically however, the loss introduced by modulators is non-trivial, and would degrade Bob's reconstruction of the input state. Instead we applied the photocurrents to a bright coherent optical beam, and combined this encoding beam and Bob's entangled beam with controlled phase on a 98/2 beam splitter. One beam splitter output was Bob's reconstructed output state. This scheme negates the loss introduced by the modulators, and the only loss introduced to the entanglement by Bob is then the 2 % due to the beam splitter ratio. The attenuation of the signals modulated onto the encoding beam caused by the 98/2 beam splitter was counter-acted by Bob simply increasing the gain of his encoding by a factor of 50.

Bob then provided Victor with his reconstructed state. Victor used a removable mirror to

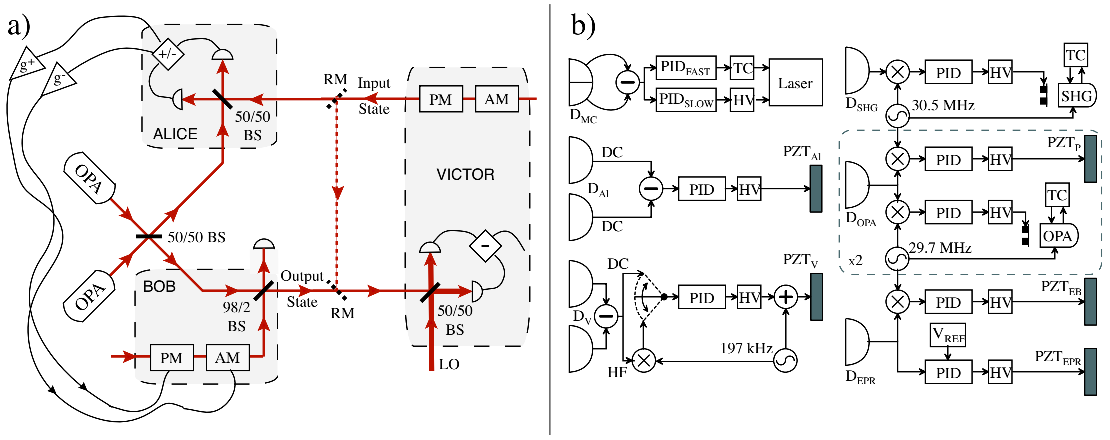

Figure 5.10: a) Optical and b) electronic apparatus for the teleportation protocol. RM: removable mirror; HV: high voltage amp; PID: proportional, integral, differential locking servo; TC: temperature controller; $D_{\rm SHG}$: SHG locking detector; $D_{\rm OPA}$: OPA locking detector; $D_{\rm EPR}$: entanglement and encoding beam locking detector; $D_{\rm MC}$: mode cleaner locking detector; $D_{\rm Al}$: Alice homodyne locking detector; $D_{\rm V}$: Victor homodyne locking detector; PZT: piezoelectric crystal; $PZT_{\rm P}$: OPA green phase PZT; PZT_{EB}: encoding beam PZT; PZT_P: OPA green phase PZT; PZT_{EPR}: entanglement locking PZT; PZT_{Al}: Alice's PZT; PZT_V: Victor's PZT.

switch his homodyne detector input to the output state. By making amplitude and phase quadrature measurements, he was then able to fully characterise the output state, and judge how well the teleportation had been performed. Normally inefficiencies in the teleportation protocol would be expected to degrade Victor's judgement of how well the process has been performed. There is one notable exception to this rule however, that of loss in Victor's homodyne. This loss appears erroneously to Victor to enhance the process, and must be accounted for. The combined loss from Victor's homodyne mode-matching and detector photodiodes was characterised and found to be $15\ \% \pm 2\ \%$. This loss was inferred out of the final results obtained by Victor.

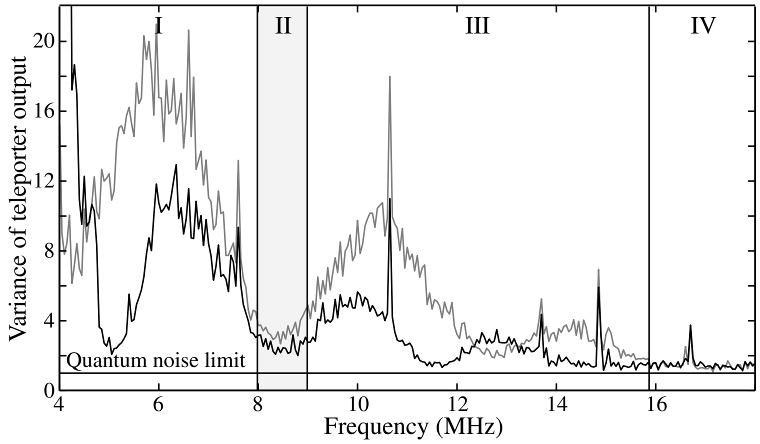

Figure 5.11: Spectral variance of the amplitude $\Delta^2\hat{X}^+_{\rm out}$ (dark trace) and the phase $\Delta^2\hat{X}^-_{\rm out}$ (light trace) quadratures of the teleported signal, normalised to the quantum noise limit of Victor's homodyne detector. The teleportation gain and feedforward phase vary over the spectra dependent on the response function of our detectors and feedforward loops. I: $g > 1$, II: $g \approx 1$, III: $g < 1$, IV: $g \approx 0$.

To characterise the behavior of our detectors and feedforward loop we analysed the amplitude and phase quadrature frequency spectra of the output state received by Victor over a wide frequency range, with $g_{8.4\,\mathrm{MHz}} \approx 1$ and no input coherent amplitude. These frequency spectra are presented in Fig. (5.11). The transfer functions of the detectors and feedforward loop, and the frequency dependence of our entanglement all have a bearing on the output spectra. A definite phase relationship must be maintained between the fed-forward signal and the fluctuations of the second entangled beam to get maximum cancellation of the fluctuations from the entanglement. The phase response of our electronics, BNC cables, and detectors is not flat, causing cycling of the relative phase, this results in cycling between maximum and minimum cancellation of the entangled beam fluctuations. We see this in Fig. (5.11) as a sinusoidal modulation of both the amplitude and phase spectra with 3-4 MHz period. We arranged the feedforward phase so that a maximum cancellation point occurred at 8.4 MHz for both the amplitude and phase quadratures. The amplitude of the sinusoidal modulation depends on both the amplitude response of our electronics and the size of the quadrature fluctuations of our entangled beams. Over the frequency range of the measurements presented in Fig. (5.11) both the response of our electronics, and the amplitude and phase quadrature variances of our entanglement ($\Delta^2\hat{X}_x^{\pm}$ and $\Delta^2\hat{X}_y^{\pm}$) decrease with increasing frequency. At low frequencies (region I) we then have $g > 1$ and this, coupled with the large variances of our entangled beams, results in the sinusoid having a large amplitude. Around 8.4 MHz (region II) $g \approx 1$ and the feedforward phase is optimised, so that $\Delta^2\hat{X}_{\mathrm{out}}^{\pm}$ are minimised, this is the region in which we performed our teleportation protocol. At higher frequencies (region III) $g < 1$ so that the feedforward has a smaller effect on the output variances, and in region IV there is effectively no feedforward ($g \approx 0$) and the output variances is simply the variance of Bob's entangled beam. With careful engineering of the feedforward loop electronics, and smart choice of Bob's optical beam path and the length of the feedforward electronic cables, a flat frequency response could probably have been achieved, this is perhaps a goal for later experiments.

5.4.2 Teleportation results

A sample of the data obtained from our teleporter is shown in Fig. 5.12. Parts (a) and (b) show the amplitude and phase quadrature noise of the output state at 8.4 MHz measured by Victor, as a function of time. The complete system maintained lock for long periods. Given the assumption that all noise sources introduced during the teleportation process, including the entanglement and the input state, were Gaussian, Fig. 5.12 (c) and (d) contain suffice information to fully characterise the teleportation run. Every teleportation run consisted of four spectra such as these, as well as a quantum noise calibration (not shown). Also drawn in each part of Fig. 5.12 are lines corresponding to the classical limit (solid line @ 4.8 dB) and the no-cloning limit (dashed line @ 3 dB). The data in (c) and (d) show Victor's measurement of the amplitude and phase quadratures over a 100 kHz bandwidth centered around 8.4 MHz. Over this range the noise floor of the system was constant, which could be easily verified by switching the coherent amplitude of the input state off and on. We obtained $\Delta^2\hat{X}_{\mathrm{in}}^{\pm}(8.4\,\mathrm{MHz})$ and $\Delta^2\hat{X}_{\mathrm{out}}^{\pm}(8.4\,\mathrm{MHz})$ respectively, from the average of $\Delta^2\hat{X}_{\mathrm{in}}^{\pm}(\omega)$ and $\Delta^2\hat{X}_{\mathrm{out}}^{\pm}(\omega)$ at nearby frequencies. Henceforth, if the ω in expressions such as these is neglected it implies that the measurement is at 8.4 MHz, (for example $\Delta^2\hat{X}_{\mathrm{in}}^{\pm} = \Delta^2\hat{X}_{\mathrm{in}}^{\pm}(8.4\,\mathrm{MHz})$).

$$\begin{aligned}
\Delta^2\hat{X}_{\mathrm{in}}^{\pm} &= \frac{\int_{8.35\,\mathrm{MHz}}^{8.37\,\mathrm{MHz}} \Delta^2\hat{X}_{\mathrm{in}}^{\pm}(\omega)d\omega + \int_{8.43\,\mathrm{MHz}}^{8.45\,\mathrm{MHz}} \Delta^2\hat{X}_{\mathrm{in}}^{\pm}(\omega)d\omega}{0.04\,\mathrm{MHz}} \\
\Delta^2\hat{X}_{\mathrm{out}}^{\pm} &= \frac{\int_{8.35\,\mathrm{MHz}}^{8.37\,\mathrm{MHz}} \Delta^2\hat{X}_{\mathrm{out}}^{\pm}(\omega)d\omega + \int_{8.43\,\mathrm{MHz}}^{8.45\,\mathrm{MHz}} \Delta^2\hat{X}_{\mathrm{out}}^{\pm}(\omega)d\omega}{0.04\,\mathrm{MHz}}
\end{aligned}$$

Using $\Delta^2\hat{X}_{\mathrm{in}}^{\pm}$ and $\Delta^2\hat{X}_{\mathrm{out}}^{\pm}$ it was then possible to extract the input and output coherent amplitudes ($\alpha^{\pm}$) from the input $\Delta^2\hat{M}_{\mathrm{in}}^{\pm}$ and output $\Delta^2\hat{M}_{\mathrm{out}}^{\pm}$ variance measurements at 8.4 MHz (see

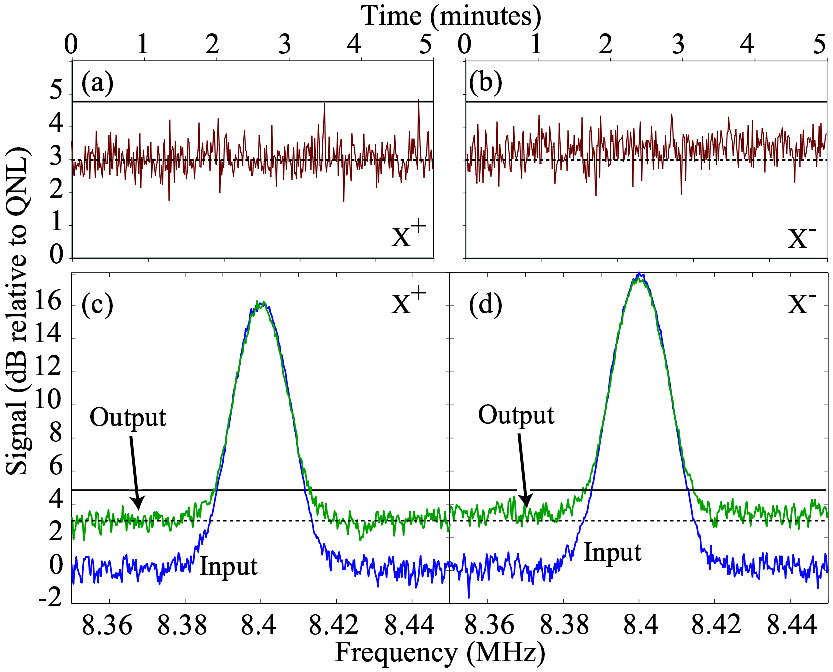

Figure 5.12: The input and output states of the teleporter, as measured by Victor. (a) and (b) show the amplitude and phase noise of the output state at 8.4 MHz. (c) and (d) show the input and output of the teleporter, when probed with a signal at 8.4 MHz. In all cases, the dotted line is the no-cloning limit, while the solid line is the classical limit. All data has been corrected to account for the detection losses of Victor. Resolution Bandwidth=10 kHz, Video Bandwidth=30 Hz.

Section 2.7.3).

$$\alpha^{\pm}_{\rm in} = \frac{\sqrt{\Delta^2\hat{M}^{\pm}_{\rm in} - \Delta^2\hat{X}^{\pm}_{\rm in}}}{2} \tag{5.29}$$

$$\alpha^{\pm}_{\rm out} = \frac{\sqrt{\Delta^2\hat{M}^{\pm}_{\rm out} - \Delta^2\hat{X}^{\pm}_{\rm out}}}{2} \tag{5.30}$$

The amplitude and phase quadrature gains of the teleportation run could then be directly calculated ($g^{\pm} = \alpha^{\pm}_{\rm out}/\alpha^{\pm}_{\rm in}$), and all of the measures of teleportation discussed in Section 5.3 could be obtained.

Fidelity analysis

The fidelity results obtained from all of our teleportation runs are displayed in Fig. 5.13. As discussed in Section 5.3.1, an important parameter of any study of fidelity is the area of phase space from which the inputs states are produced. Fig. 5.13 (d) shows the area of phase space that our experiment has probed. All points shown here satisfied $\mathcal{F} > 0.5$. This area was limited in radius by the increasing sensitivity of fidelity to gain as $\alpha_{\rm in}$ increases (see Fig. 5.4), and small $\alpha^{\pm}_{\rm in}$ were avoided so that the teleportation gain of both quadratures could be accurately verified. A summary of all our fidelity results is shown in Fig. 5.13 (c) as a function of deviation from unity gain. Fig. 5.13 (a) and (b) each display a subset of our fidelity results for input states with particular coherent amplitudes. The solid curves show the best possible performance of our system, based on our entanglement, detection efficiency, dark noise, and assuming equal gain on each quadrature. In

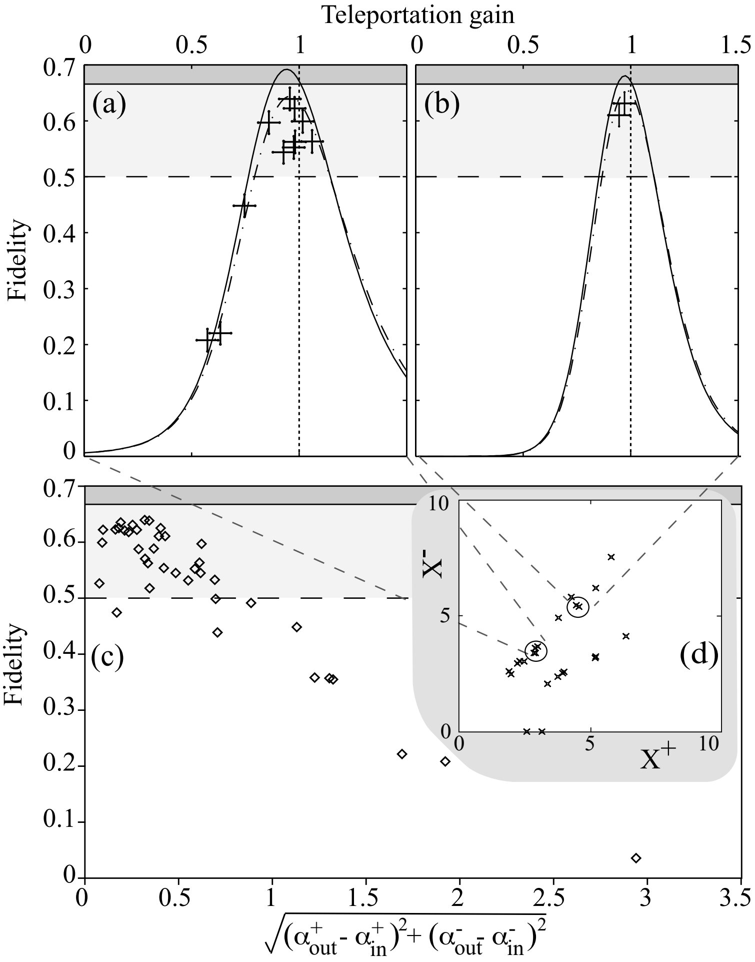

Figure 5.13: Measured fidelity plotted; versus teleportation gain, $g = \sqrt{g^+g^-}$, in (a) and (b); versus coherent amplitude separation between input and output states in (c); and on phase space in (d). In (a) the input signal size was $(\alpha^+, \alpha^-) \approx (2.9, 3.5)$ and in (b) $(\alpha^+, \alpha^-) \approx (4.5, 5.4)$. $g^{\pm}$ were calculated as the ratio of the input and output coherent amplitudes. The dashed (solid) lines show the classical (no-cloning) limits of teleportation at unity gain. The solid curves are calculated optima based on the characterisation of our entanglement in Chapter 4, and the efficiency of the protocol. The dot-dashed curves include the experimental asymmetric gains: for (a) $g^- = 0.84g^+$ and for (b) $g^- = 0.92g^+$.

both plots the highest fidelity occurs for gain less than unity. The increased fidelity is less obvious in (b) where the signal is approximately twice as large as that in (a). In fact, in the limit of a vacuum input state, the fidelity criterion will be satisfied perfectly by a classical teleporter (i.e. one with the entangled state replaced by two coherent states) with zero gain. These results demonstrate the necessity of obtaining and verifying the correct gain settings for any implementation of continuous variable teleportation. Obtaining the correct gain setting is actually one of the more troublesome experimental details. To illustrate this point, we have plotted the dashed curves on (a) and (b) for a teleporter with asymmetric quadrature gains. Such asymmetry was not unusual in our system, and explains the variability of the results shown in Fig. 5.13 (a).

In our experiment the amplitude and phase quadrature teleportation gains were adjusted to the desired level by encoding a large coherent modulation on the input state ($\alpha^{\pm}_{\rm in} \gg \sqrt{\Delta^2\hat{X}^{\pm}_{\rm in}}$ and $\alpha^{\pm}_{\rm out} \gg \sqrt{\Delta^2\hat{X}^{\pm}_{\rm out}}$). The modulation transferred to the output state was then measured, since the noise on the input and output states was negligible compared to the signal the gain could be

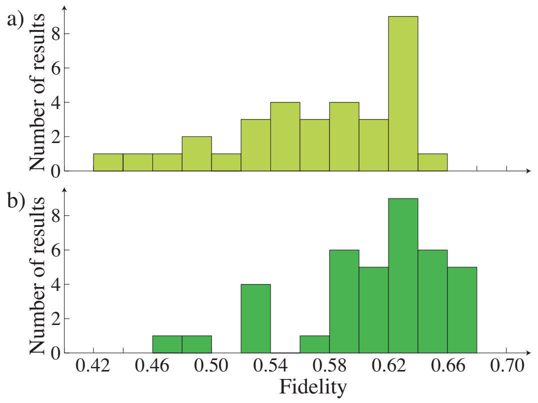

Figure 5.14: Histogram of the fidelity obtained from our teleportation experiment comparing fidelities obtained a) when the gain is experimentally verified, and b) when unity teleportation gain is assumed.

obtained directly $g^{\pm} \approx \sqrt{\Delta^2\hat{M}^{\pm}_{\rm out}/\Delta^2\hat{M}^{\pm}_{\rm in}}$, and then optimised to the desired level. In some experiments characterisation such as this were used to yield the final teleportation gain used to calculate fidelity. In the work of Zhang *et al.* [162] they adjust the gain to unity, and then assume that it remains at unity throughout the teleportation run. In a perfect experimental situation this procedure will work perfectly well. In our experiment however, we found that no matter how well the gain was set initially, the teleportation gain would drift slightly during the course of an experimental run. Since the fidelity is extremely sensitive to gain (see Fig. 5.4) even very small drifts in the gain can lead to significant degradation. We therefore believe that it is important to experimentally verify the gain of teleportation during each teleportation run. Fig. 5.14 illustrates this point, displaying a histogram of the complete set of our teleportation fidelity results calculated firstly using the teleportation gain measured during each run (Fig. 5.14 a)), and secondly by assuming that the gain was adjust correctly beforehand to unity (Fig. 5.14 b)). We see quite significant differences in the two distributions. The maximum fidelity we observed with experimentally verified gain was $\mathcal{F} = 0.64 \pm 0.02$ with $g = 1.02 \pm 0.05$, without experimentally verifying the gain however, we thrice observed $\mathcal{F} > 2/3$. For comparison, the quantum teleportation experiments of Furusawa *et al.* [93] and Zhang *et al.* [162] achieved fidelities of $\mathcal{F} = 0.58 \pm 0.02$ and $\mathcal{F} = 0.61 \pm 0.02$, respectively.

Signal transfer and conditional variance analysis

As discussed in Section 5.3, there are merits to analysing teleportation in a state independent manner. Here, we present our teleportation results analysed in terms of signal transfer and conditional variances between the input and output states. We display the results on a T-V diagram as described in Section 5.3.2, and also present them in terms of the gain normalised conditional variance measure $\mathcal{M}$ introduced in Section 5.3.3.

Our T-V results are shown in Fig. 5.15. The classical limit curve shows the ideal achievable result as a function of gain if the entanglement was replaced with two coherent states, and the efficiency of the protocol was unity. The unity gain curve shows the locus of points obtained at unity teleportation gain with increasing entanglement. Finally, a theoretical optimum (as a function of gain) is shown for our experimental parameters. By varying our experimental conditions, particularly the gain, we have mapped out some portion of the T-V graph. Perhaps the most striking feature of these results are the points with $T_q > 1$, the best of which has $T_q = 1.06 \pm 0.03$. Since only one party may have $T_q > 1$, this shows that Bob has maximal information about the

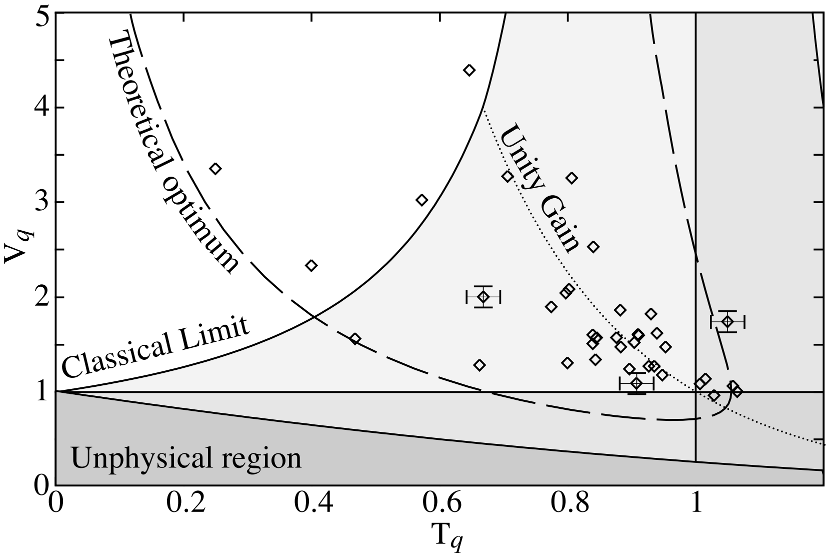

Figure 5.15: T-V graph of the experimental results. The dashed theoretical optimum was calculated based on the characterisation of entanglement in Chapter 4 and experimental losses. Representative error bars are shown for some points.

input signal and we have broken the information cloning limit. The lowest observed conditional variance product was $V_q = 0.96 \pm 0.10$. This point also had $T_q = 1.04 \pm 0.03$. This is the first observation of both $T_q > 1$ and $V_q < 1$, as well as the first simultaneous observation of both. With unity gain simultaneously observing both $T_q > 1$ and $V_q < 1$ would imply breaking of the no-cloning limit for teleportation (i.e $\mathcal{F} > 2/3$). This particular point, however, had a fidelity of only 0.63 ± 0.03. The main reason for this low fidelity is asymmetric gain, the amplitude gain was $g^+ = 0.92 \pm 0.08$ while the phase gain was $g^- = 1.12 \pm 0.08$. Such gain errors have a dramatic impact on the measured fidelity because the output state then has a different classical amplitude ($\alpha^\pm$) to the input. On the other hand, they have only a minor effect on T_q and V_q.

Fig. 5.16 shows $\mathcal{M}$ as a function of teleportation gain for our experimental results. As discussed in Sections 5.3.3 and 5.3.5, $\mathcal{M}$ has real physical significance. An observation of $\mathcal{M} < 1$ implies not only that entanglement must have been used in the teleportation protocol, but also that the protocol could be used to perform entanglement swapping. We have experimentally demonstrated $\mathcal{M} < 1$ for a wide range of gains from $g_{\text{min}} = 0.58$ to $g_{\text{max}} = 1.21$, and achieved an optimum of $\mathcal{M} = 0.22 \pm 0.02$ at $g = 1.06 \pm 0.07$.

5.4.3 Experimental loopholes

A number of loopholes exist in experimental demonstrations of quantum teleportation, and to some degree, any demonstration relies on the integrity of Alice, Bob and Victor. We consider two examples here. The first is shown in Fig. 5.17. Here Victor has encoded no signal on the phase quadrature of the input state ($\alpha_{\text{in}}^- = 0$). Somehow, Bob has discovered this is the case - perhaps there is an eavesdropper inside Victor's station, or Victor himself is corrupt. Bob can then reduce his phase quadrature teleportation gain below unity to minimise the phase reconstruction noise with no fidelity cost. In the case of a classical teleportation protocol Bob could simply turn his phase quadrature feedforward off, and it would appear to Victor that the phase quadrature had been reconstructed perfectly. In this example, however, the teleportation protocol does utilise entanglement, and the optimum strategy for Bob is to leave the phase quadrature feedforward

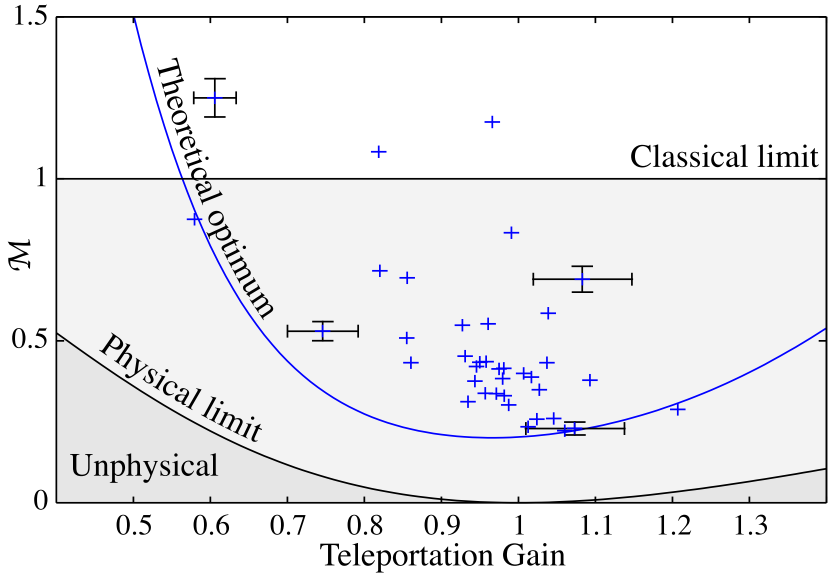

Figure 5.16: Plot of our experimental $\mathcal{M}$ results as a function of teleportation gain. Representative error bars are shown for some points. The theoretical optimum was calculated based on the characterisation of entanglement in Chapter 4 and experimental losses; and the unphysical region is arrived at from Eq. (5.22).

on, just with reduced gain. Fig. 5.17 c) shows the strong asymmetry then created between the reconstruction of the amplitude and phase quadratures. Victor, when analysing the fidelity finds an artificially enhanced value of $\mathcal{F}' = 0.70$. We see that it is essential for Alice and Bob to obtain no information about the orientation of the input coherent amplitude. In our experiment this was achieved by spatially isolating Victor's station from those of Alice and Bob, and by varying the amplitude and phase quadrature coherent amplitudes $\alpha^{\pm}_{\text{in}}$ independently.

The second example of an experimental teleportation loophole considered here is the effect of uncharacterised loss μ introduced before Victor's homodyne detector. Let us for simplicity, take the case of unity gain teleportation. If the input state is coherent the loss has no effect on $\Delta^2\hat{X}^{\pm}_{\text{in}}$, and the coherent amplitude becomes

$$\alpha^{\pm\prime}_{\text{in}} = \sqrt{(1-\mu)}\alpha^{\pm}_{\text{in}} \tag{5.31}$$

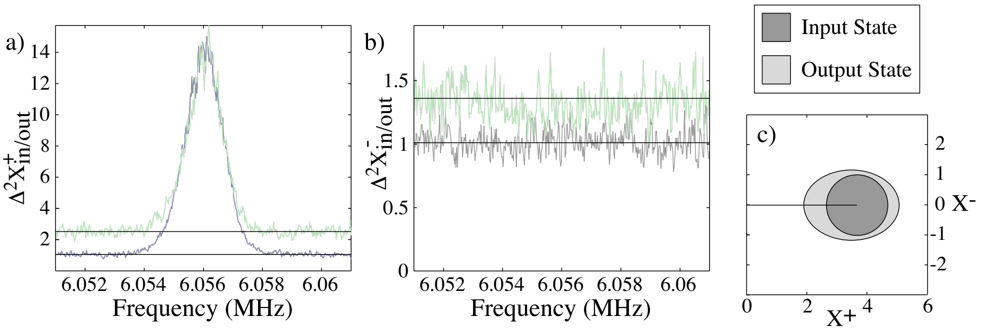

Figure 5.17: Experimental demonstration of teleportation loophole when no phase signal is applied. a) and b) show the amplitude and phase noise of the output state at 8.4 MHz; and c) shows the standard deviation contours of the Wigner functions of the input and output states inferred from the measurements in a) and b).

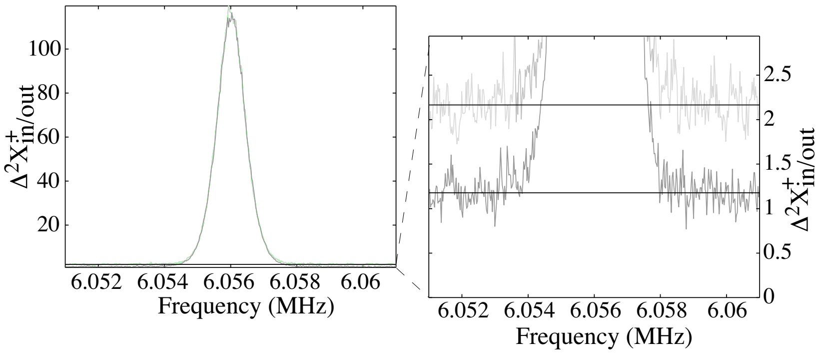

Figure 5.18: Experimental demonstration of teleportation loophole when 50 % of unaccounted for loss is introduced in Victor's measurement. Dark traces: input state, light traces: output state. This demonstration was performed on a purely classical teleporter so that $\Delta^2\hat{X}_{\rm sqz} = 1$.

The output state unlike the input is thermal ($\Delta^2\hat{X}^{\pm}_{\rm out} > 1$). The loss, then, does have an effect on $\Delta^2\hat{X}^{\pm}_{\rm out}$ and we have

$$\alpha^{\pm\,\prime}_{\rm out} = \sqrt{(1-\mu)}\alpha^{\pm}_{\rm in} \tag{5.32}$$

$$\Delta^2\hat{X}^{\pm\,\prime}_{\rm out} = (1-\mu)\Delta^2\hat{X}^{\pm}_{\rm out} + \mu \tag{5.33}$$

We see that for all μ, $g' = \alpha^{\pm\,\prime}_{\rm out}/\alpha^{\pm\prime}_{\rm in} = 1$; and in the limit of $\mu \to 1$, $\Delta^2\hat{X}^{\pm\,\prime}_{\rm out} \to 1$. Since $\Delta^2\hat{X}^{\pm\prime}_{\rm in} = \Delta^2\hat{X}^{\pm}_{\rm in} = 1$ we find that as the loss increases $\mathcal{F}' \to 1$. In the experimental verification of this loophole we deliberately introduce $\mu = 0.5$ of unaccounted for loss, and perform a classical teleportation protocol. This is a special situation, and it can be shown that exactly one quanta of additional noise should be measured by Victor, rather than the two - one from measurement and one from reconstruction - that are really added during the protocol. Therefore, according to Victor, the teleportation process will have been performed at the no cloning limit $\mathcal{F}' = 2/3$, rather than the true performance of $\mathcal{F} = 1/2$. Fig. 5.18 shows our experimental demonstration of this loophole for the amplitude quadrature. We see that, indeed, with $\mu = 0.5$, only one quanta of noise is added to the output state. This example demonstrates how essential it is for any teleportation protocol, to characterise carefully, and account for, the efficiency of Victor's detection system.

5.5 Conclusion

In this Chapter we reported the demonstration of stably locked quantum teleportation of the amplitude and phase quadratures of an optical field. We characterised the teleportation using fidelity, a T-V diagram, and a measure derived in this Chapter - the gain normalised conditional variance product. The optimum directly observed fidelity was $\mathcal{F} = 0.64 \pm 0.02$. This was limited, not by the strength of our entanglement resource, or by the efficiency of the teleportation protocol, but rather by the stability with which control of the teleportation gain was possible. This can be seen from our T-V analysis, which was much less sensitive to gain. The maximum two quadrature signal transfer for our apparatus was $T_q = 1.06 \pm 0.03$; and we observed a conditional variance product of $V_q = 0.96 \pm 0.10$ and signal transfer of $T_q = 1.04 \pm 0.03$, simultaneously. These results are the first observation of $T_q > 1$ and $V_q < 1$, as well as the first simultaneous observation of both criteria. At unity gain simultaneously observing $T_q > 1$ and $V_q < 1$ ensures violation of the no-cloning limit for teleportation. The asymmetry in our gain, however, prevented a direct measurement of $\mathcal{F} > 2/3$. Based on the work of Grosshans and Grangier [155], and Ralph and Lam [148], we have derived a new measure for non-unity gain teleportation, the gain normalised conditional variance product $\mathcal{M}$. We analyse our teleportation results using this measure and demonstrate teleportation for gains from $g_{\rm min} = 0.58$ to $g_{\rm max} = 1.21$, achieving an optimum of $\mathcal{M} = 0.22 \pm 0.02 < 1$. We consider entanglement swapping characterised by a necessary and sufficient condition for entanglement, and demonstrate that the range of gains for which it is successful is dictated by $\mathcal{M}$, with an optimum, always, at $g < 1$.

Chapter 6

Quantum secret sharing

In this Chapter we propose a continuous variable quantum secret sharing scheme that is achievable with the resources developed during the course of my PhD. Conventional secret sharing is a powerful technique in computer science. The goal is to share an encoded secret between multiple players in a hierarchical fashion so that only through collaboration can some subset of players (the access structure) obtain the secret. In quantum secret sharing, the secret is replaced with an unknown quantum state. Thusfar due to experimental complexities, secret sharing of a quantum state has not yet been experimentally demonstrated. The scheme proposed here has two particularly attractive attributes: it requires only two squeezers and a feedfoward loop, and it can be performed in conjunction with a conventional secret sharing protocol providing the scheme with an arbitrary level of security.

The work presented in this Chapter has been published in the journal article 'A. Lance, T. Symul, W. P. Bowen, T. Tyc, B. C. Sanders, and P. K. Lam. *Continuous Variable (2,3) Threshold Quantum Secret Sharing Schemes.* New Journal of Physics **5**, 4 (2003).'

6.1 Introduction

In conventional cryptography, secret sharing[186] enables a dealer to distribute information to multiple players (the recipients) who are not all necessarily trustworthy. Secret sharing techniques have many present-day applications involving the management of cryptographic keys [187]. An important class of secret sharing protocols is (k, n) threshold secret sharing [187], in which any subset of k players (the access structure) must collaborate to retrieve the secret information that the dealer has distributed to $n \geq k$ players; whilst the remaining recipients outside the subset (the adversary structure) learn nothing (see Fig. 6.1 a)). Quantum resources allow secret sharing to be extended in two ways: they can guarantee, through the laws of physics, the security of classical information sharing in crypto-communication systems[188, 189, 190]; and can extend secret sharing to include the dissemination of quantum states[19, 113, 191, 192] in the context of quantum information science. This Chapter considers the second class of protocols, which have broad ramifications across quantum information science because they establish a secure method to distribute fragile quantum states in an environment in which not all parties can be trusted[19]. Teleported states, quantum computer output states, and quantum keys used for quantum cryptography can all be securely distributed using quantum secret sharing (QSS) techniques. Furthermore QSS can be used to distribute entanglement over long distances and through unreliable channels, and is an enabling step towards quantum error correction [19].

Although quantum secret sharing was originally proposed in the discrete variable regime [19], all such proposals have so far required qudits (multi-dimensional qubits), the production of which

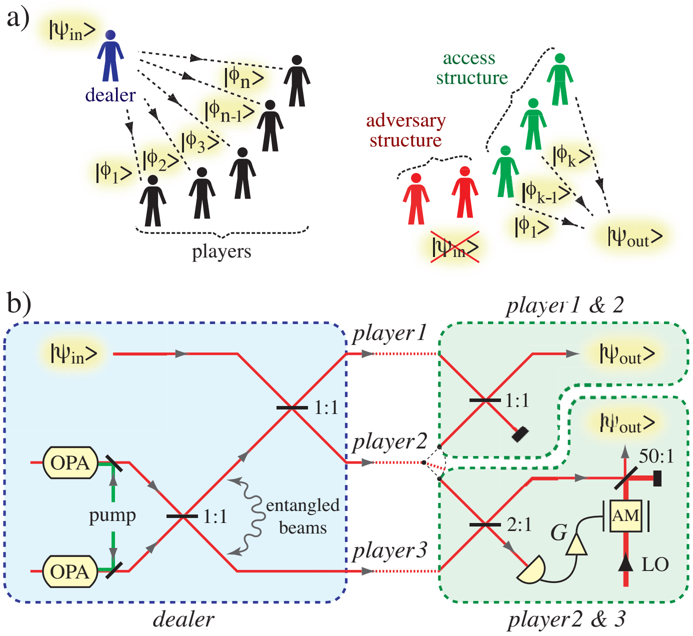

Figure 6.1: (2,3) quantum secret sharing protocol. a) shows a schematic diagram of a general quantum secret sharing protocol. b) shows the apparatus used by the dealer to encode the secret state in our particular (2,3) protocol, and the reconstruction techniques used by access structures {1,2} and {2,3}, respectively. 1:1, 2:1, and 50:1 label 1/2, 2/3, and 50/51 reflective beam splitters respectively, and HR is a highly reflective beam splitter. AM: amplitude modulator. [Figure generously provided by Andrew Lance.]

is extremely challenging. Here we consider quantum secret sharing in the continuous variable regime, which was first proposed by Tyc and Sanders [191] in 2002. They showed that continuous variable $(2,3)$ threshold quantum secret sharing could be achieved using a resource equivalent to four squeezers; and later that (k,n) threshold quantum secret sharing, in general, could be achieved with those resources[192]. This Chapter builds on the original $(2,3)$ threshold proposal of Tyc and Sanders, introducing a more experimentally feasible scheme that requires only two squeezers and an electro-optic feedforward loop, the same resources that were required to perform quantum teleportation in the previous Chapter. A diagram of the proposed experiment is given in Fig. 6.1 b). We demonstrate, also, that by introducing correlated classical noise to the shares the dealer can arbitrarily enhance the security of the quantum secret sharing protocol. This process is equivalent to combining quantum and classical secret sharing in conjunction. The classical component ensures the security of the protocol, whilst the quantum component ensures that quantum features of the secret state are faithfully reconstructed.

Similar to quantum teleportation, quantum secret sharing involves the reconstruction of an original input state at a remote location from transmitted information and available quantum resources. The processes differ in two respects, however. Firstly, in quantum teleportation the input state is destroyed during the measurement process and the reconstruction of the original state is performed subsequently (see Fig. 5.1). Only classical information and a pair of entangled beams are shared between the sender and the receiver. In quantum secret sharing, however, direct optical links containing the encoded secret are permissible between the dealer and all players. The dealer does not, therefore, perform destructive measurements on the input secret. Secondly, as a consequence of the no-cloning theorem, in quantum teleportation an ideal reconstruction of the input state can be uniquely carried out by only a single party. In quantum secret sharing on the other hand, multiple access structures, consisting of a subset of the possible permutations of collaborating players, are able to reconstruct the secret. In spite of these differences, the quality of reconstruction in a quantum secret sharing scheme can be characterised using the same techniques introduced for quantum teleportation in Section 5.3. We use fidelity and the T-V diagram for our analysis here. Although our analysis specifically considers the secret to be an unknown coherent state, the scheme is directly applicable to situations where the secret is an arbitrary unknown quantum state.

6.2 The dealer protocol

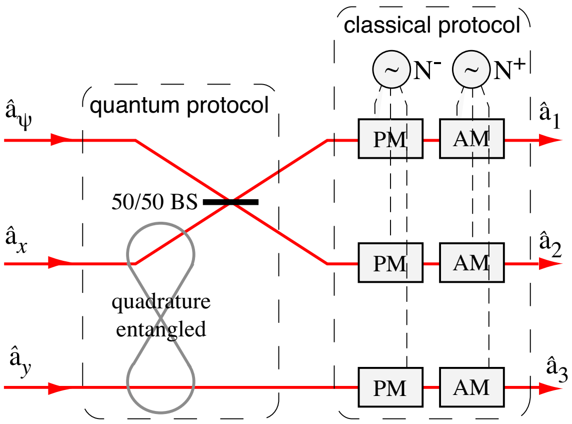

Figure 6.2: Dealer protocol for the production of three shares in a (2,3) quantum secret sharing scheme. BS: beam splitter, PM: phase modulator, AM: amplitude modulator, $N_\pm$ encoding noise.

Before examining how each access structure can reconstruct the secret state using entanglement and feedforward, we will briefly describe the dealer protocol for (2,3) threshold quantum secret sharing. As shown in Fig. 6.2, the dealer interferes the secret state with one of a pair of quadrature entangled beams on a 50/50 beam splitter, with the entanglement being of the form produced in Chapter 4. The two beam splitter outputs, and the second entangled beam form the three shares for distribution to the players in the secret sharing scheme. Such a dealer protocol was first proposed by Tyc and Sanders[191]. Here we extend their protocol, as can be seen from Fig. 6.2, so that both quantum and a classical secret sharing protocols can be run in conjunction. The quantum protocol ensures that the quantum mechanical features of the secret state can be reconstructed, while the classical protocol enhances the security of the scheme against attacks from individual players. To facilitate the classical protocol, the dealer encodes correlated noise onto each of the shares. The exact form of the correlation must be carefully chosen to coincide with the correlation exhibited by the entangled state. Choosing the encoding noise optimally the shares can be expressed as

$$\hat{a}_1 = \frac{\hat{a}_\psi + \hat{a}_x + N}{\sqrt{2}} \tag{6.1}$$

$$\hat{a}_2 = \frac{\hat{a}_\psi - \hat{a}_x - N}{\sqrt{2}} \tag{6.2}$$

$$\hat{a}_3 = \hat{a}_y + N^*, \tag{6.3}$$

where $\hat{a}_\psi$, $\hat{a}_x$ and $\hat{a}_y$ are the annihilation operators corresponding to the secret state and the two entangled beams, respectively; and $N = (N^+ + iN^-)/2$ is the encoding noise with $*$ being the complex conjugate. Since the encoding noise is known to the dealer, $[N^+, N^-] = 0$.

The quadrature entanglement utilised in the dealer protocol could be generated in a number of ways, as discussed in Chapter 4. Here, however, to maintain consistency within this thesis, we consider the entanglement to be generated by interfering a pair of squeezed beams, denoted $\hat{a}_{\mathrm{sqz},1}$ and $\hat{a}_{\mathrm{sqz},2}$, with $\pi/2$ relative phase on a 50/50 beam splitter. In this case, the annihilation operators describing the entangled beams are given by Eqs. (4.1) and (4.2) in Chapter 4. If the squeezed beams are generated using intra-resonator optical parametric amplification (OPA) as described in Chapter 3, the encoding noise can be introduced to each share conveniently by electro-optically modulating the non-linear crystals within the OPA resonators with white noise in a frequency band around the sideband frequency of the secret state. This modulation then provides noise of exactly the form required in Eqs. (6.1), (6.2), and (6.3).

6.3 The {1,2} reconstruction protocol

To reconstruct the secret state, players 1 and 2 (henceforth denoted by {1,2}) need only complete a Mach-Zehnder interferometer, reversing the process used to encode the secret. Choosing the correct relative phase, the output fields from the interferometer are

$$\hat{a}'_1 = \frac{\hat{a}_1 + \hat{a}_2}{\sqrt{2}} = \hat{a}_\psi \tag{6.4}$$

$$\hat{a}'_2 = \frac{\hat{a}_1 - \hat{a}_2}{\sqrt{2}} = \hat{a}_x + N, \tag{6.5}$$

so that the secret state is perfectly reconstructed on the output field $\hat{a}'_1$ independent of the strength of the entanglement. In contrast, successful reconstruction of the secret state for {2,3} and {1,3} requires more complex protocols as a result of the asymmetry of the two shares involved. Henceforth, the focus of this Chapter will be on experimental techniques to implement this reconstruction process, and methods that can then be used to characterise the success of the process. We focus particularly on the {2,3} reconstruction protocol since a demonstration for either one of {2,3} or {1,3} is immediately generalisable to the other.

6.4 The {2,3} reconstruction protocol

In their original proposal Tyc and Sanders [191] suggested using a pair of phase sensitive amplifiers to perform the {2,3} reconstruct protocol. They demonstrated that in the limit that the phase sensitive amplifiers worked perfectly, and that the entanglement utilised by the dealer when sharing the secret was perfect, the secret state could be reconstructed without degradation. This proposal however, requires significant resources, an entangled pair and two phase sensitive amplifiers. Furthermore, the phase sensitive amplifiers must have precisely controlled gain and high non-linearity. As discussed in Section 2.10 high non-linearity can be achieved by using high peak power pulsed light sources, either in Q-switched or mode-locked setups, or by enhancing the optical intensity within optical resonators. However, both of these techniques cause significant coupling of vacuum fields into the state that they are acting on. The pulsed systems often suffer distortion of optical wave fronts in the non-linear medium, resulting in poor optical interference and losses; and resonators, although the wavefront of the output field is typically very good, couple in vacuum fields via intra-resonator losses, the input coupler, and the second harmonic pump field (see Section 3.4.2). An experimental demonstration of this reconstruction protocol would be extremely difficult using existing technology. In this Section we present an alternative {2,3} protocol that uses carefully chosen beam splitter ratios and electro-optic feedforward[113], rather than the phase sensitive amplifiers in [191].

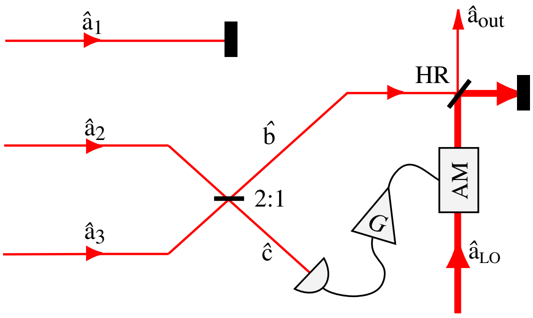

Figure 6.3: The reconstruction protocol for the {2,3} access structure using an electro-optic feedforward loop. 2:1 labels a $2/3$ reflective beam splitter, HR labels a highly reflective beam splitter, AM labels the amplitude modulator, and G is the feedforward gain.

Unlike access structure {1,2}; {2,3} cannot simply complete a Mach-Zehnder interferometer to recover the secret state. The Mach-Zehnder worked for {1,2} because the magnitudes of both the entangled state and the encoding noise contributions in shares 1 and 2 are equal. If the shares are interfered on a 50/50 beam splitter with correct relative phase, these contributions cancel on one output. The magnitudes of both the entangled state and noise contributions in shares 2 and 3 are not equal however. So that if {2,3} attempted to reconstruct the secret state by combining their shares on a 50/50 beam splitter the entangled field held by player 3 would dominate over all other terms on both output fields, and the scheme would fail. Varying the beam splitter ratio, however, the magnitudes of both the entangled state and noise contributions from the two shares, can be equalised on one of the beam splitter outputs. This occurs for a 2/3 reflective beam splitter[1]. If the shares contributed by the players are combined with π relative phase on the beam splitter the amplitude and phase quadratures of the beam splitter output fields are given by

$$\hat{X}_b^+ = \frac{1}{\sqrt{3}}\left(\hat{X}^-_{\mathrm{sqz},2} - \hat{X}^-_{\mathrm{sqz},1} + \hat{X}^+_\psi - 2N^+\right) \tag{6.6}$$

$$\hat{X}_b^- = \frac{1}{\sqrt{3}}\left(\hat{X}^+_{\mathrm{sqz},1} - \hat{X}^+_{\mathrm{sqz},2} + \hat{X}^-_\psi\right) \tag{6.7}$$

$$\hat{X}_c^+ = \frac{1}{2\sqrt{6}}\left[\left(\hat{X}^-_{\mathrm{sqz},1} - \hat{X}^-_{\mathrm{sqz},2}\right) - 3\left(\hat{X}^+_{\mathrm{sqz},1} + \hat{X}^+_{\mathrm{sqz},2}\right) + 2\left(\hat{X}^+_\psi + N^+\right)\right] \tag{6.8}$$

$$\hat{X}_c^- = \frac{1}{2\sqrt{6}}\left[\left(\hat{X}^+_{\mathrm{sqz},2} - \hat{X}^+_{\mathrm{sqz},1}\right) - 3\left(\hat{X}^-_{\mathrm{sqz},1} + \hat{X}^-_{\mathrm{sqz},2}\right) + 2\left(\hat{X}^-_\psi - 3N^-\right)\right], \tag{6.9}$$

where the sub-scripts b and c label the two output fields. We see that both the anti-squeezed quadratures of the squeezed beams used to generate our entanglement ($\hat{X}^-_{\mathrm{sqz},1}$ and $\hat{X}^-_{\mathrm{sqz},2}$), and the encoding noise (N^+ and N^-), do not appear in the phase quadrature of output b. This is a result of cancellation achieved though our choice of beam splitter ratio and relative phase. In the limit of ideal squeezing ($\{\Delta^2\hat{X}^+_{\mathrm{sqz},1}, \Delta^2\hat{X}^+_{\mathrm{sqz},2}\} \to 0$) the fluctuations of the squeezed quadratures also become negligible on this output quadrature, and $\hat{X}_b^- \to \hat{X}_\psi^-/\sqrt{3}$ so that then only the phase quadrature of the secret state appears on the phase quadrature of output field b. Examining the amplitude

---

[1] It is also interesting to consider other beam splitter ratios. Choosing a different ratio is the secret sharing equivalent of moving away from the unity gain regime of quantum teleportation. For simplicity, we do not include an analysis of this situation here.

quadrature $\hat{X}_b^+$ of output field b, however, we find that the phase quadratures of the squeezed fields used the generate the entanglement are present. Therefore, as $\{\Delta^2\hat{X}^+_{\rm sqz,1}, \Delta^2\hat{X}^+_{\rm sqz,2}\} \to 0$ the amplitude quadrature of the secret state becomes more and more obscured by anti-squeezed fluctuations. This occurs because, while the phase quadratures of the entangled beams (and the phase quadrature encoding noise) are directly-correlated, the amplitude quadratures (and the amplitude quadrature encoding noise) are anti-correlated. Thus, if the phase quadratures of the entangled beams are arranged to cancel on one beam splitter output, their amplitude quadratures must be present. If we examine the other beam splitter output field (field c), however, we find that its amplitude quadrature $\hat{X}_c^+$ also contains terms from the anti-squeezed quadratures of the squeezed beams, and from the amplitude quadrature encoding noise. Detecting $\hat{X}_c^+$, and applying it via electro-optic feedforward with appropriately chosen gain to $\hat{X}_b^+$, cancels these fluctuations on $\hat{X}_b^+$. Typically, in feedforward schemes the fluctuations are directly applied to optical fields using optical modulators (see Section 2.4). This process can be quite inefficient, however, and can be avoided here by divorcing the modulators from field b as shown in Fig. 6.3. Instead, we use a similar scheme to that used in the teleportation experiment of Chapter 5. The detected signal from $\hat{X}_c^+$ is applied off-line to a strong local oscillator field. The signal on the local oscillator can then be encoded on output field b using a highly reflective beam splitter as shown in Fig. 6.3. The efficiency of the process is then determined simply by the beam splitter reflectivity which can be very high, rather than the efficiency of the modulators. The resulting output quadratures are given by $\hat{X}^\pm_{\rm out} = \sqrt{1-\epsilon}\hat{X}^\pm_b + \sqrt{\epsilon}\hat{X}^\pm_{\rm LO}$, where $\hat{X}^\pm_{\rm LO}$ are the amplitude and phase quadratures of the local oscillator. In the limit of high beam splitter reflectivity, $\epsilon \to 0$, the amplitude and phase quadratures of the output field are given by

$$\begin{aligned}\hat{X}^+_{\rm out} &\simeq \hat{X}^+_b + K(\omega)\delta i\\ \hat{X}^-_{\rm out} &\simeq \hat{X}^-_b,\end{aligned}\tag{6.10}$$

where $K(\omega)$ is a gain transfer function which takes into account the response of the electro-optic feedforward circuit and the reflectivity of the HR beam splitter. $\delta i(\omega)$ is the frequency component at ω of the detected photocurrent from field c, given by

$$\delta i = \sqrt{\eta}\alpha_c(t)\left[\frac{\sqrt{\eta}}{2\sqrt{6}}\left[\left(\hat{X}^-_{\rm sqz,1}-\hat{X}^-_{\rm sqz,2}\right)-3\left(\hat{X}^+_{\rm sqz,1}+\hat{X}^+_{\rm sqz,2}\right)+2\left(N^+ + \hat{X}^+_\psi\right)\right]+\sqrt{1-\eta}\hat{X}^+_d\right],\tag{6.11}$$

where η is the detection efficiency of the feedforward detector and $\hat{X}^+_d$ arises from the corresponding vacuum field. The output quadrature fluctuations can then be re-expressed as

$$\begin{aligned}\hat{X}^+_{\rm out} &= \left(\frac{1}{\sqrt{3}}+\frac{G}{\sqrt{6}}\right)\hat{X}^+_\psi + \left(\frac{G}{2\sqrt{6}}-\frac{1}{\sqrt{3}}\right)\left(\hat{X}^-_{\rm sqz,1}-\hat{X}^-_{\rm sqz,2}\right)\\ &\quad -\frac{G}{2}\sqrt{\frac{3}{2}}\left(\hat{X}^+_{\rm sqz,1}+\hat{X}^+_{\rm sqz,2}\right)+G\sqrt{\frac{1-\eta}{\eta}}\hat{X}^+_d+\left(\frac{2}{\sqrt{3}}-\frac{G}{\sqrt{6}}\right)N^+ \qquad (6.12)\\ \hat{X}^-_{\rm out} &= \sqrt{\frac{1}{3}}\hat{X}^-_\psi+\sqrt{\frac{1}{3}}\left(\hat{X}^+_{\rm sqz,1}-\hat{X}^+_{\rm sqz,2}\right), \qquad (6.13)\end{aligned}$$

where $G = \eta K(\omega)\alpha_c(t)$ is the total gain of the feedforward loop. If $G = 2\sqrt{2}$, we see that the anti-squeezed quadratures and encoding noise terms in Eq. (6.12) are eliminated. In the limit of perfect detection efficiency and large squeezing, we obtain

$$\hat{X}^{+}_{\mathrm{out}} = \sqrt{3}\hat{X}^{+}_{\psi} \tag{6.14}$$

$$\hat{X}^{-}_{\mathrm{out}} = \frac{1}{\sqrt{3}}\hat{X}^{-}_{\psi}. \tag{6.15}$$

Hence this protocol allows players 2 and 3 to co-operate to reconstruct a squeezed version of the secret, $\hat{a}_{\psi}$. The quantum statistics of the secret state can therefore, in the ideal case, be perfectly reconstructed. Of course, in principle the reconstructed state should be of identical form to the input state. This can be achieved here by using a single unitary squeezer such as those discussed in Chapter 3. By comparison, the original Tyc and Sanders reconstruction protocol required two unitary squeezers[191], so that in any case the scheme presented here is significantly less demanding. It should be pointed out, however, that the result of Eqs. (6.14) and (6.15) is only possible if quantum resources (i.e. entanglement) are shared between the players in the protocol. The unitary squeezer required to transform the reconstructed state into the same form as the input, on the other hand, requires only local resources and no entanglement. Therefore, it is reasonable to conclude that the essence of the quantum secret sharing reconstruction protocol is contained within the feedforward scheme rather than the unitary transform. For these reasons, we consider that the feedforward scheme in-and-of-itself constitutes a {2,3} reconstruction protocol for quantum secret sharing. It should also be noted that the squeezing exhibited on the reconstructed state is deterministically known. Therefore, if the quantum secret sharing protocol was utilised within a quantum information network, the squeezing could potentially be taken into account by simply adjusting the alphabet used by the network in subsequent processes; in this situation a unitary squeezer becomes unnecessary.

6.5 Characterisation of the reconstructed state

Quantum secret sharing can be characterised in a similar manner to that used to characterise quantum teleportation in Chapter 5. Whilst the secret state can be arbitrary, we simplify the characterisation by assuming that it is a coherent state. We characterise the fidelity achievable by each access structure, which for a coherent input state and Gaussian entanglement is given by Eq. (5.6), and calculate the corresponding reconstruction noise, and signal transfer defined respectively in Eqs. (5.7) and (5.8). Since in quantum secret sharing schemes the secret can be transmitted through optical (quantum) channels, the classical limits of each of these measures are different to those derived in Chapter 5 for quantum teleportation. Furthermore, three players, and therefore three permutations of access structures are now involved so a true assessment of the success of the scheme requires an average of the results achieved by each access structure.

It is relatively easy to show that without any entanglement resource the average fidelity achievable for any (k,n) quantum secret sharing scheme is limited by

$$\mathcal{F}^{(k,n)}_{\mathrm{ave}} \leq \frac{k}{n}, \tag{6.16}$$

which for a (2,3) protocol reduces to

$$\mathcal{F}^{(2,3)}_{\mathrm{ave}} = \frac{1}{3}\left(\mathcal{F}_{\{1,2\}} + \mathcal{F}_{\{1,3\}} + \mathcal{F}_{\{2,3\}}\right) \leq \frac{2}{3}. \tag{6.17}$$

where the subscripts i and j in $\mathcal{F}_{\{i,j\}}$ denote the collaborating players. Remember that for our protocol, the {1,2} access structure can, in theory, achieve a perfect reconstruction independent of whether entanglement is available to the dealer so that $\mathcal{F}_{\{1,2\}} = 1$. Since the $\{$1,3$\}$ and $\{$2,3$\}$ access structures are symmetric we find from Eq. (6.17) that when entanglement is not available to the dealer the optimum fidelity achievable by each of these structures is $\{\mathcal{F}_{\{1,3\}}, \mathcal{F}_{\{2,3\}}\} = 1/2$. Therefore, assuming that the $\{$1,2$\}$ access structure can perform the Mach-Zehnder interferometer required for them to reconstruct the secret state perfectly, the quantum secret sharing protocol is successful if

$$\{\mathcal{F}_{\{1,3\}}, \mathcal{F}_{\{2,3\}}\} \geq 1/2. \tag{6.18}$$

Let us now examine how the availability of entanglement to the dealer affects the reconstruction fidelity achieveable by the $\{$2,3$\}$ and $\{$1,3$\}$ access structures. We find that due to the unitary squeezing operation performed on the reconstructed state in our protocol, the directly calculated fidelity is extremely poor[113]. To obtain a fair analysis of the protocol we perform the reverse unitary squeezing operation, amplifying the phase quadrature of the reconstructed state by a factor of $\sqrt{3}$,[2] before the comparison is made. Assuming that the feedforward detector is ideal ($\eta = 1$), that the feedforward gain is $G = 2\sqrt{2}$, and that the squeezed beams used by the dealer to generate entanglement have equal squeezing ($\Delta^2\hat{X}^+_{\rm sqz} = \Delta^2\hat{X}^+_{\rm sqz,1} = \Delta^2\hat{X}^+_{\rm sqz,2}$), Eqs. (5.6), (6.4), (6.12), and (6.13) provide the reconstruction fidelities then achievable by each access structure

$$\begin{aligned} \mathcal{F}_{\{1,2\}} &= 1 && (6.19)\\ \mathcal{F}_{\{1,3\}} = \mathcal{F}_{\{2,3\}} &= \frac{1}{1+\Delta^2\hat{X}^+_{\rm sqz}}. && (6.20) \end{aligned}$$

$\mathcal{F}_{\{1,2\}}$ is always unity since in this case secret state reconstruction only requires a simple Mach-Zehnder interferometer, and in the limit of perfect entanglement ($\Delta^2\hat{X}^+_{\rm sqz} \to 0$) the fidelity achievable by the other two access structures also approaches unity. If any entanglement is available to the dealer ($\Delta^2\hat{X}^+_{\rm sqz} < 1$), the $\{$1,2$\}$ and $\{$2,3$\}$ access structures can achieve $\mathcal{F} > 0.5$, so that quantum secret sharing can be demonstrated with our protocol for any level of squeezing, and for ideal squeezing can be performed perfectly. Notice that the anti-squeezed quadratures of the squeezed beams used by the dealer ($\hat{X}^-_{\rm sqz,1}$ and $\hat{X}^-_{\rm sqz,2}$), and the noise she encodes on the shares (N^+ and N^-), have no contribution to Eq. (6.20). This is the result of having chosen the feedforward gain $G = 2\sqrt{2}$ and $2/3$'s beam splitter reflectivity, so that the quantum secret sharing protocol is operating in a regime equivalent to the unity gain regime for quantum teleportation discussed in Section 5.3.1.

Let us now characterise the secret sharing protocol in terms of reconstruction noise on the output (V_q) and signal transfer from the secret state to the output (T_q), as defined in Eqs. (5.8) and (5.7), respectively. Perfect reconstruction of the secret state is achieved when no noise is add on reconstruction ($V_q = 0$), and any signals on the secret state are completely retained ($T_q = 2$). Unlike fidelity, both of these parameters are independent of unitary squeezing operations, so that the unitary squeezing operation performed on the output state for the fidelity analysis is not required here. Before analysing our specific reconstruction protocol, we must determine criteria to delineate between classical and quantum secret sharing regimes. Similarly to the fidelity criterion discussed earlier, such criteria may be constructed from the average reconstruction noise, and the average signal transfer of the three access structures. It is relatively easy to show that if no entanglement is available to the dealer, the average reconstruction noise and signal transfer are

---

[2] and correspondingly, deamplifying the amplitude quadrature by the same factor

limited by

$$\begin{aligned}\sqrt{V_{q,\mathrm{ave}}} &= \frac{1}{3}\left(\sqrt{V_{q,\{1,2\}}}+\sqrt{V_{q,\{1,3\}}}+\sqrt{V_{q,\{2,3\}}}\right) \geq \frac{1}{3} &\quad (6.21)\\ T_{q,\mathrm{ave}} &= \frac{1}{3}\left(T_{q,\{1,2\}}+T_{q,\{1,3\}}+T_{q,\{2,3\}}\right) \leq \frac{4}{3}. &\quad (6.22)\end{aligned}$$

Since for our dealer protocol, the {1,2} access structure is able to perfectly reconstruct the secret state independent of whether or not the dealer has access to entanglement, $V_{q,\{1,2\}} = 0$ and $T_{q,\{1,2\}} = 2$ can always be achieved. Without entanglement the other two access structures, being symmetric, are therefore limited by

$$\begin{aligned}V_{q,\{1,3\}} = V_{q,\{2,3\}} &\geq 1/4 &\quad (6.23)\\ T_{q,\{1,3\}} = T_{q,\{2,3\}} &\leq 1. &\quad (6.24)\end{aligned}$$

Assuming again that the feedforward detector is ideal ($\eta = 1$), and that the magnitudes of the encoding noise on the amplitude and phase quadratures of the shares are equal ($\Delta^2 N = \Delta^2 N^+ = \Delta^2 N^-$), the signal transfer and reconstruction noise for the {1,3} and {2,3} access structures are given as a function of gain by

$$\begin{aligned}T_{q,\{1,3\}} &= T_{q,\{2,3\}} = \frac{1}{1+2\Delta^2\hat{X}^+_{\mathrm{sqz}}} &\quad (6.25)\\ &\quad +\frac{\left(2+\sqrt{2}G\right)^2}{\left(2+\sqrt{2}G\right)^2+\left(G-2\sqrt{2}\right)^2\left(\Delta^2\hat{X}^-_{\mathrm{sqz}}+2\Delta^2 N\right)+9G^2\Delta^2\hat{X}^+_{\mathrm{sqz}}}\\ V_{q,\{1,3\}} &= V_{q,\{2,3\}} = \frac{\Delta^2\hat{X}^+_{\mathrm{sqz}}}{2}\left[G^2\Delta^2\hat{X}^+_{\mathrm{sqz}}+\frac{1}{9}\left(G-2\sqrt{2}\right)^2\left(\Delta^2\hat{X}^-_{\mathrm{sqz}}+2\Delta^2 N\right)\right], &\quad (6.26)\end{aligned}$$

where to obtain these expressions we have used Eqs. (5.7), (5.8), (6.12), and (6.13). Taking the specific gain of $G = 2\sqrt{2}$, we see that in the limit of perfect entanglement ($\Delta^2\hat{X}^+_{\mathrm{sqz}} \to 0$), the signal is perfectly transferred to the output state ($T_{q,\{2,3\}} = 2$) and no noise is introduced in the process ($V_{q,\{2,3\}} = 0$).

Most quantum secret sharing schemes require, not only that the access structure can retrieve the secret state, but also that individually each player is unable to do so. Let us, therefore, examine the signal transfer from the secret state to each of the individual shares, and the noise obscuring the secret on these shares. The signal transfer and reconstruction noise for the individual players can be shown from Eqs. (5.7), (5.8), (6.1), (6.2), and (6.3) to be given by

$$\begin{aligned}T_{q,\{1\}} = T_{q,\{2\}} &= \frac{4}{2+\Delta^2\hat{X}^+_{\mathrm{sqz}}+\Delta^2\hat{X}^-_{\mathrm{sqz}}+2\Delta^2 N} &\quad (6.27)\\ T_{q,\{3\}} &= 0 &\quad (6.28)\\ 4V_{q,\{1\}} = 4V_{q,\{2\}} = V_{q,\{3\}} &= \left(\frac{1}{2}\left(\Delta^2\hat{X}^+_{\mathrm{sqz}}+\Delta^2\hat{X}^-_{\mathrm{sqz}}\right)+\Delta^2 N\right)^2. &\quad (6.29)\end{aligned}$$

Clearly no signal is transferred to player 3 individually since no part of the secret state is distributed to him. The signal transfer to players 1 and 2 is maximised at $\{T_{q,\{1\}}, T_{q,\{2\}}\} = 1$ when no entanglement is available to the dealer ($\Delta^2\hat{X}^+_{\mathrm{sqz}} = \Delta^2\hat{X}^-_{\mathrm{sqz}} = 1$) and he encodes no noise onto the shares ($\Delta^2 N = 0$). As the strength of the dealers entanglement improves ($\Delta^2\hat{X}^+_{\mathrm{sqz}} \to 0$, and consequently $\Delta^2\hat{X}^-_{\mathrm{sqz}} \to \infty$), or alternatively, as the level of encoding noise increases ($\Delta^2 N \to 1$)

the signal transfer to players 1 and 2 individually approaches zero. Similarly, players 1 and 2 individually experience minimum reconstruction noise when the dealer has no entanglement and chooses not to utilise encoding noise. As the squeezing improves, or the level of encoding noise increases, the reconstruction noise for each player increases. We see that, for large squeezing, or large encoding noise, the secret state is completely shrouded from all three players individually.

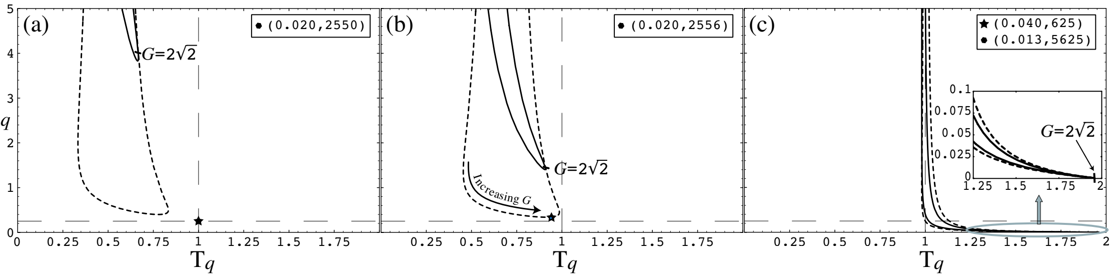

Figure 6.4: T-V diagrams for the feedforward scheme with squeezing levels of (a) $\Delta^2\hat{X}^+_{\rm sqz} = 1$, (b) $\Delta^2\hat{X}^+_{\rm sqz} = 0.6$, and (c) $\Delta^2\hat{X}^+_{\rm sqz} = 0.01$. The lines represent the reconstruction achieved by the $\{2,3\}$ access structure with varying feedforward gain, and the points represent the reconstruction achieved by players $\{1\}$ or $\{2\}$ alone. The dashed lines and stars are the results achieved in the absence of encoding noise, whilst the solid lines and circles are achieved with an encoding noise level of $\Delta^2 N = 100$. The detector efficiency is assumed to be perfect ($\eta = 1$) and the squeezing resources pure $\Delta^2\hat{X}^+_{\rm sqz}\Delta^2\hat{X}^-_{\rm sqz} = 1$. The coordinates of points lying outside the plotted region are displayed in insets.

Similarly to our analysis of quantum teleportation, we can represent the signal transfer and reconstruction noise of a quantum secret sharing protocol as a function of the feedforward gain on a T-V diagram. Fig. 6.4 shows this representation of our protocol for three different levels of squeezing, in Fig. 6.4 a) no squeezing is used so that $\Delta^2\hat{X}^+_{\rm sqz} = 1$, in Fig. 6.4 b) $\Delta^2\hat{X}^+_{\rm sqz} = 0.6$ and in Fig. 6.4 c) $\Delta^2\hat{X}^+_{\rm sqz} = 0.01$. In all cases we have assumed that the squeezed states are pure, i.e. that $\Delta^2\hat{X}^+_{\rm sqz}\Delta^2\hat{X}^-_{\rm sqz} = 1$. Let us first consider the case where no noise is encoded onto the shares so that $\Delta^2 N = 0$. The dashed curves show the portion of the T-V diagram mapped out by our protocol with each level of squeezing as the feedforward gain varies. As the level of squeezing increases the curve, in general, moves towards higher $T_{q,\{2,3\}}$ and lower $V_{q,\{2,3\}}$; and as discussed earlier, in the limit of infinite input squeezing, the collaborating players can reconstruct the secret perfectly, with $T_{q,\{2,3\}} \to 2$ and $V_{q,\{2,3\}} \to 0$ at a feedforward gain of $G = 2\sqrt{2}$. When the squeezing is not perfect, however, the optimum feedforward gain for the collaborating players is always less than $2\sqrt{2}$, as shown in Fig. 6.4(a) and (b). The star points in Fig. 6.4 represent the maximum information retrievable by $\{1\}$ or $\{2\}$ individually. When the dealer only has access to entanglement of moderate strength, and our protocol is analysed on the T-V diagram, the individual players can reconstruct the secret with reasonable quality (see Fig. 6.4 (a) and (b)), and in the case of weak entanglement an individual player can even obtain a better reconstruction of the secret state than is achieved by the access structure. In this situation, the single player has won because the collaborating players are restricted to use the optical setup shown in Fig. 6.3. By varying the beam splitter splitter ratio of the 2:1 beam splitter, the collaborating players can do better that the individual player for any non-zero level of squeezing. In the limit of strong entanglement the individual players achieve an extremely poor reconstruction of the input state, with $T_{q,\{i\}} \to 0$ and $V_{q,\{i\}} \to \infty$, as shown in Fig. 6.4 c).

The dealer can enhance the security of our protocol against individual attacks by encoding correlated noise $N^\pm$ onto each share. The effect of 20 dB of this noise is shown in Fig. 6.4 by the solid lines for the collaborating players, and by circles for the single players. We see that in this case, to ensure that the noise is completely cancelled, the optimum feedforward gain for the collaborating players becomes $G = 2\sqrt{2}$ for all levels of entanglement. The optimum $T_{q,\{2,3\}}$ and $V_{q,\{2,3\}}$ for both the collaborating and individual players degrades due to this noise. For the collaborating players, the degradation occurs because the players are forced to operate at $G = 2\sqrt{2}$ to cancel the encoding noise. For the individual players, however, no means are available to cancel the encoding noise, so that the degradation is much more severe. If the dealer encodes a high level of noise, the individual players obtain virtually no information about the secret with $T_{q,\{i\}} \rightarrow 0$ and $V_{q,\{i\}} \rightarrow \infty$. In this regime, the collaborating players obtain a much better reconstruction than the single players for all levels of input squeezing.

6.6 The cups and balls magic trick without a trick

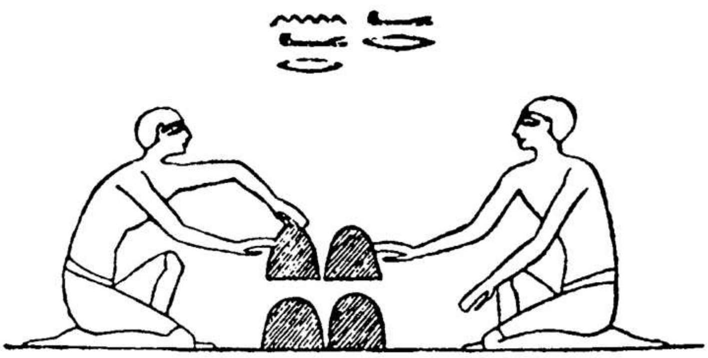

Figure 6.5: Wall painting from the tomb of Beni Hassan, Egypt 2500 BC.

If you will permit an editorial, I would like to examine the analogy between {2,3} quantum secret sharing and the cups and balls magic trick. Cups and balls is commonly believed to be the oldest of magic tricks. It has been argued that a mural dated to 2500 BC in the crypt of Baqet III outside the village of Beni Hassan in Egypt captures two men playing the trick. The mural is depicted in Fig. 6.5. It will probably never be known whether these two men were truly enacting the cups and balls trick, but still it is an old trick with written records dating back to the first century AD. The trick begins with three cups and a ball. The magician places the ball under one cup, shuffles the cups, and then asks the audience to guess which cup the ball is under. Of course, as the name implies she performs a 'trick', and somehow the ball is never under the cup the audience chooses[3]. Now imagine you are a quantum magician, or the dealer in a quantum secret sharing protocol, and you want to perform this trick. You take your quantum ball, the secret state, and split it into three parts shrouding each with part of an entangled state, or cup. Let's not worry about shuffling the states around, but rather simply ask the audience to choose any cup (share) that holds part of the secret. They, believing they cannot lose, choose one, and you the magician are then at liberty to use the other two to reconstruct the secret. . . . and voilà, no matter which share the audience chooses you have the secret state, and they nothing. So using the techniques of quantum secret sharing a quantum magician can perform this age old magic trick without a trick! Of course, the conventional magician often extends his trick, putting a ball under one cup, shuffling the three cups, and then revealing that a ball is now under each of the cups. This, we know, is impossible for quantum states. So thankfully some things will always remain as they

---

[3] I will not spoil the trick for you by explaining how it works here.

were perhaps intended to be - magic!

6.7 Conclusion

$(\mathrm{T_q}, \mathrm{V_q})$		clas,$\bar{N}$	clas,N	quan,$\bar{N}$	quan,N
Adversary Structure	1	(1,1/4)	$(0,\infty)$	$(0,\infty)$	$(0,\infty)$
	2	(1,1/4)	$(0,\infty)$	$(0,\infty)$	$(0,\infty)$
	3	(0,1)	$(0,\infty)$	$(0,\infty)$	$(0,\infty)$
Access Structure	{1,2}	(2,0)	(2,0)	(2,0)	(2,0)
	{1,3}	(1,1/4)	(2/3,4)	(2,0)	(2,0)
	{2,3}	(1,1/4)	(2/3,4)	(2,0)	(2,0)

Table 6.1: Summary of the performances of the quantum secret sharing protocol with (quan) and without (clas) quadrature entanglement; and with (N) and without encoding noise ($\bar{N}$). Parameters listed are the best achievable (T_q, V_q) values for the protocol utilising a 2:1 beam splitter.

This Chapter presented a new (2,3) threshold quantum secret sharing protocol. This scheme utilises a pair of quadrature entangled fields of the form produced in Chapter 4 and an electro-optic feedforward loop. We have shown that the ideal protocol produces output states that are related by a single unitary squeezing operation to the original secret states. We show that by encoding Gaussian noise on the shares, it is possible to guarantee security against attacks from individual players. Table 6.1 summarises the performances of our proposed feedforward quantum secret sharing scheme when entanglement is, and is not, available to the dealer; and with, and without, encoding noise on the shares distributed by the dealer.

We have recently implemented this proposal in the laboratory. Although I will not detail those results here, the optimum average fidelity achieved so far is $\mathcal{F}_{\rm ave}^{(2,3)} = (0.73 \pm 0.04) > 2/3$[38]. This is, to our knowledge, the first experimental demonstration of secret sharing of a quantum state.

Part III

Interaction of optical fields with atomic ensembles

Overview

In the previous three Chapters we presented results on the generation of continuous variable entanglement, its application to quantum teleportation, and a potential application to quantum secret sharing. The demonstration of quantum information protocols such as these is essential to the realisation of a quantum information network. However, it is generally accepted that realistic quantum information networks will consist of atomic nodes, where information is processed, connected by optical links[9, 10, 107, 108, 109, 110]. To integrate optical protocols into such a quantum information network methods must be developed to optimise the interaction between optical and atomic quantum states. The optimum configuration for the atomic nodes is still the focus of vigorous research, with semi-conductor materials[193], rare earth doped crystals [194], trapped ions[195, 196], single atoms in high finesse resonators[197, 198, 199], super-conducting materials[200], and atomic ensembles[20, 21, 201, 202], all holding promise. For the continuous variable optical states analysed predominantly in this thesis, the most viable option is probably to use atomic ensembles.

Recently, the transfer of continuous variable polarisation states to the spin state of an atomic ensemble has been experimentally demonstrated [20]. Furthermore, polarisation states do not require the universal local oscillator required for other continuous variable quantum information networks. In the continuous variable regime polarisation states, therefore, appear to be the most likely candidate for the optical links in a quantum information network. The first two Chapters of this Part of my thesis examine the breath of continuous variable polarisation states, and discuss how these states can be generated through transformations of the quadrature squeezed and quadrature entangled states of Chapters 3 and 4. In Chapter 7 we experimentally demonstrate various forms of polarisation squeezing[36, 203], and show that three of the four Stokes operators that describe polarisation states can be simultaneously squeezed. Chapter 8 transforms quadrature entanglement to polarisation entanglement[33, 204]. Interacting this polarisation entanglement with appropriately prepared atomic ensembles at two nodes of a network could produce a macroscopic spin entangled state between the nodes [202]. Finally, we propose a new form of polarisation entanglement, created from two quadrature entangled pairs, which displays strong correlations between three of the Stokes operators.

Effective communication of entanglement over long distances is a prerequisite to the implementation of a quantum information network. Given that any optical channel is likely to have inherent inefficiencies, it is expected that quantum state purification and storage techniques[139, 140, 141], and a quantum repeater architecture[205] will be required to perform this communication successfully. A number of proposals exist for such a system [110, 205] but most remain outside the reach of present-day technology. One proposal using the optical manipulation of atomic ensembles and conditional measurements does, however, appear viable with available technology[21]. Chapter 9 of this thesis reports the demonstration of the enabling step towards this system. The experiment was performed in Jeff Kimble's laboratories at the California Institute of Technology [206]. The main scientific result of the work was the generation of non-classically correlated photon pairs from an atomic ensemble. This experiment could have application not only to quantum information networks [21], but also to quantum state engineering [207], and to the implementation of a single photon source 'on demand'.

Chapter 7

Polarisation squeezing

In this Chapter we analyse the polarisation state of light on a quantum Poincaré sphere. We investigate several method to produce polarisation squeezed states using the resource described in Chapter 3. In one case, we demonstrate simultaneous polarisation squeezing of three of the four Stokes operators characterising the polarisation state of a field.

The work presented here has been published in the journal articles:

- W. P. Bowen, R. Schnabel, H.-A. Bachor, and P. K. Lam. *Polarization Squeezing of Continuous Variable Stokes Parameters.* Physical Review Letters **88**, 093601 (2002).
- R. Schnabel, W. P. Bowen, N. Treps, T. C. Ralph, H.-A. Bachor, and P. K. Lam. *Stokes operator squeezed continuous variable polarization states.* Physical Review A **67**, 012316 (2003).

7.1 Introduction

In the discrete regime quantum polarisation states have been vigorously studied, both theoretically and experimentally, with investigations of fundamental problems of quantum mechanics, such as Bell's inequality [67, 120, 208, 209], and of potential applications such as quantum cryptography [112, 210, 211, 212] and quantum computation [17]. By contrast, quantum polarisation states in the continuous variable regime have received little attention. Recently however, interest in continuous variable aspects of quantum polarisation states has been growing. This growth in interest is primarily due to the apparent applicability of continuous variable polarisation states to quantum information networks. It is generally accepted that a realistic quantum information network must consist of nodes of atoms where quantum information algorithms are processed, linked by optical channels (see for example [9, 10, 107, 108, 109, 110]). In such a system optical quantum states must be transferable to the atomic nodes and visa versa. This quantum state transfer has been demonstrated between continuous variable polarisation states and spin states of an atomic ensemble[20, 202]. Continuous variable polarisation states can be carried by a bright laser beam, providing high bandwidth capabilities and therefore faster signal transmission rates than discrete variable systems; and perhaps surprisingly they retain the discrete variable advantage of not requiring the universal local oscillator necessary for other proposed continuous variable quantum networks. This advantage, although technical, would result in a significant simplification of the infrastructure required for the network.

The polarisation state of light has four defining parameters, the Stokes operators, one of which for a polarised beam, is redundant. This compares to two parameters, the amplitude and phase quadratures, for the most commonly studied continuous variable system. Polarisation squeezing can be achieved for each of these four variables, and for some of them simultaneously. Several methods for generating continuous variable polarisation squeezed states have been proposed, most using nonlinearity provided by Kerr-like media and optical solitons [213, 214, 215, 216, 217, 218, 219, 220, 221]. The two experimental demonstrations prior to our work reported here, however, were achieved by combining a dim quadrature squeezed beam with a bright coherent beam on a polarising beam splitter [20, 202, 222]. In both cases only the properties of the state relevant to the experimental outcome were characterised. The full characterisation of a continuous variable polarisation state requires measurements of the fluctuations in both the orientation, and the length of the Stokes vector on a Poincaré sphere.

In this Chapter we present the complete experimental characterisation of the Stokes vector fluctuations for four different quantum polarisation states. We make use of ideas recently published by Korolkova *et al.* [218]. Their concept of squeezing more than one Stokes operator of a laser beam and a simple scheme to measure the Stokes operator variances are realised. We experimentally compare polarisation squeezed states generated from a single quadrature squeezed beam to those produced from two quadrature squeezed beams. In the following Section we present a description of the theory of Stokes operators in the continuous variable regime. Therein, we decompose the Stokes operators that describe polarisation states into pairs of field annihilation operators using the Schwinger bosonic representation[223]. This provides a clear description of optical polarisation states in terms of the formalism introduced in Chapter 2. In the experimental Section we characterise the polarisation fluctuations of a single amplitude squeezed beam from one of our OPAs. It can be seen that only the fluctuations of the length of the Stokes vector are below that of a coherent state (ie. squeezed). Grangier *et al.* [222] and Hald *et al.* [20] converted this to squeezing of the Stokes vector orientation by combining the quadrature squeezed beam with a much brighter coherent beam on a polarising beam splitter. We experimentally investigate this situation and indeed show that the Stokes vector orientation is then squeezed. This result is compared with measurements on polarisation states generated by combining both of our quadrature squeezed beams on a polarising beam splitter[203, 218]. Operating our OPAs in the amplification and deamplification regimes, respectively, we observed ‘pancake-like’ and ‘cigar-like’ uncertainty volumes on the Poincaré sphere. Both the orientation and the length of the Stokes vector were squeezed for the ‘cigar-like’ uncertainty volume. In the final Section we discuss several schemes for encoding information on continuous variable polarisation states of light. A conventional fiber-optic communication protocol is compared with optimised coherent beam and squeezed beam protocols. We show that the channel capacity of the ‘cigar-like’ polarisation squeezed states exceeds the channel capacity of coherent states, quadrature squeezed states, and all other polarisation squeezed states.

It should be mentioned that subsequently to the work presented here, polarisation squeezing has been demonstrated in a pair of exquisite experiments, one utilising the Kerr non-linearity in optical fibres [224], and the other a cloud of cold Cesium atoms in a high finesse resonator [225]. An number of interesting theoretical proposals for the generation and utilisation of polarisation squeezing have also since been published [226, 227, 228].

7.2 Theoretical background

In classical optics the polarisation state of a light beam can be described as a Stokes vector on a Poincaré sphere, as shown in Fig. 7.1 a). It can be fully characterised by the four Stokes parameters[229]: S_0 measures the intensity of the beam; and S_1, S_2, and S_3 characterise its polarisation and form a cartesian axis system. If the Stokes vector points in the direction of S_1, S_2, or S_3, the polarised part of the beam is horizontally, linearly at 45°, or right-circularly polarised, respectively. A pair of beams will not interfere if their Stokes vectors point in opposite directions. The radius of the classical Poincaré sphere is given by $S = (S_1^2 + S_2^2 + S_3^2)^{1/2}$ which

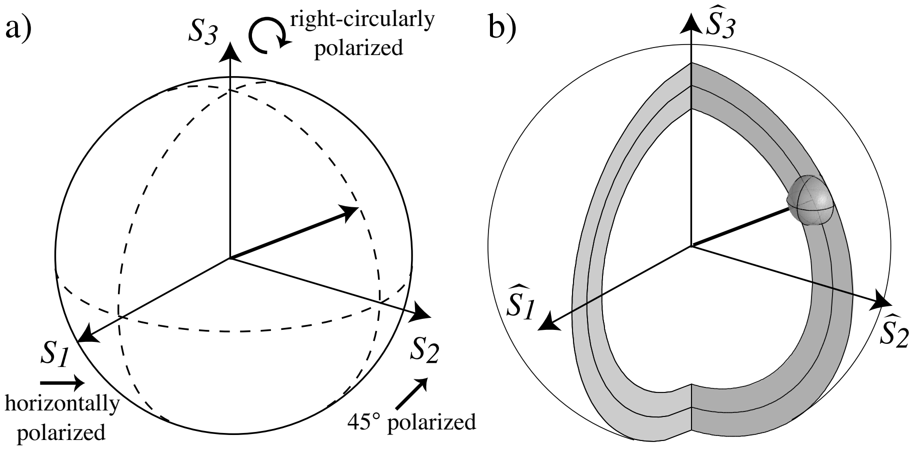

.

Figure 7.1: Diagram of a) classical and b) quantum Stokes vectors mapped on a Poincaré sphere; the ball at the end of the quantum vector visualises the quantum noise in $\hat{\mathrm{S}}_1$, $\hat{\mathrm{S}}_2$, and $\hat{\mathrm{S}}_3$; and the non-zero quantum sphere thickness visualises the quantum noise in $\hat{\mathrm{S}}_0$.

describes the average intensity of the polarised part of the radiation. The degree of polarisation of a beam is given by the ratio of the intensity of the polarised part, to the total intensity S/S_0. For quasi-monochromatic laser light which is almost completely polarised S_0 is a redundant parameter, completely determined by the other three parameters ($S_0 = S$ in classical optics). The four Stokes parameters can be directly obtained from the mean values of the simple experiments shown in Fig. 7.2.

An equivalent representation of polarisation states of light is given by the 4 elements of the coherence matrix (Jones matrix). The relations between these elements and the Stokes parameters can be found in [230]. In contrast to the coherence matrix elements the Stokes parameters are observables and therefore can be associated with Hermitian operators. The quantum mechanical Stokes operators are defined in much the same way as their classical counterparts. Following [231, 232] we expand the Stokes operators in terms of the annihilation $\hat{a}$ and creation $\hat{a}^\dagger$ operators of the constituent horizontally (subscript H) and vertically (subscript V) polarised modes

$$\begin{aligned}
\tilde{S}_0 &= \tilde{a}_H^\dagger \tilde{a}_H + \tilde{a}_V^\dagger \tilde{a}_V && (7.1)\\
\tilde{S}_1 &= \tilde{a}_H^\dagger \tilde{a}_H - \tilde{a}_V^\dagger \tilde{a}_V && (7.2)\\
\tilde{S}_2 &= \tilde{a}_H^\dagger \tilde{a}_V e^{i\theta} + \tilde{a}_V^\dagger \tilde{a}_H e^{-i\theta} && (7.3)\\
\tilde{S}_3 &= i\tilde{a}_V^\dagger \tilde{a}_H e^{-i\theta} - i\tilde{a}_H^\dagger \tilde{a}_V e^{i\theta}, && (7.4)
\end{aligned}$$

where θ is the phase difference between the H,V-polarisation modes. The commutation relations of the annihilation and creation operators directly result in Stokes operator commutation relations,

$$[\tilde{S}_1, \tilde{S}_2] = 2i\tilde{S}_3\ , \quad [\tilde{S}_2, \tilde{S}_3] = 2i\tilde{S}_1\ , \quad [\tilde{S}_3, \tilde{S}_1] = 2i\tilde{S}_2\ . \qquad (7.5)$$

Apart from a normalisation factor, these relations are identical to the commutation relations of the Pauli spin matrices. In fact the three Stokes operators in Eq. (7.5) and the three Pauli spin matrices both generate the special unitary group of symmetry transformations SU(2) of Lie algebra[233]. This group obeys the same algebra as the three-dimensional rotation group, so that distances in three dimensions are invariant. Therefore the operator $\tilde{S}_0$ is also rotationally invariant and commutes with the other three Stokes operators ($[\tilde{S}_0, \tilde{S}_j] = 0$, with $j = 1, 2, 3$). The noncommutability of the other Stokes operators $\tilde{S}_1$, $\tilde{S}_2$ and $\tilde{S}_3$ precludes the simultaneous exact measurement of their physical quantities. As a direct consequence of Eq. (7.5) the Stokes operator variances are restricted by the uncertainty relations [231]

$$\Delta^2\tilde{S}_1\Delta^2\tilde{S}_2 \geq |\langle\tilde{S}_3\rangle|^2 \tag{7.6}$$

$$\Delta^2\tilde{S}_2\Delta^2\tilde{S}_3 \geq |\langle\tilde{S}_1\rangle|^2 \tag{7.7}$$

$$\Delta^2\tilde{S}_3\Delta^2\tilde{S}_1 \geq |\langle\tilde{S}_2\rangle|^2. \tag{7.8}$$

In general this results in non-zero variances in the individual Stokes operators as well as in the radius of the Poincaré sphere (see Fig. 7.1b)). The quantum noise in the Stokes operators even effects the definitions of the degree of polarisation [213, 216] and the Poincaré sphere radius. It can be shown from Eqs. (2.4) and (7.1)-(7.4) that the quantum Poincaré sphere radius is different from its classical analogue, $\langle\tilde{S}\rangle = \langle\tilde{S}_0^2 + 2\tilde{S}_0\rangle^{1/2}$. Furthermore, the noncommutability of the Stokes operators implies that entanglement of Stokes operators is possible between two beams, which is the topic of the next Chapter. Three observables are involved, compared to two for quadrature entanglement, and the entanglement between two of them relies on the mean value of the third.

The Stokes operators of a light beam can be characterised using the same apparatus as the classical Stokes parameters (Fig. 7.2), and including an analysis of the fluctuations inherent in the measurement outcomes[218]. If the variances of the Stokes operators are much smaller than their coherent amplitudes, the Stokes operator expectation values can be approximated by

$$\langle\tilde{S}_0\rangle = \alpha_H^2(t) + \alpha_V^2(t) = \langle\tilde{n}\rangle \tag{7.9}$$

$$\langle\tilde{S}_1\rangle = \alpha_H^2(t) - \alpha_V^2(t) \tag{7.10}$$

$$\langle\tilde{S}_2\rangle = 2\alpha_H(t)\alpha_V(t)\cos\theta \tag{7.11}$$

$$\langle\tilde{S}_3\rangle = 2\alpha_H(t)\alpha_V(t)\sin\theta. \tag{7.12}$$

These expressions are identical to the Stokes parameters in classical optics. Here $\langle\tilde{n}\rangle$ is the expectation value of the photon number operator. For a coherent beam the expectation value and

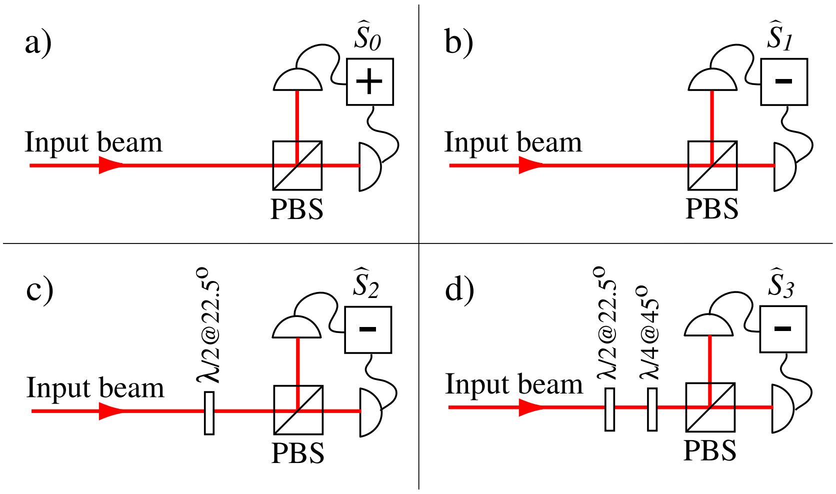

Figure 7.2: Apparatus required to measure each of the Stokes operators. PBS: polarising beam splitter, $\lambda/2$ and $\lambda/4$: half- and quarter-wave plates respectively, the plus and minus signs imply that an electrical sum or difference has been taken.

variance of $\tilde{n}$ have the same magnitude, this magnitude equals the quantum noise limit. The variances of the Stokes operators in the frequency domain are given by

$$\Delta^2\hat{S}_0 = \alpha_H^2(t)\Delta^2\hat{X}_H^+ + \alpha_V^2(t)\Delta^2\hat{X}_V^+ + 2\alpha_H(t)\alpha_V(t)\left\langle\delta\hat{X}_H^+\delta\hat{X}_V^+\right\rangle \tag{7.13}$$

$$\Delta^2\hat{S}_1 = \alpha_H^2(t)\Delta^2\hat{X}_H^+ + \alpha_V^2(t)\Delta^2\hat{X}_V^+ - 2\alpha_H(t)\alpha_V(t)\left\langle\delta\hat{X}_H^+\delta\hat{X}_V^+\right\rangle \tag{7.14}$$

$$\Delta^2\hat{S}_2(\theta) = \alpha_H^2(t)\Delta^2\hat{X}_V^{-\theta} + \alpha_V^2(t)\Delta^2\hat{X}_H^{\theta} + 2\alpha_H(t)\alpha_V(t)\left\langle\delta\hat{X}_V^{-\theta}\delta\hat{X}_H^{\theta}\right\rangle \tag{7.15}$$

$$\Delta^2\hat{S}_3(\theta) = \Delta^2\hat{S}_2\left(\theta - \frac{\pi}{2}\right). \tag{7.16}$$

where we assume that $\{\Delta^2\hat{X}_H^\theta, \Delta^2\hat{X}_V^\theta\} \ll \alpha_V(t)^2$ for all θ, and therefore neglect terms not scaled by either $\alpha_H(t)$ or $\alpha_V(t)$. We see that the variances of Stokes operators can be expressed in terms of the quadrature operator variances of the constituent horizontally and vertically polarised modes. Polarisation squeezed states can now be defined in a straight forward manner. If the constituent horizontally and vertically polarised modes are both coherent $\Delta^2\hat{X}_H^{\theta_1} = \Delta^2\hat{X}_V^{\theta_1} = 1$, and $\langle\delta\hat{X}_V^{\theta_1}\delta\hat{X}_H^{\theta_2}\rangle = 0$ for all $\{\theta_1, \theta_2\}$, and the variances of all four Stokes operators are at the quantum noise limit $\langle\tilde{n}\rangle$. A Stokes operator is therefore said to be squeezed if its variance falls below the quantum noise of a coherent beam of equal power. We have chosen arbitrarily to decompose Eqs. (7.13)-(7.16) in terms of the H, V-polarisation basis here. This decomposition is independent of the actual procedure of generating a polarisation squeezed beam, but this particular basis makes it particularly evident that overlapping horizontally and vertically polarised quadrature squeezed beams produces a single polarisation squeezed beam. Throughout the work presented here we assume that the horizontally and vertically polarised constituent modes are uncorrelated so that $\langle\delta\hat{X}_V^{\theta_1}\delta\hat{X}_H^{\theta_2}\rangle = 0$ for all $\{\theta_1, \theta_2\}$, Eqs. (7.13)-(7.16) then reduce to

$$\Delta^2\hat{S}_0 = \Delta^2\hat{S}_1 = \alpha_H^2(t)\Delta^2\hat{X}_H^+ + \alpha_V^2(t)\Delta^2\hat{X}_V^+ \tag{7.17}$$

$$\Delta^2\hat{S}_2(\theta) = \cos^2\theta\Big(\alpha_V^2(t)\Delta^2\hat{X}_H^+ + \alpha_H^2(t)\Delta^2\hat{X}_V^+\Big) + \sin^2\theta\Big(\alpha_V^2(t)\Delta^2\hat{X}_H^- + \alpha_H^2(t)\Delta^2\hat{X}_V^-\Big) \tag{7.18}$$

$$\Delta^2\hat{S}_3(\theta) = \sin^2\theta\Big(\alpha_V^2(t)\Delta^2\hat{X}_H^+ + \alpha_H^2(t)\Delta^2\hat{X}_V^+\Big) + \cos^2\theta\Big(\alpha_V^2(t)\Delta^2\hat{X}_H^- + \alpha_H^2(t)\Delta^2\hat{X}_V^-\Big). \tag{7.19}$$

It can be seen from Eqs. (7.17), (7.18), and (7.19) that if the relative phase between the horizontally and vertically polarised constituent modes is set to $\theta = 0$ or $\theta = \pi/2$ the polarisation squeezed beam generated from two amplitude squeezed beams ($\{\Delta^2\hat{X}_H^+, \Delta^2\hat{X}_V^+\} < 1$) can have $\hat{S}_0$ and two additional Stokes operators, in theory, perfectly squeezed, while the forth is anti-squeezed. Utilising only one quadrature squeezed beam it is not possible to simultaneously squeeze any two of $\hat{S}_1$, $\hat{S}_2$, and $\hat{S}_3$ to better than 3 dB below the quantum noise limit ($\Delta^2\hat{S}_i + \Delta^2\hat{S}_j \geq \langle\tilde{n}\rangle$, with $i, j \in \{1, 2, 3; i \neq j\}$).

7.3 Experiment

Prior to the work presented here, polarisation squeezed states were generated by combining a strong coherent beam with a single weak amplitude squeezed beam [20, 222]. In both of those experiments the variance of only one Stokes operator was determined, and therefore the polarisation state was not fully characterised. In this Chapter we experimentally characterise the mean and variance of all four Stokes operators for these states. We then extend the work to polarisation squeezed states produced from two amplitude/phase squeezed beams.

7.3.1 Measuring the Stokes operators

Instantaneous values of the Stokes operators of all polarisation states analysed here were obtained with the apparatus shown in Fig. 7.2. The uncertainty relations of Eqs. (7.6), (7.7), and (7.8) dictate that $\hat{S}_1$, $\hat{S}_2$, and $\hat{S}_3$ cannot in general be measured simultaneously. The beam under interrogation was split on a polarising beam splitter and the two outputs were detected on a pair of high quantum efficiency photodiodes with 30 MHz bandwidth; the resulting photocurrents were added and subtracted to yield photocurrents containing the instantaneous values of $\hat{S}_0$ and $\hat{S}_1$, respectively. To measure $\hat{S}_2$ the polarisation of the beam was rotated by 45° with a half-wave plate before the polarising beam splitter and the detected photocurrents were subtracted. To measure $\hat{S}_3$ the polarisation of the beam was again rotated by 45° with a half-wave plate and a quarter-wave plate was introduced before the polarising beam splitter such that a horizontally polarised input beam became right-circularly polarised. Again the detected photocurrents were subtracted. The expectation value of each Stokes operator was equal to the DC output of the detection device and the variance was obtained by passing the output photocurrent into a Hewlett-Packard E4405B spectrum analyser. Every polarisation state interrogated in this work had a total power $|\langle \tilde{S}_0 \rangle|$ of roughly 2 mW.

An accurate characterisation of the quantum noise limit was required to determine whether any given Stokes operator was squeezed. This was measured by operating a single OPA without the second harmonic pump. The seed power was adjusted so that the output power was equal to that of the beam being interrogated. In this configuration the detection setup for $\hat{S}_2$ (see Fig. 7.2c)) functions exactly as a homodyne detector measuring vacuum noise scaled by the OPA output power, the variance of which is the quantum noise limit. Throughout each experimental run the power was monitored and was always within 2% of the power of the coherent calibration beam. This led to a conservative error in our frequency spectra of ±0.05 dB.

The Stokes operator variance spectra reported here were taken over the range from 3 to 10 MHz. The darknoise of the detection apparatus was always more than 4 dB below the measured traces and was taken into account. Each displayed trace is the average of three measurement results normalised to the quantum noise limit and smoothed over the resolution bandwidth of the spectrum analyser which was set to 300 kHz. The video bandwidth of the spectrum analyser was set to 300 Hz.

As is the case for all continuous variable quantum optical experiments, the efficiency of the Stokes operator measurements was critical. The overall detection efficiency of the interrogated beams was 76%. The loss came primarily from three sources: loss in escape from the OPAs (14%), detector inefficiency (7%), and loss in optics (5%). In the experiment where a squeezed beam was overlapped with a coherent beam additional loss was incurred due to poor mode-matching between the beams and the detection efficiency was 71%. Depolarising effects are thought to be another significant source of loss for some polarisation squeezing proposals [213]. In our scheme the non-linear processes (OPAs) are divorced from the polarisation manipulation (wave plates and polarising beam splitters), and depolarising effects are insignificant.

7.3.2 Quantum polarisation states from a single squeezed beam

We first characterise the polarisation state of a single bright amplitude squeezed beam provided by one of our OPAs, as shown in Fig. 7.3. The squeezed beam was horizontally polarised, resulting in Stokes operator expectation values of $\langle \hat{S}_0 \rangle = \langle \hat{S}_1 \rangle = |\alpha_H(t)|^2$ and $\langle \hat{S}_2 \rangle = \langle \hat{S}_3 \rangle = 0$. The variance spectra of the operators were measured and are displayed in Fig. 7.4. Both $\hat{S}_0$ and $\hat{S}_1$ were squeezed, a result that is unsurprising since the laser beam used was amplitude squeezed and impinged on a single detector in this detector setup. The measurements performed, therefore,

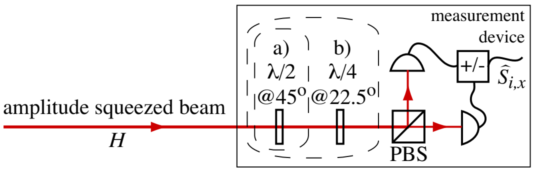

Figure 7.3: Apparatus used to produce and analyse a single amplitude squeezed beam. Optics in a) and b) were included to measure the variance and the expectation value of $\hat{S}_2$ and $\hat{S}_3$, respectively.

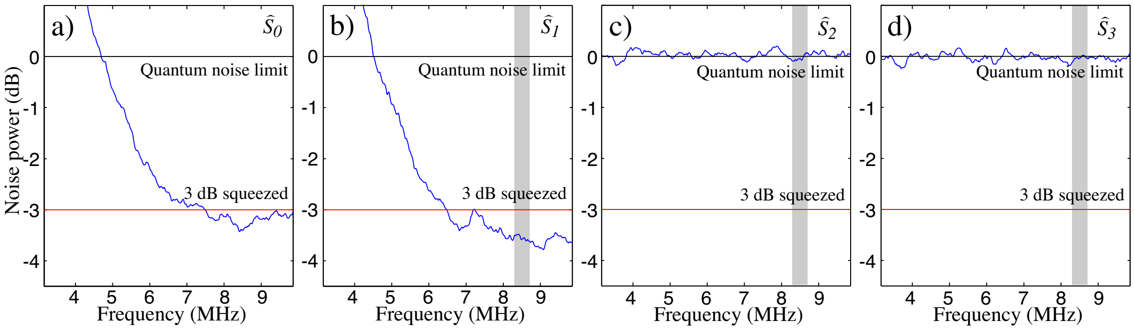

Figure 7.4: Measured variance spectra of quantum noise on $\hat{S}_0$, $\hat{S}_1$, $\hat{S}_2$, and $\hat{S}_3$ for a single bright amplitude squeezed beam; normalised to the quantum noise limit. The shaded region was used to construct the Poincaré sphere representation in Fig. 7.11 b).

equated to a measurement of the amplitude quadrature variance. For the measurements of $\hat{S}_2$ and $\hat{S}_3$ the beam intensity was divided equally between the two detectors. The electronic subtraction yielded vacuum noise scaled by the beam intensity, thus both variance measurements were at the quantum noise limit. It is apparent from these measurements that only the length of the Stokes vector is well determined; the orientation is just as uncertain as it would be for a coherent state.

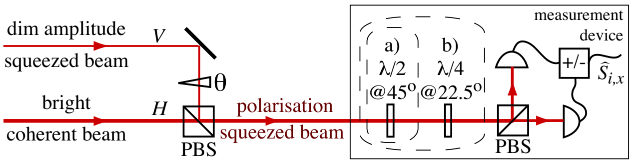

Figure 7.5: Apparatus used to produce and analyse the polarisation squeezed beam produced by overlapping a dim quadrature squeezed beam with a bright coherent beam. Optics in a) and b) were included to measure the variance and the expectation value of $\hat{S}_2$ and $\hat{S}_3$, respectively.

To obtain squeezing of the orientation of the Stokes vector Grangier *et al.* [222] and Hald *et al.* [20] overlapped a dim quadrature squeezed beam with a bright orthogonally polarised coherent beam. We consider this situation next (as shown in Fig. 7.6). Since two beams are now involved, the relative phase θ becomes important. A DC and an RF error-signal, both dependent on θ, were extracted from the Stokes operator measurement device. Together, these error signals allowed us to lock θ to either 0 or $\pi/2$ rads in all of the following experiments. We mixed a bright horizontally polarised coherent beam with a dim vertically polarised amplitude squeezed beam. Since the horizontally polarised beam was much more intense than the vertically polarised beam, the Stokes operator expectation values became $\langle\hat{S}_0\rangle \approx \langle\hat{S}_1\rangle \approx |\alpha_H(t)|^2$ and $\langle\hat{S}_2\rangle \approx \langle\hat{S}_3\rangle = 0$. The Stokes operator variances obtained for this polarisation state are shown in Fig. 7.6, with $\hat{S}_2$ now anti-

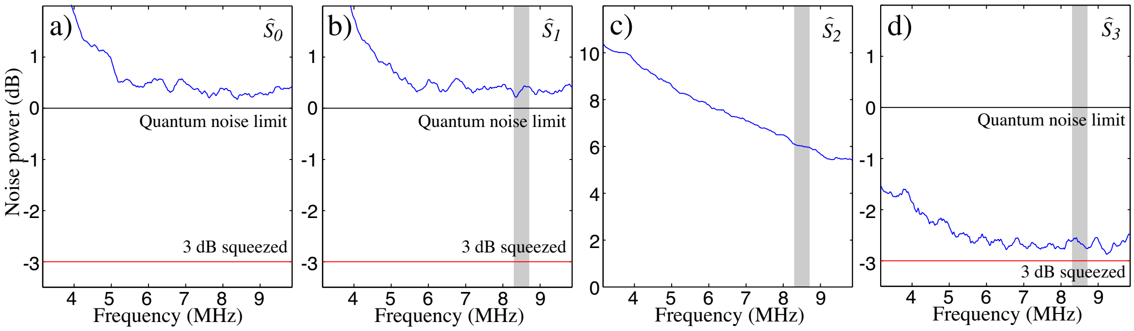

Figure 7.6: Measured variance spectra of quantum noise on $\hat{S}_0$, $\hat{S}_1$, $\hat{S}_2$, and $\hat{S}_3$ for a vacuum amplitude squeezed and a bright coherent input beams; normalised to the quantum noise limit. The shaded region was used to construct the Poincaré sphere representation in Fig. 7.11 c).

squeezed and $\hat{S}_3$ squeezed, so that the orientation of the Stokes vector on the $\hat{S}_3$ axis is determined to better than the quantum noise limit, and is therefore squeezed. The variances of $\hat{S}_0$ and $\hat{S}_1$ were slightly above the quantum noise limit because of residual noise from our laser resonant relaxation oscillation. The experiment carried out with θ locked to 0 rads is not shown, in this case the measured variances of $\hat{S}_2$ and $\hat{S}_3$ were swapped, and in fact the Stokes vector remained pointing along $\hat{S}_1$, so that the quantum noise was rotated on the Poincaré sphere as shown in Fig. 7.10 b).

7.3.3 Quantum polarisation states from two quadrature squeezed beams

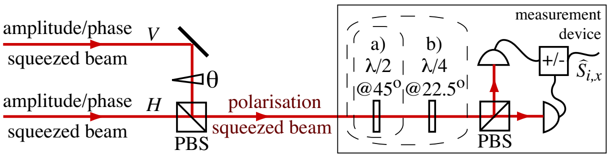

Figure 7.7: Apparatus used to produce and analyse the beam produced by combining two quadrature squeezed beams. Optics in a) and b) were included to measure the variance and the expectation value of $\hat{S}_2$ and $\hat{S}_3$, respectively.

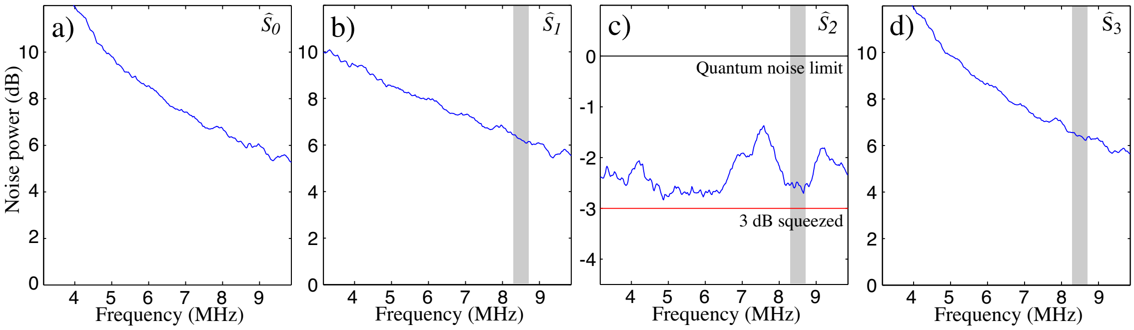

Figure 7.8: Measured variance spectra of quantum noise on $\hat{S}_0$, $\hat{S}_1$, $\hat{S}_2$, and $\hat{S}_3$ for two locked phase squeezed input beams; normalised to the quantum noise limit. The shaded region was used to construct the Poincaré sphere representation in Fig. 7.11 d).

The two experiments described in Section 7.3.2 demonstrated how it is possible to squeeze the length and orientation of the Stokes vector. In this Section we demonstrate that it is possible to do

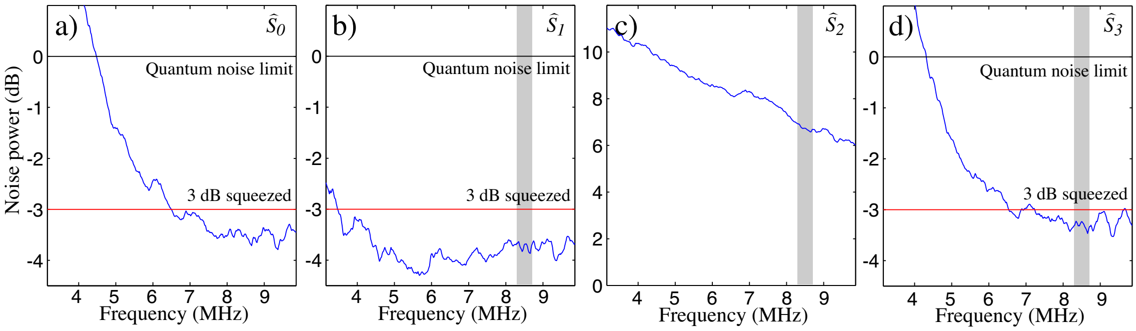

Figure 7.9: Measured variance spectra of quantum noise on $\hat{S}_0$, $\hat{S}_1$, $\hat{S}_2$, and $\hat{S}_3$ for two locked amplitude squeezed input beams; normalised to the quantum noise limit. The shaded region was used to construct the Poincaré sphere representation in Fig. 7.11 e).

both simultaneously. The two quadrature squeezed beams produced in our OPAs were combined with orthogonal polarisation on a polarising beam splitter [218] as shown in Fig. 7.7. This produced an output beam with Stokes operator variances as given by Eqs. (7.17), (7.18), and (7.19). Both input beams had equal power ($\alpha_H(t) = \alpha_V(t) = \alpha/\sqrt{2}$) and both were squeezed in the same quadrature. The Stokes operators and their variances were again determined as shown in Fig. 7.2. The relative phase between the quadrature squeezed input beams θ was locked to $\pi/2$ rads producing a right-circularly polarised beam with Stokes operator means of $\langle\hat{S}_1\rangle = \langle\hat{S}_2\rangle = 0$ and $\langle\hat{S}_0\rangle = \langle\hat{S}_3\rangle = |\alpha|^2$.

First both OPA pump beams were phase locked to amplification, this produced two phase squeezed beams. Fig. 7.8 shows the measurement results obtained; $\hat{S}_0$, $\hat{S}_1$ and $\hat{S}_3$ were all anti-squeezed and $\hat{S}_2$ was squeezed throughout the range of the measurement. The optimum noise reduction of $\hat{S}_2$ was 2.8 dB below the quantum noise limit and was observed at 4.8 MHz. Our OPAs are particularly sensitive to phase noise coupling in from the MgO:LiNbO$_3$ crystals. We attribute the structure in the frequency spectra of $\hat{S}_2$ to this. The poorer squeezing observed here was a combined result of this sensitivity to phase noise, and the coupling of green pump noise onto the squeezed states that occurs when the OPAs operate in the amplification regime (see Section 3.5.2). Apart from this structure and the coupling of pump noise into the squeezing, these results are very similar to those produced by a single squeezed beam and a coherent beam; the orientation of the Stokes vector is squeezed. However, here the uncertainty in the length of the Stokes vector is greater than that for a coherent state so the polarisation state, although produced from two quadrature squeezed beams, is actually less well defined.

Fig. 7.9 shows the measurement results obtained with the OPAs locked to deamplification, and with both OPAs therefore providing amplitude squeezed beams. Again we interrogated the combined beam and found $\hat{S}_0$, $\hat{S}_1$ and $\hat{S}_3$ all to be squeezed from 4.5 MHz to the limit of our measurement, 10 MHz. $\hat{S}_2$ was anti-squeezed throughout the range of the measurement. Between 7.2 MHz and 9.6 MHz $\hat{S}_0$, $\hat{S}_1$ and $\hat{S}_3$ were all more than 3 dB below the quantum noise limit. The squeezing of $\hat{S}_0$ and $\hat{S}_3$ was degraded at low frequencies due our lasers resonant relaxation oscillation. Since this noise was correlated it canceled in the variance of $\hat{S}_1$. The maximum squeezing of $\hat{S}_0$ and $\hat{S}_2$ was 3.8 dB and 3.5 dB respectively and was observed at 9.3 MHz. The maximum squeezing of $\hat{S}_1$ was 4.3 dB at 5.7 MHz. The repetitive structure at 4, 5, 6, 7, 8 and 9 MHz was caused by electrical pick-up in our SHG resonator emitted from a separate experiment operating in the laboratory. In this case both the orientation and the length of the Stokes vector were squeezed.

Finally we point out that the variances of $\hat{S}_1$ in Figs. 7.6, 7.8 and 7.9 were all squeezed at frequencies down to 3 MHz and even below, whereas Fig. 3.11 shows a clear degradation below 4 MHz. This improved performance is due to electrical noise cancellation of our correlated laser relaxation oscillation noise similar to the optical cancellation demonstrated in Section 3.7.

7.4 Poincaré sphere visualisation of polarisation states

The previous Section provided detailed experimental characterisations for each of the optical polarisation states investigated in this Chapter. Fig. 7.11 visualises the fluctuations at 8.5 MHz on the Poincaré sphere. The standard deviation contour-surfaces shown for each state provide an accurate representation of the states three-dimensional noise distribution, assuming that the noise is Gaussianly distributed. The quantum polarisation noise of a coherent state forms a sphere of noise as portrayed in Fig. 7.11 a). The noise volumes b) to e) visualise the polarisation states generated by a single bright amplitude squeezed beam; and by combining a dim amplitude squeezed beam and a bright coherent beam, two phase squeezed beams, and two amplitude squeezed beams on a polarising beam splitter, respectively. In all cases the Poincaré sphere has been rotated so that the Stokes vector coherent amplitude is vertically orientated. There was no fundamental bias in the orientation of the quantum Stokes vector in our experiment. By varying the angle of an additional half-wave plate in the polarisation squeezed beam or by varying θ any orientation could be achieved. In fact, as mentioned earlier our experiments were also carried out with θ locked to 0 rads. This had the effect of rotating the Stokes vector and its quantum noise by $\pi/2$ around $\hat{S}_1$. Nearly identical results were obtained but on alternative Stokes operators. Fig. 7.10 shows Poincaré sphere representations of this rotation for the polarisation states produced by two amplitude squeezed beams (Fig. 7.10 a)), and by one squeezed beam and a coherent state (Fig. 7.10 b)).

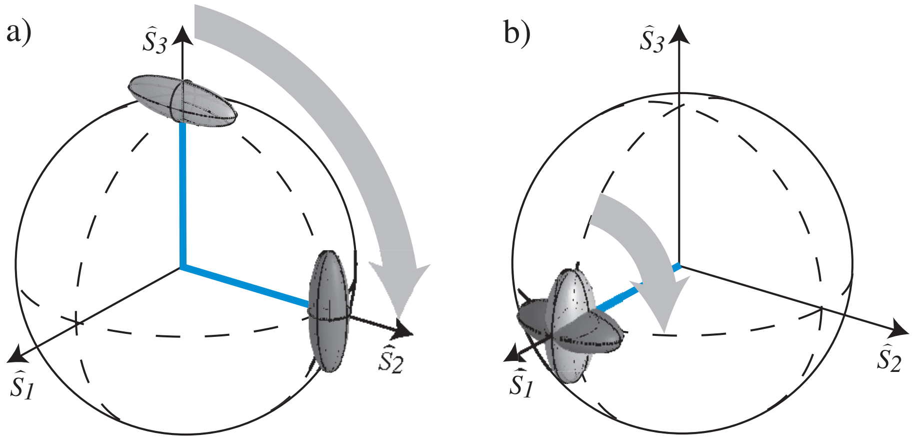

Figure 7.10: Visualisation of measured quantum noise and measured Stokes vectors of four polarisation states mapped onto the Poincaré sphere. The states were generated from a) two bright amplitude squeezed inputs and b) a bright coherent beam and a amplitude squeezed vacuum. The rotations in a) and b) were achieved by a $\theta = \pi/2$ phase shift between the input beams to the polarising beam splitter.

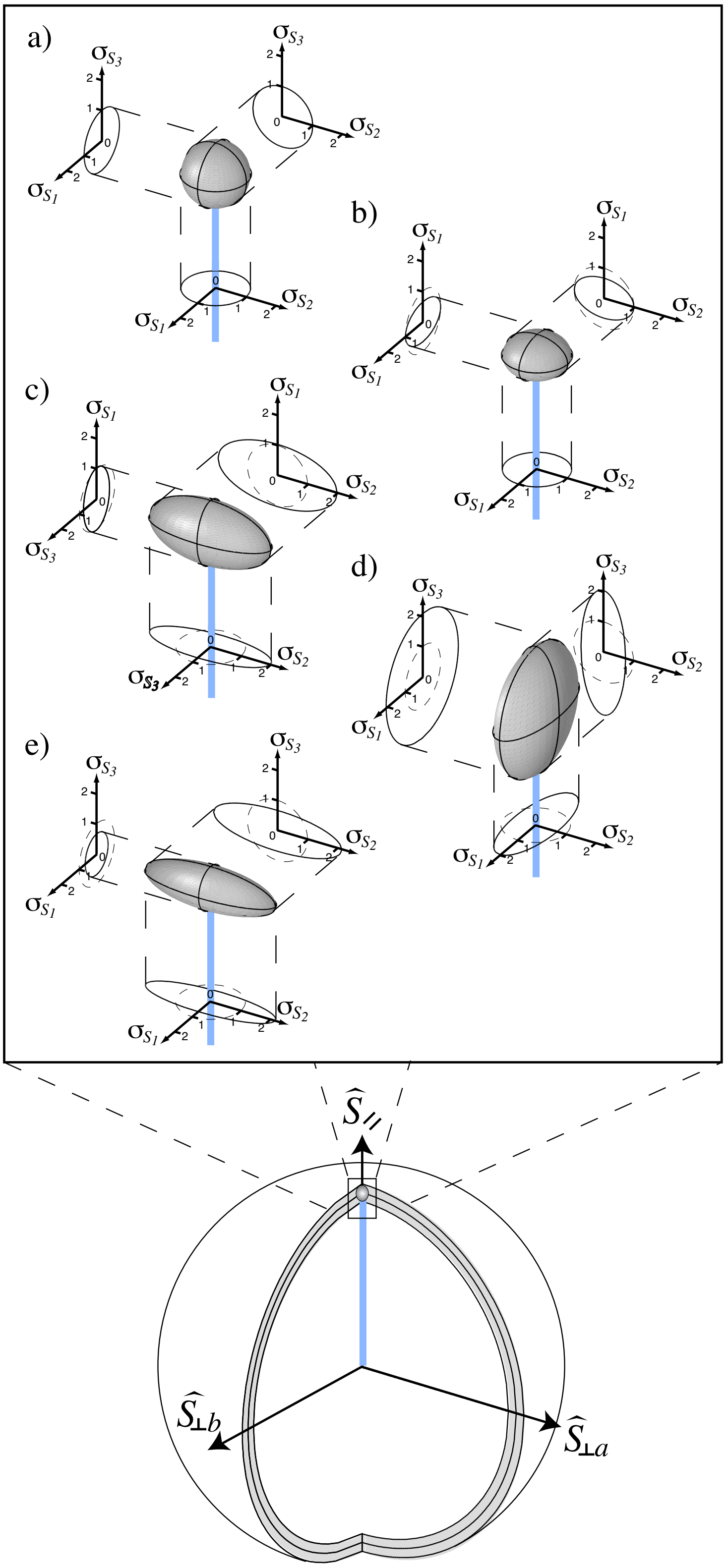

Figure 7.11: Measured quantum polarisation states at 8.5 MHz from different combinations of polarising beam splitter input beams. a) single coherent beam, b) bright squeezed beam, c) coherent beam and squeezed vacuum, d) two phase squeezed beams and e) two amplitude squeezed beams. The surface of the ellipsoids defines the standard deviation of the noise normalised to the quantum noise limit. $\hat{S}_{//}$ denotes the Stokes operator aligned in the direction of the Stokes vector coherent amplitude.

7.5 Channel capacity achievable using polarisation squeezed beams

The reduced level of fluctuations in polarisation squeezed light can be used to improve the channel capacity of communication protocols. Let us consider information encoded on the sidebands of a bandwidth limited laser beam. We assume that only direct detection is employed, or in other words, that phase sensitive techniques such as homodyne measurement are not available. This is not an artificial constraint since phase sensitive techniques are technically difficult to implement and are rarely utilised in conventional optical communications systems.

An upper bound to the amount of information that can be carried by a bandwidth limited additive white Gaussian noise channel is given by the Shannon capacity C in Eq. (4.51) [156]. Since quantum mechanics imposes uncertainty relations on non-commuting observables, the optical state used in a communication channel ultimately limits its capacity. For good overviews of quantum noise limited channel capacities I recommend [234] and [235]. Here, we wish to compare the channel capacities achievable with pure coherent, quadrature squeezed, and polarisation squeezed states for a given average sideband photon number $\bar{n}$, which in this case is given by the sum of the average photon numbers in each of the constituent horizontally and vertically polarised modes

$$\bar{n} = \left\langle \hat{a}_H^\dagger \hat{a}_H \right\rangle + \left\langle \hat{a}_V^\dagger \hat{a}_V \right\rangle , \tag{7.20}$$

The mean photon number $\bar{n}$ takes into account sideband photons present both as a result of squeezing, and of signal encoding. As discussed in Section 4.3.4 without squeezing and signal modulation $\bar{n} = 0$.

First let us consider strategies that might be employed in communication channels utilising a coherent beam. In conventional optical communication systems the polarisation degrees of freedom are ignored completely and information is encoded only on $\hat{S}_0$ as intensity fluctuations. Taking $\alpha_V(t) = 0$ the variance of the Stokes operator $\hat{S}_0$ is given by $\Delta^2\hat{S}_0 = \alpha_H(t)^2(\Delta^2\hat{X}_H^+ + \Delta^2\hat{\mathcal{S}}_H^+)$ in accordance with Eq. (7.17), where $\hat{\mathcal{S}}_H^+$ is the signal encoded on the amplitude quadrature of the horizontally polarised beam. For this one-dimensional coherent channel $\Delta^2\hat{X}_H^+ = 1$ so that the signal to noise ratio is given by $\mathrm{SNR} = \Delta^2\hat{\mathcal{S}}_H^+$. From Eq. (7.20) we find that for this arrangement the average photon number per bandwidth per time in the field is $\bar{n} = \Delta^2\hat{\mathcal{S}}_H^+/4$, so that the Shannon capacity of the channel as a function of $\bar{n}$ is given by

$$C_{\mathrm{coh}}^{i} = \frac{1}{2}\log_2(1 + 4\bar{n}) . \tag{7.21}$$

This is a non-optimal strategy however. Examining Eqs. (7.5) and (7.9)-(7.12) we see that it is possible to choose an arrangement for which two of the Stokes operators commute and so can be measured simultaneously. Indeed it is easy to show that such simultaneous measurements can be made using only linear optics and direct detection. In particular let us assume that $\alpha_H(t) = \alpha_V(t)$ such that $\hat{S}_2$ and $\hat{S}_3$ commute, and use $\hat{S}_2$ and $\hat{S}_3$ as two independent information channels. Then $\hat{S}_2 = \hat{S}_0$ and the information in both dimensions can be simultaneously extracted by subtracting and adding, respectively, the photocurrents from a single pair of detectors. Assuming equal signal to noise ratios $\mathrm{SNR}_2 = \mathrm{SNR}_3$ we find that $\Delta^2\hat{\mathcal{S}}_2 = \Delta^2\hat{\mathcal{S}}_3 = 2\bar{n}$, and the channel capacity may be written

$$\begin{aligned} C_{\mathrm{coh}}^{ii} &= \frac{1}{2}\log_2(1 + \mathrm{SNR}_2) + \frac{1}{2}\log_2(1 + \mathrm{SNR}_3) && (7.22) \\ &= \log_2(1 + 2\bar{n}) . && (7.23) \end{aligned}$$

This channel capacity is always greater than that of Eq. (7.21) and for large $\bar{n}$ is 100 % greater.

For sufficiently high $\bar{n}$ a further improvement in channel capacity can be achieved. Consider placing signals on all three Stokes operators. Because of the non-commutation of $\hat{S}_1$ with $\hat{S}_2$ and $\hat{S}_3$ it is not possible to read out all three signals without a measurement penalty. Suppose the receiver adopts the following strategy: divide the beam on a beam splitter with transmissivity ϵ and then measure $\hat{S}_1$ on the reflected output and $\hat{S}_2$ and $\hat{S}_3$ on the other output. Division of the beam will reduce the measured signal to noise ratios due to the injection of a vacuum field at the beam splitter such that $\mathrm{SNR}_1 = (1-\epsilon)\Delta^2\hat{\mathcal{S}}_1$, $\mathrm{SNR}_2 = \epsilon\Delta^2\hat{\mathcal{S}}_2$ and $\mathrm{SNR}_3 = \epsilon\Delta^2\hat{\mathcal{S}}_3$. We find that for large $\bar{n}$ an optimum is reached with $\epsilon = 2/3$ and with the mean signal photon number used in the encoding on each Stokes operator being $\bar{n}_1 = \bar{n}_2 = \bar{n}_3 = \bar{n}/3$. Hence the channel capacity is

$$\begin{aligned} C^{iii}_{\mathrm{coh}} &= \frac{1}{2}\log_2(1+\mathrm{SNR}_1) + \frac{1}{2}\log_2(1+\mathrm{SNR}_2) + \frac{1}{2}\log_2(1+\mathrm{SNR}_3) && (7.24) \\ &= \frac{1}{2}\log_2\left(1+\frac{4}{9}\bar{n}\right) + \log_2\left(1+\frac{8}{9}\bar{n}\right). && (7.25) \end{aligned}$$

This capacity beats that of Eq. (7.23) for $\bar{n} > 7.56$. In summary the optimum coherent channel capacity examined here is given by Eq. (7.25) for average photon numbers $\bar{n} > 7.56$ and by Eq. (7.23) for lower values, see Fig. 7.12 traces c) and d).

Now let us examine the effect of polarisation squeezing on the channel capacity. Consider first the simple case of intensity modulation on a single squeezed beam, which is equivalent to using a squeezed beam in the first coherent case considered (case i). The channel capacity can be maximised by optimising the fraction of photons that are introduced through squeezing and through signal encoding. For large photon numbers we find that the photons should be balanced equally between these two roles. For an average photon number per bandwidth per time of 1, 1/3 of the photons per bandwidth per time should be used to generate squeezing. The maximum channel capacity using an amplitude squeezed beam and encoding only on the amplitude quadrature can be shown to be [234]

$$C^{i}_{\mathrm{1sqz}} = \log_2(1+2\bar{n}), \qquad (7.26)$$

This capacity beats only the corresponding coherent state communication channel. It is as effective as the two Stokes operator coherent channel, but is less effective than the three Stokes operator coherent channel for large photon numbers.

Consider now a polarisation squeezed beam produced by combining a minimum uncertainty squeezed beam and an orthogonally polarised coherent beam on a polarising beam splitter, as was experimentally demonstrated in Section 7.3.2. Suppose, as in the two Stokes operator coherent case, that $\hat{S}_2$ and $\hat{S}_3$ commute and arrange that $\hat{S}_2$ has fluctuations at the quantum noise level while $\hat{S}_3$ is optimally squeezed. Again signals are encoded on $\hat{S}_2$ and $\hat{S}_3$. The channel capacity can be maximised by adjusting the relative signal sizes on the two Stokes operators for fixed average photon number as a function of the squeezing. Here 1/3 of the photons are used to generate squeezing and 2/3 are split equally to encode signals on $\hat{S}_2$ and $\hat{S}_3$. The resulting maximum channel capacity is

$$C^{ii}_{\mathrm{1sqz}} = \frac{3}{2}\log_2\left(1+\frac{4}{3}\bar{n}\right). \qquad (7.27)$$

This always beats all three coherent state cases considered here, but in the limit of large $\bar{n}$ the advantage is minimal since the scaling with photon number is the same as that of C^{iii}_{coh} in Eq. (7.25).

If the polarisation squeezed beam is produced from two amplitude squeezed beams as in Section 7.3.3 the enhancement becomes more significant. Suppose again that $\hat{S}_2$ and $\hat{S}_3$ commute but now that both are optimally squeezed. Again encoding on $\hat{S}_2$ and $\hat{S}_3$, and varying the signal strength as a function of squeezing to maximise the channel capacity for a given $\bar{n}$. The maximum is reached when the photons are used equally to generate squeezing and to encode information. The channel capacity for this arrangement is given by

$$C^{ii}_{2\mathrm{sqz}} = 2\log_2(1+\bar{n}), \tag{7.28}$$

which for large $\bar{n}$ is 33% greater than both the optimum coherent scheme and the scheme using a single quadrature squeezed beam. Unlike the coherent state case, no further improvement of the channel capacity can be obtained by encoding the information on three Stokes operators.

Fig. 7.12 plots the channel capacities as a function of total mean photons per bandwidth per time itilised, for each of the communication channels analysed in this Section. Finally we assess

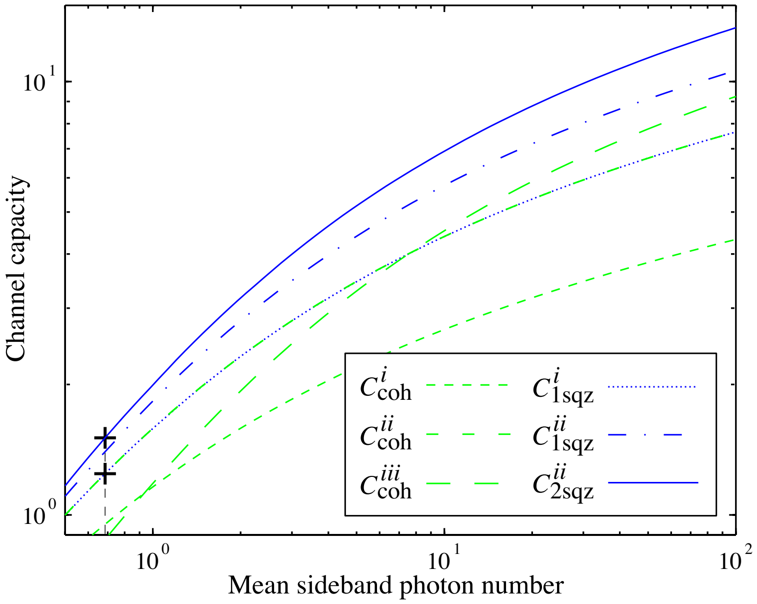

Figure 7.12: Calculated channel capacities for various continuous variable polarisation states. The cross on the upper curve marks the channel capacity which could be achieved using the polarisation squeezed state we generated by combining two amplitude squeezed beams on a polarising beam splitter, and the lower cross marks the equivalent channel capacity achieved by the optimum coherent state scheme.

the channel capacities that could in principle be achieved using the polarisation squeezed state generated by combining two amplitude squeezed beams on a polarising beam splitter in our experiment. The polarisation squeezing achieved in Fig. 7.9 implies that, assuming the squeezed beams were pure and operating the communication scheme at sideband frequencies between 8 MHz and 10 MHz, 0.17 sideband photons per bandwidth per time were present in each of the two channels. This is an optimum quantum resource to transmit signals encoded using an average of 0.68 sideband photons per bandwidth per time. Signals sufficiently high above detector dark noise would achieve a channel capacity that is around 21% greater than the ideal channel capacity achievable from a coherent beam with the same average sideband photon number. This is illustrated by the crosses in Fig. 7.12.

7.6 Conclusion

In this Chapter we have generated and characterised polarisation squeezed states, and represented them on the quantum Poincaré sphere as shown in Fig. 7.11. In particular we analysed the polarisation properties of the coherent state and the amplitude squeezed state; and of the polarisation squeezed states generated by combining a dim amplitude squeezed state with a bright coherent state; two phase squeezed states; and two amplitude squeezed states; with orthogonal polarisation on a polarising beam splitter. When combining a pair of amplitude squeezed states we demonstrated strong squeezing of three of the four Stokes operators. We analysed the channel capacities of several communication protocols using continuous variable polarisation states. For a given average photon number $\bar{n}$, we found that polarisation states produced from two amplitude squeezed beams can provide a 33% greater channel capacity than both the optimum communication channel using coherent states and the optimum scheme using a single amplitude squeezed state.

Chapter 8

Continuous variable polarisation entanglement

This Chapter investigates continuous variable polarisation entanglement. We generate and characterise this form of entanglement between a pair of Stokes operators on two optical beams. This is achieved by first producing quadrature entanglement in the manner discussed in Chapter 4, and by performing local operations to transform it onto a polarisation basis. We extend the inseparability criteria proposed by Duan *et al.*[130] and the Einstein-Podolsky-Rosen paradox criteria proposed by Reid and Drummond[134, 135] to Stokes operators; and use them to characterise the entanglement. By using two quadrature entangled pairs it is possible to extend our polarisation entanglement scheme to entangle three orthogonal Stokes operators between a pair of beams, although with a bound $\sqrt{3}$ times more stringent than for the quadrature entanglement.

The work presented in this Chapter has been published in the journal articles:

- W. P. Bowen, N. Treps, R. Schnabel, and P. K. Lam. *Experimental demonstration of continuous variable polarization entanglement.* Physical Review Letters **89**, 253601 (2002).
- W. P. Bowen, N. Treps, R. Schnabel, T. C. Ralph, and P. K. Lam. *Continuous variable polarization entanglement, experiment and analysis.* Journal of Optics B: Quantum and Semi-Classical Optics **5**, pp. S467 (2003).

8.1 Introduction

In this Chapter we report the experimental transformation of the quadrature entanglement of Chapter 4 onto a polarisation basis. The transformation is achieved by combining each quadrature entangled beam with an orthogonally polarised bright coherent beam on a polarising beam splitter. A characterisation of the resulting polarisation entanglement is achieved by generalising standard techniques for quadrature entanglement. As discussed in Chapter 4, many method have been proposed to characterise quadrature entanglement. Two commonly used criteria are the inseparability criterion proposed by Duan *et al.*[130] and the EPR paradox criterion proposed by Reid and Drummond[134, 135]. Both criteria are based explicitly on the uncertainty relation between the observables under interrogation. Using the standard uncertainty principle we generalise both criteria to an arbitrary pair of operators and then to Stokes operators in particular. We show that the polarisation entanglement we generate strongly satisfies both criteria. Interacting this entanglement with a pair of distant atomic ensembles could entangle the atomic spin states.

The concept of continuous variable polarisation entanglement was introduced in the work of Korolkova *et al.*[218]. In their paper they proposed that such entanglement could be generated by interfering a pair of polarisation squeezed beams, each produced from two amplitude squeezed beams, on a 50/50 beam splitter; just as quadrature entanglement can be generated with a pair of quadrature squeezed beams. Such an experiment would require twice the resources necessary for the implementation presented here. Korolkova *et al.*[218] also perform the first generalisation of the inseparability and EPR paradox criteria to Stokes operators. Their Stokes operator EPR paradox criterion is identical to that derived here. Their inseparability criterion is, however, only valid when the Stokes operators of interest are aligned orthogonally to the Stokes vector (see Fig. 7.1). This contrasts our expression, which is valid for arbitrary Stokes vector orientation.

The ability to generate and manipulate pairs of photons that, when their polarisation is analysed, demonstrate entanglement is a key tool of quantum optics. These states have allowed for many fundamental studies such as tests of Bells inequality[119, 120, 121]; and also perhaps more technologically minded studies like that of quantum computation[10]. An interesting analogy may be made between this discrete variable polarisation entanglement and the continuous variable equivalent investigated in this Chapter. Discrete polarisation entanglement is commonly observed between all three Stokes operators, and is basis independent. That is, correlations will exist between measurements on the two photons when any arbitrary Stokes operator is measured. Since the entanglement discussed here is generated from a single quadrature entangled pair, in which entanglement is observed between only two quadratures, it is perhaps unsurprising that all three Stokes operators are not entangled. However, when two quadrature entangled pairs are utilised, we show that it is possible to simultaneously entangle all three Stokes operators, but only if the quadrature entanglement is strong enough to beat a bound $\sqrt{3}$ times stronger than that for the inseparability criterion. In contrast to discrete polarisation entanglement the entanglement is not basis independent. That is, observation of entanglement between three specific Stokes operators does not ensure entanglement between any three arbitrary Stokes operators.

Similarly to the case of polarisation squeezing in the previous Chapter, subsequent to the work presented here experimental demonstrations of polarisation entanglement were performed utilising both the Kerr non-linearity in optical fibres [236], and a cloud of cold Cesium atoms in a high finesse resonator [237]. Some interesting new schemes for the generation of polarisation entanglement have also been published [226, 238].

8.2 Theory

8.2.1 Characterising entanglement

We characterise our polarisation entanglement by transforming the inseparability criterion proposed by Duan *et al.*[130] and the Einstein-Podolsky-Rosen (EPR) paradox criterion proposed by Reid and Drummond[134, 135] used in Chapter 4 to polarisation observables. In general, a necessary and sufficient criterion for entanglement should identify entanglement of any observables between a pair of sub-systems. Clearly however, a realistic criterion must be based on some finite set of observables. In this thesis the term *polarisation entanglement* refers to entanglement that can be verified through measurements of only polarisation properties of the light field, and similarly *quadrature entanglement* refers to entanglement that can be verified through measurements performed solely on field quadratures.

Both the EPR and Inseparability criteria rely explicitly on the uncertainty relations between the observables involved and were initially proposed between the amplitude and phase quadratures of light beams. Given the uncertainty principle between an arbitrary pair of observables $\hat{A}$ and $\hat{B}$

$$\begin{aligned} \Delta^2\hat{A}\Delta^2\hat{B} &\geq \left|\left\langle \delta\hat{A}\delta\hat{B}\right\rangle\right|^2 && (8.1)\\ &\geq \frac{\left|[\delta\hat{A},\delta\hat{B}]\right|^2}{4} + \frac{\left|\left\langle \delta\hat{A}\delta\hat{B}+\delta\hat{B}\delta\hat{A}\right\rangle\right|^2}{4}, && (8.2)\end{aligned}$$

it is possible to generalise both criteria to any pair observables. Within some environment the commutation relation $[\delta\hat{A},\delta\hat{B}]$ is a general property between the observables involved, and is independent of the properties of particular states; on the other hand the correlation function $|\langle\delta\hat{A}\delta\hat{B}+\delta\hat{B}\delta\hat{A}\rangle|^2$ measures correlation between the observables $\hat{A}$ and $\hat{B}$ for the particular state and is therefore dependent on the state properties. For this reason the correlation function term is generally neglected in the uncertainty relation. We neglect it here to obtain the standard uncertainty relation

$$\Delta^2\hat{A}\Delta^2\hat{B} \geq \frac{\left|[\delta\hat{A},\delta\hat{B}]\right|^2}{4}. \quad (8.3)$$

When using this relation the entanglement criteria discussed herein become sufficient, but not necessary, for entanglement.

In Section 8.5 we will consider the correlation function for the particular states discussed explicitly and show that it has an insignificant contribution. Throughout this thesis we label the two beams to be interrogated for entanglement with the subscripts x and y respectively. In general these beams will give different values for the correlation function. This leads to an ambiguous contribution to the uncertainty relation. We assume that beams x and y are interchangeable in the sense that all experimental outcomes are independent of their exchange. This is the situation relevant to our experiment and results in equal values of the correlation function for the two beams

$$\left|\left\langle \delta\hat{A}\delta\hat{B}+\delta\hat{B}\delta\hat{A}\right\rangle\right|^2 = \left|\left\langle \delta\hat{A}_x\delta\hat{B}_x+\delta\hat{B}_x\delta\hat{A}_x\right\rangle\right|^2 = \left|\left\langle \delta\hat{A}_y\delta\hat{B}_y+\delta\hat{B}_y\delta\hat{A}_y\right\rangle\right|^2. \quad (8.4)$$

The inseparability criterion

The inseparability criterion as originally proposed characterises the separability of the amplitude $\hat{X}^+$ and phase $\hat{X}^-$ quadratures of a pair of optical beams. For states with Gaussian noise statistics this criterion has been shown to be a necessary and sufficient criterion for entanglement[130]. As was shown in Chapter 4, when beams x and y are perfectly interchangeable and their fluctuations are symmetrical between the amplitude and phase quadratures the inseparability criterion can be written as

$$\Delta^2_{x\pm y}\hat{X}^+ + \Delta^2_{x\pm y}\hat{X}^- < 2. \quad (8.5)$$

Throughout this thesis $\Delta^2_{x\pm y}\hat{O}$ is the minimum of the variance of the sum or difference of the operator $\hat{O}$ between beams x and y, $\Delta^2_{x\pm y}\hat{O} = \min\langle(\delta\hat{O}_x\pm\delta\hat{O}_y)^2\rangle/2$. Given the Heisenberg uncertainty relation of equation 8.3 the measure in Eq. (8.5) can be generalised to any pair of observables $\hat{A}$, $\hat{B}$

$$\Delta^2_{x\pm y}\hat{A} + \Delta^2_{x\pm y}\hat{B} < |[\delta\hat{A},\delta\hat{B}]|. \quad (8.6)$$

To allow direct analysis of our experimental results, we define the degree of inseparability $\mathcal{I}(\hat{A}, \hat{B})$ in a similar manner to that performed in Chapter 4, normalised such that if $\mathcal{I}(\hat{A}, \hat{B}) < 1$ the state is inseparable, and therefore entangled

$$\mathcal{I}(\hat{A}, \hat{B}) = \frac{\Delta^2_{x\pm y}\hat{A} + \Delta^2_{x\pm y}\hat{B}}{2|[\delta\hat{A}, \delta\hat{B}]|}. \tag{8.7}$$

It should be noted that this measure may be generalised to a wider set of states by arranging it in a product form[146, 147], and indeed this was the form used to measure quadrature entanglement in Chapter 4

$$\mathcal{I}_{\text{product}}(\hat{A}, \hat{B}) = 2\frac{\sqrt{\Delta^2_{x\pm y}\hat{A}\Delta^2_{x\pm y}\hat{B}}}{|[\delta\hat{A}, \delta\hat{B}]|}. \tag{8.8}$$

In this form the measure is independent of equal local squeezing operations performed on x and y. Since the sum and product measures involve the same level of experimental complexity the product should, in general, be preferred. For the experimental configuration of this Chapter the measures are equivalent. Since the sum form was the original form proposed by Duan *et al.*[130] we use it here.

The EPR paradox criterion

The EPR paradox was first discussed by Einstein *et al.* as a demonstration of the physically unsatisfactory nature of quantum mechanics [16]. The EPR paradox criterion utilised here was proposed by Reid and Drummond[134, 135] and is based on the observation of non-classical correlations between two beams. That is, the ability to infer (although not simultaneously) both variables of interest on beam x to better than their Heisenberg uncertainty limit, after measurements on beam y. The EPR paradox criterion is a sufficient condition for entanglement and was used to characterise our quadrature entanglement in Chapter 4. Between the amplitude and phase quadratures of a pair of beams it is given by Eq. (4.29). Utilising the uncertainty relation of Eq. (8.3) this criterion can also be generalised to arbitrary observables

$$\Delta^2_{x|y}\hat{A}\Delta^2_{x|y}\hat{B} < \frac{|[\delta\hat{A}, \delta\hat{B}]|^2}{4}, \tag{8.9}$$

where $\Delta^2_{x|y}\hat{O}$ is the variance of operator $\hat{O}$ in sub-system x conditioned on its measurement in sub-system y and is given by

$$\begin{aligned} \Delta^2_{x|y}\hat{O} &= \Delta^2\hat{O}_x - |\langle\delta\hat{O}_x\delta\hat{O}_y\rangle|^2/\Delta^2\hat{O}_y & (8.10)\\ &= \min_g \langle(\delta\hat{O}_x + g\delta\hat{O}_y)^2\rangle, & (8.11) \end{aligned}$$

and the gain g is an experimentally adjustable parameter. In a manner similar to that in Chapter 4, we express the criterion in terms of the *degree of EPR paradox* $\mathcal{E}(\hat{A}, \hat{B})$ normalised so that $\mathcal{E}(\hat{A}, \hat{B}) < 1$ implies observation of the EPR paradox

$$\mathcal{E}(\hat{A}, \hat{B}) = 4\frac{\Delta^2_{x|y}\hat{A}\Delta^2_{x|y}\hat{B}}{|[\delta\hat{A}, \delta\hat{B}]|^2}. \tag{8.12}$$

8.2.2 Generalisation of entanglement criteria to Stokes operators

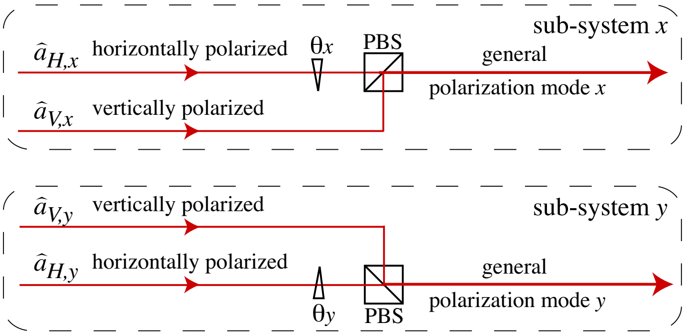

Figure 8.1: Production of a pair of arbitrary polarisation modes. PBS: polarising beam splitter.

From Eqs. (7.5) and (8.1) it is clear that the Stokes operator variances are restricted by the uncertainty relations[231, 232]

$$\begin{aligned}\Delta^2\hat{S}_1\Delta^2\hat{S}_2 &\geq \left|\left\langle\hat{S}_3\right\rangle\right|^2+\frac{1}{4}\left|\left\langle\delta\hat{S}_1\delta\hat{S}_2+\delta\hat{S}_2\delta\hat{S}_1\right\rangle\right|^2\\ \Delta^2\hat{S}_2\Delta^2\hat{S}_3 &\geq \left|\left\langle\hat{S}_1\right\rangle\right|^2+\frac{1}{4}\left|\left\langle\delta\hat{S}_2\delta\hat{S}_3+\delta\hat{S}_3\delta\hat{S}_2\right\rangle\right|^2\\ \Delta^2\hat{S}_3\Delta^2\hat{S}_1 &\geq \left|\left\langle\hat{S}_2\right\rangle\right|^2+\frac{1}{4}\left|\left\langle\delta\hat{S}_3\delta\hat{S}_1+\delta\hat{S}_1\delta\hat{S}_3\right\rangle\right|^2,\end{aligned} \tag{8.13}$$

where here, in contrast to the analysis in Chapter 7, we have included the contribution from the correlation function. These uncertainty relations result in, typically, non-zero variances in the individual Stokes operators (see Fig. 7.1b)), and are ultimately what enables the verification of polarisation entanglement.

As discussed in Chapter 7, any polarisation mode can be decomposed in terms of constituent horizontally and vertically polarised modes, with some phase angle θ between them. Here we consider a pair of arbitrary modes x and y, decomposed in this way as shown in Fig. 8.1. The inseparability criterion of Eq. (8.7) was arrived at assuming that beams x and y were interchangeable; i.e. assuming that the outcome of any experiment in which they were involved would be independent of their exchange. In our experiment this condition is naturally satisfied, since our horizontally polarised modes are generated symmetrically on a 50/50 beam splitter, and the vertical constituents are identical coherent states. In order to satisfy the interchangeability condition assumed here, the expectation values and variances of the horizontally (vertically) polarised input beams must be the same

$$\alpha_H(t) = \langle\tilde{a}_{H,x}\rangle = \langle\tilde{a}_{H,y}\rangle \tag{8.14}$$

$$\alpha_V(t) = \langle\tilde{a}_{V,x}\rangle = \langle\tilde{a}_{V,y}\rangle, \tag{8.15}$$

$$\Delta^2\hat{X}_H^{\pm} = \Delta^2\hat{X}_{H,x}^{\pm} = \Delta^2\hat{X}_{H,y}^{\pm} \tag{8.16}$$

$$\Delta^2\hat{X}_V^{\pm} = \Delta^2\hat{X}_{V,x}^{\pm} = \Delta^2\hat{X}_{V,y}^{\pm}, \tag{8.17}$$

and the relative phase between horizontally and vertically polarised modes for subsystems x and y must be related by $\theta = \theta_x = \pm\theta_y + m\pi$ where m is an integer. Given these assumptions it is possible to calculate $\mathcal{I}(\hat{S}_i, \hat{S}_j)$ and $\mathcal{E}(\hat{S}_i, \hat{S}_j)$ from Eqs. (7.1)-(7.5), (8.7), and (8.12). From consideration of our experimental setup, we find some further simplifications possible. We assume that the horizontal and vertical inputs are not correlated,

$$\begin{aligned}\langle\delta\hat{X}^{\pm}_{H,x/y}\delta\hat{X}^{\pm}_{V,x/y}\rangle &= 0 &(8.18)\\ \langle\delta\hat{X}^{\pm}_{H,x/y}\delta\hat{X}^{\mp}_{V,x/y}\rangle &= 0, &(8.19)\end{aligned}$$

and that each input beam does not exhibit internal amplitude/phase quadrature correlations

$$\begin{aligned}\left\langle\delta\hat{X}^{+}_{H,x/y}\delta\hat{X}^{-}_{H,x/y}+\delta\hat{X}^{-}_{H,x/y}\delta\hat{X}^{+}_{H,x/y}\right\rangle &= 0 &(8.20)\\ \left\langle\delta\hat{X}^{+}_{V,x/y}\delta\hat{X}^{-}_{V,x/y}+\delta\hat{X}^{-}_{V,x/y}\delta\hat{X}^{+}_{V,x/y}\right\rangle &= 0. &(8.21)\end{aligned}$$

Finally we assume that the vertically polarised input modes are bright ($\alpha_V(t)^2 \gg 1$) so that second order terms are negligible. Given these assumptions the Stokes operator expectation values for both beams x and y are given by Eqs. (7.9)-(7.12); Eq. (8.7) then provides the degree of inseparability for each of the three permutations of Stokes operators

$$\begin{aligned}\mathcal{I}(\hat{S}_1,\hat{S}_2) &= \frac{\Delta^2_{x\pm y}\hat{S}_1+\Delta^2_{x\pm y}\hat{S}_2}{4\sin\theta|\alpha_H(t)\alpha_V(t)|} &(8.22)\\ \mathcal{I}(\hat{S}_1,\hat{S}_3) &= \frac{\Delta^2_{x\pm y}\hat{S}_1+\Delta^2_{x\pm y}\hat{S}_3}{4\cos\theta|\alpha_H(t)\alpha_V(t)|} &(8.23)\\ \mathcal{I}(\hat{S}_2,\hat{S}_3) &= \frac{\Delta^2_{x\pm y}\hat{S}_2+\Delta^2_{x\pm y}\hat{S}_3}{2|\alpha_H(t)^2-\alpha_V(t)^2|}, &(8.24)\end{aligned}$$

and Eq. (8.12) gives the degree of EPR paradox for each permutation

$$\begin{aligned}\mathcal{E}(\hat{S}_1,\hat{S}_2) &= \frac{\Delta^2_{x|y}\hat{S}_1\Delta^2_{x|y}\hat{S}_2}{|sin\theta\alpha_H(t)\alpha_V(t)|^2} &(8.25)\\ \mathcal{E}(\hat{S}_1,\hat{S}_3) &= \frac{\Delta^2_{x|y}\hat{S}_1\Delta^2_{x|y}\hat{S}_3}{|cos\theta\alpha_H(t)\alpha_V(t)|^2} &(8.26)\\ \mathcal{E}(\hat{S}_2,\hat{S}_3) &= 4\frac{\Delta^2_{x|y}\hat{S}_2\Delta^2_{x|y}\hat{S}_3}{|\alpha_H(t)^2-\alpha_V(t)^2|^2}. &(8.27)\end{aligned}$$

Notice that when $\theta = m\pi$ where m is an integer the denominators of Eqs (8.22) and (8.25) become zero. It is then not possible to verify the presence of entanglement between $\hat{S}_1$ and $\hat{S}_2$. Since our measure is only a sufficient criterion for entanglement, this result does not exclude its existence, only our ability to measure it. In this situation a more detailed entanglement criterion, including the correlation function, is required. The same is true if $\alpha_H(t)$ or $\alpha_V(t)$ equal zero; between $\hat{S}_1$ and $\hat{S}_3$ when $\theta = (m+1/2)\pi$; and between $\hat{S}_2$ and $\hat{S}_3$ when $|\alpha_H(t)| = |\alpha_V(t)|$. Section 8.5 includes a discussion of this effect. In our experiment however, we took care to characterise the entanglement in regimes for which the measures of Eqs. (8.7) and (8.12) are effective.

8.3 Experiment

8.3.1 Transformation to polarisation entanglement

The quadrature entanglement produced in Chapter 4 was transformed onto a polarisation basis by combining each quadrature entangled beam (horizontally polarised) on a polarising beam splitter with a much more intense vertically polarised coherent beam ($\alpha_V(t)^2 = 30\alpha_H(t)^2$) (see Fig. 8.2).

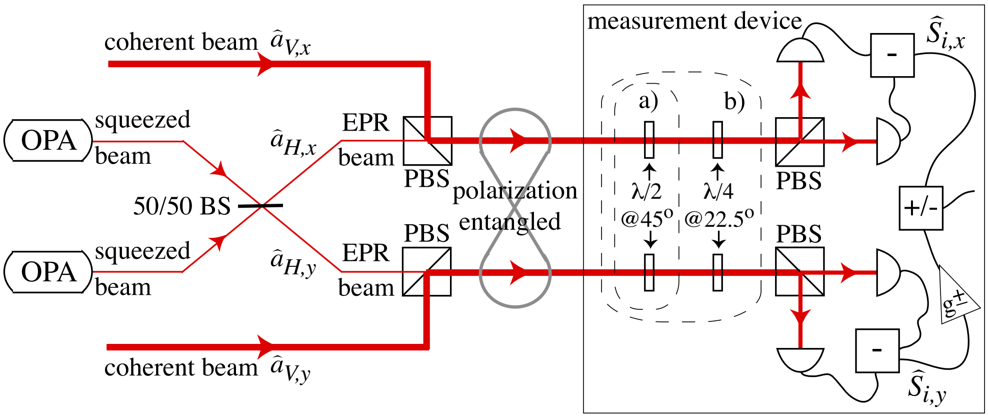

Figure 8.2: Experimental production and characterisation of continuous variable polarisation entanglement. The optics within a) are included to measure $\hat{S}_2$, and those within b) to measure $\hat{S}_3$. BS: beam splitter, PBS: polarising beam splitter.

The overlap efficiency between the modes was observed to be 91%, and the relative phase between the horizontal and vertical input modes θ was controlled to be $\pi/2$. In this situation the denominators of Eqs. (8.23) and (8.26) are equal to zero, so that it is not possible to verify entanglement between $\hat{S}_1$ and $\hat{S}_3$. We therefore only characterise the entanglement criteria for the other two combinations of Stokes operators ($\hat{S}_1$ and $\hat{S}_2$; and $\hat{S}_2$ and $\hat{S}_3$).

8.3.2 Individual characteristics of the two polarisation entangled beams

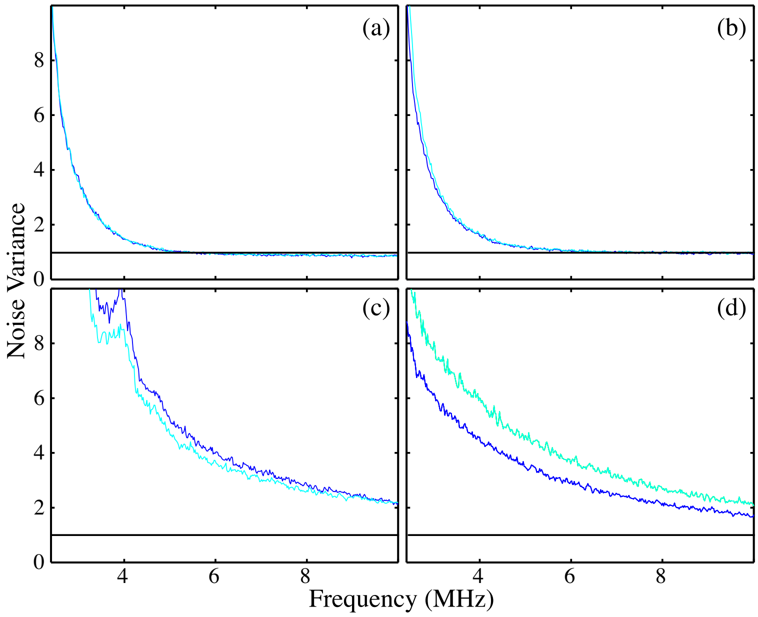

Figure 8.3: Experimental measurement of the Stokes operator variances of the entangled beams, (a) $\Delta^2\hat{S}_0$, (b) $\Delta^2\hat{S}_1$, (c) $\Delta^2\hat{S}_2$, (d) $\Delta^2\hat{S}_3$; the black traces are for beam x and the grey traces for beam y.

The Stokes operators of each of the polarisation entangled beams were measured in the same manner as those in Chapter 7 (see Fig. 7.2). Initially each beam was split on a polarising beam splitter and the two outputs detected with a pair of Epitaxx ETX500 photodiodes. The sum of the two photocurrents gave a measurement of $\hat{S}_0$, and the difference, $\hat{S}_1$. With the inclusion of a half-wave plate before the polarising beam splitter, the difference yielded an instantaneous value for $\hat{S}_2$, and with a quarter-wave plate $\hat{S}_3$ (see Fig. 8.2). Fig. 8.3 presents variance spectra for all four Stokes operators of the polarisation entangled beams measured independently. All of the results presented in this Chapter were taken over the sideband frequency range from 2 to 10 MHz and are the average of ten consecutive traces. Every trace was more than 4.5 dB above the measurement dark noise which was taken into account. All four spectra shown here exhibit high levels of noise at low frequencies. This is primarily due to resonant relaxation oscillation noise from our laser. The spectra in Fig. 8.3 (a) display $\hat{S}_0$ for the two polarisation entangled beams. Each spectra is equivalent to the total intensity noise of the constituent coherent and quadrature entangled beams. Since the coherent beam was much brighter than the entangled beam its contribution to the spectra is dominant. This caused the spectra of $\hat{S}_1$ (Fig. 8.3 (a)), being the difference of the intensity noise of the constituent beams, to be almost identical to those for $\hat{S}_0$. Both $\hat{S}_0$ and $\hat{S}_1$ display laser relaxation oscillation noise at low frequencies but become quantum noise limited at frequencies above 5 MHz. The fact that they are quantum noise limited implies that entanglement involving either is unlikely. Both the spectra for $\hat{S}_2$ and $\hat{S}_3$ are well above the quantum noise limit throughout the measurement range. This is because the highly noisy fluctuations of the quadrature entangled beams have been mapped onto these operators, and suggests that they may be entangled.

8.3.3 Measurement of the degree of inseparability

A clearer signature of entanglement was evident in the form of strong correlations of both $\hat{S}_2$ and $\hat{S}_3$ between the two resulting beams. We quantified the inseparability and EPR paradox criteria for entanglement of these beams. This quantification of $\mathcal{I}(\hat{S}_i, \hat{S}_j)$ and $\mathcal{E}(\hat{S}_i, \hat{S}_j)$ required measurements of $\alpha_V(t)$, $\alpha_H(t)$, $\Delta^2_{x\pm y}\hat{S}_i$, and $\Delta^2_{x|y}\hat{S}_i$. We determined $\alpha_V(t)^2$ directly by blocking the horizontally polarised modes and measuring the power spectrum of the subtraction between the two homodynes, this also gave α_H^2 since the ratio $\alpha_V(t)^2/\alpha_H(t)^2$ was measured to equal thirty.

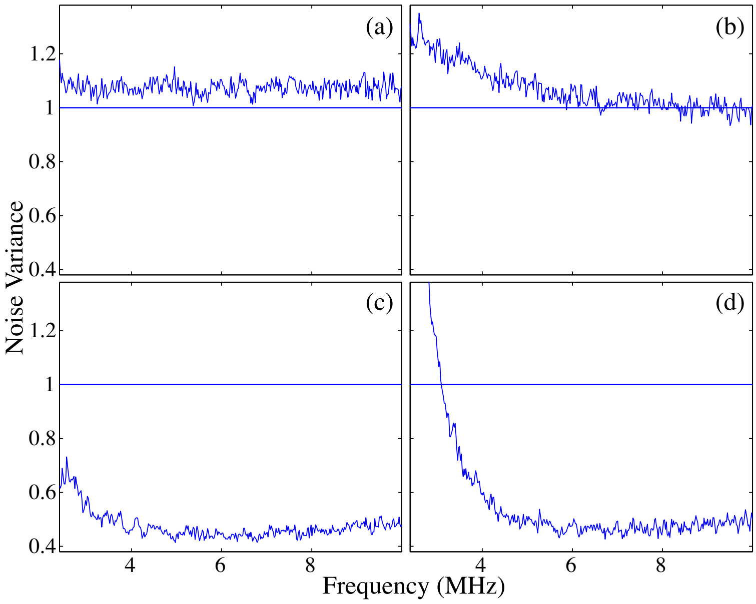

Figure 8.4: Experimental measurement of $\Delta^2_{x\pm y}\hat{S}_i$ normalised to the two beam quantum noise limit. (a) $\Delta^2_{x\pm y}\hat{S}_0$, (b) $\Delta^2_{x\pm y}\hat{S}_1$, (c) $\Delta^2_{x\pm y}\hat{S}_2$, (d) $\Delta^2_{x\pm y}\hat{S}_3$

The variance of the unity gain electronic sum or subtraction of the Stokes operator measurements between the polarisation entangled beams was obtained in a spectrum analyser at a resolution bandwidth of 300 kHz and video bandwidth of 300 Hz. This resulted in spectra for $\Delta^2_{x\pm y}\hat{S}_i$. These spectra are displayed in Fig. 8.4. From Fig. 8.4(a) and (b) we see that any correlation of $\hat{S}_0$ or $\hat{S}_1$ between the beams is restrained at the quantum noise limit. On the other hand $\hat{S}_2$ and $\hat{S}_3$ both show correlation to well below the quantum noise limit.

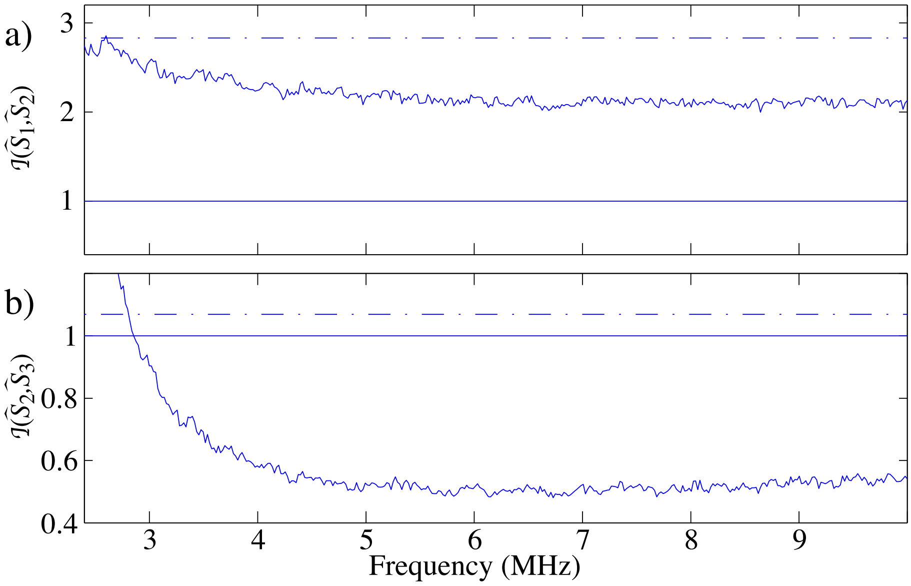

Figure 8.5: Experimental measurement of a) $\mathcal{I}(\hat{S}_1,\hat{S}_2)$, and b) $\mathcal{I}(\hat{S}_2,\hat{S}_3)$; values below unity indicate entanglement. The dashed line is the corresponding measurement inferred between two coherent beams.

$\mathcal{I}(\hat{S}_1,\hat{S}_2)$ and $\mathcal{I}(\hat{S}_2,\hat{S}_3)$ were obtained from Eqs. (8.22) and (8.24), and the measurements of $\Delta^2_{x\pm y}\hat{S}_1$, $\Delta^2_{x\pm y}\hat{S}_2$, $\Delta^2_{x\pm y}\hat{S}_3$, $\alpha_H(t)$ and $\alpha_V(t)$. The resulting spectra are shown in Fig. 8.5. The dashed lines indicate the results a pair of coherent beams would produce. Both traces are below this line throughout almost the entire measurement range, this is an indication that the light is in a non-classical state. At low frequencies both traces were degraded by noise introduced by the relaxation oscillation of our laser. $\mathcal{I}(\hat{S}_2,\hat{S}_3)$ shows polarisation entanglement, however as expected $\mathcal{I}(\hat{S}_2,\hat{S}_3)$ is far above unity. The best entanglement was observed at 6.8 MHz with $\mathcal{I}(\hat{S}_2,\hat{S}_3)=0.49$.

8.3.4 Measurement of the degree of EPR paradox

We determined the degree of EPR paradox in a similar manner to that used above for the degree of inseparability. This time, rather than taking the direct unity gain sum or difference between the measurements on beams x and y, we took the sum or difference with a gain g chosen to minimise the resulting variances (see Eq. 8.11). Effectively this is asking the question: given a measurement on beam y how well can I infer the value of that variable for beam x? Fig. 8.6 shows the measured conditional variance spectra of beam x for $\hat{S}_2$ and $\hat{S}_3$.

The conditional variance spectra for $\hat{S}_2$ (Fig. 8.6(a)) was obtained from the subtraction of measurements from the two beams, and therefore the relaxation oscillation of our laser, which is strongly correlated between the beams, was almost completely removed. The spectra for $\hat{S}_3$, however, was obtained from the sum of measurements from the two beams, in this case the relaxation oscillation noise is not removed. This is analogous to the results found for quadrature entanglement in Chapter 4, and resulted in very significant degradation of the conditional spectra for $\hat{S}_3$ (Fig. 8.6(b)).

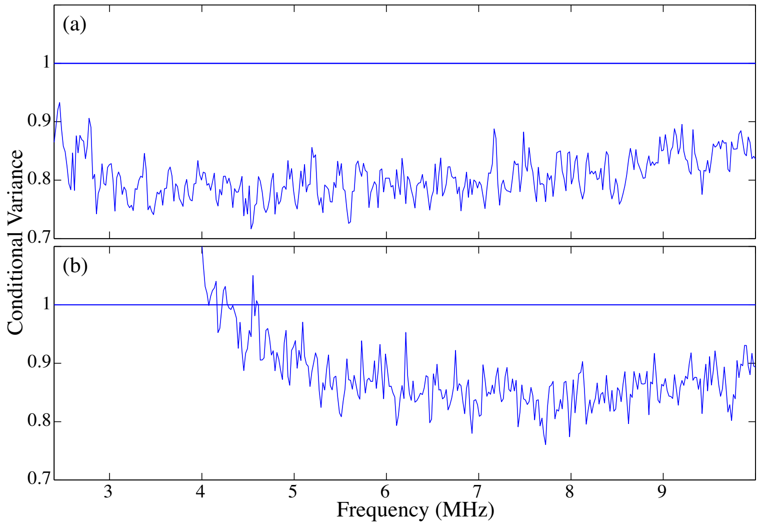

Figure 8.6: Experimental measurement of the Stokes operator conditional variances a) $\Delta^2_{x|y}\hat{S}_2$, b) $\Delta^2_{x|y}\hat{S}_3$, normalised to the single beam quantum noise limit.

The EPR paradox criterion is the product of the two spectra and is shown in Fig. 8.7. Even with the degradation of the conditional variance of $\hat{S}_3$, the EPR Paradox criterion was verified at frequencies above 4 MHz. The optimum value was $\mathcal{E}(\hat{S}_2, \hat{S}_3) = 0.72$, which was also observed at 6.8 MHz.

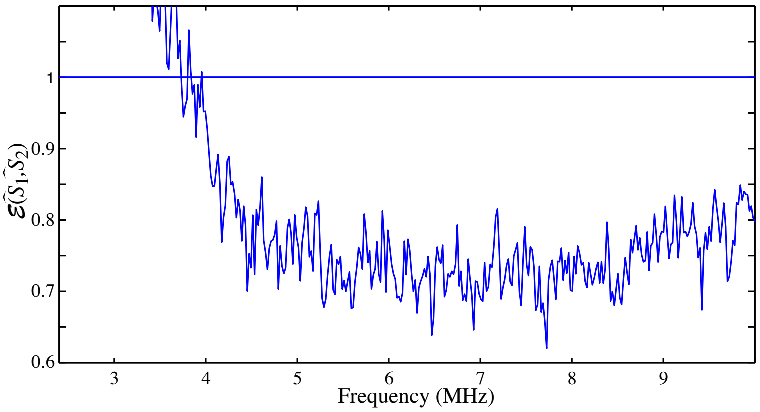

Figure 8.7: Experimental measurement of the degree of EPR paradox $\mathcal{E}(\hat{S}_2, \hat{S}_3)$ for a polarisation entangled state..

It is illustrative to consider our knowledge of beam x before any measurement, and after measurement of $\hat{S}_2$ or $\hat{S}_3$. This can be visualised similarly to the polarisation squeezing reported in Chapter 7, in terms of noise balls on a Poincaré sphere and is shown in Fig. 8.8. Fig. 8.8 a) shows the knowledge of the polarisation of beam x at 6.8 MHz without any measurement on beam y. $\hat{S}_1$ is quantum noise limited, whereas both $\hat{S}_2$ and $\hat{S}_3$ have variances well above the quantum noise limit, as can be seen also in Fig. 8.3. Upon measurement of either $\hat{S}_2$ or $\hat{S}_3$ on beam y, that Stokes operator on beam x becomes known to an accuracy better than the quantum noise limit (see Fig. 8.8 b) and Fig. 8.8 c) respectively). The product of the uncertainty of $\hat{S}_2$ and $\hat{S}_3$ is then below the uncertainty relation between the two Stokes operators (the dashed circles in Fig. 8.8).

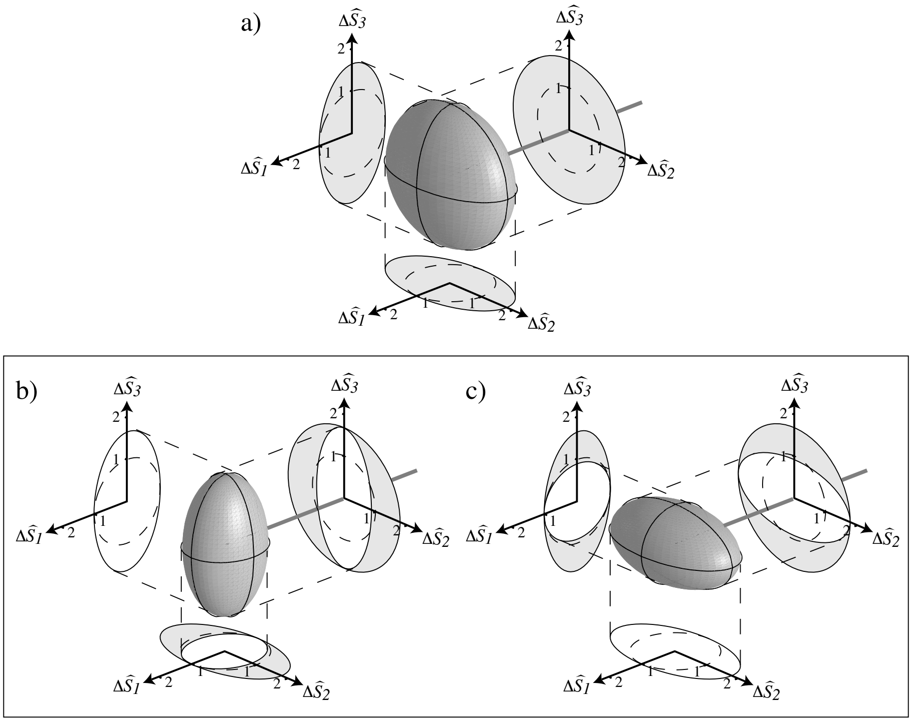

Figure 8.8: a) Knowledge of the polarisation of beam x before any measurement on beam y; b) conditional knowledge of beam x after measurement of $\hat{S}_2$ on beam y; c) conditional knowledge of beam x after measurement of $\hat{S}_3$ on beam y. The dashed circles define the limit of classical correlation. These representations were generated from results at 6.8 MHz.

8.3.5 An explanation of the transformation between quadrature and polarisation entanglement

The Schwinger bosonic representation allows the decomposition of any spin-like operator into a pair of mode operators of the quantum harmonic oscillator [223]. A clearer understanding of the transformation between quadrature and polarisation entanglement presented here may be gained by using this representation to decompose the Stokes operators in terms of quadrature operators. Making assumptions relevant to our experiment discussed earlier ($\alpha_H(t)^2 \ll \alpha_V(t)^2$, $\theta = \pi/2$, and $\langle \delta\hat{X}_H^{\mp}\delta\hat{X}_V^{\pm}\rangle = 0$), we find from Eqs. (7.1)-(7.4), that the Stokes operator variances of a beam expressed in terms of its horizontally and vertically polarised components are given by

$$\Delta^2\hat{S}_0 = \alpha_V(t)^2\Delta^2\hat{X}_V^+ \tag{8.28}$$
$$\Delta^2\hat{S}_1 = \alpha_V(t)^2\Delta^2\hat{X}_V^+ \tag{8.29}$$
$$\Delta^2\hat{S}_2 = \alpha_V(t)^2\Delta^2\hat{X}_H^- \tag{8.30}$$
$$\Delta^2\hat{S}_3 = \alpha_V(t)^2\Delta^2\hat{X}_H^+. \tag{8.31}$$

The amplitude fluctuations of the bright vertically polarised input beam $\hat{X}_V^+$ have been mapped onto $\hat{S}_1$ and since $\alpha_H(t)^2 \ll \alpha_V(t)^2$ also onto $\hat{S}_0$. The phase and amplitude fluctuations of the weak horizontally polarised input beam have been mapped onto $\hat{S}_2$ and $\hat{S}_3$, respectively. It is interesting to note that the phase fluctuations of the vertically polarised beam play no role in defining the polarisation of the output. They result in overall phase fluctuations on the output which have no effect on its polarisation. It is a simple step, then, to derive the sum or difference variances $\Delta^2_{x\pm y}\hat{S}_i$ between two beams x and y

$$\begin{aligned}
\Delta^2_{x\pm y}\hat{S}_1 &= \alpha_V(t)^2\Delta^2_{x\pm y}\hat{X}^+_V && (8.32)\\
\Delta^2_{x\pm y}\hat{S}_2 &= \alpha_V(t)^2\Delta^2_{x\pm y}\hat{X}^-_H && (8.33)\\
\Delta^2_{x\pm y}\hat{S}_3 &= \alpha_V(t)^2\Delta^2_{x\pm y}\hat{X}^+_H. && (8.34)
\end{aligned}$$

It is interesting that any one of these sum or difference variances can become arbitrarily small without the presence of entanglement. This is achieved simply by squeezing the quadrature of interest on the input modes of both x and y. For example, if both horizontally polarised inputs are phase quadrature squeezed then $\Delta^2_{x\pm y}\hat{S}_2$ can become arbitrarily small. This however, has the natural consequence of $\Delta^2_{x\pm y}\hat{S}_3$ becoming very large. Interestingly, there is no such consequence for $\Delta^2_{x\pm y}\hat{S}_1$. Amplitude quadrature squeezing of the vertical inputs allows $\Delta^2_{x\pm y}\hat{S}_1$ to become arbitrarily small, and has no effect on $\Delta^3_{x\pm y}\hat{S}_2$ and $\Delta^2_{x\pm y}\hat{S}_3$. It is therefore possible to make both $\Delta^2_{x\pm y}\hat{S}_1$ and (say) $\Delta^2_{x\pm y}\hat{S}_2$ diminishingly small (and therefore their sum also) without any entanglement present. This is the essence of why normalisation of the inseparability and EPR paradox criteria must be performed relative to the uncertainty relation between the operators (Eqs. (7.10-7.12)) rather than the quantum noise limit (which is a constant independent of the orientation of the Stokes vector). We see that with $\alpha_H(t)^2 \ll \alpha_V(t)^2$, the uncertainty relation between $\hat{S}_1$ and $\hat{S}_2$ also becomes diminishingly small, so that $\mathcal{I}(\hat{S}_1, \hat{S}_2)$ and $\mathcal{E}(\hat{S}_1, \hat{S}_2)$ (Eqs. (8.22) and (8.25)) remain greater than unity. In contrast, for quadrature entanglement, the two normalisation procedures are equivalent.

Using Eqs. (8.22-8.24) and (8.32-8.34) the degrees of inseparability $\mathcal{I}(\hat{S}_1, \hat{S}_2)$ and $\mathcal{I}(\hat{S}_2, \hat{S}_3)$, can now be expressed in terms of quadrature sum or difference variances of the input horizontally and vertically polarised modes

$$\begin{aligned}
\mathcal{I}(\hat{S}_1, \hat{S}_2) &= \frac{\alpha_V(t)}{\alpha_H(t)}\left(\frac{\Delta^2_{x\pm y}\hat{X}^+_V + \Delta^2_{x\pm y}\hat{X}^-_H}{4}\right) && (8.35)\\
\mathcal{I}(\hat{S}_2, \hat{S}_3) &= \left(1+\frac{\alpha_H(t)^2}{\alpha_V(t)^2}\right)\left(\frac{\Delta^2_{x\pm y}\hat{X}^+_H + \Delta^2_{x\pm y}\hat{X}^-_H}{2}\right) && (8.36)\\
&= \frac{1}{2}\left(1+\frac{\alpha_H(t)^2}{\alpha_V(t)^2}\right)\mathcal{I}(\hat{X}^+_H, \hat{X}^-_H). && (8.37)
\end{aligned}$$

From Eq. (8.35) we see that if the ratio of vertical to horizontal coherent amplitudes $\alpha_V(t)/\alpha_H(t)$ doubles, to retain a given degree of inseparability $\mathcal{I}(\hat{S}_1, \hat{S}_2)$ the level of correlation between $\hat{X}^+_{V,x}$ and $\hat{X}^+_{V,y}$, and between $\hat{X}^-_{H,x}$ and $\hat{X}^-_{H,y}$ must also double. Thus as $\alpha_V(t)/\alpha_H(t)$ increases the level of correlation required for $\mathcal{I}(\hat{S}_1, \hat{S}_2)$ to fall below unity and therefore to demonstrate inseparability quickly becomes experimentally unachievable. In the limit of vacuum horizontal input states ($\alpha_H(t) = 0$), $\mathcal{I}(\hat{S}_1, \hat{S}_2)$ becomes infinite and verification of entanglement is impossible. In contrast, Eq. (8.37) shows that in this situation $\mathcal{I}(\hat{S}_2, \hat{S}_3)$ becomes identical to the criterion for quadrature entanglement (Eq. (8.5)) between the two horizontally polarised inputs. So we see that quadrature entanglement between the horizontally polarised inputs is transformed to polarisation entanglement between $\hat{S}_2$ and $\hat{S}_3$.

The asymmetry between the results for $\mathcal{I}(\hat{S}_1, \hat{S}_2)$ and $\mathcal{I}(\hat{S}_2, \hat{S}_3)$ arises from the the Stokes vector orientation of the two polarising beam splitter output states. These Stokes vectors are aligned almost exactly along $\hat{S}_1$ (since $\alpha_H(t)^2 \ll \alpha_V(t)^2$). This results in an asymmetry in the commutation relations of Eq. (7.5) and a corresponding bias in the uncertainty relations that define the inseparability criterion.

8.4 Polarisation entanglement of all three Stokes operators

So far, we have demonstrated polarisation entanglement between two Stokes operators. However, the polarisation of light has three degrees of freedom, and all three can be entangled. This leads to a much more complex quantum state, somewhat analogous to discrete polarisation entanglement between pairs of photons where the correlation is independent of the basis of measurement. In the continuous variable description, however, the Stokes operator orientation imposes a peculiar basis for the description of polarisation fluctuations which forbids a complete analogy to the discrete case. Here, we extend the work of [218] to propose a possible configuration for continuous variable entanglement between all three Stokes operators.

Due to the dependence of the Stokes operator uncertainty relations on their mean fields, symmetric three Stokes operator entanglement requires that the Stokes operator mean fields are also symmetric. We therefore equate the expectation values of all three Stokes operators for both beams $|\langle\hat{S}_i\rangle| = \alpha(t)^2$. This leads to restrictions on the intensities of the horizontal and vertical states

$$\alpha_V(t)^2 = \frac{\sqrt{3}-1}{2}\alpha(t)^2 \tag{8.38}$$

$$\alpha_H(t)^2 = \frac{\sqrt{3}+1}{2}\alpha(t)^2, \tag{8.39}$$

and to conditions on the phase relationship between the horizontal and vertical input states

$$\theta_x = \frac{\pi}{4} + \frac{\pi}{2}m_x \tag{8.40}$$

$$\theta_y = \frac{\pi}{4} + \frac{\pi}{2}m_y, \tag{8.41}$$

where m_x and m_y are integers. The three degrees of inseparability of Eqs. (8.22,8.23,8.24) then become symmetric

$$\mathcal{I}(\hat{S}_i, \hat{S}_j) = \frac{\Delta^2_{x\pm y}\hat{S}_i + \Delta^2_{x\pm y}\hat{S}_j}{2\alpha(t)^2}. \tag{8.42}$$

We assume that the two horizontally polarised inputs, and the two vertically polarised inputs, are quadrature entangled with the same degree of correlation such that

$$\Delta^2_{x\pm y}\hat{X}^+_H = \Delta^2_{x\pm y}\hat{X}^-_H = \Delta^2_{x\pm y}\hat{X}^+_V = \Delta^2_{x\pm y}\hat{X}^-_V = \Delta^2_{x\pm y}\hat{X}. \tag{8.43}$$

To simultaneously minimise each of $\Delta^2_{x\pm y}\hat{S}_i$ it is necessary that $\theta_x = -\theta_y + m\pi$. After making this assumption we find that the sum or difference variances between beams x and y of all three Stokes operators are equal, and can be related directly to $\Delta^2_{x\pm y}\hat{X}$

$$\Delta^2_{x\pm y}\hat{S}_1 = \Delta^2_{x\pm y}\hat{S}_2 = \Delta^2_{x\pm y}\hat{S}_3 = \sqrt{3}\alpha(t)^2\Delta^2_{x\pm y}\hat{X}. \tag{8.44}$$

Using this relationship, with the polarisation commutation relations of Eqs. (7.5) and the general inseparability criteria Eq. (8.7), the polarisation inseparability criteria can also be directly related to $\Delta^2_{x\pm y}\hat{X}$

$$\mathcal{I}(\hat{S}_i, \hat{S}_j) = \sqrt{3}\Delta^2_{x\pm y}\hat{X}, \tag{8.45}$$

and the entanglement is equivalent between any two Stokes operators. The condition for entanglement can then be expressed as a simple criterion on the quadrature entanglement between the input beams

$$\mathcal{I}(\hat{S}_i, \hat{S}_j) < 1 \Longleftrightarrow \mathcal{I}(\hat{X}^+, \hat{X}^-) < \frac{1}{\sqrt{3}}, \tag{8.46}$$

where $\mathcal{I}(\hat{X}^+, \hat{X}^-) = \mathcal{I}(\hat{X}^+_H, \hat{X}^-_H) = \mathcal{I}(\hat{X}^+_V, \hat{X}^-_V)$. The factor of $\frac{1}{\sqrt{3}}$ arises from the projection of the quadrature properties onto a polarisation basis in which the Stokes vector is pointing at equal angle ($\cos^{-1}(\frac{1}{\sqrt{3}})$) from all three Stokes operator axes. In principle it is possible to have all three Stokes operators perfectly entangled. In other word, ideally the measurement of any Stokes operator of one of the beams could allow the exact prediction of that Stokes operator from the other beam (see Fig. 8.9). However, contrary to the discrete photon case, here the analysis basis orientation is fixed by the Stokes vector orientation, and rotating this basis would change the commutation relations and therefore the uncertainty relations that verification of the entanglement replies upon. The experimental production of this symmetric polarisation entanglement is a straightforward extension of the experiment reported here, however a significant step-up in resources is required. Four squeezed beams rather than two are required, and due to the projection factor $\frac{1}{\sqrt{3}}$ a higher level of squeezing in each beam is necessary. This entanglement resource would, however, enable the demonstration of maximal continuous variable polarisation teleportation as discussed in [34].

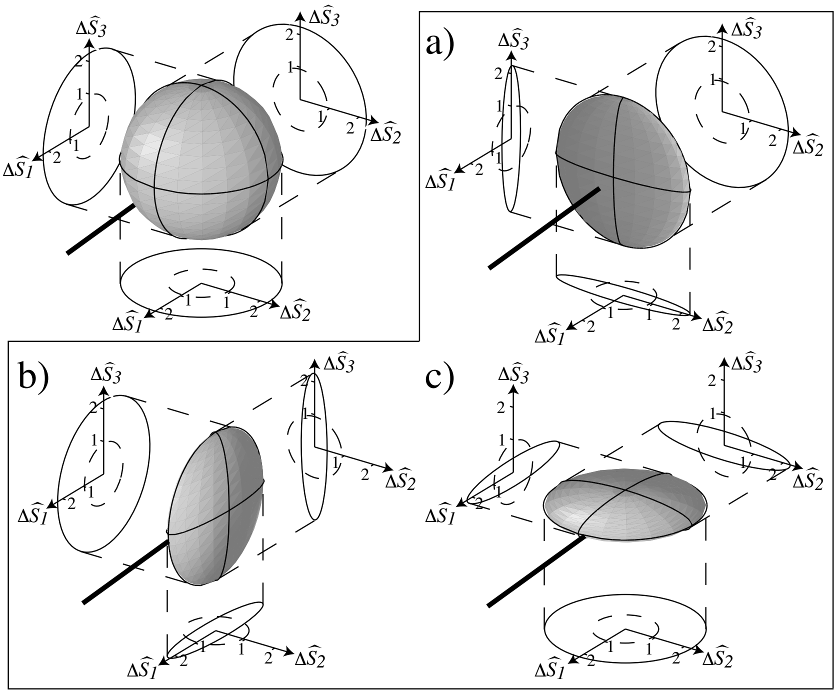

Figure 8.9: Poincaré sphere representation of the conditional knowledge of one polarisation entangled beam obtained through measurements on the other, where the entanglement is produced from four quadrature squeezed beams, each with squeezed quadrature variance of 0.1. The top left figure represents the knowledge of beam y before any measurement of beam x. a), b), and c) represent the conditional knowledge of beam y given measurements of $\hat{S}_1$, $\hat{S}_2$, and $\hat{S}_3$ respectively on beam x. If the conditional knowledge is better than the dashed circles the state is entangled.

8.5 A look at the correlation function

Throughout this Chapter we have neglected the correlation function term in the uncertainty relations, this resulted in sufficient, but not necessary, conditions for entanglement. Unlike the commutation relation, the correlation function is state dependent. We would like to look at some of the problems associated with this here, and then examine the values of the correlation functions for the two states discussed specifically in this Chapter. Again assuming that $\alpha_V(t) \gg 1$ so that higher order terms can be neglected, the correlation functions for each of the three permutations of Stokes operators are found to be

$$\begin{aligned} \left|\left\langle \delta\hat{S}_1\delta\hat{S}_2 + \delta\hat{S}_2\delta\hat{S}_1 \right\rangle\right|^2 &= 4\cos^2\theta\alpha_H(t)^2\alpha_V(t)^2\left(\Delta^2\hat{X}^+_H - \Delta^2\hat{X}^+_V\right)^2 && (8.47) \\ \left|\left\langle \delta\hat{S}_1\delta\hat{S}_3 + \delta\hat{S}_3\delta\hat{S}_1 \right\rangle\right|^2 &= 4\sin^2\theta\alpha_H(t)^2\alpha_V(t)^2\left(\Delta^2\hat{X}^+_H - \Delta^2\hat{X}^+_V\right)^2 && (8.48) \\ \left|\left\langle \delta\hat{S}_2\delta\hat{S}_3 + \delta\hat{S}_3\delta\hat{S}_2 \right\rangle\right|^2 &= 4\sin^2\theta cos^2\theta\Big[\alpha_V(t)^2\left(\Delta^2\hat{X}^+_H - \Delta^2\hat{X}^-_H\right) && (8.49) \\ &\quad +\alpha_H(t)^2\left(\Delta^2\hat{X}^+_V - \Delta^2\hat{X}^-_V\right)\Big]^2. \end{aligned}$$

We can, naively, include these correlation functions in the Stokes operator uncertainty relations as shown in Eqs. (8.13); and it seems, obtain more general expressions for the polarisation inseparability criteria $\mathcal{I}_{\rm corr}(\hat{S}_i,\hat{S}_j)$, of the form

$$\mathcal{I}_{\rm corr}(\hat{S}_i,\hat{S}_j) = \frac{\Delta^2_{x\pm y}\hat{S}_i + \Delta^2_{x\pm y}\hat{S}_j}{\sqrt{|[\delta\hat{S}_i,\delta\hat{S}_j]|^2 + |\langle\delta\hat{S}_i\delta\hat{S}_j + \delta\hat{S}_j\delta\hat{S}_i\rangle|^2}} \tag{8.50}$$

Let us consider, for example, $\mathcal{I}_{\rm corr}(\hat{S}_1,\hat{S}_3)$, and take $\theta = \theta_x = \theta_y = \pi/2$ as in our experiment. Using Eqs. (7.11), (8.32), (8.34), and (8.48) and under the restrictions previous stated (Eqs. (8.14-8.21) and $\alpha_V(t) \gg 1$) we find that

$$\mathcal{I}_{\rm corr}(\hat{S}_1,\hat{S}_3) = \frac{\alpha_V(t)}{\alpha_H(t)}\left(\frac{\Delta^2_{x\pm y}\hat{X}^+_V + \Delta^2_{x\pm y}\hat{X}^+_H}{|\Delta^2\hat{X}^+_H - \Delta^2\hat{X}^+_V|}\right) \tag{8.51}$$

The problem with including the correlation term in the inseparability criterion now becomes apparent. Consider that beams x and y are independent coherent states, and therefore clearly separable. Perfectly correlated classical noise can be applied to $\hat{X}^+_{H,x}$ and $X^+_{H,y}$ (or $\hat{X}^+_{V,x}$ and $X^+_{V,y}$) using electronics (classical communication) and amplitude modulators (local operations). It is well know that classical communication and local operations are unable to induce entanglement so, after introduction of this correlated noise, beams x and y must remain separable. By varying the amplitude of the noise (via classical amplification) both $\Delta^2\hat{X}^+_{H,x}$ and $\Delta^2\hat{X}^+_{H,y}$ can be made arbitrarily large. The correlation function between $\hat{S}_1$ and $\hat{S}_3$ (Eq. (8.48)) and hence the general uncertainty product (the denominator of Eq. (8.51)) can then also be made arbitrarily large. Since the noise is perfectly correlated between beams x and y however, it can be arranged to have *no* effect on the sum or difference variances $\Delta^2_{x\pm y}\hat{S}_1$ and $\Delta^2_{x\pm y}\hat{S}_3$. Therefore, the numerator of Eq. (8.51) remains unchanged, whilst the denominator may be made arbitrarily large. So as the amplitude of the noise increases $\mathcal{I}_{\rm corr}(\hat{S}_1,\hat{S}_3) \rightarrow 0$, and it appears that beams x and y become entangled. This problem arises because including the correlation function term in the uncertainty product implicitly assumes that no information is available about the correlation from an alternative source. Since, the modulation considered here is correlated between the beams, measurements on one beam can provide information about the state of the other, and therefore the uncertainty relations including the correlation function calculated from a single beam are invalid. In order to derive a general necessary and sufficient criteria for polarisation entanglement a much more detailed analysis of the correlation function would be required, we do not present that here.

Let us now consider the two particular states discussed in this Chapter. In the first case, where entanglement was experimentally observed between $\hat{S}_2$ and $\hat{S}_3$, the relative phase between the horizontal and vertical input modes was controlled to be $\theta = \pi/2$. The correlation functions between $\hat{S}_1$ and $\hat{S}_2$, and between $\hat{S}_2$ and $\hat{S}_3$ (Eqs. (8.47) and (8.49)) were then both equal to zero. Therefore for our experimental configuration the inseparability criteria in Eqs. (8.22) and (8.24) are necessary and sufficient, and represent a hard boundary between polarisation entangled and non-polarisation entangled states. The entanglement between all three pairs of Stokes operators proposed in Section 8.4 is highly symmetrical, $\Delta^2\hat{X}^{\pm}_{H,x} = \Delta^2\hat{X}^{\pm}_{H,y} = \Delta^2\hat{X}^{\pm}_{V,x} = \Delta^2\hat{X}^{\pm}_{V,y}$. In this case all three correlation functions can be seen to be zero, and all three inseparability criteria are therefore necessary and sufficient.

8.6 Summary and conclusion

This Chapter presented the first generation of continuous variable polarisation entanglement. This entanglement was achieved by transformation of the quadrature entanglement discussed in Chapter 4 onto a polarisation basis. In order to characterise the entanglement we generalised both the inseparability criterion of Duan *et. al* [130], and the EPR paradox criteria of Reid and Drummond [134, 135] to polarisation states. We utilised the standard uncertainty relation in this generalisation, which results in sufficient polarisation entanglement criteria. We briefly considered the generalised uncertainty relation, which includes the correlation function. We demonstrated that the correlation function is zero for the two situations considered in this Chapter, and therefore the inseparability and EPR paradox criteria derived are, for these cases, necessary and sufficient. A form of the criteria that is, in general, necessary and sufficient, is a problem for future analysis. In our experiment both criteria were observed to be well inside the regime for entanglement between the Stokes operators $\hat{S}_2$ and $\hat{S}_3$. Finally, we have shown that with an available resource of four quadrature squeezed beams it is possible for all three Stokes operators to be perfectly entangled, although with a bound $\sqrt{3}$ times lower (stronger) than that for quadrature entanglement.

Chapter 9

Non-classical photon pairs from an atomic ensemble

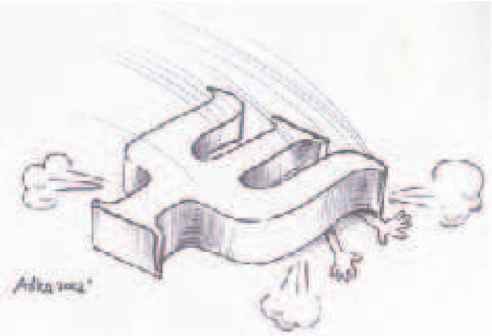

'The sudden collapse of the wavefunction' - Aśka Dolińska 2002

In this Chapter we report the generation of non-classical photon pairs from an atomic ensemble. The experiment presented here utilised optical Raman pulses to manipulate an ensemble of Cesium atoms in a magneto-optic trap. The state of the ensemble was conditioned into a symmetric entangled state through photon counting measurements on emitted fields. The presence of entanglement was verified by demonstrating a violation of the Cauchy-Schwarz inequality. Our scheme has applications to long-distance quantum communication [21], quantum state engineering [207], and could provide a single photon source 'on demand'. The work presented here was performed in collaboration with Alex Kuzmich in the laboratories of Jeff Kimble at the California Institute of Technology. The Physics involved is related to that in the other Chapters of this thesis, but has not been directly introduced previously. Here, only sufficient background is provided to allow a reasonable understanding of the experiment. For a more comprehensive approach I recommend the books of Scully and Zubairy [239], and Gardiner and Zoller [240].

The work presented in this Chapter has been published in the journal article 'A. Kuzmich, W. P. Bowen, A. D. Boozer, A. Boca, C. W. Chou, L.-M. Duan and H. J. Kimble *Generation of Nonclassical Photon Pairs for Scalable Quantum Communication with Atomic Ensembles.* Nature **423**, pp. 731 (2003)'.

9.1 Introduction

Many applications in quantum information science require extremely high levels of non-linearity. The quantum logic gates required for universal quantum computation [241], for example, require non-linearity large enough that the presence of a single photon significantly changes the system. The previous Chapters of this thesis utilised the second order non-linearity of Lithium

Niobate in a regime where the optical fields were far away from any atomic resonances. This is a very controllable, low noise source of non-linearity, however with present technology the non-linearity provided is orders of magnitude away from that necessary to facilitate most of the components required for quantum computation and communication. The non-linearity of the atom-field interaction can be enormously enhanced by moving to optical frequencies near atomic resonances. Quantum computation and communication techniques are currently being investigated within this regime using semi-conductor materials[193], rare earth doped crystals [194], trapped ions[195, 196], single atoms in high finesse resonators [9, 110, 197, 198, 199, 242], and cold atom clouds [20, 21, 201, 202]. Each of these systems has its own strengths and weaknesses, and at present it is unclear which holds the highest potential for the ultimate realisation of universal quantum computation and communication. In this Chapter we present the experimental demonstration of a new and potentially powerful technique using cold atomic ensembles. Atomic ensembles have been shown to enable some truly remarkable techniques for the storage, manipulation, and out-coupling of optical quantum states [20, 201, 202, 243, 244, 245]. In the work presented here we combine this potential with conditional measurement. The power of conditional measurement in quantum information protocols has recently become apparent [17, 246, 247], in particular as an enabling technology for scalable linear quantum computation [17].

The experiment reported here was based on a recent proposal by Duan, Lukin, Cirac, and Zoller (*DLCZ*) [21] using atomic ensembles for scalable long distance quantum communication and distribution of entanglement over quantum networks. In the proposal of *DLCZ* atomic ensembles throughout the communication system are manipulated using bright optical pulses on appropriate Raman transitions. On the interaction of an optical pulse with a given ensemble, the atoms in the ensemble probabilistically and collectively emit a Raman field. A photon counting event from this field then conditions the ensemble into a symmetric entangled state, which can be manipulated via further Raman pulses. By using a quantum repeater architecture [205] the entanglement can be distributed over long distances. *DLCZ* incorporated both entanglement purification[139, 140, 141] and quantum memory[11, 12] into their scheme, in a manner well within the capabilities of present day technology. Other similar proposals based on alternative technology, on the other hand, are still well out of reach [110, 205].

Our experiment demonstrates the first enabling step towards the *DLCZ* protocol. We examined only a single atomic ensemble, manipulated with Raman pulses, and conditioned through single photon detection. The ensemble consisted of cold Cesium atoms in a magneto-optic trap (MOT). A *write* pulse was focussed into the ensemble, so that with small probability a photon was emitted in the spatial mode of our detection device. The emission of a photon resulted in an atomic excitation symmetrically distributed throughout the interacting atoms, which was conditioned by a detection event. A subsequent *read* pulse interrogated the ensemble, and resulted in a second photon, delayed by the separation of the pulses and emitted into the same spatial mode at the first. We demonstrated the non-classical character of the correlations between the photons by testing for violation of the Cauchy-Schwarz inequality. We found a strong violation, with $[g_{12}^2 = (5.45 \pm 0.11)] \nleq [g_{11}g_{22} = (2.97 \pm 0.08)]$, where g_{ij} are normalised correlation functions for the fields (i, j); 1 and 2 label the fields emitted from the ensemble as a result of the *write* and *read* pulses, respectively. Usefulness in the *DLCZ* protocol aside, this experiment furthers techniques in quantum state engineering[207], and demonstrates an important technological advance in the field of quantum optics. In contrast to prior investigations of nonclassical correlations between photon pairs produced in atomic cascades [248] and in parametric down conversion [249], in our experiment the photons were separated by a programmable time interval $\delta t = 405$ ns, which was limited in principle only by the coherence lifetime between the two ground atomic levels. This coherence lifetime was dictated by the Larmor precession of the atomic spin state in the MOT magnetic fields, and could potentially be extended to several seconds using spin-polarised samples in optical-dipole or magnetic traps[250]. Thus, with some further engineering effort, our system could be used to provide single photons ‘on demand’, and thus enable previously unrealisable experiments involving the inference of many photons[22].

Recently, a similar experiment to ours has been performed by van der Wal *et. al* [251] using Rubidium atoms in a vapour cell. In their experiment, they demonstrated that the techniques proposed by *DLCZ* could be used to produce two mode squeezing between the fields emitted from their ensemble.

9.2 Proposal for quantum communication with atomic ensembles

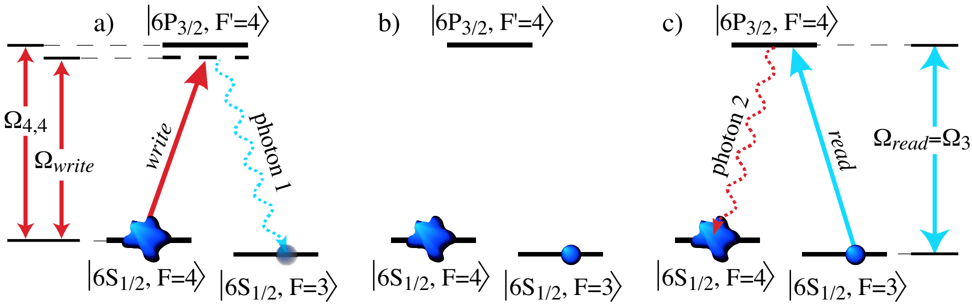

Figure 9.1: Sequence of events used to generate non-classically correlated photon pairs from an ensemble of Cesium atoms. a) The *write* pulse facilitates spontaneous Raman scattering from the $|6S_{1/2}, F = 4\rangle$ Cesium ground state to the $|6S_{1/2}, F = 3\rangle$ ground state, emitting a field with frequency around $\Omega_{3,4}$. b) Photon detection of that field conditions the ensemble into a symmetric entangled state with a single atomic excitation to the $|6S_{1/2}, F = 3\rangle$ ground state distributed evenly through the participating atoms. c) After a programmable time delay the *read* pulse transfers that excitation back into the $|6S_{1/2}, F = 4\rangle$ ground state releasing a single photon with frequency around $\Omega_{4,4}$.

The experiment discussed in this Chapter was facilitated by collectively enhanced Raman scattering in an ensemble of cold Cesium atoms. The atomic energy level structure relevant to this process is shown in Fig. 9.1 a). The ensemble of atoms are initially prepared in the $|6S_{1/2}, F = 4\rangle$ ground state through optical pumping. A laser pulse which we term the *write* pulse here, with frequency Ω_{write} tuned near the $|6S_{1/2}, F = 4\rangle \leftrightarrow |6P_{3/2}, F' = 4\rangle$ transition then induces spontaneous Raman scattering into the initially empty $|6S_{1/2}, F = 3\rangle$ ground level, emitting an optical field of frequency near $\Omega_{3,4}$. If only one atom was involved in the process, the emission would occur in a purely spontaneous manner, randomly into 4π steradians. When an ensemble is involved, however, a single spontaneous Raman scattering event causes a chain of stimulated Raman scatterings, in a manner directly analogous to superfluorescence in a medium composed of inverted two-level atoms[252]. The result is a *collective enhancement* of the atom-photon interaction between the ensemble and optical fields within the spatial mode defined by the *write* pulse. This collective enhancement couples the $|6S_{1/2}, F = 3\rangle$ and $|6S_{1/2}, F = 4\rangle$ ground levels in a similar manner to a bright optical pulse at frequency $\Omega_{3,4}$. Collective enhancement offers an attractive alternative to other techniques presently available to strengthen the atom-photon interaction. The most well known method used is cavity quantum electro-dynamics [9, 110] where the enhancement is achieved by placing the atoms inside an optical resonator of extremely high finesse (~100,000). Recently a number of inspiring results have come from this technology [197, 198, 199, 242], however it still remains extremely challenging.

The complete Hamiltonian describing the three level system used to facilitate our experiment is quite complex. By making a number of simplifying assumptions however, the underlying behaviour of the system becomes evident. Firstly, since the *write* pulse coupling the levels $|6S_{1/2}, F = 4\rangle$ and $|6P_{3/2}, F' = 4\rangle$ is bright and remains undepleted throughout the process, it can be treated in a purely classical manner. Furthermore, in the limit that the detuning $\Delta = \Omega_{write} - \Omega_{4,4}$ between the *write* pulse and the atomic transition is large compared to the Rabi frequency Ω_{Rabi}, spontaneous emission from the $|6P_{3/2}, F' = 4\rangle$ level can be neglected. In practise, our experiment was not operated with large detuning, and we will present an analysis of the spontaneous emission from $|6P_{3/2}, F' = 4\rangle$ later in this Chapter. Here, however, we retain the assumption to allow an intuitive interpretation of the processes involved in the experiment. Given these two assumptions the excited state $|6P_{3/2}, F' = 4\rangle$ can be adiabatically eliminated from the Hamiltonian describing the system [240]. The exact spatial and temporal structure of the fields emitted from the ensemble are, in general, a complex function of the geometry of the atomic sample and the shape and timing of the *write* pulse[253]. A full treatment of this relationship is beyond the scope of this thesis. For a sufficiently dense atomic ensemble the fields are emitted into the spatial mode of the *write* pulse[253]. Here, we therefore only consider fields emitted into that mode. The Hamiltonian H_{ensemble} describing collectively enhanced Raman scattering in an atomic ensemble is then given by [21]

$$H_{\text{ensemble}} = \hbar\Omega_{4,4}\tilde{a}^\dagger\tilde{a} + \hbar\left(\frac{\sqrt{N}\Omega_{\text{Rabi}}g_c}{\Delta}\right)\left(\tilde{\mathcal{S}}^\dagger\tilde{a}^\dagger + \tilde{\mathcal{S}}\tilde{a}\right), \tag{9.1}$$

where g_c is the non-linear interaction strength which is analogous to Λ for second order optical non-linear processes (see Section 2.10), $\tilde{a}$ describes the field coupling the atomic levels $|6S_{1/2}, F = 3\rangle$ and $|6P_{3/2}, F' = 4\rangle$ in the spatial mode defined by the *write* pulse, and $\tilde{\mathcal{S}}$ is the collective atomic mode defined by

$$\tilde{\mathcal{S}} = \frac{1}{\sqrt{N_a}}\sum_i \tilde{\mathcal{S}}_i \tag{9.2}$$

$$= \frac{1}{\sqrt{N_a}}\sum_i |6S_{1/2}, F = 4\rangle_i \langle 6S_{1/2}, F = 3|, \tag{9.3}$$

where the summation is taken over all N atoms within the mode of the optical field. The quantum Langevin equation (Eq. (2.99)) can then be used to yield equations of motion for the optical field mode $\tilde{a}$ and the collective atomic mode $\tilde{\mathcal{S}}$. Solving these equations and using boundary conditions similar to Eq. (2.108) Duan *et al.* found that the collectively enhanced Raman scattered field, termed ‘field 1’ here, and the collective atomic mode were in a two mode squeezed state (see [21] and the attached supplementary information). Assuming that the interaction is weak so that most of the atoms remain in the $|6S_{1/2}, F = 4\rangle$ ground level, this state can be expressed in the Schrödinger picture as [21]

$$|\Psi_{\mathcal{S},1}\rangle = |\psi_{\mathcal{S}}, \psi_1\rangle = \sqrt{1-p}\sum_n\left(\tilde{\mathcal{S}}^\dagger\tilde{a}^\dagger\sqrt{p}\right)^n|0\rangle_{F=3}|0\rangle_{\text{field 1}} \tag{9.4}$$

$$= \sqrt{1-p}\sum_n p^{\frac{n}{2}}|n\rangle_{F=3}|n\rangle_{\text{field 1}}, \tag{9.5}$$

where p is the probability that field 1 contains a non-zero number of photons. p is related to the two-mode squeeze factor r relevant to this atom-light system, $p = \tanh^2 r$ (see Section 2.2 for a definition of the squeeze factor), and is a complex function of the optical pulse width, the Rabi frequency, the detuning, the non-linear interaction strength, and the atomic cross-section (N/L), where L is the length of the atomic ensemble [21].

Collective enhancement of the atom-photon interaction has been investigated previously in the context of spin squeezing [11, 254, 255, 256, 257], which has recently been experimentally demonstrated [20, 201, 202]. Unlike spin squeezing experiments which rely on homodyne detection, the *DLCZ* scheme implemented here involves photon counting techniques, which facilitate a different and potentially powerful type of atomic ensemble conditioning. Assuming that the probability of excitation is low ($p \ll 1$) and ideal conditions, detection of a photon, termed 'photon 1' throughout, from field 1 collapses the state of our atomic mode to $|\psi_{\mathcal{S}}\rangle = |1\rangle_{F=3}$, so that a single atomic excitation is present in the $|6S_{1/2}, F = 3\rangle$ hyperfine ground state (see Fig. 9.1 b)). This single excitation is distributed in a symmetrised, coherent manner throughout the atomic ensemble. In the ideal case the conditioned state of the ensemble is then [21]

$$|\Phi\rangle = \frac{1}{\sqrt{N}} \sum_{j=1}^{N} \left|6S_{1/2}, F=4\right\rangle_1 \ldots \left|6S_{1/2}, F=3\right\rangle_j \ldots \left|6S_{1/2}, F=4\right\rangle_N . \tag{9.6}$$

The excitation can be stored in the atomic ensemble for periods on order the lifetime of the coherence between the ground levels $|6S_{1/2}, F = 3\rangle$ and $|6S_{1/2}, F = 4\rangle$.

The atomic excitation can be converted into a field excitation, 'field 2', on demand and with high probability, with a specified emission direction and a programmable pulse shape [21, 110, 207, 258]. This conversion is achieved with a laser pulse, the *read* pulse, with frequency tuned near the frequency $\Omega_{3,4}$ of the $|6S_{1/2}, F = 3\rangle \rightarrow |6P_{3/2}, F' = 4\rangle$ transition, as shown in Fig. 9.1 c). Illuminating the atomic ensemble with this pulse affects the transfer $|6S_{1/2}, F = 3\rangle \rightarrow |6S_{1/2}, F = 4\rangle$, with the accompanying emission of a second Raman photon, 'photon 2', on the $|6P_{3/2}, F' = 4\rangle \rightarrow |6S_{1/2}, F = 4\rangle$ transition. For an optically thick atomic ensemble, field 2 is emitted with high probability into the spatial mode defined by field 1, offset in time by δt [253]. So that, using an appropriate series of laser pulses, a pair of temporally and spatially correlated photons, with tunable temporal separation, can be generated from an atomic ensemble.

9.3 Verification of the non-classical nature of the fields

In this Section we derive an experimentally verifiable criterion for the non-classicality of the correlations between fields 1 and 2. The analysis given here is based on the work of Clauser [248], and the supplementary information attached to [206].

9.3.1 A Cauchy-Schwarz inequality based on coincidence rates

In our experiment we are interested in the rate of photon counting coincidences between the fields 1 and 2 emitted by the atomic ensemble as a result of the *write* and *read* pulses, respectively. Let us take the mean arrival times for fields 1 and 2 at their respective photodetectors to be t_1 and t_2, and gate the photodetectors *ON* for an interval T around their respective mean arrival time (see Fig. 9.3). The average coincidence rate C_{ij} for photon counting events between the fields i and j then given by [248]

$$C_{ij} = \eta_i \eta_j \int_{-\frac{T}{2}}^{+\frac{T}{2}} \int_{-\frac{T}{2}}^{+\frac{T}{2}} \left\langle \tilde{a}_i^{\dagger}(t_i + t')\tilde{a}_i(t_i+t')\tilde{a}_j^{\dagger}(t_j+t'')\tilde{a}_j(t_j+t'') \right\rangle dt'dt'', \tag{9.7}$$

where $i \in \{1, 2\}$, and η_i is the effective efficiency of detector i which can include properties characteristic to the detectors such as electronic gain factors.

In order to clearly delineate between classical and quantum mechanical correlations we will now couch our analysis in terms of a quasi-probability distribution, the *P-representation* [259, 260]. The *P*-representation is closely related to the Wigner function described in Section 2.2.1, indeed, the Wigner function is obtained by convoluting the *P*-representation with a symmetric Gaussian of unit radius. The *P*-representation describes a given state as a weighted ensemble of coherent states. Unlike a classical probability distribution however, when representing some quantum states the weighting factors can become negative or highly singular. Indeed, it is this manifestly quantum mechanical behaviour that we use to distinguish between classical and quantum mechanical correlations. The Optical Equivalence Theorem allows us to relate a general form of the expectation value in Eq. (9.7) to the *P*-representation [230]

$$\left\langle \tilde{a}_i^\dagger \tilde{a}_i \tilde{a}_j^\dagger \tilde{a}_j \right\rangle = \int P(\alpha_i, \alpha_j) \alpha_i^* \alpha_i \alpha_j^* \alpha_j d\alpha_i d\alpha_j, \tag{9.8}$$

where $\{i, j\} \in \{1, 2\}$, and $d\alpha_{i,j} = d\Re\{\alpha_{i,j}\} d\Im\{\alpha_{i,j}\}$. Here α_i and α_j represent the coherent amplitudes of the ensemble of coherent state pairs used to construct fields i and j, and the weighting of each pair is given by the parameter $P(\alpha_i, \alpha_j)$. $P(\alpha_i, \alpha_j)$ has the property that

$$\int P(\alpha_i, \alpha_j) d\alpha_i d\alpha_j = 1, \tag{9.9}$$

and strongly resembles a classical probability function. As discussed above, however, it is not always a well-behaved function and can be negatively or singularly valued. If $P(\alpha_1, \alpha_2)$ is well behaved, however, it is entirely analogous to a classical probability distribution. This implies both that the state may be modelled perfectly using a hidden-variable model of quantum mechanics, and that it satisfies the Cauchy-Schwarz inequality

$$\begin{aligned} &\left[\int P(\alpha_1, \alpha_2) \left[\alpha_1^* \alpha_1 \alpha_2^* \alpha_2\right] d\alpha_1 d\alpha_2\right]^2 \\ &\qquad \leq \int P(\alpha_1, \alpha_1') \left[\alpha_1^* \alpha_1 {\alpha_1'}^* \alpha_1'\right] d\alpha_1 d\alpha_1' \times \int P(\alpha_2, \alpha_2') \left[\alpha_2^* \alpha_2 {\alpha_2'}^* \alpha_2'\right] d\alpha_2 d\alpha_2', \end{aligned} \tag{9.10}$$

where $P(\alpha_i, \alpha_i') = \int P(\alpha_1, \alpha_2) d\alpha_j \int P(\alpha_1', \alpha_2') d\alpha_j'$, $i \neq j$. Violation of this Cauchy-Schwarz inequality necessarily implies that the *P*-representation of the state is not well-behaved and therefore, in our case, that non-classical correlations exist between the fields emitted from the atomic ensemble. By comparison with Eqs. (9.7), and (9.8) we find that this inequality can be directly translated into one between the observed mean coincidence rates between and within fields 1 and 2

$$C_{12}^2 \leq C_{11} C_{22}. \tag{9.11}$$

For a given level of correlation, these coincidence rates are directly proportional to the rate of singles counts on the two detectors S_1 and S_2. It is convenient then to normalise inequality (9.11) with respect to these singles rates

$$\left[\frac{C_{12}}{S_1 S_2}\right]^2 \leq \left[\frac{C_{11}}{S_1^2}\right] \times \left[\frac{C_{22}}{S_2^2}\right], \tag{9.12}$$

with

$$S_i = \eta_i \int_{-\frac{T}{2}}^{+\frac{T}{2}} \left\langle \tilde{a}_i^\dagger(t{+}t')\tilde{a}_i(t{+}t')\right\rangle dt', \tag{9.13}$$

where $i \in \{1,2\}$. Assuming that each trial of the experiment is independent from all other trials, the singles rates can be written in terms of the coincidence rates C'_{ij} where here the $'$ signifies that the coincidence rates are measured between different trials of the experiment,

$$S_i S_j = C'_{ij}. \tag{9.14}$$

Inequality (9.12) can then be written compactly in terms of the normalised correlations functions $g_{ij} = C_{ij}/C'_{ij}$

$$g_{12}^2 \leq g_{11}g_{22}. \tag{9.15}$$

This inequality presents an experimentally verifiable criterion for the non-classicality of the correlations displayed by the fields emitted from our atomic ensemble.

The coincidence rates C_{12} and C'_{12} between the fields 1 and 2 emitted in our experiment could be directly measured. The single field coincidence rates C_{ii} and C'_{ii} however, are more difficult to determine. For each emitted field i we characterised the relevant single field coincidence rates by splitting the field on a 50/50 beam splitter, and measuring cross-correlations between the two output fields (denoted with subscripts a and b here). Assuming that, after tracing over all other fields, field i is well-behaved and has a positive definite *P*-representation[1], it is relatively easy to show from Eqs. (9.7), (9.8), and (9.9) that the measured coincidence rates $C_{ab}^{(i)}$ and $C_{ab}^{(i)\prime}$ between the beam splitter outputs are related to the desired single field coincidence rates by $C_{ab}^{(i)} = C_{ii}/4$, and $C_{ab}^{(i)\prime} = C'_{ii}/4$. We see then that $g_{ii} = g_{ab}^{(i)}$, so that the correlation function obtained from these measurements is exactly the auto-correlation function for field i.

Note that a similar analysis to that presented above can be performed using the Wigner function, and a similar result is obtained, however for the situation considered here the desired delineation between classical and quantum mechanical correlations appears more naturally using the *P*-representation. Note also that, strictly speaking, our experimental protocol measured the detection rate of photon 2, conditional on the detection of photon 1. These conditional rates are directly proportional to the coincidence rates discussed in the analysis above, and since inequality (9.15) takes the ratio of coincidence rates, it is equally valid to conditional rates. For a more detailed analysis of this point I direct you to the supplementary notes attached to [206].

9.3.2 Expected violations of the Cauchy-Schwarz inequality

Now that we have a criterion for non-classicality of the correlation between a pair of fields, let us examine the level of non-classicality of the fields emitted from an atomic ensemble during the protocol given in Section 9.2. This is determined by six coincidence rate measurements: those between fields 1 and 2, and within each of the fields; both within a single experimental trial and between two independent trials. First let us determine the state that each of these measurements is performed on. From Eq. (9.5) we find that in the ideal case after both the *write* and *read* pulses,

---

[1] Individually both fields 1 and 2 emitted from our atomic ensemble are in thermal states, so that this assumption is valid for our experimental situation.

but before detection, fields 1 and 2 emitted from our ensemble are in the correlated state

$$|\Psi_{12}\rangle = |\psi_1, \psi_2\rangle = \sqrt{1-p}\sum_{n=0}^{\infty} p^{\frac{n}{2}}\, |n\rangle_{\text{field 1}}\, |n\rangle_{\text{field 2}}\,, \tag{9.16}$$

where $|\psi_i\rangle$ is the wave-packet of field i. Coincidence rate measurements on this state correspond to measurements of C_{12}, the between field coincidence rate within a single experimental trial. On the other hand, when the coincidence rate measurements between fields 1 and 2 are performed on independent trials so that C'_{12} is obtained, fields 1 and 2 are uncorrelated, and the overall state is

$$|\Psi_{1\otimes 2}\rangle = |\psi_1\rangle \otimes |\psi_2\rangle\,. \tag{9.17}$$

The coincidence rates within field i can be determined by splitting the field on a 50/50 beam splitter and measuring coincidence rates between the two output fields $\psi_a^{(i)}$ and $\psi_b^{(i)}$. Neglecting phase factors, since we are photon counting, the beam splitter output state is given by

$$|\Psi_{ab}^{(i)}\rangle = |\psi_a^{(i)}, \psi_b^{(i)}\rangle = \sqrt{1-p}\sum_{n=0}^{\infty}\left(\frac{p}{2}\right)^{\frac{n}{2}}\sum_{m=0}^{n}\sqrt{\frac{n!}{m!(n-m)!}}\,|m\rangle_{\text{field 1}}\,|n-m\rangle_{\text{field 2}}\,. \tag{9.18}$$

Coincidence rate measurements on this state correspond to a measurement of $C_{ab}^{(i)} = C_{ii}/4$. Similarly to the above case, when the coincidence rate measurements are performed on independent experimental trials yielding $C_{ab}^{(i)\prime} = C'_{ii}/4$, fields a and b are uncorrelated, and the overall state is

$$|\Psi_{a\otimes b}^{(i)}\rangle = |\psi_a^{(i)}\rangle \otimes |\psi_b^{(i)}\rangle \tag{9.19}$$

In this Schrödinger picture, the coincidence rate between a pair of fields x and y, in the state $|\Psi\rangle = |\psi_x, \psi_y\rangle$ is given by

$$C_\Psi = \frac{1}{\Delta t}\sum_{i=1}^{\infty}\sum_{j=1}^{\infty} ij\,\left|\langle ij|\Psi\rangle\right|^2 \tag{9.20}$$

where Δt is the time interval between consecutive trials, and we have assumed perfect detection efficiency. The coincidence rates for each of the states given in Eqs. (9.16), (9.17), (9.18), and (9.19) can then be calculated. After a bit of work we find

$$C_{12} = \frac{1}{\Delta t}\left[\frac{p\,(1+p)}{(1-p)^3}\right], \tag{9.21}$$

and

$$C'_{12} = C'_{11} = C'_{22} = \frac{C_{11}}{2} = \frac{C_{22}}{2} = \frac{1}{\Delta t}\left[\frac{p}{1-p}\right]^2. \tag{9.22}$$

The correlation functions g_{12}, g_{11}, and g_{22} can then be directly determined from Eq. (9.15), and we find

$$g_{12} = \frac{C_{12}}{C'_{12}} = \frac{1+p}{p\,(1-p)}, \tag{9.23}$$

and

$$g_{11} = g_{22} = \frac{C_{ii}}{C'_{ii}} = 2, \tag{9.24}$$

where $i \in \{1, 2\}$. The simple relation $g_{11} = g_{22} = 2$ is the expected result if fields 1 and 2 are both individually in thermal states. We then find that the Cauchy-Schwarz inequality should be violated with the ratio between $[g_{12}]^2$ and $g_{11} \times g_{22}$ being

$$\begin{aligned} R &\equiv \frac{[g_{12}]^2}{g_{11} \times g_{22}} && (9.25) \\ &= \frac{1}{4}\left[\frac{1+p}{p(1-p)}\right]^2 && (9.26) \\ &\gg 1 \quad \forall \quad p. && (9.27) \end{aligned}$$

We see that for all transition probabilities p the Cauchy-Schwarz inequality is predicted to be strongly violated by the fields emitted from the atomic ensemble system of Section 9.2, with $R \to \infty$ as $p \to \{0, 1\}$. Of course, as $p \to 1$ the photon number variance of state $|\Psi_{12}\rangle$ becomes extremely large. In this regime detectors with the ability to distinguish the number of photons in the state are required. Such detectors are not presently available. When $p \to 0$ however, the probability of detecting more than one photon in fields 1 and 2 becomes vanishingly small, so that the detectors utilised are only required to distinguish between the situations ‘no photons present’ and ‘photons present’. Such detectors are readily available. In our experiment $p \sim 0.01$, so that we were well within this regime. In ideal circumstances our experiment could then violate the Cauchy-Schwarz inequality by as much as $R \sim 2600$. Of course, in an experimental situation imperfections arise, such as photodetector counts from sources unrelated to the Raman process, and detection inefficiencies. These imperfections can seriously degrade the observed violation; however, as we have shown above, so long as $R > 1$ the state of fields 1 and 2 cannot be described by a well-behaved P-distribution, so that by definition, they are non-classically correlated.

9.4 Experimental realisation

9.4.1 Experimental configuration

Fig. 9.2 shows the experimental apparatus utilised in our demonstration of non-classically correlated photon generation from an atomic ensemble. The ensemble of Cesium atoms used in our experiment was confined by a magneto-optical trap (MOT) inside a vacuum chamber. As the name suggests the MOT consisted of two components: magnetic fields which provided a potential to confine the atoms, and optical fields to cool the atoms. The arrangement of the optical fields is shown in Fig. 9.2 c) and was as follows. Three orthogonal sets of counter-propagating optical fields detuned from the $|6S_{1/2}, F = 4\rangle \leftrightarrow |6P_{3/2}, F' = 4\rangle$ transition utilised the Doppler effect to cool and trap the atoms in the atomic energy level $|6S_{1/2}, F = 4\rangle$, and an optical field on the $|6S_{1/2}, F = 3\rangle \leftrightarrow |6P_{3/2}, F' = 4\rangle$ transition repumped any atoms excited into the $|6S_{1/2}, F = 3\rangle$ level, back into the trapped $|6S_{1/2}, F = 4\rangle$ level. Further details regarding magneto-optic trapping will not be presented here, a good analysis can be found in [250]. The cooling and trapping fields were produced by injection seeding a semi-conductor diode laser with the output of an external grating diode laser (see Fig. 9.2 a)) which was itself locked to the $|6S_{1/2}, F = 4\rangle \leftrightarrow |6P_{3/2}, F' = 4\rangle$ transition. Throughout the work presented here the optical fields were locked to atomic transitions using the configuration shown in Fig. 9.2 b). The

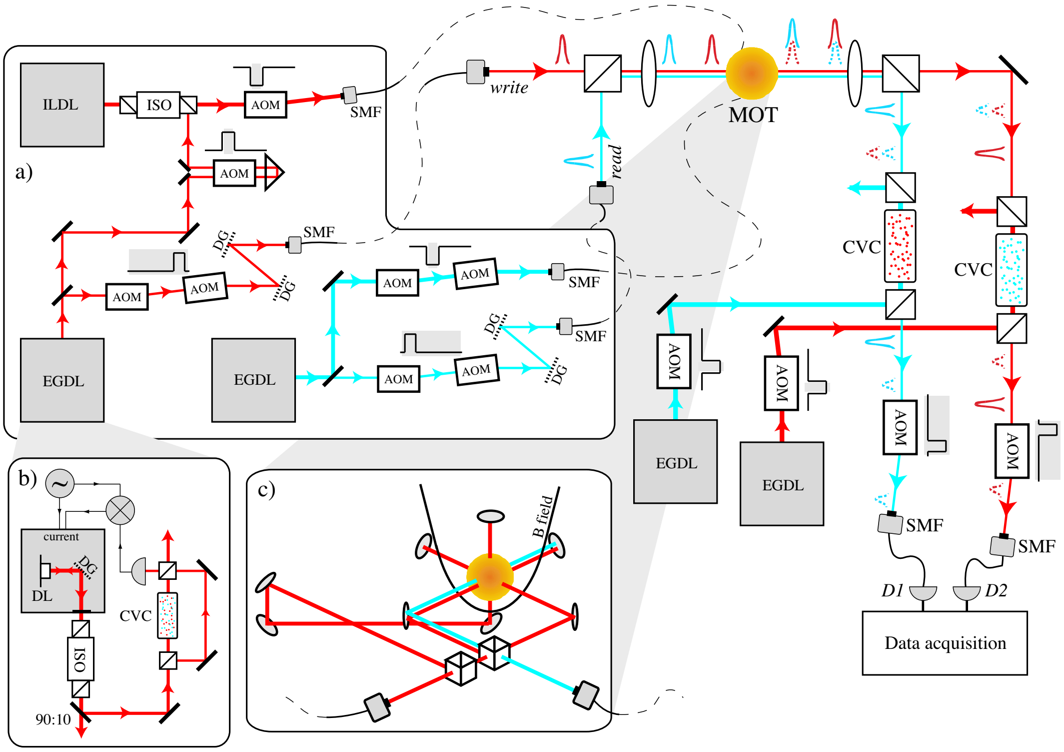

Figure 9.2: Apparatus to generate single photons from an atomic ensemble. Inset a) shows the setup used to generate and switch the MOT fields and the *write* and *read* pulses. Inset b) shows the technique used to lock each EGDL to the relevant atomic transition. Inset c) shows the MOT configuration. Fields with frequency near the frequency $\Omega_{4,4}$ of the $|6S_{1/2}, F = 4\rangle \leftrightarrow |6P_{3/2}, F' = 4\rangle$ transition are colored red (dark), and those near the frequency $\Omega_{3,4}$ of the $|6S_{1/2}, F = 3\rangle \leftrightarrow |6P_{3/2}, F' = 4\rangle$ transition, blue (light). The shaded interval in the timing diagram for each AOM defines the interval in which the experimental trial is performed. DL: diode laser, EGDL: External grating diode laser, ILDL: injection locked diode laser, *D1*, *D2*: single photon detectors, SMF: single mode fibre, CVC: Cesium vapour cells used as a frequency reference and to spectrally filter the MOT outputs, ISO: Optical isolator, AOM: acousto-optic modulator, DG: diffraction grating.

diode current is modulated, resulting in a phase modulation on the output field from the diode laser. A proportion of the output field is passed through a Cesium vapour cell in a Doppler-free spectroscopy configuration. Demodulating the transmitted field at the modulation frequency provides an error signal that is applied to the diode current to lock the laser to the transition. This locking technique is analogous to the sideband locking technique described in Section 2.5.2. The repumping field was produced directly from an external grating diode laser, locked to the $|6S_{1/2}, F = 3\rangle \leftrightarrow |6P_{3/2}, F' = 4\rangle$ transition. We chopped the cooling and trapping, and repumping fields from *ON* to *OFF* with a period of $\Delta t = 4\ \mu$s using acousto-optic modulators (AOMs). For both fields a pair of AOMs were used in the configuration shown in Fig. 9.2 a), this ensured that during the *OFF* intervals minimal light from the cooling and trapping, and repumping fields was present. The MOT was therefore also switched *ON* and *OFF* with period $\Delta t = 4\ \mu$s, as shown in Fig. 9.3. Within each period, the MOT fields were gated *OFF* for an interval of $1\ \mu$s and *ON* for an interval of $3\ \mu$s. During the *OFF* times less than 0.1% of the atoms were measured to be present in the $|6S_{1/2}, F = 3\rangle$ level. The experimental trials were performed within each consecutive *OFF* time.

The *write* and *read* fields used to condition the atomic ensemble were provided by the same

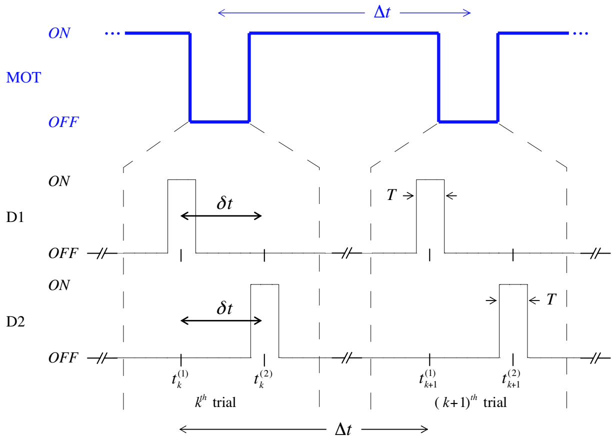

Figure 9.3: This diagram illustrates the timing sequence for coincidence detection for a series of independent trials $\{k\}$ during intervals when the cooling and trapping, and repumping fields are gated *OFF*. Photon counting events are recorded only during the gating windows of duration T centered on the times $\{t_k^{(1)}, t_k^{(2)}\}$ for the k^{th} trial of the experiment.

external cavity diode lasers as the MOT cooling and trapping, and repumping fields. They were shaped into pulses with pairs of AOMs as shown in Fig. 9.2 a). In both cases the pulse width was $\sim$ 45 ns (FWHM), and the separation between the pulses was $\delta t \sim$ 405 ns. A *write*, *read* pulse pair was generated within each MOT *OFF* interval, with the *write* pulse arriving at the atomic ensemble $\sim$ 450 ns after the MOT was switched. This relatively long separation between MOT switching and the first pulse was required to ensure that the MOT field intensity had decayed to a negligible level prior to the experiment, and that any atoms in the $|6P_{3/2}, F' = 4\rangle$ level when the MOT was switched *OFF* had spontaneously decayed away prior to the *write* pulse. Similarly, since the *write* pulse was near-resonant, the minimum interval between the *write* and *read* pulses was determined by spontaneous decay events $|6P_{3/2}, F' = 4\rangle \rightarrow |6S_{1/2}, F = 4\rangle$ caused by the *write* pulse. Note that, since the lifetime of the $|6P_{3/2}, F' = 4\rangle$ level is much shorter than the coherence time between the two ground levels, direct observation of spontaneous emission could always be avoided by choosing a sufficiently large interval between the *write* and *read* pulses. This spontaneous decay process does however transfer some atoms into the $|6S_{1/2}, F = 3\rangle$ level. In our case, several hundred atoms were transferred in this manner per trial. Since spontaneous decay is a random process no coherence was present between these atoms, and therefore when the *read* pulse affected the transfer $|6S_{1/2}, F = 3\rangle \rightarrow |6S_{1/2}, F = 4\rangle$, their emission was randomly distributed over 4π steradians. Correspondingly, detection events of this nature were suppressed by the fractional solid angle of our detection apparatus, $\delta\theta/4\pi \simeq 2 \times 10^{-5}$. The model of Section 9.2 which neglects spontaneous emission can therefore be applied to our experiment.

The *write* and *read* pulses were coupled into single mode fibres and combined on a polarising beam splitter, with observed visibility of greater than 95 %. The output field was focussed to a waist of $\sim$ 30 μm within the atomic ensemble. The *write* pulse generated a co-propagating collectively enhanced Raman scattered field, field 1 at frequency near $\Omega_{3,4}$, and the *read* pulse converted the resulting atomic excitation into a co-propagating field excitation, field 2, at frequency near $\Omega_{4,4}$.

To ensure that fields 1 and 2 were emitted into identical spatial modes it was important that the resonant optical thickness $\gamma_{4,4}$ of the atomic sample at the frequency of the *write* pulse was greater than unity [253]. We measured $\gamma_{4,4} = 4.5 \pm 0.5$ for a continuous field at frequency Ω_{write}, corresponding to an intensity attenuation on propagation through the MOT of $e^{-\gamma_{4,4}}$. Taking into account the MOT field and trap geometry, this attenuation provides a rough estimate of the atomic density in the trap of $\rho \sim 3.6 \times 10^{10}$ atoms/cm^3. This allows us to estimate another important parameter in the experiment, the number of atoms N contained within the overlap volume V of the *read* and *write* pulses and the atomic ensemble. The geometry of the trap, and focussing of the *read* and *write* pulses dictates an overlap volume of $V \sim 2.8 \times 10^{-6}$ cm^3, so that $N \sim 1.0 \times 10^5$ atoms.

At this point we would like to begin coincidence counting between the fields. However, each field was co-propagating and time-overlapped with a bright pulse (the *write* or *read* pulse) and prior to any photon counting measurements, this pulse had to be filtered out. The frequency separation between field and pulse in both cases was $\Omega_{3,4} - \Omega_{4,4} = 9$ GHz which is too small for dielectric filters or even resonators to be effective. We achieved this filtering in two stages, as shown in Fig. 9.2. Firstly, we separated the *write* pulse and field 2 from the *read* pulse and field 1 using a polarising beam splitter. This separation attenuated the *write* and *read* pulses by a factor of $> 10^2$ relative to fields 1 and 2, respectively. The polarisation of fields 1 and 2 depends on the particulars of the hyperfine manifolds forming the atomic energy levels $|6S_{1/2}, F = 3\rangle$ and $|6S_{1/2}, F = 4\rangle$. A reasonable assumption is that given the complexity of each manifold, both fields average out to be circularly polarised. This polarisation filtering, therefore, reduces the efficiency of the protocol by ~ 50 %[2].

The second stage of filtering was provided using Cesium vapour cells. Field 1 and the residual component of the *write* pulse propagated through a cell, ‘cell 1’ in which the Cesium atoms were optically pumped into the $|6S_{1/2}, F = 4\rangle$ ground level[261]. The residual component of the *write* pulse, which was at frequency $\Omega_{4,4}$, was then strongly attenuated by an additional factor $> 10^6$. Field 1, on the other hand, was transmitted with efficiency of ~ 80 %. Similarly, field 2 and the residual component of the *read* pulse propagated through another cell, ‘cell 2’. The atoms in this cell were pumped into the $|6S_{1/2}, F = 3\rangle$ ground level, and therefore the *read* pulse was strongly attenuated whilst field 2 was transmitted. The optical pumping of the Cesium vapour cells was achieved with bright optical fields with frequency near that of the transmitted light (see Fig. 9.2). These pumping fields were generated by external grating diode lasers, and to optimise the optical pumping their frequencies were scanned over the Doppler width of the relevant transition at a rate fast compared to the atomic time scales. The optical pumps were switched *OFF* for the interval over which the experimental trial was performed to minimise their contribution to the background photon counts. These cells effectively blocked the original (*write*, *read*) pulses, while transmitting the associated $(1, 2)$ photons.

The field transmitted through cell 1 consisted of the desired field (field 1), and after a tunable delay of δt, the *read* pulse. Since these two fields were time resolved, it was a relatively easy task to remove the *read* pulse. This was achieved by passing the field through an AOM which was switched *ON* for a short period around field 1 as shown in Fig. 9.3. The intensity of the *read* pulse was then sufficiently attenuated so as not to damage our photodetectors. After detection electronic gating could be implemented to remove any counts outside the window shown in Fig. 9.3. A similar technique was applied to the field transmitted through cell 1 to remove the *write* pulse which was time advanced by δt from field 2. Fields 1 and 2 were then each coupled into a single mode fibre and directed to a photodetector. The temporal profiles and timing of the *read* and *write* pulses could be analysed by interchanging the frequencies for optical pumping of the filter cells. Fig. 9.4 shows typical pulse profiles accumulated over many trials, where the time origin is set to coincide with the approximate center of the *write* pulse. As well as providing temporal profiles for the *write* and *read* pulses, this configuration allowed us to optimise the efficiency of

---

[2] This efficiency reduction is not fundamental, and could be eliminated for example by used a spin polarised atomic ensemble.

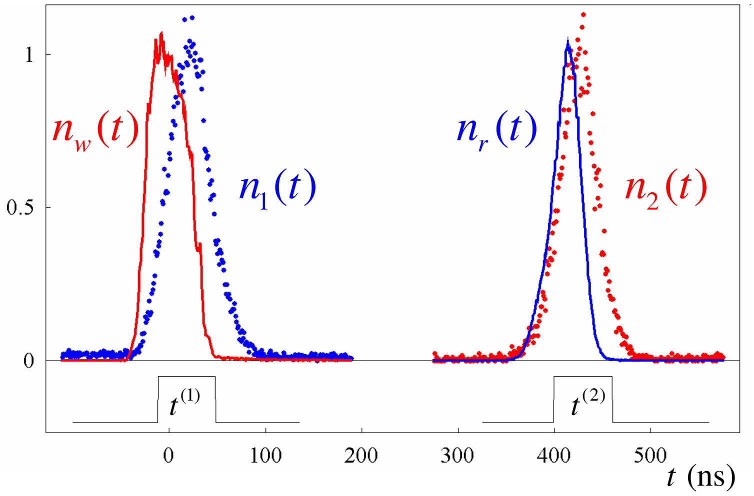

Figure 9.4: Normalised temporal profiles of the *write* and *read* pulses, and fields 1 and 2. The pulses around $t = 0$ are from photodetector *1* for the *write* pulse $n_w(t)$ (solid trace) and for field 1, $n_1(t)$ (points). The pulses around $t = 405$ ns are from photodetector *2* for the *read* pulse $n_r(t)$ (solid trace) and for photon 2, $n_2(t)$ (points).

transmission from the MOT to the detectors, ensuring that the imaging system efficiently collected the collectively enhanced Raman scattered light from the atomic ensemble in a field mode with the same structure as that of the *write* and *read* pulses [253]. The total transmission efficiency for fields 1 and 2 from the MOT to the relevant detector was measured to be $\eta_{\text{trans}} \simeq 0.3$, and the overall quantum efficiency of the photodetectors was approximately $\eta_{\text{det}} \simeq 0.5$ (photon in to TTL pulse out).

9.4.2 Observed singles rates and their implications

With the filter cells in their standard configuration; that is, set so that fields 1 and 2 are transmitted to detectors 1 and 2; respectively, we were able to analyse the singles rate observed by each detector. An unexpected and serious limitation of using diode lasers to produce the *read* and *write* pulses was discovered at this point, which was that they spontaneously emit over a broad spectrum. In our case approximately 2 % of the output power of each diode laser was contained in this spectrum. This background light is efficiently transmitted through our MOT and the optical filtering cells, and without attenuation, made a much larger contribution to the singles counts at detectors 1 and 2 than the fields emitted from the atomic ensemble. We attenuated this background light by placing a pair of diffraction gratings into each of the *write* and *read* fields before they were coupled into their respective single mode fibres and passed through the MOT (see Fig. 9.2). These gratings reduced the spectrum of this broad spectrum spontaneous emission to ~ 10 GHz. Further attenuation by a factor of between 10^2 and 10^3 was achieved by the crossed-polariser arrangement of the polarising beam splitters on either side of the MOT. Diode laser spontaneous emission was one of the limiting features of our experiment. In future experiments further attenuation could be achieved using Fabry-Perot étalons, or an alternative laser source.

With this spurious diode laser emission attenuated, we characterised the rate of singles emitted from our atomic ensemble and observed by each detector. For comparison with the profiles of the *write* and *read* pulses, normalised temporal profiles for these rates are displayed in Fig. 9.4. The intensity of the *write* pulse was kept low in our experiment, with only $\sim 10^3$ photons per pulse. This resulted in a time lag for the onset of the singles counts observed by detector 1. We see from

Fig. 9.4 that, apart from this time lag, the temporal profile of field 1 corresponded closely to that of the *write* pulse. The mean singles rate observed at detector 1 was $S_1 \simeq 400\ \mathrm{s}^{-1}$. The probability p_1 that detector 1 provides a photon counting event in any given trial of the experiment can be related to this singles rate by

$$p_1 = \frac{S_1}{\delta t} \simeq 1.6 \times 10^{-3}. \tag{9.28}$$

By taking into account the transmission efficiency from the atomic ensemble to the detector η_{trans}, and the detection efficiency η_{det}, we can then infer the probability p of a photon, photon 1, being emitted into the mode of our detection apparatus from the atomic ensemble

$$p \simeq \frac{p_1}{\eta_{\mathrm{trans}}\eta_{\mathrm{det}}} \simeq 1.1 \times 10^{-2}, \tag{9.29}$$

which is much smaller than unity, as required for our protocol.

A photon counting event at detector 1 caused by field 1 dictates that at least one of the atoms in the ensemble has been transferred into the $|6S_{1/2}, F = 3\rangle$ atomic energy level. Since the interaction of the pulse with the atoms is to a large degree symmetric with respect to permutation of atoms, this excitation should be distributed evenly over all of the atoms involved, resulting in the entangled atomic state $|\Psi_{\mathcal{S},1}\rangle$. The *read* pulse then transfers the atomic excitation into field 2, with the resulting photon arriving at detector 2. We therefore expect to observe photon counting events at detector 2 conditioned on both the *write* and *read* pulses. Indeed, this was observed, and the resulting temporal profile for photon arrivals at detector 2 is shown in Fig. 9.4. The intensity of the *read* pulse was about 100 times greater than that of the *write* pulse, so that, in contrast to field 1, field 2 was generated promptly, and with a temporal profile corresponding to the *read* pulse. The observed singles rate at detector 2 was $S_2 \simeq 250\ \mathrm{s}^{-1}$. The efficiency $\eta_{3\to 4}$ of the transfer from atomic to field excitation can be estimated from the ratio of this rate to that observed at detector 1

$$\eta_{3\to 4} \simeq \frac{S_2}{S_1} = 0.63. \tag{9.30}$$

The *DLCZ* protocol has potential in quantum communication systems both because of its powerful nature, and due to its insensitivity to a variety of loss mechanisms, including inefficiencies in transmission and detection of fields 1 and 2. However, in an actual experiment, various non-ideal factors do lead to deterioration of correlation between fields 1 and 2. In our case, one of the most significant of such factors was uncorrelated background counts observed by our detectors. Background photon counting events from various sources were observed by detectors 1 and 2. The random nature of these counts reduced the coincidence rate between fields 1 and 2. The rate of background counts from various sources was analysed in the following way. Firstly, removing the atomic ensemble, we observed 100 background counts per second from optical fields. A proportion of these counts could be attributed to each relevant field by systematically blocking fields and examining how the background counts varied. We found that almost all of the 100 optical background counts arose from the broad spectrum emission from our diode lasers, with small contributions from the optical pumping fields and the *write* and *read* pulses. Background counts were also present due to fluorescence of the atomic ensemble. These counts could be isolated by blocking the *write* and *read* pulses, with the atomic ensemble present. 10 (20) background counts per second were observed from the atomic ensemble at detector 1 (2). Dark counts with the inputs to the fibres blocked were less than 5/s. The total background counting rates were therefore more than a factor of two smaller than the counting rates for fields 1 and 2.

9.4.3 Conditional photon statistics of the output field

To examine the non-classical nature of the correlation between fields 1 and 2 we counted coincidences, firstly between fields 1 and 2, and then within each field individually. The between-field coincidences were obtained by directing fields 1 and 2 to detectors 1 and 2 respectively and straight-forwardly analysing the coincidences between the detectors. Within-field coincidences were analysed by splitting the relevant field on a 50/50 beam splitter and analysing coincidences between the two output fields, as discussed in Section 9.3. In all cases, the detectors were gated *ON* for a duration of $T = 60$ ns around the peak of the interrogated field. The resulting photocurrents were then directed to a time-interval analyser (TIA) configured in a standard fashion for measurement of photocurrent correlations [230]. A photon count within the gating window of detector 1 acted as a *start* event for the TIA. The TIA then recorded the time separation τ between this *start* event, and a corresponding *stop* event - the detection of a photon by detector 2. Over many experimental trials, we thereby acquired time-resolved coincidences $n_{i,j}(\tau)$ between the fields i and j interrogated by detectors 1 and 2, respectively. In Section 9.3 we saw that to demonstrate violation of the Cauchy-Schwarz inequality, the coincidences both within a single experimental trial k, and between independent trials $\{k,l\}$ must be determined. Setting the maximum interval between *start* and *stop* events recorded by the TIA to be much larger than the duration of a single trial, recorded information about both coincidence types into $n_{i,j}(\tau)$.

Typical examples of the accumulated coincidences $n_{ij}(\tau)$ between fields $\{1,2\}$, $\{1,1\}$, and $\{2,2\}$ are shown in the left hand column of Fig. 9.5. All three traces are strongly peaked with successive peaks separated by the time between trials $\Delta t = 4$ μs. Notice that in all cases the number of coincidences from a single trial ($\tau > \Delta t$) is enhanced compared to those from different trials ($\tau < \Delta t$). Between the fields, this enhancement is due to the photon pairing occurring in our atomic ensemble, and within each individual field it is due to the thermal and therefore super-Poissonian nature of the field. The enhancement is shown more clearly in the plots in the right hand column of Fig. 9.5, which expand the time axis from the left hand column. In this case, the coincidence counts between independent trials $\{k,l\}$, where $l = k+1, \ldots k+10$, have been offset by $(l-k)\Delta t$, so as to coincide with the single trial data, and then averaged with $m_{ij}(\tau) = \frac{1}{10}\sum_{l=k+1}^{k+10} n_{ij}(\tau + (l-k)\Delta t)$.

To obtain a quantitative assessment of our accumulated coincidences $n_{ij}(\tau)$, we separate τ into the time interval over which single trial coincidences are observed, and that over which different trial coincidences are observed. We then sum the total number of coincidences in each of those time periods, and normalise appropriately for comparison. The total number of coincidences between trials $\{k,l\}$ of the detected fields $\{i,j\}$ can be extracted by summing $n_{i,j}(\tau)$ over the time interval $\Delta\tau = \bar{\tau}_{ij}^{\{k,l\}} \pm T$,

$$N_{ij}^{\{k,l\}} = \sum_{\tau=\bar{\tau}_{ij}^{\{k,l\}}-T}^{\bar{\tau}_{ij}^{\{k,l\}}+T} n_{i,j}(\tau), \tag{9.31}$$

with $\bar{\tau}_{ij}^{\{k,l\}}$ being the mean separation of fields $\{i,j\}$ between the trials $\{k,l\}$, given by $\bar{\tau}_{ij}^{\{k,l\}} = (l-k)\Delta t + \bar{\tau}_{ij}^{\{k,k\}}$, where $\bar{\tau}_{12}^{\{k,k\}} = \delta t$ and $\bar{\tau}_{ii}^{\{k,k\}} = 0$. The total number of single trial coincidences N_{ij} is then given directly by $N_{ij}^{\{k,k\}}$. For improved statistical accuracy, we compare these total single trial coincidences with the mean of the total coincidences from each of the different trial

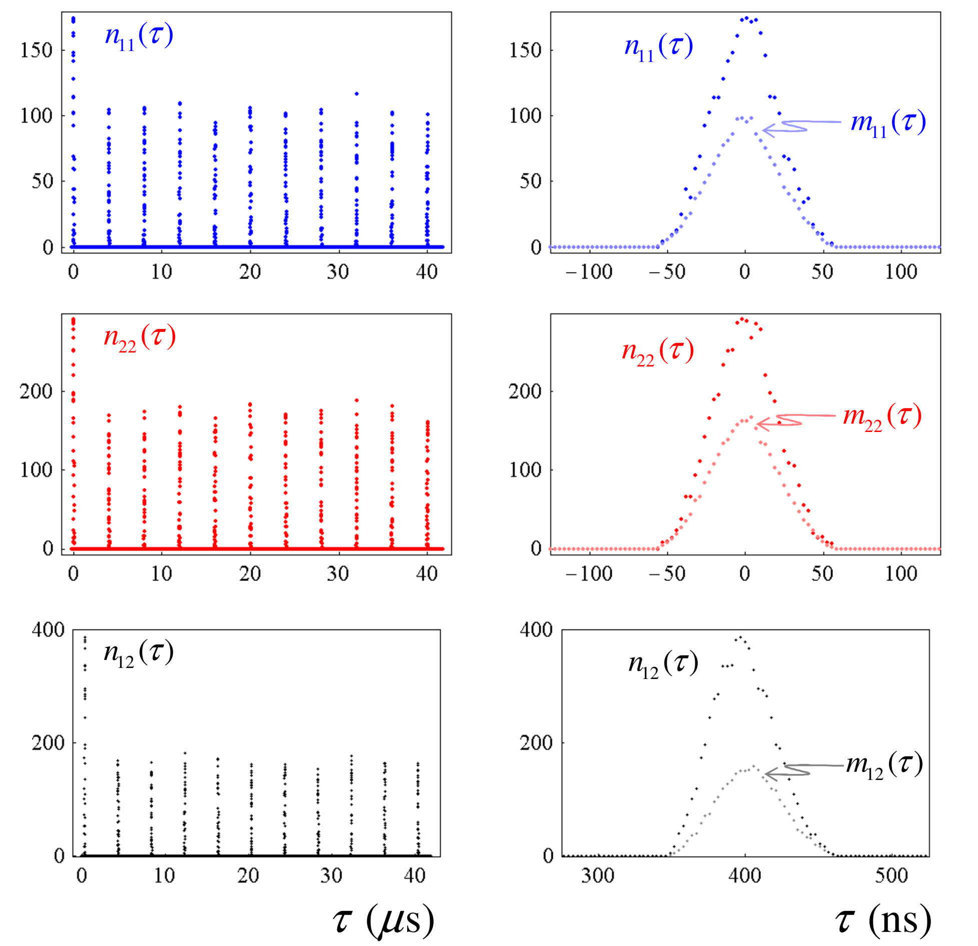

Figure 9.5: *Left column* - time-resolved coincidences $n_{ij}(\tau)$ between the $\{1,1\}$, $\{2,2\}$, and $\{1,2\}$ fields are displayed as a function of the time separation between the events τ. *Right column* - the time axis is expanded to a time interval of 250 ns with $\tau = 0$ set to the center of the gating windows for $n_{11}(\tau)$, $n_{22}(\tau)$, and $n_{12}(\tau)$, respectively. The larger peak $n_{ij}(\tau)$ corresponds to coincidences from the same trial k, while the smaller peak $m_{ij}(\tau)$ corresponds to coincidences from different trials as defined in the text.

data sets N'_{ij}.

$$N_{ij} = N_{ij}^{\{k,k\}} \tag{9.32}$$

$$N'_{ij} = \frac{1}{10}\sum_{l=k+1}^{k+10} N_{ij}^{\{k,l\}}. \tag{9.33}$$

The number of single trial and different trial coincidences between fields i and j can be related directly to the respective coincidence rates, and therefore also to the normalised correlations function g_{ij}

$$g_{ij} = \frac{C_{ij}}{C'_{ij}} = \frac{N_{ij}}{N'_{ij}}, \tag{9.34}$$

and so, determining N_{ij} and N'_{ij} $\forall\,\{i,j\} \in \{1,2\}$, provides g_{11}, g_{22}, and g_{12}, allowing a direct test of the Cauchy-Schwarz inequality.

9.4.4 Observed violations of the Cauchy-Schwarz inequality

From the data in Fig. 9.5 we find that the individual beam normalised correlations functions are

$$\begin{aligned} g_{11} &= 1.739 \pm 0.020 \quad (9.35) \\ g_{22} &= 1.710 \pm 0.015, \quad (9.36) \end{aligned}$$

which corresponds to our prediction from Section 9.3.2 that fields 1 and 2 should both individually exhibit thermal statistics with $\tilde{g}_{1,1} = \tilde{g}_{2,2} = 2$. The experimentally determined values of g_{11} and g_{22} are moderately degraded here due to various sources of background counts. By contrast, for cross-correlations between fields 1 and 2, we find

$$g_{12}(\delta t) = 2.335 \pm 0.014, \quad (9.37)$$

with $\delta t = 405$ ns, so that the correlations exhibited between the fields are stronger than those exhibited by a thermal state. The inequality of Eq. (9.15) is then given by

$$[g_{12}^2(\delta t) = 5.45 \pm 0.11] \not\leq [g_{11}g_{22} = 2.97 \pm 0.08], \quad (9.38)$$

where all errors indicate the statistical uncertainties. Clearly, this is observation is in strong contradiction with the Cauchy-Schwarz inequality. We can, therefore, conclude that fields 1 and 2 emitted from our atomic ensemble exhibit non-classical correlations.

As discussed previously, a number of non-ideal factors exist in any experimental implementation of this sort of protocol. These include inefficiencies in the detection of the light fields, random background counts, and fluorescence from uncorrelated atoms. These imperfections degrade the observed coincidences and thus the strength of violation of the Cauchy-Schwarz inequality. In Section 9.3.2 we predicted that for an excitation probability per *write* pulse of $p = 0.01$, and in ideal circumstances, the ratio of cross- to auto- correlations could be as high as $R = g_{12}^2/g_{11}g_{22} = 2600$. In our experimental demonstration we observed only $R = 1.84 \pm 0.08$. This discrepancy can be fully explained from a detailed analysis of the imperfections in our experiment. Rather than perform that analysis here, I refer you to the supplementary notes attached to [206]. The conclusion of that analysis is that, excluding detection efficiency, in our experiment the strength of Cauchy-Schwarz violation was limited mostly by uncorrelated fluorescence from individual atoms in the atomic ensemble. In future experiments this uncorrelated fluorescence could be reduced, or eliminated entirely, by moving to off-resonant excitation. A higher optical density would then be required which could be achieved in several ways, for example by increasing the intensity of the MOT cooling and trapping fields and therefore enhancing the density of atoms in the ensemble[3].

An important assumption in our derivation of a Cauchy-Schwarz inequality in Section 9.3 was the statistical independence of subsequent trials of the experiment. In our experiment we ensure the independence of these trials by reapplying the MOT after every trial. The repumper field then incoherently transfers any atomic population remaining in the $|6S_{1/2}, F = 3\rangle$ level back to the $|6S_{1/2}, F = 4\rangle$ level. An examination of the data in Fig. 9.5 supports our claim of statistical independence, with no statistically significant difference between of the number of coincidences observed between trials $\{k, l\}$ with $l = k+1, k+2, \ldots, k+10$.

---

[3] Some of these improvements have now been implemented, resulting in an enhanced ratio of cross- to auto- correlations of $R = 53 \pm 2$[262]

9.5 Conclusion

In this Chapter we reported the generation of non-classically correlated photon pairs from an atomic ensemble. This experiment represents the first enabling step towards the realisation of the *DLCZ* protocol [21] for scalable quantum communication with atomic ensembles. Although the complete *DLCZ* protocol was not demonstrated, the collective enhancement observed and optical filtering techniques developed are of critically importance to its realisation. Furthermore, our experiment provides a source of single photons in a well defined spatial mode 'on demand' [263], and has applications regarding the implementation of quantum memory [258, 264]. These intrinsic merits suggest that further investigations in the same line could significantly enhance the feasibility of universal quantum computation [17].

Chapter 10

Conclusions

10.1 Summary

This thesis investigated quantum optical techniques applicable to a quantum information network. A pair of optical parametric amplifiers producing highly squeezed output fields were developed. The field quadrature on which squeezing was observed could be stably controlled, and an optimum of 4.4 dB of squeezing below the quantum noise limit was observed. We utilised this squeezing in a number of experiments, and a summary of each is given below. The final experiment discussed in this thesis investigated quantum optical techniques related to cold atomic ensembles and conditional measurements. A summary of this experiment is also given below.

10.1.1 Quantum information protocols

Entanglement is one of the most intriguing and powerful aspects of quantum mechanics. Indeed, it is one of the core resources utilised in the field of quantum information science. We experimentally generated entanglement between the amplitude and phase quadratures of a pair of fields by interfering the outputs of our optical parametric amplifiers on a 50/50 beam splitter. The resulting state was shown to exhibit non-classical correlations through verifications of a wavefunction inseparability criterion, and the original EPR paradox gedanken experiment. We thoroughly characterised the entanglement by specifying its correlation matrix, and proposed a new characterisation technique, the photon number diagram. This technique represents the entanglement in terms of mean sideband photon numbers, and allows the efficacy of quantum information protocols using the entanglement to be directly assessed. The entanglement was used to implement a quantum teleportation protocol which was operated both in unity and non-unity gain regimes. The performance of the protocol was analysed in terms of the fidelity between the input and output states, and through a study of the signal transfer to; and reconstruction noise on; the output state. A new measure of teleportation was proposed for protocols operating in the non-unity gain regime. This measure was shown to have direct relevance to entanglement swapping protocols. We considered an application of our entanglement to quantum secret sharing. Quantum secret sharing has the potential to facilitate error correction in a quantum computer or communication system, and allows the secure transmission of information even in the presence of malicious parties and faulty communication channels. We demonstrated that quantum secret sharing can be successfully implemented using our entanglement and quantum electro-optic feedforward. Furthermore, we showed that the security of the scheme can be conveniently and arbitrarily enhanced by implementing a conventional secret sharing scheme in conjunction to the quantum mechanical scheme.

10.1.2 Interaction of optical fields with atomic ensembles

Techniques to utilise the interaction between optical fields and atomic media are essential to any feasible quantum information network. In the continuous variable regime, quantum polarisation states are of particular relevance since they have been shown to interact favourably with the collective spin state of atomic ensembles, and do not require the universal local oscillator necessary to implement a quantum information network using other continuous variable states. The polarisation state of an optical field can be characterised by its four Stokes operators. We used our pair of quadrature squeezed fields to demonstrate various forms of polarisation squeezing, and in one case demonstrated simultaneous squeezing of three of the four Stokes operators. We then extended our analysis to polarisation entangled states, demonstrating the transformation of our quadrature entanglement onto a polarisation basis. The entanglement was then evidenced by non-classical correlations between two Stokes operators. Interacting this entanglement with a pair of atomic ensembles could produce a spatially separated, macroscopic, atomic entangled state. We proposed an extension of our scheme, utilising two quadrature entangled states, that would provide entanglement between all four Stokes operators. Finally, we considered the interaction of optical Raman pulses with a Cesium atomic ensemble. Such a system has been shown to have all of the essential characteristics necessary to implement an effective quantum information network. We demonstrated the first primitive of this network by observing non-classical correlations between pairs of photons emitted from the ensemble. The non-classicality of these correlations was verified thorough a violation of the Cauchy-Schwarz inequality. Furthermore, the time interval separating the photons could be controlled experimentally, and the photons were emitted into a well defined spatial mode.

10.1.3 Progress towards quantum enhancement of measurement devices

Optical measurements are ultimately limited by the quantum noise of the optical fields involved. Squeezed fields can be used to reduce this noise and therefore improve the sensitivity of the measurement. However, most signals of interest occur in the Hz to kHz regime, and squeezing is usually limited to frequencies in the MHz. It is therefore essential to develop methods to produce squeezing at lower frequencies. In our case, as a result of classical noise on our laser source no squeezing was observed on our optical parametric amplifier outputs at frequencies below 2 MHz. Placing each optical parametric amplifier within one arm of a Mach-Zehnder interferometer, we demonstrated 29 dB of suppression of this noise, producing a stably locked squeezed vacuum with squeezing at frequencies as low as 210 kHz. Furthermore, although not discussed explicitly in this thesis, we performed the first demonstration of a two dimensional displacement measurement with accuracy better than the quantum noise limit.

10.2 Outlook

10.2.1 Potential technological improvements

The level of squeezing observed on the output fields from our optical parametric amplifiers was limited primarily by their escape efficiency. This efficiency is determined by the ratio of the output coupling to the intra-resonator losses, and could be improved by increasing the transmissivity of the output couplers. More intense second harmonic pumps would then be required for a given level of deamplification. Our modelling indicates that this could be achieved by decreasing the output coupling of the second harmonic generator. The intra-resonator losses are contributed by linear absorption in our MgO:LiNbO$_3$ crystal, imperfect optical coatings, and green induced infrared absorption. As it stands, it is difficult to see how the losses due to linear absorption and optical coatings could be reduced, and the significance of green induced infrared absorption is yet to be determined. In future optical parametric amplifier configurations, the second harmonic pump power will certainly be increased, so that at some stage green induced infrared absorption, which scales with the second harmonic power, will have an effect on the observed level of squeezing. It has been demonstrated recently that increasing the MgO doping level in MgO:LiNbO$_3$ can eliminate this form of absorption. Future investigations should therefore implement this higher level of doping. The stability of our system is currently limited due to temperature fluctuations in the optical parametric amplifiers. Implementation of a 'push-pull' temperature control system using peltier elements, with the temperature sensor closer to the MgO:LiNbO$_3$ crystal, should provide much faster and more stable control. An examination of techniques to derive optical error signals for the phase matching condition of MgO:LiNbO$_3$ is also worthwhile.

10.2.2 Future direction for the entanglement resource

The entanglement resource developed during the course of my Ph.D. has potential for many quantum information protocols. Chapter 6 describes quantum secret sharing which is one such protocol, and a scheme to produce polarisation entanglement between all four Stokes operators using a pair of these resources is given in Chapter 4. Other potential applications include quantum cryptography, where the security of communication is enforced by quantum mechanics; the creation of entanglement between a pair of spatially separated atomic ensembles; dense coding, as discussed in Chapter 4; and entanglement swapping, as discussed in Chapter 5.

Our entanglement resource could also enable further studies into the nature of quantum mechanics. A causal test of the EPR paradox is yet to be performed. Such a test would require the development of fast switching technology to switch homodyne detection between the amplitude and phase quadratures of a field, and that the entangled beams be 10-100 times further spatially separated than in our present configuration. Several proposals have also been made for tests of Bells inequality with continuous variable entanglement. Such a test is relevant since continuous variable entangled states can be thought of as more macroscopic than the microscopic particles that these tests have been performed with thus far. At present, no experimentally feasible scheme to test Bells inequality exists for our entanglement. However, with continuing experimental and theoretical development such an experiment could be feasible in the near future.

Further investigation of techniques to characterise continuous variable entanglement is also worthwhile. The photon number diagram introduced in Chapter 4 could be extended to explain all ten independent elements of the correlation matrix. The question of whether $\bar{n}_{\rm min}$ is strictly a good measure of entanglement also requires further investigation.

10.2.3 The status of quantum information networks

A truly feasible quantum information network is still far from reality. Implementation of such a system will require significant advances in our ability to store and manipulate quantum states, transfer them efficiently between atomic and optical media, and correct errors introduced during the above processes. A number of systems offer potential, and perhaps one of the most promising is atomic ensembles manipulated using optical pulses and conditionally prepared using single photon detection. In Chapter 9 we demonstrated symmetric atomic entanglement in such a system, and generated non-classically correlated photon pairs. This is the first step towards implementation of a quantum information network. The next logical step is to perform the same manipulations on a pair of atomic ensembles. A joint conditional measurement on the fields emitted from the ensembles would then prepare them in an entangled state. Further such manipulations could be performed to distribute entanglement across a network of atomic ensembles. It has been theoretically demonstrated that entanglement purification, error correction and quantum memory can be facilitated using atomic ensembles. Experimental demonstrations of these techniques are required before the feasibility of atomic ensemble quantum information networks can be accurately judged. Investigations of the limiting factors for the coherence time between the ground energy levels of the ensemble are also required.

The techniques developed in Chapter 9 for manipulating atomic ensembles to produce non-classically correlated photon pairs should in-and-of themselves be extended. We demonstrated that the spatial mode of the emitted photons was well defined, and that the arrival time for each photon was controlled by the timing of the optical pulses manipulating the ensemble. The system, therefore, has potential as a source of single photons 'on demand'. The effective implementation of this single photon source, however, requires further investigations of the spatial and temporal characteristics of the emitted photons; as well as improvements in the efficiency of the protocol, and a reduction in the level of background photon counting events.

10.2.4 Potential enhancement of measurement devices

By placing our optical parametric amplifiers within the arms of a Mach-Zehnder interferometer, we observed squeezing at frequencies as low as 210 kHz. Effective enhancement of most measurement devices, however, requires squeezing at significantly lower frequencies. The frequency of our squeezing was ultimately limited from below by uncorrelated noise introduced in the optical parametric amplifiers. As discussed in Chapter 3, this noise should become common mode if a ring resonator is used to generate the two squeezed fields instead of two independent resonators. The noise would then cancel at the dim output of our interferometer, and squeezing should be observed down to much lower frequencies. Other factors such as noise in the control system are then expect to limit the achievable frequencies, these noise sources require investigation.

One measurement system that does not require squeezing at low frequencies is the atomic force microscope. This microscope presently provides higher resolution when imaging alive cells that any alternative. Atomic force microscopes consist of a minute cantilever which can have resonance frequencies in the high MHz. Small forces due to the presence of the sample under investigation cause the amplitude and frequency of the cantilever resonance to change. These changes can be observed by reflecting an optical field from the cantilever and measuring displacements of the field. A specially configured optical field squeezed at the cantilever resonance frequency could be used to enhance the sensitivity of this measurement.

Appendix A

A more detailed analysis of quantum optical sidebands

A.1 The time domain annihilation operator

The time domain annihilation operator $a(t)$ is given by the sum of the frequency domain annihilation operators at all frequencies with appropriate phase relationships,

$$\begin{aligned} a(t) &= \int_0^\infty \hat{a}(\omega) e^{i\omega t} d\omega && \text{(A.1)} \\ &= \int_{-\infty}^\infty H(\omega)\, \hat{a}(\omega) e^{i\omega t} d\omega = \mathbb{F}^{-1}\left(H(\omega)\hat{a}(\omega)\right) && \text{(A.2)} \end{aligned}$$

where $H(\omega)$ is the Heaviside step function. Each measurement performed can be thought of as a combined measurement on all of the infinite electromagnetic oscillators defining each frequency component of the electromagnetic field being detected.

The time domain annihilation operator $a(t)$ has properties similar to its frequency domain counterpart. It satisfies the Boson commutation relation

$$[a^\dagger(t), a(t)] = 1, \tag{A.3}$$

and analogous amplitude and phase quadrature operators can be defined

$$\begin{aligned} X^+(t) &= a^\dagger(t) + a(t) = \int_0^\infty \hat{a}^\dagger(\omega) e^{-i\omega t} d\omega + \int_0^\infty \hat{a}(\omega) e^{i\omega t} d\omega && \text{(A.4)} \\ X^-(t) &= i\left(a^\dagger(t) - a(t)\right) = i\int_0^\infty \hat{a}^\dagger(\omega) e^{-i\omega t} d\omega - i\int_0^\infty \hat{a}(\omega) e^{i\omega t} d\omega. && \text{(A.5)} \end{aligned}$$

It is then relatively easy to show that for $\omega > 0$

$$\mathbb{F}\left(X^\pm(t)\right) = \hat{X}^\pm(\omega), \tag{A.6}$$

so that the frequency domain quadrature operators can be obtained from measurements in the time domain.

A.1.1 Annihilation operators in a rotating frame

In an experimental situation we usually have an intense laser beam at frequency $\Omega \approx 10^{14}$ Hz. The fastest detectors presently available can resolve frequencies as high as 10^{10} Hz; but this is still four orders of magnitude smaller than our laser frequency. We therefore cannot distinguish time domain fluctuations in the frequency regime of interest, and require other less direct methods to measure the properties of the electromagnetic oscillators in this system. One such method, and the one used throughout this thesis, is to detect the laser field on a photodiode and analyse the Fourier components of the resulting photocurrent. This mixes the fluctuations of the field down by the laser frequency, shifting fluctuations at frequencies close to the laser carrier frequency into an observable frequency range.

A typical laser field has a very narrow linewidth $\delta\nu$, with the power within that linewidth of its peak frequency Ω being much larger than the power in the same linewidth around any other frequency

$$\int_{\Omega-\delta\nu}^{\Omega+\delta\nu} \left\langle \hat{a}^{\dagger}(\omega)\hat{a}(\omega)\right\rangle d\omega \gg \int_{\Omega'-\delta\nu}^{\Omega'+\delta\nu} \left\langle a^{\dagger}(\omega)\hat{a}(\omega)\right\rangle d\omega \tag{A.7}$$

for all $\Omega' < \Omega-\delta\nu$ and $\Omega' > \Omega+\delta\nu$. Therefore only the field amplitude inside the laser linewidth and fluctuations that beat with it will be observed on detection. Let us, therefore, transform our analysis to the rotating frame of the light field, $\tilde{a}_{\mathrm{rotate}}(t) = a(t)e^{-i\Omega t}$, $\omega \rightarrow \omega + \Omega$, Eq. (A.2) can then be written

$$\tilde{a}_{\mathrm{rotate}}(t) = \int_{-\infty}^{\infty} H(\Omega+\omega)\hat{a}_{\Omega+\omega}(\omega)e^{i\omega t}d\omega, \tag{A.8}$$

where $\hat{a}_{\Omega+\omega}(\omega)$ is the annihilation operator for the electromagnetic oscillator at frequency $\Omega+\omega$, which in this frame rotating at Ω appears at frequency ω. $\tilde{a}_{\mathrm{rotate}}(t)$ satisfies the Boson commutation relation, and results in rotating time domain quadrature operators defined in an identical manner to those in Eqs. (A.4) and (A.5). We can obtain the rotating frequency domain annihilation operator by taking the Fourier transform of $\tilde{a}_{\mathrm{rotate}}(t)$

$$\hat{a}_{\mathrm{rotate}}(\omega) = \mathbb{F}\Big(\delta\tilde{a}_{\mathrm{rotate}}(t)\Big) = H(\Omega+\omega)\hat{a}_{\Omega+\omega}(\omega). \tag{A.9}$$

The rotating frequency domain quadrature operators at frequency $\omega > -\Omega$ can then be directly related to the quadrature operators of the electromagnetic oscillator at frequency $\Omega+\omega$, and can be obtained from the Fourier transform of the relevant rotating time domain quadrature operator

$$\hat{X}^{\pm}_{\mathrm{rotate}}(\omega) = \mathbb{F}\left(\tilde{X}^{\pm}_{\mathrm{rotate}}(t)\right) = \hat{X}^{\pm}_{\Omega+\omega}(\omega). \tag{A.10}$$

A.2 Detection of an optical field

We have just seen how the quadrature operators of individual electromagnetic oscillators can be extracted from the respective time domain quadrature operators. We will now look at how these operators can be observed in an experiment.

The linewidth of a typical laser is usually much smaller than its oscillation frequency $\delta\nu \ll \Omega$. In our case $\delta\nu \approx \Omega/10^{11}$, and is approximately 5000 times smaller than the frequencies where measurements were taken for this thesis. The large coherent amplitude of the laser typically obscures the quantum fluctuations of electromagnetic oscillators within its linewidth. We therefore concentrate on the quantum fluctuations at $\omega > \delta\nu$. In this case it is reasonable to neglect the quantum fluctuations within the laser linewidth; and to approximate the laser as a mono-chromatic field at frequency Ω with coherent amplitude $\alpha(t)$. Eq. (A.8) then becomes

$$\begin{aligned}\tilde{a}_{\mathrm{rotate}}(t) &= \int_{-\delta\nu}^{\delta\nu} \hat{a}_{\Omega+\omega}(\omega)e^{i\omega t}d\omega \qquad \text{(A.11)}\\ &\quad + \int_{-\infty}^{\infty}\left[H(-\omega-\delta\nu)+H(\omega-\delta\nu)\right]H(\Omega+\omega)\hat{a}_{\Omega+\omega}(\omega)e^{i\omega t}d\omega\\ &= \alpha(t)+\int_{-\infty}^{\infty}\left[H(-\omega-\delta\nu)+H(\omega-\delta\nu)\right]H(\Omega+\omega)\hat{a}_{\Omega+\omega}(\omega)e^{i\omega t}d\omega. \qquad \text{(A.12)}\end{aligned}$$

We define the coherent amplitude of the laser $\alpha(t)$ to be real and positive here, without loss of generality.

Let us now consider the result of photodetection of $\tilde{a}_{\mathrm{rotate}}(t)$. The photodetection process is described by the photoelectric effect, with electrons being liberated from a material when it is subjected to a radiant field. Within the bandwidth B of the detectors, the photocurrent produced is directly proportional to the number of photons in the field

$$i(t) = g_D\tilde{n}(t) = g_D\tilde{a}^\dagger(t)\tilde{a}(t), \qquad \text{(A.13)}$$

where g_D is the gain of the detection process. Given that $B < \Omega$, detection of the field given in Eq. (A.12) would therefore result in the photocurrent

$$\begin{aligned}i(t) &= g_D\tilde{a}^\dagger_{\mathrm{rotate}}(t)\tilde{a}_{\mathrm{rotate}}(t) \qquad \text{(A.14)}\\ &= g_D\Big(\alpha(t)+\int_{-B}^{B}\left[H(-\omega-\delta\nu)+H(\omega-\delta\nu)\right]\hat{a}_{\Omega+\omega}(\omega)e^{i\omega t}d\omega\Big)^\dagger \times\\ &\qquad \Big(\alpha(t)+\int_{-B}^{B}\left[H(-\omega-\delta\nu)+H(\omega-\delta\nu)\right]\hat{a}_{\Omega+\omega}(\omega)e^{i\omega t}d\omega\Big) \qquad \text{(A.15)}\\ &= g_D\alpha(t)^2 + \qquad \text{(A.16)}\\ &\qquad g_D\alpha(t)\int_{-B}^{B}\left[H(-\omega-\delta\nu)+H(\omega-\delta\nu)\right]\left(\hat{a}_{\Omega+\omega}(\omega)e^{i\omega t}+\hat{a}^\dagger_{\Omega+\omega}(\omega)e^{-i\omega t}\right)d\omega.\end{aligned}$$

Here, since the power within the laser linewidth of its peak frequency Ω is much larger than the power in the same linewidth around any other frequency (see Eq. (A.7)), we have neglected all terms that do not contain $\alpha(t)$. This process is termed the *linearisation approximation*. Since the optical beams used for the majority of the work presented in this thesis were bright, it is valid throughout, with the exception of Chapter 9 where experiments were performed involving single photon Fock states. Detailed discussions of the linearisation approximation may be found in the theses of Ping Koy Lam [75] and Ben Buchler [76].

Let us now take the Fourier transform of the detected photocurrent given in Eq. (A.16), at frequencies above the laser linewidth and below the bandwidth of our detectors it is given by

$$\begin{aligned}i(\omega) &= \mathbb{F}(\delta i(t)) \qquad \text{(A.17)}\\ &= g_D\alpha(t)\left[\mathbb{F}\left(\int_{-B}^{B}\hat{a}_{\Omega+\omega}(\omega)e^{i\omega t}d\omega\right)+\mathbb{F}\left(\int_{-B}^{B}\hat{a}^\dagger_{\Omega+\omega}(\omega)e^{-i\omega t}d\omega\right)\right] \qquad \text{(A.18)}\\ &= g_D\alpha(t)\left[\hat{a}^\dagger_{\Omega-\omega}(\omega)+\hat{a}_{\Omega+\omega}(\omega)\right] \qquad \text{(A.19)}\\ &= g_D\alpha(t)\hat{X}^+_{\Omega+\omega}(\omega), \qquad \text{(A.20)}\end{aligned}$$

So we see that the component of the Fourier transform of the detected photocurrent at frequency

ω yields the amplitude quadrature of the electromagnetic oscillator at frequency ω. Of course, the current $i(\omega)$ contains components at both positive and negative frequencies. In practise we do not distinguish between the components at frequencies $\pm\omega$ and rather analyse the current

$$I(\omega) = i(\omega) + i(-\omega) = g_D \alpha(t) \left(\hat{X}^+_{\Omega+\omega}(\omega) + \hat{X}^+_{\Omega-\omega}(-\omega) \right). \tag{A.21}$$

It is then clear that we are performing a joint measurement on electromagnetic oscillators at frequencies $\pm\omega$. The annihilation operator associated to this measurement $\hat{a}_{\text{sideband}}(\omega)$, which we term the *sideband annihilation operator*, is given by

$$\hat{a}_{\text{sideband}}(\omega) = \frac{1}{\sqrt{2}} \left(\hat{a}_{\Omega-\omega}(-\omega) + \hat{a}_{\Omega+\omega}(\omega) \right), \tag{A.22}$$

where we have introduced the factor of $1/\sqrt{2}$ to retain the Boson commutation relation.

A.3 System time delays and the sideband operator

In the previous analysis we showed that the sideband annihilation operator under interrogation in our experiments is given by the sum of the annihilation operators at frequencies $\Omega \pm \omega$, and can be obtained from the Fourier transform of the rotating time domain annihilation operator. To analyse a typical system we propagate the rotating time domain field annihilation operator through the system, using the linearisation approximation where necessary, and after detection perform a Fourier transform to yield the relevant frequency domain operator. However, in this case, we do not have access to $\tilde{a}_{\text{rotate}}(t)$, but rather $\tilde{a}_{\text{rotate}}(t+\delta t(\omega))$, where $\delta t(\omega)$ is the time delay associated with propagation through the system and is, in general, a function of ω. This time delay rotates the phase of each of the electromagnetic oscillators comprising the field by $\phi(\omega) = \omega \delta t(\omega)$. This phase shift must be taken into account when calculating $\hat{a}_{\text{sideband}}(\omega)$[1]. It is relatively easy to show that

$$\hat{a}_{\text{rotate}}(\omega) = e^{-i\phi(\omega)} \mathbb{F} \left(\delta \tilde{a}_{\text{rotate}}(t + \delta t(\omega)) \right). \tag{A.23}$$

Assuming that $\phi(-\omega) = -\phi(\omega)$, which is valid for the situations considered in this thesis, we then see that

$$\hat{a}_{\text{sideband}}(\omega) = e^{-i\phi(\omega)} \mathbb{F} \left(\delta \tilde{a}_{\text{sideband}}(t + \delta t(\omega)) \right), \tag{A.24}$$

where the phase delay $\phi(\omega)$ is given by

$$e^{-i\phi(\omega)} = \sqrt{\frac{\mathbb{F}^\dagger \big(\tilde{a}_{\text{rotate}}(t + \delta t(\omega)) \big)}{\mathbb{F} \big(\tilde{a}^\dagger_{\text{rotate}}(t + \delta t(\omega)) \big)}}. \tag{A.25}$$

Note that we are ultimately only interested in the variances of the appropriate sideband quadrature operators. These variances are independent of $\phi(\omega)$, so that an explicit calculation or measurement of $\phi(\omega)$ is not required. Throughout this thesis we have, as is convention, neglected to explicitly include the $\phi(\omega)$ term.

---

[1] If it is not taken into account the rotating frequency domain quadrature operators become complex. Since they are defined as $\hat{X}^+_{\text{sideband}}(\omega) = \hat{a}_{\text{sideband}}(\omega) + \hat{a}^\dagger_{\text{sideband}}(\omega)$ and $\hat{X}^-_{\text{sideband}}(\omega) = i(\hat{a}^\dagger_{\text{sideband}}(\omega) - \hat{a}_{\text{sideband}}(\omega))$ which are necessarily real, this poses a contradiction.

In the above we have shown that even though our detectors have a bandwidth smaller than the frequency of the electromagnetic oscillators we are interrogating, our detection technique can provide measurements on the amplitude quadrature of a valid annihilation operator $\hat{a}_{\rm sideband}(\omega)$. This operator can be related to the annihilation operators of a pair of electromagnetic oscillators at frequencies ω away from the laser frequency. This pair of operators can be thought of as sidebands on either side of the carrier, and henceforth we term this composite system the *sideband picture*. We have shown also that $\hat{a}_{\rm sideband}(\omega)$ can be obtained from the Fourier transform of the rotating time domain annihilation operator.

Electronic circuits

B.1 Detector circuits

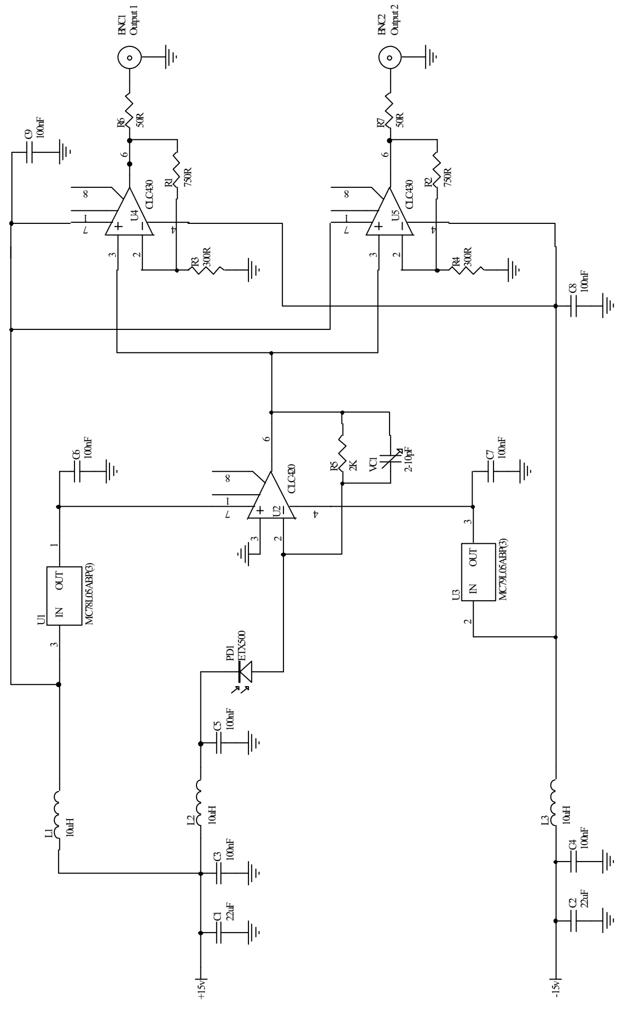

Figure B.1: Typical low noise, high quantum efficiency RF detector circuit. Original design: Malcolm Gray, Artwork: Russell Koehne. Note that this schematic is only an example of the detectors we used to detect quadrature fluctuations. Each circuit was typically modified to be optimised for the level of power available, the frequency of interest, and the sensitivity of the application to detector darknoise.

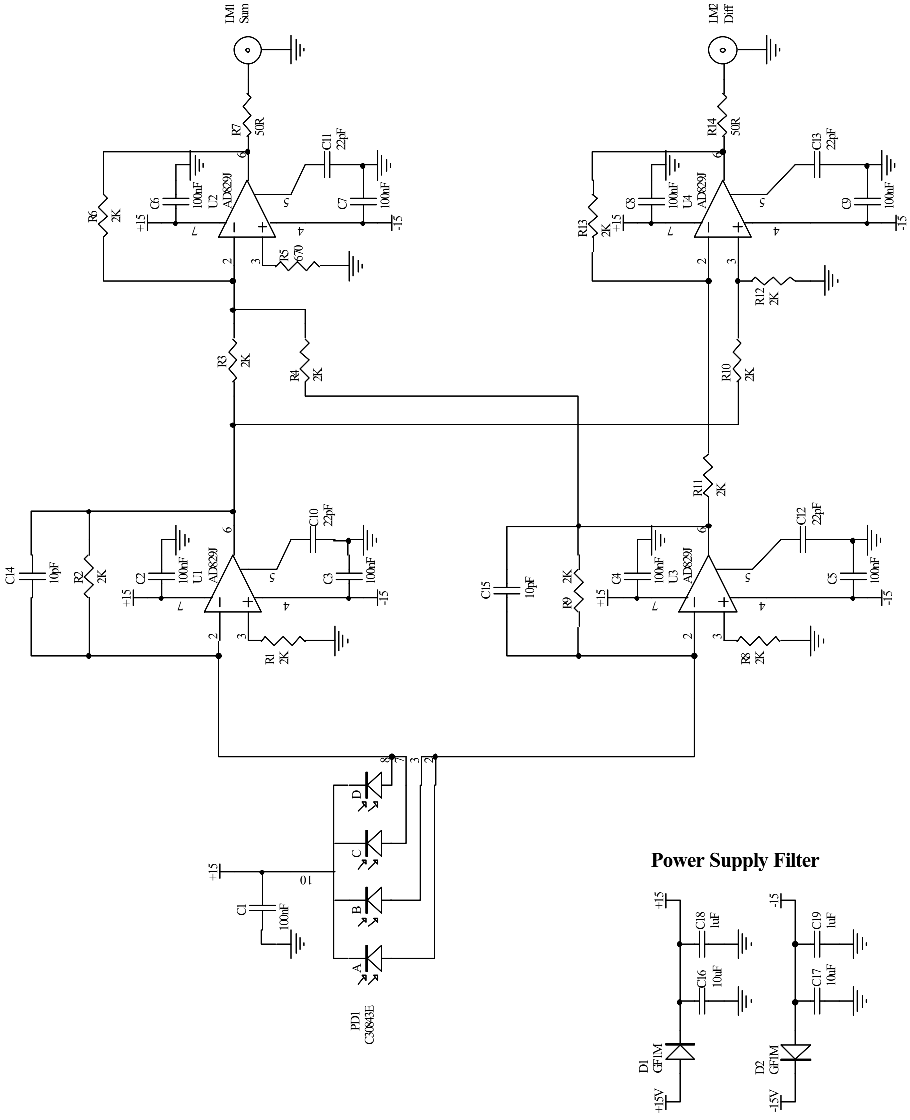

Figure B.2: Tilt detector circuit. Original design: Malcolm Gray, Artwork: Russell Koehne.

B.2 High voltage amplifier circuit

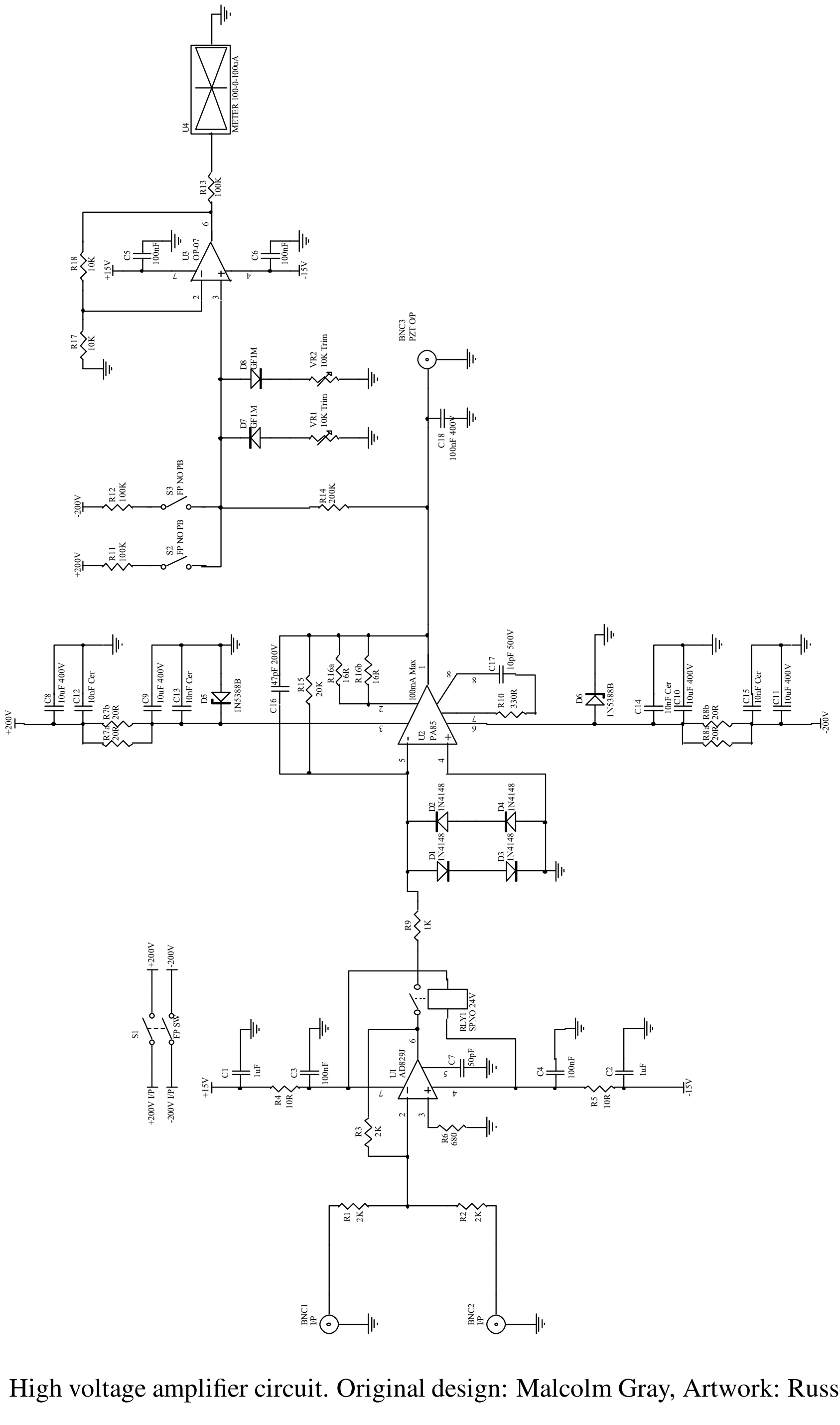

Figure B.3: High voltage amplifier circuit. Original design: Malcolm Gray, Artwork: Russell Koehne.

B.3 Servo circuits

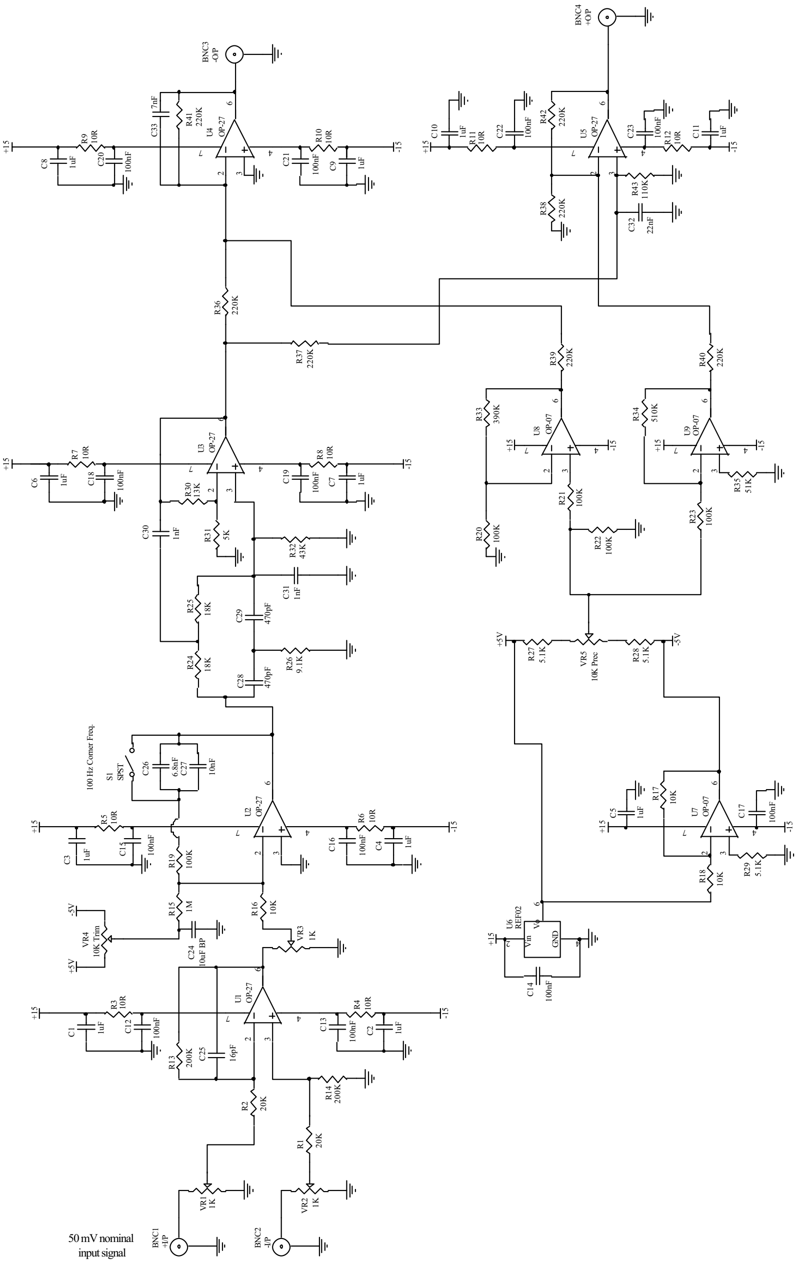

Figure B.4: Typical Piezo servo circuit. Original design: Malcolm Gray, Artwork: Russell Koehne. Note that the exact design of the Piezo servos used in the experiments reported in this thesis, although all based on the design reporduced here, varied from servo to servo.

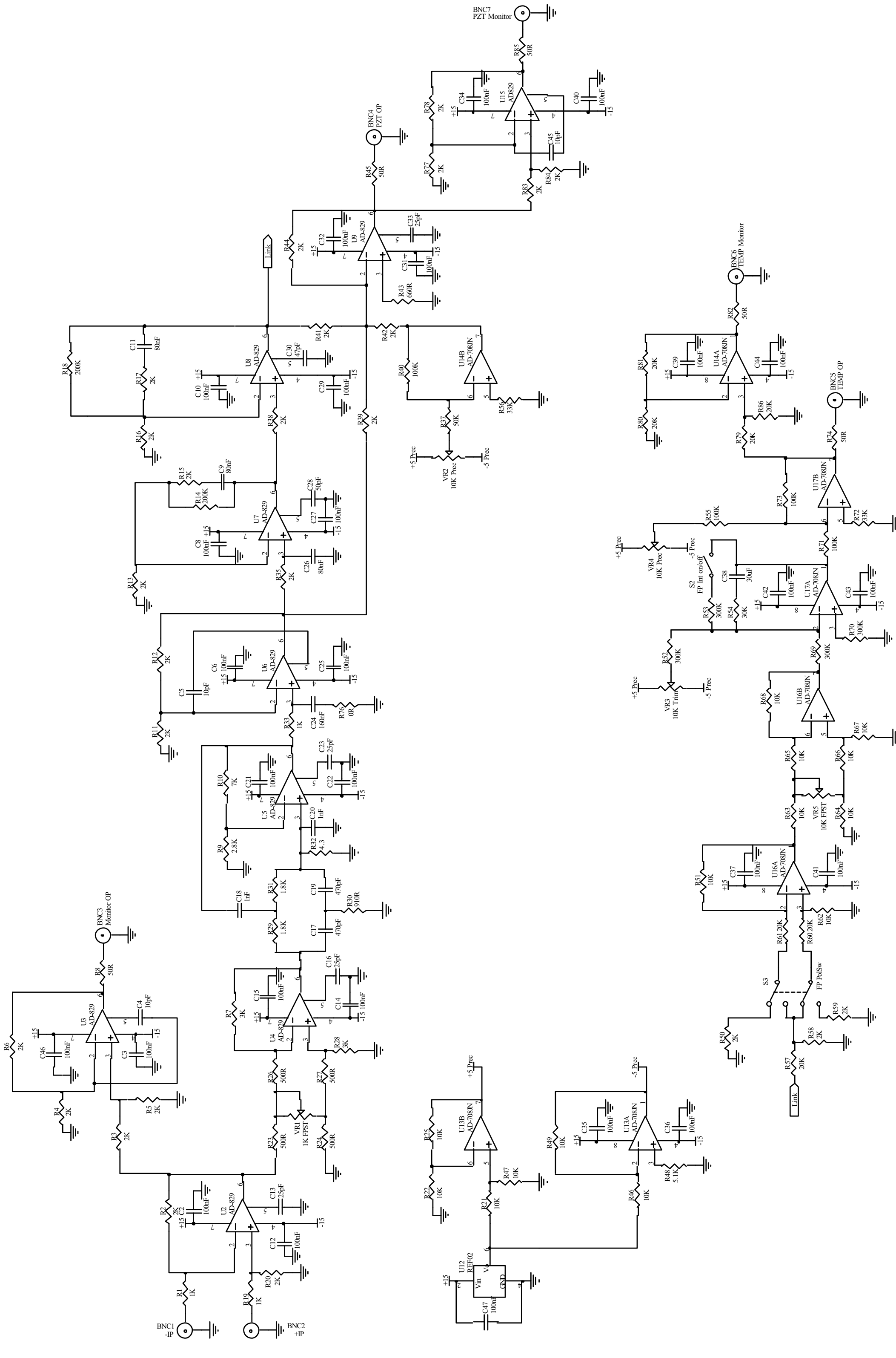

Figure B.5: Laser controlling servo circuit. Original design: Malcolm Gray, Artwork: Russell Koehne.

B.4 Temperature controller circuits

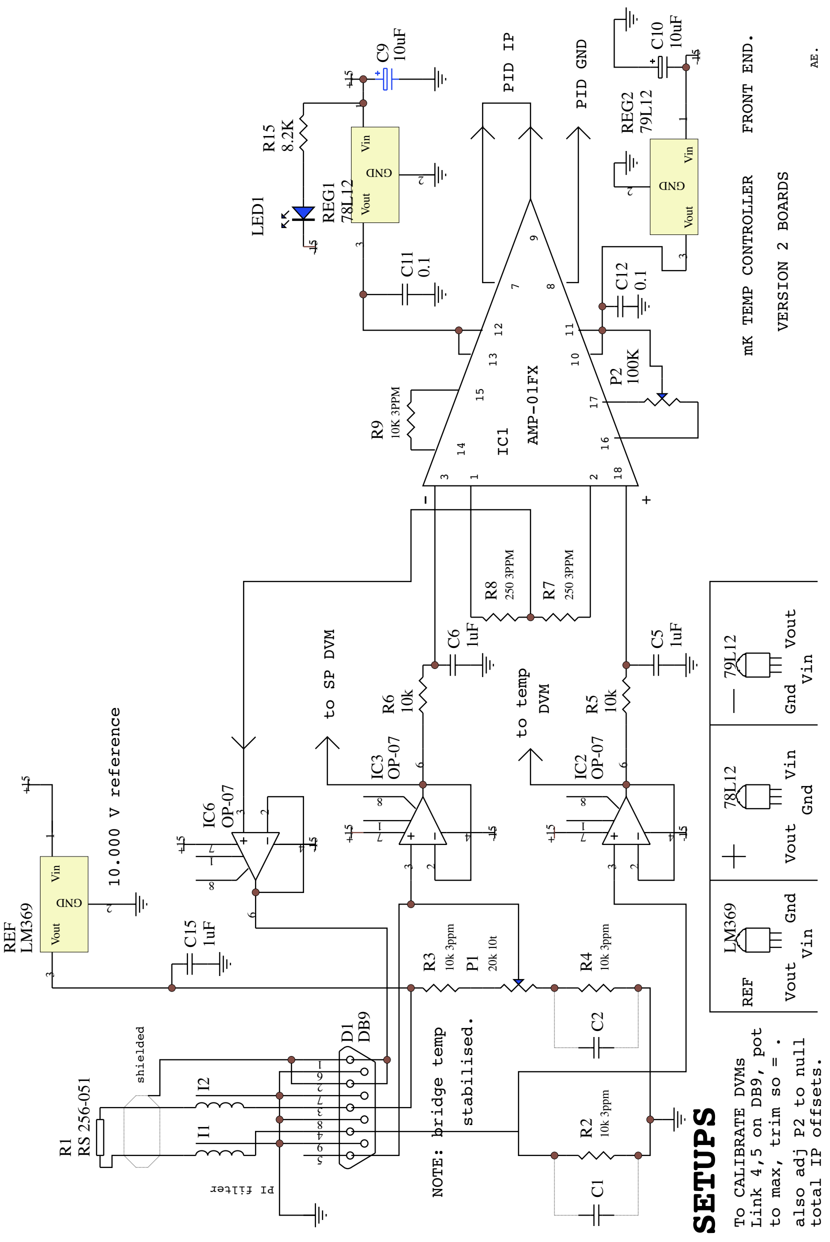

Figure B.6: Front end interface of home built milli-Kelvin temperature controller. Original design: Matthew Taubman. Modified: Andrew White and Ping Koy Lam, Artwork: Russell Koehne.

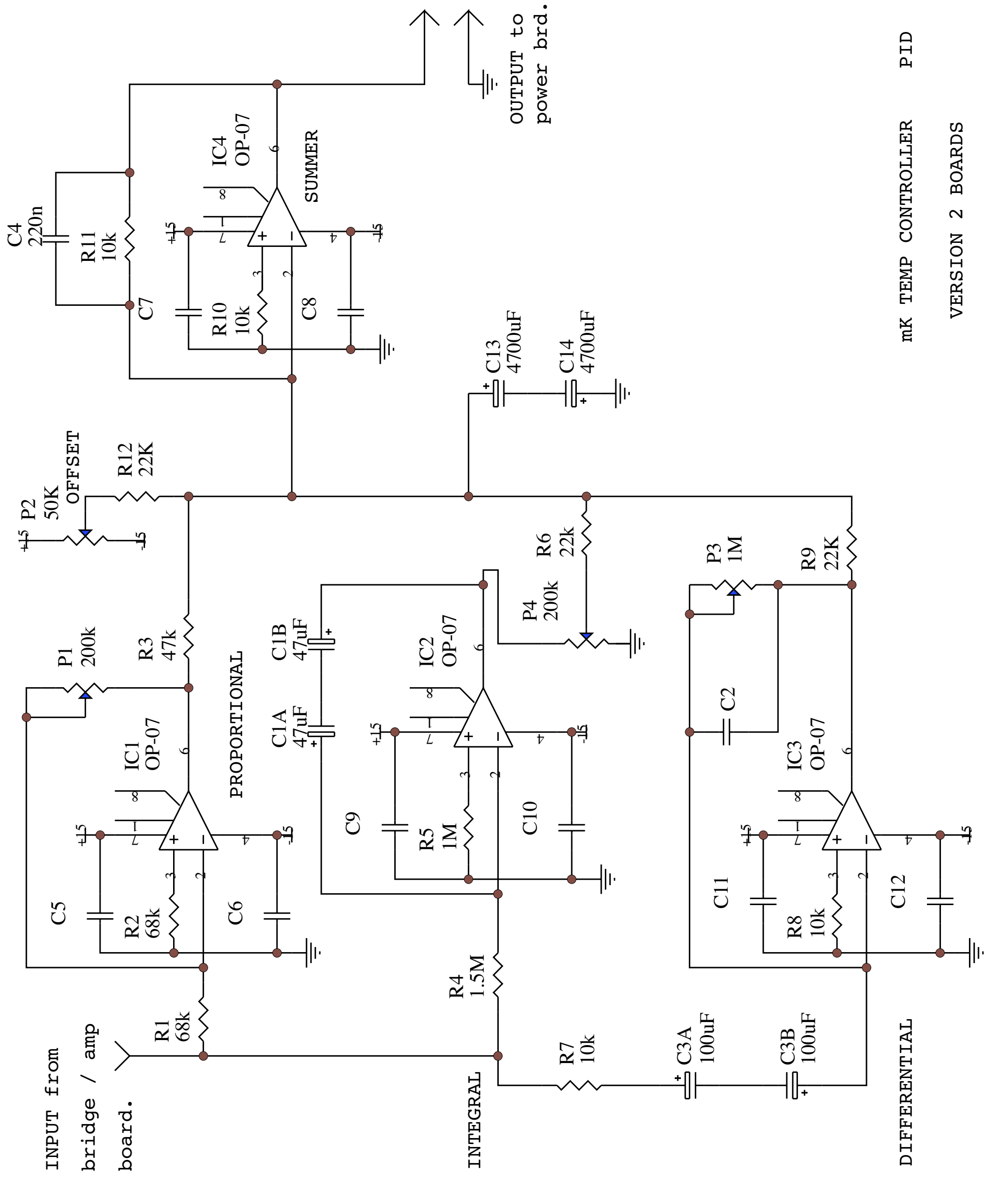

Figure B.7: Servo circuit of home built milli-Kelvin temperature controller. Original design: Matthew Taubman. Modified: Andrew White and Ping Koy Lam, Artwork: Russell Koehne.

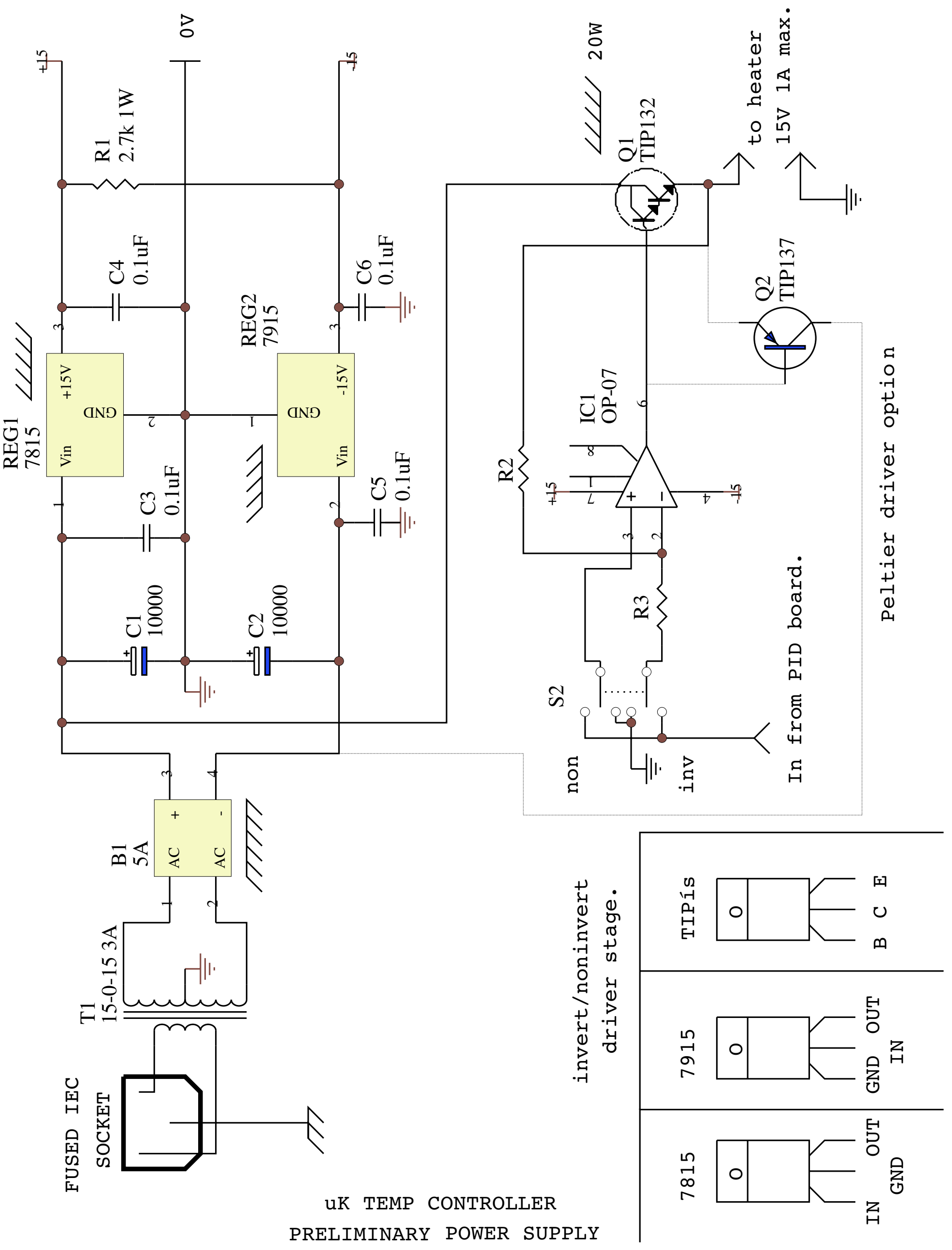

Figure B.8: Power supply of home built milli-Kelvin temperature controller. Original design: Matthew Taubman. Modified: Andrew White and Ping Koy Lam, Artwork: Russell Koehne.

Appendix C

Sundry equipment and mechanical components

Component	Manufacturer	Part number	Notes
Sundry			
Optical table	Newport	RS2000-410-12	1.2×3×0.3 m
Optical table isolation legs	Newport	I-2000-N19.5	N/A
Spectrum analyser	Hewlett Packard	E4405B	N/A
Power meter	Newport	840-C	N/A
Hemilithic MgO:LiNbO$_3$ crystal	N/A	PMS Optik	5×7.5×2.5 mm
Crystal ovens	ANU Physics	N/A	N/A
Opto-electronic devices			
532 nm optical isolator	Linos photonics	501013202	40 dB iso.
1064 nm optical isolator	Gsänger	FR 1060/5	40 dB iso.
Phase modulators	Gsänger	LM0202-PHAS	N/A
Amplitude modulators	Gsänger	LM0202 P 5W IR	N/A
Optical mounts			
Flipper mirror mounts	New Focus	9891M	1 inch
Flip-up mirror mounts	New Focus	9897M	1 inch
Corner mounts	New Focus	9809M	1 inch
Optics mounts	New Focus	9807M	1 inch
Kinematic Stages	New Focus	9081M	N/A
Optics mounts	Radiant Dyes	RD2-L-3025	1 inch
Lees Optics mounts	Linos	LM2	1 inch
XY mounts	OWIS GmbH	14.202.0025	25 mm
XYZ mounts	Newport	M-LP-1-XYZ	1 inch
Misc. optical stands	ANU Physics	N/A	height 7.5 mm
Basic mounts	Thorlabs	FMP100	1 inch
Kinematic Platforms	Thorlabs	KM1-B/M	N/A
Prism mounts	Thorlabs	PM1/M	N/A
Rotation mounts	Thorlabs	RSP1/M	1 inch
Detectors			
High efficiency photodiodes	Epitaxx	ETX500	N/A
Quadrant detectors	ANU Physics	N/A	InGaAs
RF detectors	ANU Physics	CLC420/430	InGaAs
Monitor detectors	ANU Physics	N/A	Silicon

Electronic items			
2 MHz HP filters	Dunestar	400-HPF	N/A
Variable attenuators	RLC electronics	LAV-50-B	N/A
Low-pass filters	Mini-circuits	BLP-1.9,5, . . .	N/A
High-pass filters	Mini-circuits	BHP-25,50, . . .	N/A
Fixed attenuators	Mini-circuits	CAT-1,3, . . .	N/A
Low noise amplifiers	Mini-circuits	ZFL-500	N/A
High power amplifiers	Mini-circuits	ZHL-1A	N/A
Biased tees	Mini-circuits	ZFBT-4R2GW	25 dB iso.
Power splitters	Mini-circuits	ZSC-2-1	N/A
Mixers	Mini-circuits	ZP-1	N/A
Hybrid junctions	M/A-COM	HH-106	2-200 MHz
PZTs	Piezomechanik	500/10-5/5	80 kHz res. freq.
PZTs	Piezomechanik	500/15-8/5	80 kHz res. freq.
Power Supplies	Hewlett-Packard	E3612A	120 V/0.25 A
Signal generators	Hewlett-Packard	HP 8656A	N/A
Signal generators	SRS	DS345	N/A
HV amps	ANU Physics	N/A	MK III
Servos	ANU Physics	N/A	MK III
Biased tees	ANU Physics	N/A	$f_{3\mathrm{dB}} \sim 500$ kHz

Table C.1: Sundry equipment used for the experiments of this thesis.

Bibliography

[1] M. Xiao, L.-A. Wu, and H. J. Kimble, *Precision measurement beyond the shot-noise limit*, Phys. Rev. Lett. **59**, 278 (1987).

[2] E. S. Polzik, J. Carri, and H. J. Kimble, *Atomic spectroscopy with squeezed light for sensitivity beyond the vacuum-state limit*, Appl. Phys. B **55**, 279 (1992).

[3] N. Treps, U. Andersen, B. C. Buchler, P. K. Lam, A. Maître, H.-A. Bachor, and C. Fabre, *Surpassing the standard quantum limit for optical imaging using nonclassical multimode light*, Phys. Rev. Lett. **88**, 203601 (2002).

[4] A. N. Boto, P. Kok, D. S. Abrams, S. L. Braunstein, C. P. Williams, and J. P. Dowling, *Quantum interferometric optical lithography: exploiting entanglement to beat the diffraction limit*, Phys. Rev. Lett. **85**, 2733 (2000).

[5] I. L. Chuang and M. A. Nielsen, *Quantum information and quantum computation.*, Cambridge University Press, Cambridge, U.K., 2000.

[6] C. Fabre, J. B. Fouet, and A. Maître, *Quantum limits in the measurement of very small displacements in optical images*, Opt. Lett. **25**, 76 (1999).

[7] P. W. Shor, Algorithms for quantum computation: discrete logarithms and factoring, in *Proceedings of the 35th annual symposium on foundations of computer science*, page 124, IEEE Computer Society Press, New York, 1994.

[8] L. K. Grover, *Quantum mechanics helps in searching for a needle in a haystack*, Phys. Rev. Lett. **79**, 325 (1997).

[9] J. I. Cirac, P. Zoller, H. J. Kimble, and H. Mabuchi, *Quantum state transfer and entanglement distribution among distant nodes in a quantum network*, Phys. Rev. Lett. **78**, 3221 (1997).

[10] D. P. DiVincenzo, *Quantum computation*, Science **270**, 255 (1995).

[11] A. Kuzmich, K. Mølmer, and E. S. Polzik, *Spin squeezing in an ensemble of atoms illuminated with squeezed light*, Phys. Rev. Lett. **79**, 4782 (1997).

[12] M. D. Lukin, *Trapping and manipulating photon states in atomic ensembles*, Rev. Mod. Phys. **75**, 457 (2003).

[13] J. Hald and E. S. Polzik, *Mapping a quantum state of light onto atoms*, J. Opt. B **3**, S83 (2001).

[14] C. M. Caves, *Quantum-mechanical noise in an interferometer*, Phys. Rev. D. **23**, 1693 (1981).

[15] S. L. Braunstein and A. K. Pati, *Quantum Information with Continuous Variables*, Kluwer Academic Publishers, Dordrecht, 2003.

[16] A. Einstein, B. Podolsky, and N. Rosen, *Can quantum-mechanical description of physical reality be considered complete?*, Phys. Rev. **47**, 777 (1935).

[17] E. Knill, R. Laflamme, and G. Milburn, *A scheme for efficient quantum computation with linear optics*, Nature **409**, 46 (2001).

[18] R. E. S. Polkinghorne and T. C. Ralph, *Continuous variable entanglement swapping*, Phys. Rev. Lett. **83**, 2095 (1999).

[19] R. Cleve, D. Gottesman, and H.-K. Lo, *How to share a quantum secret*, Phys. Rev. Lett. **83**, 648 (1999).

[20] J. Hald, J. L. Sørensen, C. Schori, and E. S. Polzik, *Spin squeezed atoms: a macroscopic entangled ensemble created by light*, Phys. Rev. Lett. **83**, 1319 (1999).

[21] L.-M. Duan, M. Lukin, J. I. Cirac, and P. Zoller, *Long-distance quantum communication with atomic ensembles and linear optics*, Nature **414**, 413 (2001).

[22] G. Jaeger and A. V. Sergienko, *Multi-photon quantum interferometry*, in E. Wolf, 'Progress in Optics' Elsevier Science B.V. **42**, 277 (2001).

[23] N. Treps, N. B. Grosse, W. P. Bowen, C. Fabre, H.-A. Bachor, and P. K. Lam, *A quantum laser pointer*, Science **301**, 940 (2003).

[24] N. Treps, N. B. Grosse, W. P. Bowen, M. T. L. Hsu, A. Maître, C. Fabre, H.-A. Bachor, and P. K. Lam, *Nano-displacement measurements using spatially multimode squeezed light*, Submitted J. Opt. B., available online: http://arXiv.org/abs/quant-ph/0311122 (2003).

[25] T. Symul, W. P. Bowen, R. Schnabel, N. Treps, B. C. Buchler, T. C. Ralph, A. M. Lance, N. B. Grosse, A. Dolińskà, J. W. Wu, J. R. Gao, C. Fabre, H.-A. Bachor, and P. K. Lam, Optical squeezing in temporal, polarization and spatial domains, in *Proceedings of the SPIE conference on fluctuations and noise in photonics and quantum optics, no. 5111*, 2003.

[26] M. J. Lawrence, W. P. Bowen, H.-A. Bachor, R. L. Byer, and M. M. Fejer, *Squeezed singly resonant second harmonic generation in periodically poled Lithium Niobate*, J. Opt. Soc. Am. B **19**, 1592 (2002).

[27] W. P. Bowen, R. Schnabel, N. Treps, H.-A. Bachor, and P. K. Lam, *Recovery of continuous wave squeezing squeezing at low frequencies*, J. Opt. B. **4**, 421 (2002).

[28] D. A. Shaddock, B. C. Buchler, W. P. Bowen, M. B. Gray, and P. K. Lam, *Modulation-free control of a continuous-wave second-harmonic generator*, J. Opt. A **2**, 400 (2000).

[29] H.-A. Bachor, P. K. Lam, W. P. Bowen, R. Schnabel, S. Bennetts, B. C. Buchler, and T. C. Ralph, Optical quantum information processing: experiments with CW laser light, in *Proceedings of the 1st International Conference on Experimental Implementation of Quantum Computation*, page 220, 2001.

[30] W. P. Bowen, P. K. Lam, and T. C. Ralph, *Biased EPR entanglement and its application to teleportation*, J. Mod. Opt. **50**, 801 (2003).

[31] W. P. Bowen, R. Schnabel, P. K. Lam, and T. C. Ralph, *A characterization of continuous variable entanglement*, Phys. Rev. A. **69**, 012304 (2004).

[32] W. P. Bowen, N. Treps, B. C. Buchler, R. Schnabel, T. C. Ralph, T. Symul, and P. K. Lam, *Unity and non-unity gain quantum teleportation*, IEEE J.S.T.Q.E. **9**, 1519 (2003).

[33] W. P. Bowen, N. Treps, R. Schnabel, T. C. Ralph, and P. K. Lam, *Continuous variable polarization entanglement, experiment and analysis*, J. Opt. B. **5**, S467 (2003).

[34] A. Doliǹskà, B. C. Buchler, W. P. Bowen, T. C. Ralph, and P. K. Lam, *Teleportation of continuous variable polarization states*, Phys. Rev. A **68**, 052308 (2003).

[35] P. K. Lam, W. P. Bowen, and T. C. Ralph, *Quantum teleportation with Einstein-Podolsky-Rosen optical entanglement*, The Physicist **39**, 72 (2002).

[36] R. Schnabel, W. P. Bowen, N. Treps, H.-A. Bachor, and P. K. Lam, *Stokes operator squeezed continuous variable polarization states*, Phys. Rev. A. **67**, 012316 (2003).

[37] R. Schnabel, W. P. Bowen, N. Treps, B. C. Buchler, T. C. Ralph, P. K. Lam, and H.-A. Bachor, *Optical experiments beyond the quantum limit: squeezing, entanglement, and teleportation*, Optics and Spectroscopy **94**, 711 (2002).

[38] A. Lance, T. Symul, W. P. Bowen, B. C. Sanders, and P. K. Lam, *Sharing a secret quantum state*, Submitted Phys. Rev. Lett., available online: http://arXiv.org/abs/quant-ph/0311015 (2003).

[39] E. Schrödinger, *Der stetige übergang von der mikro- zur makromechanik*, Naturwissenschaften **14**, 664 (1926).

[40] T. H. Maiman, *Stimulated optical radiation in Ruby masers*, Nature **187**, 493 (1960).

[41] R. J. Glauber, *The quantum theory of optical coherence*, Phys. Rev. **130**, 2529 (1963).

[42] W. H. Louisell, A. Yariv, and A. E. Siegman, *Quantum fluctuations and noise in parametric processes. I*, Phys. Rev. **124**, 1646 (1961).

[43] H. Takahasi, *Advances in communication systems*, volume 1, edited by A. Balakrishnan, Academic Press, New York, 1965.

[44] D. Stoler, *Equivalence classes of minimum uncertainty packets*, Phys. Rev. D. **1**, 3217 (1970).

[45] D. Stoler, *Equivalence classes of minimum-uncertainty packets. II*, Phys. Rev. D. **4**, 1925 (1971).

[46] H. P. Yuen, *Two-photon coherent states of the radiation field*, Phys. Rev. A. **13**, 2226 (1976).

[47] R. E. Slusher, L. W. Hollberg, B. Yurke, J. C. Mertz, and J. F. Valley, *Observation of squeezed states generated by four-wave mixing in an optical Cavity*, Phys. Rev. Lett. **55**, 2409 (1985).

[48] R. E. Slusher, B. Yurke, Ph. Grangier, A. LaPorta, D. F. Walls, and M. Reid, *Squeezed-light generation by four-wave mixing near an atomic resonance*, J. Opt. Soc. Am. B. **4**, 1453 (1987).

[49] M. E. Anderson, D. F. McAlister, M. G. Raymer, and M. C. Gupta, *Pulsed squeezed-light generation in $\chi^{(2)}$ nonlinear media*, J. Opt. Soc. Am. B. **14**, 3180 (1997).

[50] R. M. Shelby, M. D. Levenson, S. H. Perlmutter, R. G. DeVoe, and D. F. Walls, *Broadband parametric deamplification of quantum noise in an optical fiber*, Phys. Rev. Lett. **57**, 691694 (1986).

[51] L.-A. Wu, H. J. Kimble, J. L. Hall, and H. Wu, *Generation of squeezed states by parametric down conversion*, Phys. Rev. Lett. **57**, 2520 (1986).

[52] L.-A. Wu, M. Xiao, and H. J. Kimble, *Squeezed states of light from an optical parametric oscillator*, J. Opt. Soc. Am. B. **4**, 1465 (1987).

[53] K. Schneider, R. Bruckmeier, H. Hansen, S. Schiller, and J. Mlynek, *Bright squeezed-light generation by a continuous-wave semimonolithic parametric amplifier*, Opt. Lett. **21**, 1396 (1996).

[54] S. F. Pereira, M. Xiao, H. J. Kimble, and J. L. Hall, *Generation of squeezed light by intracavity frequency doubling*, Phys. Rev. A. **38**, 4931 (1988).

[55] R. Movshovich, B. Yurke, P. G. Kaminsky, A. D. Smith, A. H. Silver, R. W. Simon, and M. V. Schneider, *Observation of zero-point noise squeezing via a Josephson-parametric amplifier*, Phys. Rev. Lett. **65**, 1419 (1990).

[56] M. Rosenbluh and R. M. Shelby, *Squeezed optical solitons*, Phys. Rev. Lett. **66**, 153156 (1991).

[57] R. M. Shelby and M. Rosenbluh, *Generation of pulsed squeezed light in a mode-locked optical parametric oscillator*, Appl. Phys. B. **55**, 226 (1992).

[58] A. M. Fox, J. J. Baumberg, M. Dabbicco, B. Huttner, and J. F. Ryan, *Squeezed light generation in semiconductors*, Phys. Rev. Lett. **74**, 1728 (1995).

[59] M. E. Anderson, M. Beck, M. G. Raymer, and J. D. Bierlein, *Quadrature squeezing with ultrashort pulses in nonlinear-optical waveguides*, Opt. Lett. **20**, 620 (1995).

[60] D. K. Serkland, M. M. Fejer, R. L. Byer, and Y. Yamamoto, *Squeezing in a quasi-phase-matched LiNbO3 waveguide*, Opt. Lett. **20**, 1649 (1995).

[61] J. Ries, B. Brezger, and A. I. Lvovsky, *Experimental vacuum squeezing in Rubidium vapor via self-rotation*, Phys. Rev. A **68**, 025801 (2003).

[62] G. Breitenbach, T. Müller, S. F. Pereira, J. Ph. Poizat, S. Schiller, and J. Mlynek, *Squeezed vacuum from a monolithic optical parametric oscillator*, J. Opt. Soc. Am. B **12**, 2304 (1995).

[63] K. Schneider, M. Lang, J. Mlynek, and S. Schiller, *Generation of strongly squeezed continuous-wave light at 1064 nm*, Opt. Express **2**, 59 (1998).

[64] P. K. Lam, T. C. Ralph, B. C. Buchler, D. E. McClelland, H.-A. Bachor, and J. Gao, *Optimization and transfer of vacuum squeezing from an optical parametric oscillator*, J. Opt. B. **1**, 469 (1999).

[65] W. Heisenberg, *Über den anschaulichen inhalt der quantentheoretischen kinematik und mechanik*, Zeitschrift für Physik **43**, 172 (1927).

[66] J. S. Bell, *On the Einstein-Podolsky-Rosen paradox*, Physics (N.Y.) **1**, 195 (1964).

[67] L. R. Kasday, J. Ullman, and C. S. Wu, Bull. Am. Phys. Soc. **15**, 586 (1970).

[68] V. Acosta, C. L. Cowan, and B. J. Graham, *Essentials of modern physics*, Harper and Row, Singapore, first edition, 1973.

[69] D. F. Walls and G. J. Milburn, *Quantum optics*, Springer-Verlag, Berlin, 1 edition, 1995.

[70] E. P. Wigner, *On the quantum correction for thermodynamic equilibrium*, Phys. Rev. **40**, 749 (1932).

[71] U. Leonhardt, *Measuring the quantum state of light*, Cambridge university press, Cambridge, 1997.

[72] T. Ogawa, M. Ueda, and N. Imoto, *Measurement-induced oscillations of a highly squeezed state between super- and sub-Poissonian photon statistics*, Phys. Rev. Lett. **66**, 1046 (1991).

[73] T. Ogawa, M. Ueda, and N. Imoto, *Generation of the Schrodinger-cat state by continuous photodetection*, Phys. Rev. A **43**, 6458 (1991).

[74] M. Ueda, N. Imoto, H. Nagaoka, and T. Ogawa, *Continuous quantum-nondemolition measurement of photon number*, Phys. Rev. A **46**, 2859 (1992).

[75] P. K. Lam, *Applications of quantum electro-optic control and squeezed light*, PhD thesis, the Australian National University, 1998.

[76] B. C. Buchler, *Electro-optic control of quantum measurements*, PhD thesis, the Australian National University, 2001.

[77] D. A. Shaddock, *Advanced interferometry for gravitational wave detection*, PhD thesis, the Australian National University, 2000.

[78] C. W. Gardiner and M. J. Collett, *Input and output in damped quantum systems: Quantum stochastic differential equations and the master equation.*, Phys. Rev. A **31**, 3761 (1985).

[79] R. W. P. Drever, J. L. Hall, F. W. Kowalski, J. Hough, G. M. Ford, A. J. Munley, and H. Ward, *Laser phase and frequency stabilization using an optical resonator*, Appl. Phys. B **31**, 97 (1983).

[80] D. A. Shaddock, M. B. Gray, and D. E. McClelland, *Frequency locking a laser to an optical cavity by use of spatial mode interference*, Opt. Lett. **24**, 1499 (1999).

[81] K. G. Baigent, *Automatic modematching of a laser beam into an optical cavity*, Honours Thesis, the Australian National University, 1996.

[82] B. E. A. Saleh and T. C. Teich, *Fundamentals of photonics*, John Wiley and Sons, 1991.

[83] D. A. Shaddock, *Personal communication.*, (1999).

[84] R. W. Boyd, *Nonlinear optics*, Academic Press,London, 1992.

[85] R. C. Eckhardt, C. D. Nabors, W. J. Kozlovsky, and R. L. Byer, *Optical parametric oscillator frequency tuning and control*, J. Opt. Soc. Am. B **8**, 646 (1991).

[86] G. J. Milburn and D. F. Walls, *Squeezed states and intensity fluctuations*, Phys. Rev. A **27**, 392 (1983).

[87] H. M. Wiseman, M. S. Taubman, and H.-A. Bachor, *Feedback-enhanced squeezing in second harmonic generation*, Phys. Rev. A. **51**, 3227 (1995).

[88] T. J. Kane and R. L. Byer, *Monolithic, unidirectional single-mode Nd:YAG ring laser*, Opt. Lett. **10**, 65 (1985).

[89] I. Freitag and H. Welling, *Investigation on amplitude and frequency noise of injection-locked diode-pumped Nd:YAG lasers*, Appl. Phys. B **58**, 537 (1994).

[90] N. Uehara, *Ring mode cleaner for the initial LIGO 10 Watt laser*, Internal report, Ginzton Laboratory, Stanford University (1997).

[91] L. A. Lugiato, G. Strini, and F. DeMartini, *Squeezed states in 2$^{\mathrm{nd}}$-harmonic generation*, Opt. Lett. **8**, 256 (1983).

[92] A. G. White, *Classical and quantum dynamics of optical frequency conversion*, Australian National University, 1997.

[93] A. Furusawa, J. L. Sørensen, S. L. Braunstein, C. A. Fuchs, H. J. Kimble, and E. S. Polzik, *Unconditional quantum teleportation*, Science **282**, 706 (1998).

[94] Y. Furukawa, K. Kitamura, A. Alexandrovski, R. K. Route, M. M. Fejer, and G. Foulon, *Green-induced infrared absorption in MgO doped LiNbO*$_3$, Appl. Phys. Lett. **78**, 1970 (2001).

[95] A. C. Boccara, D. Fournier, and J. Badoz, *Thermo-optical spectroscopy: detection by the 'mirage effect'*, Appl. Phys. Lett. **36**, 130 (1980).

[96] S. Meshkov, *Gravitational waves, proceedings of the 3rd E. Amaldi conference, AIP conf. proc. no. 523*, AIP, New York, 2000.

[97] K. Bergman and H. A. Haus, *Squeezing in fibres with optical pulses*, Opt. Lett. **16**, 663 (1991).

[98] T. Hirano and M. Matsuoka, *Generation of broadband squeezed states pumped by CW mode-locked pulses*, Appl. Phys. B **55**, 233 (1992).

[99] K. McKenzie, D. A. Shaddock, D. E. McClelland, B. C. Buchler, and P. K. Lam, *Experimental demonstration of a squeezing-enhanced power-recycled Michelson interferometer for gravitational wave detection*, Phys. Rev. Lett. **88**, 231102 (2002).

[100] M. Shirasaki and H. A. Haus, *Squeezing of pulses in a nonlinear interferometer*, J. Opt. Soc. Am. B **7**, 30=34 (1990).

[101] T. C. Ralph and A. G. White, *Retrieving squeezing from classically noisy light in second-harmonic generation*, J. Opt. Soc. Am. B **12**, 833 (1995).

[102] Z. Y. Ou, S. F. Pereira, H. J. Kimble, and K. C. Peng, *Realization of the Einstein-Podolsky-Rosen paradox for continuous variables*, Phys. Rev. Lett. **68**, 3663 (1992).

[103] D. Deutsch, Quantum theory, the Church-Turing principle and the universal quantum computer, in *Proceedings of the Royal Society of London A, no. 400*, pages 97–117, 1985.

[104] E. Schrödinger, *Die gegenwärtige situation in der quantenmechanik*, Naturwissenschaften **23**, 807 (1935).

[105] W. P. Bowen, R. Schnabel, P. K. Lam, and T. C. Ralph, *An experimental investigation of criteria for continuous variable entanglement*, Phys. Rev. Lett. **90**, 043601 (2003).

[106] E. Knill and R. Laflamme, *Theory of quantum error-correcting codes*, Phys. Rev. A **55**, 900 (1997).

[107] J. I. Cirac and P. Zoller, *Quantum computations with cold trapped ions*, Phys. Rev. Lett. **74**, 4091 (1995).

[108] A. Kuzmich and E. S. Polzik, *Atomic quantum state teleportation and swapping*, Phys. Rev. Lett. **85**, 5639 (2000).

[109] L.-M. Duan, J. I. Cirac, P. Zoller, and E. S. Polzik, *Quantum communication between atomic ensembles using coherent light*, Phys. Rev. Lett. **85**, 5643 (2000).

[110] S. J. van Enk, J. I. Cirac, and P. Zoller, *Photonic channels for quantum communication.*, Science **279**, 205 (1998).

[111] W. P. Bowen, N. Treps, B. C. Buchler, R. Schnabel, T. C. Ralph, H.-A. Bachor, T. Symul, and P. K. Lam, *Experimental investigation of continuous variable quantum teleportation*, Phys. Rev. A. **67**, 032302 (2003).

[112] C. H. Bennett, *Quantum cryptography using any two nonorthogonal states*, Phys. Rev. Lett. **68**, 3121 (1992).

[113] A. Lance, T. Symul, W. P. Bowen, T. Tyc, B. C. Sanders, and P. K. Lam, *Continuous variable (2,3) threshold quantum secret sharing schemes*, New J. Phys. **5**, 4 (2003).

[114] E. Bleuler and H. L. Bradt, *Correlation between the states of polarization of the two quanta of annihilation radiation*, Phys. Rev. **73**, 1398 (1948).

[115] S. J. Freedman and J. F. Clauser, *Experimental test of local hidden-variable theories*, Phys. Rev. Lett. **28**, 938 (1972).

[116] C. Faraci, D. Gutkowski, S. Notarrigo, and A. R. Pennisi, *An experimental test of the EPR paradox*, Lettere Al Nuovo Cimento **9**, 607 (1974).

[117] M. Lamehi-Rachti and W. Mittig, *Quantum mechanics and hidden variables: A test of Bell's inequality by measurement of the spin correlation in low-energy proton-proton scattering*, Phys. Rev. D **14**, 2543 (1976).

[118] J. G. Rarity and P. R. Tapster, *Experimental violation of Bell's inequality based on phase and momentum*, Phys. Rev. Lett. **64**, 2495 (1990).

[119] A. Aspect, Ph. Grangier, and G. Roger, *Experimental tests of realistic local theories via Bell's theorem*, Phys. Rev. Lett. **47**, 460 (1981).

[120] A. Aspect, Ph. Grangier, and G. Roger, *Experimental realization of Einstein-Podolsky-Rosen-Bohm gedankenexperiment: a new violation of Bell's inequality*, Phys. Rev. Lett. **49**, 91 (1982).

[121] A. Aspect, J. Dalibard, and G. Roger, *Experimental test of Bell's inequality using time-varing analyzers*, Phys. Rev. Lett. **49**, 1804 (1982).

[122] C. H. Bennett, G. Brassard, C. Crepeau, R. Jozsa, A. Peres, and W. K. Wootters, *Teleporting an unknown quantum state via dual classical and Einstein-Podolsky-Rosen channels*, Phys. Rev. Lett. **70**, 1895 (1993).

[123] C. H. Bennett and S. J. Wiesner, *Communication via one- and two-particle operators on Einstein-Podolsky-Rosen states*, Phys. Rev. Lett. **69**, 2881 (1992).

[124] T. C. Ralph and E. H. Huntington, *Unconditional continuous-variable dense coding*, Phys. Rev. A. **66**, 042321 (2002).

[125] P. Hariharan and B. Sanders, *Quantum phenomena in optical interferometry*, Progress in Optics **36**, 49 (1996).

[126] Z. Y. Ou, S. F. Pereira, and H. J. Kimble, *Realization of the Einstein-Podolsky-Rosen paradox for continuous-variables in nondegenerate parametric amplification*, App. Phys. B **55**, 265 (1992).

[127] Ch. Silberhorn, P. K. Lam, O. Weiss, F. Koenig, N. Korolkova, and G. Leuchs, *Generation of continuous variable Einstein-Podolsky-Rosen entanglement via the Kerr nonlinearity in an optical fiber*, Phys. Rev. Lett. **86**, 4267 (2001).

[128] Y. Zhang, H. Wang, X. Li, J. Jing, C. Xie, and K. Peng, *Experimental generation of bright two-mode quadrature squeezed light from a narrow-band nondegenerate optical parametric amplifier*, Phys. Rev. A. **62**, 023813 (2000).

[129] C. Schori, J. L. Sørensen, and E. S. Polzik, *Narrow-band frequency tunable light source of continuous quadrature entanglement*, Phys. Rev. A **66**, 033802 (2002).

[130] L.-M. Duan, G. Giedke, J. I. Cirac, and P. Zoller, *Inseparability criterion for continuous variable systems*, Phys. Rev. Lett. **84**, 2722 (2000).

[131] A. Peres, *Separability criterion for density matrices*, Phys. Rev. Lett. **77**, 1413 (1996).

[132] P. Horodecki, *Separability criterion and inseparable mixed states with positive partial transposition*, Phys. Lett. A **232**, 333 (1997).

[133] R. Simon, *Peres-Horodecki separability criterion for continuous variable systems*, Phys. Rev. Lett. **84**, 2726 (2000).

[134] M. D. Reid and P. D. Drummond, *Quantum correlations of phase in nondegenerate parametric oscillation*, Phys. Rev. Lett. **60**, 2731 (1988).

[135] M. D. Reid, *Demonstration of the Einstein-Podolsky-Rosen paradox using nondegenerate parametric amplification*, Phys. Rev. A. **40**, 913 (1989).

[136] D. E. Browne, J. Eisert, S. Scheel1, and M. B. Plenio, *Driving non-Gaussian to Gaussian states with linear optics*, Phys. Rev. A **67**, 062320 (2003).

[137] J. Fiurásek, *Gaussian transformations and distillation of entangled Gaussian states*, Phys. Rev. Lett. **89**, 137904 (2002).

[138] J. Eisert, S. Scheel, and M. B. Plenio, *Distilling Gaussian states with Gaussian operations is impossible*, Phys. Rev. Lett. **89**, 137903 (2002).

[139] L.-M. Duan, G. Giedke, J. I. Cirac, and P. Zoller, *Entanglement purification of Gaussian continuous variable quantum states*, Phys. Rev. Lett. **84**, 4002 (2000).

[140] L.-M. Duan, G. Giedke, J. I. Cirac, and P. Zoller, *Physical implementationfor entanglement purification of Gaussian continuous-variable quantum states*, Phys. Rev. A **62**, 032304 (2000).

[141] S. Parker, S. Bose, and M. B. Plenio, *Entanglement quantification and purification in continuous-variable systems*, Phys. Rev. A. **61**, 032305 (2000).

[142] V. Giovannetti, S. Mancini, D. Vitali, and P. Tombesi, *Characterizing the entanglement of bipartite quantum systems*, Phys. Rev. A **67**, 022320 (2003).

[143] M. S. Kim, J. Lee, and W. J. Munro, *Experimentally realizable characterizations of continuous-variable Gaussian states*, Phys. Rev. A. **66**, 030301R (2002).

[144] V. Vedral, M. B. Plenio, M. A. Rippin, and P. L. Knight, *Quantifying entanglement*, Phys. Rev. Lett. **78**, 2275 (1997).

[145] M. B. Plenio and V. Vedral, *Teleportation, entanglement and thermodynamics in the quantum world*, Contemp. Phys. **39**, 431 (1998).

[146] S. Tan, *Confirming entanglement in continuous variable quantum teleportation*, Phys. Rev. A. **60**, 2752 (1999).

[147] S. Mancini, V. Giovannetti, D. Vitali, and P Tombesi, *Entangling macroscopic oscillators exploiting radiation pressure*, Phys. Rev. Lett. **88**, 120401 (2002).

[148] T. C. Ralph and P. K. Lam, *Teleportation with bright squeezed light*, Phys. Rev. Lett. **81**, 5668 (1998).

[149] S. L. Braunstein and H. J. Kimble, *Teleportation of continuous quantum variables*, Phys. Rev. Lett. **80**, 869 (1998).

[150] L. Vaidman, *Teleportation of quantum states*, Phys. Rev. A **49**, 1473 (1994).

[151] S. L. Braunstein and H. J. Kimble, *Dense coding for continuous variables*, Phys. Rev. A. **61**, 042302 (2000).

[152] C. H. Bennett, H. J. Bernstein, S. Popescu, and B. Schumacher, *Concentrating partial entanglement by local operations*, Phys. Rev. A **53**, 2046 (1996).

[153] A. G. White, D. F. V. James, W. J. Munro, and P. G. Kwiat, *Exploring Hilbert space: Accurate characterization of quantum information*, Phys. Rev. A. **65**, 012301 (2001).

[154] F. Grosshans and Ph. Grangier, *Quantum cloning and teleportation criteria for continuous quantum variables*, Phys. Rev. A. **64**, 010301R (2001).

[155] Ph. Grangier and F. Grosshans, *Quantum teleportation criteria for continuous variables*, Los Alamos ArXiv, http://arXiv.org/abs/quant-ph/0009079 (2000).

[156] C. E. Shannon, *A mathematical theory of communication*, Bell Systems Tech. J. **27**, 379 (1948).

[157] R. M. Shelby, M. D. Levenson, and P. W. Bayer, *Guided acoustic-wave Brillouin scattering*, Phys. Rev. B **31**, 5244 (1985).

[158] M. Nielsen and I. Chuang, *Quantum computation and quantum information*, Cambridge University Press, 2000.

[159] D. Gottesman and I. L. Chuang, *Demonstrating the viability of universal quantum computation using teleportation and single-qubit operations*, Nature **402**, 390 (1999).

[160] D. Bouwmeester, J. W. Pan, K. Mattle, M. Eibl, H. Weinfurter, and A. Zeilinger, *Experimental quantum teleportation*, Nature **390**, 575 (1997).

[161] M. A. Nielsen, E. Knill, and R. Laflamme, *Complete quantum teleportation using nuclear magnetic resonance*, Nature **396**, 52 (1998).

[162] Y. Zhang, K. W. Goh, C. W. Chou, P. Lodahl, and H. J. Kimble, *Quantum teleportation of light beams*, Phys. Rev. A. **67**, 033802 (2003).

[163] S. L. Braunstein, *Quantum error correction for communication with linear optics*, Nature **394**, 47 (1998).

[164] G. Leuchs, T. C. Ralph, Ch. Silberhorn, and N. Korolkova, *Scheme for the generation of entangled solitons for quantum communication*, J. Mod. Opt. **46**, 1927 (1999).

[165] J. Zhang and K. Peng, *Quantum teleportation and dense coding by means of bright amplitude-squeezed light and direct measurement of a Bell state*, Phys. Rev. A. **62**, 064302 (2000).

[166] I. V. Sokolov, M. I. Kolobov, A. Gatti, and L. A. Lugiato, *Quantum holographic teleportation*, Opt. Comm. **193**, 175 (2001).

[167] T. Ide, H. F. Hofmann, T. Kobayashi, and A. Furusawa, *Continuous-variable teleportation of single-photon states*, Phys. Rev. A. **65**, 012313 (2002).

[168] P. van Loock and S. L. Braunstein, *Multipartite entanglement for continuous variables: A quantum teleportation network*, Phys. Rev. Lett. **84**, 3482 (2000).

[169] T. C. Ralph, P. K. Lam, and R. E. S. Polkinghorne, *Characterizing teleportation in optics*, J. Opt. B. **1**, 483 (1999).

[170] D. Boschi, S. Branca, F. De Martini, L. Hardy, and S. Popescu, *Experimental realization of teleporting an unknown pure quantum state via dual classical and Einstein-Podolsky-Rosen channels*, Phys. Rev. Lett. **80**, 1121 (1998).

[171] M. C. de Oliveira, *Teleportation of a Bose-Einstein condensate state by controlled elastic collisions*, Phys. Rev. A. **67**, 022307 (2003).

[172] G. P. Berman, G. V. Lopez, and V. I. Tsifrinovich, *Teleportation in a nuclear spin quantum computer*, Phys. Rev. A. **66**, 042312 (2002).

[173] L. Vaidman and N. Yoran, *Methods for reliable teleportation*, Phys. Rev. A **59**, 116 (1999).

[174] M. C. de Oliveira and G. J. Milburn, *Discrete teleportation protocol of continuum spectra field states*, Phys. Rev. A. **65**, 032304 (2002).

[175] S. L. Braunstein, C. A. Fuchs, H. J. Kimble, and P. van Loock, *Quantum versus classical domains for teleportation with continuous variables*, Phys. Rev. A. **64**, 022321 (2001).

[176] T. C. Ralph, *Interferometric tests of teleportation*, Phys. Rev. A. **65**, 012319 (2002).

[177] B. Schumacher, *Quantum coding*, Phys. Rev. A. **51**, 2738 (1995).

[178] S. L. Braunstein, C. A. Fuchs, and H. J. Kimble, *Criteria for continuous-variable quantum teleportation*, J. Mod. Opt. **47**, 267 (2000).

[179] P. T. Cochrane and T. C. Ralph, *Tailoring teleportation to the quantum alphabet*, Phys. Rev. A **67**, 022313 (2003).

[180] E. Arthurs and M. S. Goodman, *Quantum correlations - a generalized Heisenberg uncertainty relation*, Phys. Rev. Lett. **60**, 2447 (1988).

[181] Ph. Grangier, J. A. Levenson, and J. Ph. Poizat, *Quantum non-demolition measurements in optics*, Nature **396**, 537 (1998).

[182] F. Grosshans and Ph. Grangier, *Continuous variable quantum cryptography using coherent states*, Phys. Rev. Lett. **88**, 057902 (2002).

[183] J. F. Clauser and M. A. Horne, *Experimental consequences of objective local theories*, Phys. Rev. D **10**, 526 (1974).

[184] P. van Loock and S. L. Braunstein, *Unconditional teleportation of continuous-variable entanglement*, Phys. Rev. A. **61**, 010302R (2000).

[185] J. Zhang, C. Xie, and K. Peng, *Entanglement swapping using nondegenerate optical parametric amplifier*, Phys. Lett. A. **299**, 427 (2002).

[186] C. L. Liu, *Introduction to combinatorial mathematics*, McGraw-Hill, New York, 1968.

[187] A. Shamir, *How to share a secret*, Comm. of the ACM **22**, 612 (1979).

[188] M. Hillery, V. Buzek, and A. Bethiaume, *Quantum secret sharing*, Phys. Rev. A. **59**, 1829 (1992).

[189] A. Karlsson, M. Koashi, and N. Imoto, *Quantum entanglement for secret sharing and secret splitting*, Phys. Rev. A. **59**, 162 (1999).

[190] W. Tittel, H. Zbinden, and N. Gisin, *Experimental demonstration of quantum secret sharing*, Phys. Rev. A. **63**, 042301 (2001).

[191] T. Tyc and B. C. Sanders, *How to share a continuous-variable quantum secret by optical interferometry*, Phys. Rev. A **65**, 042310 (2002).

[192] T. Tyc, D. J. Rowe, and B. C. Sanders, *Efficient sharing of a continuous-variable quantum secret*, J. Phys. A:Math. Gen. **36**, 7625 (2003).

[193] M. Bayer, P. Hawrylak, K. Hinzer, S. Fafard, M. Korkusinski, Z. R. Wasilewski, O. Stern, and A. Forchel, *Coupling and entangling of quantum states in quantum dot molecules*, Science **291**, 451 (2001).

[194] G. J. Pryde, M. J. Sellars, and N. B. Manson, *Solid state coherent transient measurements using hard optical pulses*, Phys. Rev. Lett. **84**, 1152 (2000).

[195] Ch. Roos, Th. Zeiger, H. Rohde, H. C. Nägerl, J. Eschner, D. Leibfried, F. Schmidt-Kaler, and R. Blatt, *Quantum state engineering on an optical transition and decoherence in a Paul trap*, Phys. Rev. Lett. **83**, 4713 (1999).

[196] C. A. Sackett, D. Kielpinski, B. E. King, C. Langer, V. Meyer, C. J. Myatt, M. Rowe, Q. A. Turchette, W. M. Itano, D. J. Wineland, and C. Monroe, *Experimental entanglement of four particles*, Nature **404**, 256 (2000).

[197] C. J. Hood, T. W. Lynn, A. C. Doherty, A. S. Parkins, and H. J. Kimble, *The atom-cavity microscope: single atoms bound in orbit by single photons*, Science **287**, 1447 (2000).

[198] P. W. H. Pinkse, T. Fischer, T. P. Maunz, and G. Rempe, *Trapping an atom with single photons*, Nature **404**, 365 (2000).

[199] J. McKeever, A. Boca, A. D. Boozer, J. R. Buck, and H. J. Kimble, *Experimental realization of a one-atom laser in the regime of strong coupling*, Nature **425**, 268 (2003).

[200] J. E. Mooij, T. P. Orlando, L. Levitov, L. Tian, C. H. van der Wal, and S. Lloyd, *Josephson persistent-current qubit*, Science **285**, 1036 (1999).

[201] A. Kuzmich, L. Mandel, and N. P. Bigelow, *Generation of spin squeezing via continuous quantum non-demolition measurements*, Phys. Rev. Lett. **85**, 1594 (2000).

[202] B. Julsgaard, A. Kozhekin, and E. S. Polzik, *Experimental long-lived entanglement of two macroscopic objects*, Nature **413**, 400 (2001).

[203] W. P. Bowen, R. Schnabel, H.-A. Bachor, and P. K. Lam, *Polarization squeezing of continuous variable Stokes parameters*, Phys. Rev. Lett. **88**, 093601 (2002).

[204] W. P. Bowen, N. Treps, R. Schnabel, and P. K. Lam, *Experimental demonstration of continuous variable polarization entanglement*, Phys. Rev. Lett. **89**, 253601 (2002).

[205] H.-J. Briegel, W. Duer, J. I. Cirac, and P. Zoller, *Proposal for teleportation of an atomic state via cavity decay.*, Phys. Rev. Lett. **81**, 5932 (1999).

[206] A. Kuzmich, W. P. Bowen, A. D. Boozer, A. Boca, C. W. Chou, L.-M. Duan, and H. J. Kimble, *Generation of nonclassical photon pairs for scalable quantum communication with atomic ensembles*, Nature **423**, 731 (2003).

[207] L.-M. Duan, *Entangling many atomic ensembles with laser manipulation*, Phys. Rev. Lett. **88**, 170402 (2002).

[208] J. S. Bell, *Speakable and unspeakable in quantum mechanics*, Cambridge Univ. Press, Cambridge, 1988.

[209] J. F. Clauser and A. Shimony, *Bell's theorem. Experimental tests and implications*, Rep. Prog. Phys. **41**, 1881 (1978).

[210] S. Wiesner, *Conjugate coding*, Sigact News **15**, 78 (1983).

[211] C. H. Bennett and G. Brassard, Quantum cryptography: public key distribution and coin tossing, in *Proceedings of IEEE International Conference on Computers, Systems and Signal Processing, Bangalore, India*, pages 175–179, 1984.

[212] A. K. Ekert, *Quantum cryptography based on Bell's theorem*, Phys. Rev. Lett. **67**, 661 (1991).

[213] G. S. Agarwal and R. R. Puri, *Quantum theory of propagation of elliptically polarized light through a Kerr medium*, Phys. Rev. A. **40**, 5179 (1989).

[214] A. S. Chirkin, A. A. Orlov, and D. Yu. Paraschuk, *Quantum theory of two-mode interactions in optically anisotropic media with cubic nonlinearities: generation of quadrature- and polarization-squeezed light*, Kvantovaya Elektronika **20**, 999 (1993).

[215] A. S. Chirkin, A. A. Orlov, and D. Yu. Paraschuk, *Quantum theory of two-mode interactions in optically anisotropic media with cubic nonlinearities: generation of quadrature- and polarization-squeezed light*, Quantum Electron. **23**, 870 (1993).

[216] A. P. Alodjants, S. M. Arakelian, and A. S. Chirkin, *Polarization quantum states of light in nonlinear distributed feedback systems; quantum nondemolition measurements of the Stokes parameters of light and atomic angular momentum*, Appl. Phys. B **66**, 53 (1998).

[217] N. V. Korolkova and A. S. Chirkin, *Formation and conversion of the polarization-squeezed light*, J. Mod. Opt. **43**, 869 (1996).

[218] N. V. Korolkova, G. Leuchs, R. Loudon, T. C. Ralph, and C. Silberhorn, *Polarization squeezing and continuous-variable polarization entanglement*, Phys. Rev. A. **65**, 052306 (2002).

[219] A. P. Alodjants, S. M. Arakelian, and A. S. Chirkin, *Interaction of two polarization modes in a spatio-periodic nonlinear medium: generation of polarization-squeezed light and quantum non-demolition measurements of the Stokes parameters*, Quant. Semiclass. Opt. **9**, 311 (1997).

[220] A. P. Alodjants, A. Y. Leksin, A. V. Prokhorov, and S. M. Arakelian, *Quantum logic gates based on macroscopic nonclassical polarization states of light*, Laser Phys. **12**, 956 (2002).

[221] T. C. Ralph, W. J. Munro, and R. E. S. Polkinghorne, *Proposal for the measurement of Bell-type correlations from continuous variables*, Phys. Rev. Lett. **85**, 2035 (2000).

[222] Ph. Grangier, R. E. Slusher, B. Yurke, and A. LaPorta, *Squeezed light-enhanced polarization interferometer*, Phys. Rev. Lett. **59**, 2153 (1987).

[223] J. Schwinger, U.S. atomic energy commission report No. NYO-3071 (U.S. GPO, Washington, DC, 1952); reprinted in *Quantum theory of angular momentum*, edited by L. C. Biedenharn and H. van Dam (Academic, New York, 1965).

[224] J. Heersink, T. Gaber, S. Lorenz, O. Glöckl, N. Korolkova, and G. Leuchs, *Polarization squeezing of intense pulses with a fiber-optic Sagnac interferometer*, Phys. Rev. A **68**, 013815 (2003).

[225] V. Josse, A. Dantan, L. Vernac, A. Bramati, M. Pinard, and E. Giacobino, *Polarization squeezing with cold atoms*, Phys. Rev. Lett. **91**, 103601 (2003).

[226] U. L. Andersen and P. Buchhave, *Polarization squeezing and entanglement produced by a frequency doubler*, J. Opt. B. **5**, S486S491 (2003).

[227] V. Josse, A. Dantan, A. Bramati, M. Pinard, and E. Giacobino, *Polarization squeezing in a four-level system*, J. Opt. B **5**, S513S522 (2003).

[228] G. S. Agarwal and S. Chaturvedi, *Scheme to measure quantum Stokes parameters and their fluctuations and correlations*, J. Mod. Opt. **50**, 711 (2003).

[229] G. G. Stokes, *On the composition and resolution of streams of polarized light from different sources*, Trans. Camb. Phil. Soc. **9**, 399 (1852).

[230] L. Mandel and E. Wolf, *Optical coherence and quantum optics*, Cambridge University Press, Cambridge, 1995.

[231] J. M. Jauch and F. Rohrlich, *The theory of photons and electrons*, Springer, Berlin, second edition, 1976.

[232] B. A. Robson, *The theory of polarization phenomena*, Clarendon, Oxford, 1974.

[233] M. Kaku, *Quantum field theory*, Oxford University Press, New York, 1993.

[234] Y. Yamamoto and H. A. Haus, *Preparation, measurement and information capacity of optical quantum states*, Rev. Mod. Phys. **58**, 1001 (1986).

[235] C. M. Caves and P. D. Drummond, *Quantum limits on bosonic communication rates*, Rev. Mod. Phys. **66**, 481 (1994).

[236] O. Glöckl, J. Heersink, N. Korolkova, G. Leuchs, and S. Lorenz, *A pulsed source of continuous variable polarization entanglement*, J. Opt. B **5**, S492 (2003).

[237] V. Josse, A. Dantan, A. Bramati, M. Pinard, and E. Giacobino, *Continuous variable entanglement using cold atoms*, Available online: http://arXiv.org/abs/quant-ph/0306152 (2003).

[238] C. Simon and D. Bouwmeester, *Theory of an entanglement laser*, Phys. Rev. Lett. **91**, 053601 (2003).

[239] M. O. Scully and M. S. Zubairy, *Quantum optics*, Cambridge University Press, U.K., 1997.

[240] C. W. Gardiner and P. Zoller, *Quantum noise*, Springer, Berlin, second edition, 2000.

[241] D. P. DiVincenzo, *The physical implementation of quantum computation.*, Fortschr. Phys. **48**, 771 (2000).

[242] J. Ye, D. W. Vernooy, and H. J. Kimble, *Trapping of single atoms in cavity QED*, Phys. Rev. Lett. **83**, 4987 (1999).

[243] D. F. Phillips, A. Fleischhauer, A. Mair, R. L. Walsworth, and M. D. Lukin, *Storage of light in atomic vapor*, Phys. Rev. Lett. **86**, 783 (2001).

[244] C. Liu, Z. Dutton, C. H. Behroozi, and L. V. Hau, *Observation of coherent optical information storage in an atomic medium using halted light pulses*, Nature **409**, 490 (2001).

[245] L.-M. Duan and H. J. Kimble, *Efficient engineering of multi-atom entanglement through single-photon detections*, Phys. Rev. Lett. **90**, 253601 (2003).

[246] S. Bose, P. L. Knight, M. B. Plenio, and V. Vedral, *Proposal for teleportation of an atomic state via cavity decay.*, Phys. Rev. Lett. **83**, 5158 (1999).

[247] R. Raussendorf and H. J. Briegel, *A one-way quantum computer.*, Phys. Rev. Lett. **86**, 5188 (2001).

[248] J. F. Clauser, *Experimental distinction between the quantum and classical field-theoretic predictions for the photoelectric effect.*, Phys. Rev. D **9**, 853 (1974).

[249] L. Mandel, *Quantum effects in one-photon and two-photon interference.*, Rev. Mod. Phys. **71**, S274 (1999).

[250] H. J. Metcalf and P. van der Straten, *Laser cooling and trapping*, Springer-Verlag, 1999.

[251] C. H. van der Wal, M. D. Eisaman, A. André, R. L. Walsworth, D. F. Phillips, A. S. Zibrov, and M. D. Lukin, *Atomic memory for correlated photon states*, Science **301**, 196 (2003).

[252] M. G. Raymer and J. Mostowski, *Stimulated Raman scattering: Unified treatment of spontaneous initiation and spatial propagation*, Phys. Rev. A **24**, 1980 (1981).

[253] L.-M. Duan, J. I. Cirac, and P. Zoller, *Three-dimensional theory for interaction between atomic ensembles and free-space light*, Phys. Rev. A. **66**, 023818 (2002).

[254] M. Kitagawa and M. Ueda, *Nonlinear-interferometric generation of number-phase correlated fermion states.*, Phys. Rev. Lett. **67**, 1852 (1991).

[255] D. J. Wineland, J. J. Bollinger, W. M. Itano, and F. L. Moore, *Spin squeezing and reduced quantum noise in spectroscopy*, Phys. Rev. A. **46**, R6797 (1992).

[256] A. Kuzmich, N. P. Bigelow, and L. Mandel, *Atomic quantum non-demolition measurements and squeezing*, Europhys. Lett. A **42**, 481 (1998).

[257] K. Mølmer, *Twin-correlations in atoms*, Eur. Phys. J. D **5**, 301 (1999).

[258] M. Fleischhauer and M. D. Lukin, *Dark-state polaritons in electromagnetically induced transparency.*, Phys. Rev. Lett. **84**, 5094 (2000).

[259] R. J. Glauber, *Coherent and incoherent states of the radiation field*, Phys. Rev. **131**, 2766 (1963).

[260] E. C. G. Sudarshan, *Equivalence of semiclassical and quantum mechanical descriptions of statistical light beams*, Phys. Rev. Lett. **10**, 277 (1963).

[261] E. B. Alexandrov, M. V. Balabas, A. S. Pasgalev, A. K. Verkhovskii, and N. N. Yakobson, *Double-resonance atomic magnetometers: from gas discharge to laser pumping*, Laser Physics **6**, 244 (1996).

[262] C. W. Chou, S. V. Polyakov, A. Kuzmich, and H. J. Kimble, *Single-photon generation from stored excitation in an atomic ensemble*, Los Alamos ArXiv, http://arXiv.org/abs/quant-ph/0401147 (2004).

[263] M. Pelton, C. Santori, J. Vučković, B. Zhang, G. S. Solomon, J. Plant, and Y. Yamamoto, *Efficient source of single photons: A single quantum dot in a micropost microcavity*, Phys. Rev. Lett. **89**, 233602 (2002).

[264] C. Schori, B. Julsgaard, J. L. Sørensen, and E. S. Polzik, *Recording quantum properties of light in a long-lived atomic spin state: towards quantum memory*, Phys. Rev. Lett. **89**, 057903 (2002).